THÈSE POUR OBTENIR LE GRADE DE DOCTEUR DE L'UNIVERSITÉ DE MONTPELLIER

En Chimie et Physico-Chimie des Matériaux

École doctorale Sciences Chimiques Balard (ED 459)

Institut Charles Gerhardt UMR 5253
Institut des Biomolécules Max Mousseron UMR 5247

Plateformes multimodales ciblant l'anhydrase carbonique pour l'imagerie et la thérapie synergique de tumeurs

Présentée par Amina MERABTI

Le 04 décembre 2023

Sous la direction du Pr. Sébastien CLEMENT

et du Pr. Jean-Yves WINUM

Devant le jury composé de

Dr. Isabelle BONNAMOUR, Maître de Conférences HDR, Université Claude Bernard-Lyon 1	Rapportrice
Dr. Christine PAUL-ROTH, Maître de Conférences HDR, Université de Rennes	Rapportrice
Dr. Céline FROCHOT, Directrice de Recherche CNRS, Université de Lorraine	Présidente du Jury
Dr. Sébastien RICHETER, Maître de Conférences HDR, Université de Montpellier	Examinateur
Pr. Sébastien CLEMENT, Professeur des Universités, Université de Montpellier	Directeur de thèse
Pr. Jean-Yves WINUM, Professeur des Universités, Université de Montpellier	Co-directeur de thèse

UNIVERSITÉ DE MONTPELLIER

Remerciements

Je tiens tout d'abord à remercier le Ministère de l'Enseignement Supérieur de la Recherche Scientifique Algérien pour la bourse d'excellence qui m'a été octroyée et qui a permis le financement de cette thèse.

Je souhaite également remercier les Docteurs Isabelle BONNAMOUR, Christine PAUL-ROTH et Céline FROCHOT ainsi que le Docteur Sébastien RICHETER pour avoir aimablement acceptés d'évaluer mon travail de thèse. Je suis très honorée de votre présence au sein de mon jury de soutenance de thèse.

Je tiens aussi à exprimer ma profonde gratitude envers mes directeurs de thèse les Professeurs Sébastien CLEMENT et Jean-Yves WINUM, qui m'ont fait confiance pour mener à bien cette thèse. Je vous remercie pour votre encadrement, votre disponibilité et votre temps. Je tiens à vous remercier chaleureusement pour votre investissement envers mon travail *via* les corrections de ce manuscrit (même pendant les week-ends), les relectures d'abstracts, des posters et des communications orales.

Je veux adresser mes sincères remerciements à l'ensemble des collaborateurs qui ont participé à la réussite de ce travail.

Un grand merci à toutes les personnes qui ont égayé ma vie au sein du laboratoire. Merci pour votre bonne humeur et les beaux moments que nous avons passés ensemble.

Je tiens à remercier mes parents et mes sœurs qui ont toujours porté un intérêt à mon travail. Merci pour votre soutien et vos encouragements.

Je tiens à remercier mon fiancé qui m'a toujours soutenue et encouragée durant les trois ans de cette thèse. Merci pour ton optimisme et ton amour. Merci de m'avoir épaulée et supportée pendant ces années.

Enfin, je souhaiterais remercier toutes les personnes ayant contribué de près ou de loin à la concrétisation de ce projet.

Merci !

List of Abbreviations

A

A: Acceptor

AAZ: Acetazolamide

Abs: Absorbance

ABDA: 9,10-anthracenediyl-bis(methylene)dimalonic acid

ACQ: Aggregation Caused Quenching

AIE: Aggregation Induced Emission

AIEgen: Aggregation Induced Emission Luminogen

ATR-FTIR: Attenuated Total Reflectance Fourier Transform InfraRed

C

CA: Carbonic anhydrase

CAI: Carbonic anhydrase inhibitor

Capan-1: Pancreas cancer cell line

$CHCl_3$: Chloroform

CH_3CN: Acetonitrile

D

DMSO: Dimethyl sulfoxide

DDQ: 2,3-Dichloro-5,6-dicyano-1,4-benzoquinone

D: Donor

DCM: Dichloromethane

DIPA: *N*,*N*-Diisopropylethylamine

DFT: Density functional theory

DLI: Daily light integral

DLS: Dynamic Light Scattering

DMA: 9,10-Dimethylanthracene

DMF: *N,N*-dimethylformamide

F

FRET: Förster resonance energy transfer

H

HIF: Hypoxia-Inducible Factor

HOMO: Highest Occupied Molecular Orbital

HRMS: High resolution mass spectrometry

I

ISC : Intersystem crossing

L

LDL: Low-density lipoprotein

LUMO : Lowest Unoccupied Molecular Orbital

N

NPs: Nanoparticles

NIR: Near infrared

NMR: Nuclear Magnetic Resonance

P

PEG : Poly(ethylene glycol)

PS: Photosensitizer

PDT: Photodynamic therapy

PTT: Photothermal therapy

R

RIM: Restriction of Intramolecular Movement

RIR: Restriction of Intramolecular Rotation

RIV: Restriction of Intramolecular Vibration

ROS: Reactive Oxygen Ppecies

S

SOC: Spin-Orbital Coupling

T

TCI: Thiochromenocarbazole Imide

TEA: Triethylamine

TFA: Trifluoroacetic Acid

THF: Tetrahydrofuran

TME: Tumor microenvironment

T_n: triplet state

TPE: 1,1,2,2-tetraphenylethene

TOF: Time of flight

U

UV-Vis: Ultraviolet-visible

Table of Contents

Chapter I: General introduction and thesis outlines

I. Photodynamic therapy 1

I.1 History of Photodynamic therapy 1

I.2 Mechanism of PDT: 3

I.3 Light Sources: 4

I.4 Subcellular localization 5

I.5 Mechanism of Cell Death in Photodynamic Therapy 6

I.5.1 Apoptosis 7

I.5.2 Necrosis 7

I.5.3 Immunological Mechanisms 8

I.6 Photosensitizers in PDT 8

I.6.1 First generation PS 9

I.6.2 Second generation PS 9

I.6.3 Third generation PS 10

I.7 Molecular Design Strategies for PS 13

I.7.1 PSs Based on conventional Core Structures 13

I.7.2 Attaching Heavy Atoms 14

I.7.3 AIEgens based PSs 16

I.7.3.1 AIE mechanisms 17

I.7.3.2 Examples of AIEgens based PS 17

I.8 Combination Therapy 20

I.9 Advantages and applications of PDT 22

I.10 Challenges of PDT 23

I.10.1 Tumor- targeting efficiency 23

I.10.2 Light propagation through Tissues 23

I.10.3 Tumor Hypoxia 24

II. Carbonic anhydrases 25

II.1 Structure of hCAs 26

II.2 Catalytic mechanisms of hCAs 27

II.3 Expression of hCA IX and hCA XII 28

II.4 Pathologies associated to hCAs 29

II.5 Inhibitors of hCAs 31

II.6 Inhibition mechanism of hCAs 31

II.6.1 The zinc binders as CAIs 31
II.6.2 CAIs anchoring to the zinc-coordinated water/hydroxide ion 32
II.6.3 CA inhibition by occlusion of the active site entrance 32
II.6.4 Out of the active site binding 32
III. Objectives of thesis 34
IV. Outlines of thesis 35
V. References: 36
I. Abstract 48
I.1 Area Covered 48
I.2 Expert Opinion 48
I.3 Article highlights 49
II. Introduction 50
III. Carbonic anhydrase inhibitors with potential applications in photodynamic therapy 53
IV. Conclusion 60
V. Expert opinion 60
VI. References: 64
I. Abstract: 70
II. Introduction: 71
III. Results and Discussion 73
III.1 Design and synthesis 73
III.2 Optical properties 75
III.3 Singlet oxygen ($^1O_2$) generation 77
III.4 Carbonic anhydrase inhibition assays 78
III.5 Biological assays 79
III.6 Conclusion 82
III.7 Experimental Section 82
IV. References 85
VI. Supplementary data 88
IV.1 Chemistry 88
IV.1.1 Materials 88
IV.1.2 Instruments and methods 88
IV.1.3 Synthesis 89

IV.2 Characterization 91
IV.3 Optical properties 109
IV.4 CA inhibition assays 111
IV.5 Biological assays 112
I. Abstract 116
II. Introduction 117
III. Results and discussion 118
III.1 Design and synthesis 118
III.2 Optical properties 119
III.3 Carbonic anhydrase inhibition assays 121
III.4 Biological studies *in vitro* 122
III.5 Biological studies *in vivo* 123
III.6 Conclusions 125
IV. References 126
V. Supplementary data 130
V.1 Chemistry 130
V.1.1 Materials 130
V.2 General instruments 130
V.3 Synthesis and characterization 131
V.4 Optical properties 144
V.5 CA inhibition assays 145
V.6 Biological assays 146
I. Abstract 152
II. Introduction 153
III. Results and Discussion 158
III.1 Design and synthesis 158
III.2 Optical properties 161
III.3 Carbonic anhydrase inhibition assays 163
III.4 Singlet oxygen ($^1O_2$) generation 164
IV. Conclusion 166
V. Experimental section 166
V.1 Materials 166
V.2 Instruments and methods 166
V.3 Synthesis 167

VII. References: 172
General Conclusion 178
Future Perspectives.....179
Résumé en français 180
Résumé en français 182
Résumé 188
Abstract 188

List of figures

Chapter I

Figure 1. Representation of the clinical application of PDT 3

Figure 2. Modified Jablonski diagram of the PDT action mechanism 4

Figure 3. Light Propagation through the Tissues 5

Figure 4. (a) Main targets during PDT and (b) their related effects on cell death 5

Figure 5. Cytolytic activity of oxygen-consumed PDT 7

Figure 6. Basic structures of some examples of photosensitizers used in PDT 8

Figure 7. Structures of first generation PS 9

Figure 8. Structures of some second-generation PSs 10

Figure 9. Some examples of third generation PSs (conjugated with targeting agents) 11

Figure 10. Structure of PSs Approved for Anticancer PDT 12

Figure 11. Molecular structure of Radachlorin: chlorin e6 (I), chlorin p6 (II) and purpurin (III) 13

Figure 12. Physical model of $^1O_2$ generation, depicting the S_1–T_1 ISC process and the proposed strategy for increasing $^1O_2$ generation 15

Figure 13. Structure of D–A–D PS obtained adapted 16

Figure 14. Fluorescence images of solutions or suspensions of perylene and 1,1,2,3,4,5-hexaphenylsilole in THF/water mixtures with different fractions of water (f_w) 16

Figure 15. Representative examples of AIEgens and their working mechanisms 17

Figure 16. **(A)** Schematic illustration of T-TTD NP, **(B)** Growth inhibition of MDA-MB-231, MCF-7 and NIH 3T3 cells in the presence of different concentrations of T-TTD NPs with light irradiation (0.25 W cm−2, 2 min), Cell apoptosis imaging using FITC-tagged Annexin V in MDA-MB-231, **(C)** MCF-7, **(D)** NIH 3T3 (E) cells incubated with T-TTD NPs after light irradiation 18

Figure 17. illustration of Chemical structures of WP5, P5 and G. 19

Figure 18. Illustration of synthesis and application of BTPE NPs for improved PDT 20

Figure 19. (A) Structures of berberine dimers BD1-BD3 and tetramer BD4,**(B)** Construction de nanocomposites AuNSs- BD3 @HA 22

Figure 20. Hydration of CO_2 reaction catalyzed by carbonic anhydrase (hCA II). 25

Figure 21. Ribbon diagram of hCA II structure, which has been chosen as representative hCA isoform. The active site Zn^{2+}..... 26
Figure 22. The active site of hCA II..... 27
Figure 23. Catalytic mechanism of reversible hydration of CO_2 to HCO_3^- and a proton in the presence of α-CAs 28
Figure 24. Regulation of hypoxia-induced gene expression mediated by the HIF-1 transcription factor 29
Figure 25. Some hCAIs structures 31
Figure 26. Mechanism of CA inhibition..... 33

Chapter II

Figure 27. The photochemical reactions involved in type I and type II PDT..... 51
Figure 28. hCA IX-targeted PDT strategy with a conjugate hCA IX inhibitor (CAi) – photosensitizer (Ps)..... 52
Figure 29. Examples of selected Ps systems conjugated with CA inhibitors. 54
Figure 30. Structure of porphyrin-CA Inhibitor hybrid molecules. 55
Figure 31. Selected structures of photoactivated metal complexes bearing CA inhibitors. ... 56
Figure 32. Structures of selected BODIPY based carbonic anhydrase IX inhibitors. 58

Chapter III

Figure 33. Structure of CAI-PS..... 73
Figure 34. UV-Visible absorption and emission spectra of porphyrin 6 76
Figure 35. Emission spectra of **Coum-prop,** porphyrin **6**, and porphyrin **7**, in DMSO..... 77
Figure 36. Time dependent photodecomposition of DMA photosensitized by porphyrins **5**, **6**, **7** and **ZnTPP**..... 78
Figure 37. Cytotoxic study of compounds..... 80
Figure 38. Fluorescence imaging of pancreas cancer cells (Capan-1) incubated with porphyrins **5**, **6** and **7**.. 81
Figure 39. Analysis of PDT efficiency.. 81
Figure 40. ^{1}H NMR spectrum of compound **(2-[2-(2-Hydroxyethoxy)ethoxy]ethyl 4-methylbenzenesulfonate) (A)**. 91
Figure 41. $^{13}C\{^1H\}$ NMR spectrum of compound **(2-[2-(2-Hydroxyethoxy)ethoxy]ethyl 4-methylbenzenesulfonate) (A)**. 91

Figure 42. ATR-FTIR spectrum of compound **(2-[2-(2-Hydroxyethoxy)ethoxy]ethyl 4-methylbenzenesulfonate) (A).** 92
Figure 43. High resolution ESI-TOF mass spectrum of compound **(2-[2-(2-hydroxyethoxy)ethoxy]ethyl 4-methylbenzenesulfonate) (A).** 92
Figure 44. ^{1}H NMR spectrum of compound **2 (2-(2-(2-azidoethoxy)ethoxy)ethanol) (B).** 93
Figure 45. $^{13}C\{^{1}H\}$ NMR spectrum of compound **2 (2-(2-(2-azidoethoxy)ethoxy)ethanol) (B)** 93
Figure 46. ATR-FTIR spectrum of compound **(2-(2-(2-azidoethoxy)ethoxy)ethanol) (B).** 94
Figure 47. High resolution ESI-TOF mass spectrum of compound **(2-(2-(2-azidoethoxy)ethoxy)ethanol) (B).** 94
Figure 48. ^{1}H NMR spectrum of compound **(2-(2-(2-Azidoethoxy)ethoxy)ethyl 4-methylbenzenesulfonate) (1).** 95
Figure 49. $^{13}C\{^{1}H\}$ NMR spectrum of compound **(2-(2-(2-azidoethoxy)ethoxy)ethyl 4-methylbenzenesulfonate) (1).** 95
Figure 50. ATR-FTIR spectrum of compound **(2-(2-(2-azidoethoxy)ethoxy)ethyl 4-methylbenzenesulfonate) (1).** 96
Figure 51. High resolution ESI-TOF mass spectrum of compound **1 (2-(2-(2-azidoethoxy)ethoxy)ethyl 4-methylbenzenesulfonate) (1).** 96
Figure 52. ^{1}H NMR spectrum of compound **4 (4-[2-[2-(2-Azidoethoxy)ethoxy]ethoxy]benzaldehyde) (2).** 97
Figure 53. $^{13}C\{^{1}H\}$ NMR spectrum of compound **4 (4-[2-[2-(2-Azidoethoxy)ethoxy]ethoxy]benzaldehyde) (2).** 97
Figure 54. FTIR-ATR spectrum of **4 (4-[2-[2-(2-Azidoethoxy)ethoxy]ethoxy]benzaldehyde) (2).** 98
Figure 55. High resolution ESI-TOF (positive mode) mass spectrum of **compound 4 (4-[2-[2-(2-Azidoethoxy)ethoxy]ethoxy]benzaldehyde) (2).** 98
Figure 56. ^{1}H NMR spectrum (400 MHz, $CDCl_3$, 298K) of porphyrin **3.** 99
Figure 57. $^{13}C\{^{1}H\}$ NMR spectrum (126 MHz, $CDCl_3$, 298K) of porphyrin **3.** 99
Figure 58. ATR-FTIR spectrum of porphyrin **3.** 100
Figure 59. High resolution ESI-TOF (positive mode) mass spectrum of porphyrin **3.** 100
Figure 60. ^{1}H NMR spectrum (400 MHz, $CDCl_3$, 298K) of porphyrin **4**. 101
Figure 61. $^{13}C\{^{1}H\}$ NMR spectrum (126 MHz, $CDCl_3$, 298K) of porphyrin **4.** 101

Figure 62. ATR-FTIR spectrum of porphyrin **4.** 102
Figure 63. High resolution ESI-TOF (positive mode) mass spectrum of porphyrin **4.** 102
Figure 64. ^{1}H NMR spectrum (400 MHz, $[D_6]$DMSO, 298K) of porphyrin **5.** 103
Figure 65. $^{13}C\{^{1}H\}$ NMR spectrum (126 MHz, $[D_6]$DMSO, 298K) of porphyrin **5** 103
Figure 66. ATR-FTIR spectrum of porphyrin **5.** 104
Figure 67. High resolution ESI-TOF mass spectrum of porphyrin **5.** 104
Figure 68. ^{1}H NMR spectrum of porphyrin **6.** 105
Figure 69. $^{13}C\{^{1}H\}$ NMR spectrum of porphyrin **6.** 105
Figure 70. ATR-FTIR spectrum of porphyrin **6.** 106
Figure 71. High resolution ESI-TOF mass spectrum of porphyrin **6.** 106
Figure 72. ^{1}H NMR spectrum of porphyrin **7.** 107
Figure 73. $^{13}C\{^{1}H\}$ NMR spectrum of porphyrin **7**. 107
Figure 74. ATR-FTIR spectrum of porphyrin **7.** 108
Figure 75. High resolution ESI-TOF mass spectrum of porphyrin **7**. 108
Figure 76. UV-Visible and emission spectra of porphyrin **5** 109
Figure 77. UV-Visible absorption and emission spectra of porphyrin **7** 109
Figure 78. UV-Visible absorption and emission spectra of Coum-prop in DMSO. 110
Figure 79. Excitation spectra of porphyrins **6** and **7**. 110
Figure 80. UV-Visible absorption spectrum of porphyrin 6 and emission spectrum of Coum-prop and **5** 111

Chapter IV

Figure 81. UV-visible absorption and emission spectra of CAi-CTI 4 120
Figure 82. (A) Toxicity study in human breast cancer cell line (MDA-MB 231) incubated with **4**, **6**, **7**. **(B)** Phototoxic effect of **4**, **6**, **7** on MDA-MB 231 cells **(C)** Confocal microscopy imaging of living MDA-MB-231 cells incubated with **4**, **6**, **7** 122
Figure 83. Casper zebrafish embryos injected with 10 nL of **4**, **6**, **7** 124
Figure 84. **(A)** Casper zebrafish embryos injected with **4**. **(B)** 24 h after injection. **(C)** The fluorescence intensity of the xenografts before and 24 h after irradiation 125
Figure 85. ^{1}H NMR spectrum of compound **3**. 134
Figure 86. $^{13}C\{^{1}H\}$ NMR spectrum of compound **3**. 134
Figure 87. High resolution ESI-TOF mass spectrum of compound **3**. 135

Figure 88. ATR-FTIR spectrum of compound **3.** 135
Figure 89. ^{1}H NMR spectrum of compound **4**. 136
Figure 90. $^{13}C\{^{1}H\}$ NMR spectrum of compound **4**. 136
Figure 91. High resolution ESI-TOF mass spectrum of compound **4**. 137
Figure 92. ATR-FTIR spectrum of compound **4**. 137
Figure 93. ^{1}H NMR spectrum of compound **5**. 138
Figure 94. $^{13}C\{^{1}H\}$ NMR spectrum of compound **5**. 138
Figure 95. High resolution ESI-TOF mass spectrum of compound **5**. 139
Figure 96. ATR-FTIR spectrum of compound **5**. 139
Figure 97. ^{1}H NMR spectrum of compound **6**. 140
Figure 98. $^{13}C\{^{1}H\}$ NMR spectrum of compound **6**. 140
Figure 99. High resolution ESI-TOF mass spectrum of compound **6**. 141
Figure 100. ATR-FTIR spectrum of compound **6.** 141
Figure 101. ^{1}H NMR spectrum of compound **7**. 142
Figure 102. $^{13}C\{^{1}H\}$ NMR spectrum of compound **7**. 142
Figure 103. High resolution ESI-TOF mass spectrum of compound **7**. 143
Figure 104. ATR-FTIR spectrum of compound **7.** 143
Figure 105. UV-visible absorption and emission spectra of compound **5** 144
Figure 106. UV-visible absorption and emission spectra of compound **6** 144
Figure 107. UV-visible absorption and emission spectra of compound **6**. 145

Chapter V

Figure 108. Examples of recent structure of PS systems conjugated with CA inhibitors. 154
Figure 109. Comparison of the evolution of the fluorescence between a « ACQ » fluorophore like perylene and an AIE fluorophore like 1,1,2,3,4,5-hexaphenylsilole (HPS) in function of water content. 155
Figure 110. Examples of some AIEgens structure used as PSs for photodynamic therapy. .. 157
Figure 111. Structure of AIE PS for photodynamic therapy. 158
Figure 112. UV-Visible absorption spectra of TPEs **9**, **15a** and **15b** 162
Figure 113. **A)** Emission spectra of TPEs **9**, **15a** and **15b B)** Plot of I/I_0 values vs. water fractions. 163

Figure 114. Time-dependent absorption changes of a ABDA solution in water without PS or with **RB**, **9**, **15a** and **15b** 165

List of tables

Chapter I

Table 1. Photosensitizers Approved for Anticancer PDT adapted from. 12
Table 2. Diseases related to α-hCAs adapted from..... 30

Chapter II

Table 3. Summary of key conditions used in hCA IX/XII-targeted photodynamic therapy. 59
Table 4. Advantages and drawbacks of the main selected CAi featuring Ps. 61

Chapter III

Table 5. Photophysical data of porphyrins **5**-**7**. 76
Table 6. Inhibitory activity of compounds **4**-**7** against **hCA I**, **hCA II**, **hCA IX** and **hCA XII** 79

Chapter IV

Table 7. Summary of the main spectroscopic and photophysical data for all studied CAi-CTI hybrid systems. 120
Table 8. Inhibitory activity of CAi-CTI **4**–**7** against **hCA I**, **hCA II**, **hCA IX** and **hCA XII**..... 121

Chapter V

Table 9. Optical characteristic of the synthesized PSs. 161
Table 10. Inhibitory activity of **TPEs** against **hCA I**, **hCA II**,**hCA IV, hCA IX** and **hCA XII**..... 164

List of schemes

Chapter III

Scheme 1. Synthesis of the tetra-azido based porphyrin platform……74

Scheme 2. Synthesis of the tetra-CAI based porphyrins……75

Scheme 3: Synthesis of compound **1**……89

Chapter IV

Scheme 4. Synthetic route to CAi-based CTIs……119

Scheme 5: Synthesis of compound **3**……131

Scheme 6: Synthesis of CAi-based BTIs……132

Chapter V

Scheme 7. Synthetic route towards photosensitizer **5**……159

Scheme 8. Synthesis of PS **9**……160

Scheme 9. Synthetic pathway towards PSs **15a** and **15b**……161

List of publications

- **Carbonic anhydrase inhibitors featuring a porphyrin scaffold: synthesis, optical and biological properties** Merabti, A.; Roger, M.; Nguyen, C.; Nocentini, A.; Gerbier, P.; Richeter, S.; Gary-Bobo, M.; Supuran, C. T.; Clément, S.; Winum, J. Y., *Eur. J. Org. Chem.* **2022**, 2022 (21), e202101538.
- **Are tumor-associated carbonic anhydrases genuine therapeutic targets for photodynamic therapy?** Merabti, A.; Richeter, S.; Supuran, C. T.; Clement, S.; Winum, J.-Y., *Expert Opin. Ther. Targets* **2023,** 27(9), 817.
- **Thiochromenocarbazole imide-based photosensitizers decorated with carbonic anhydrase inhibitors for the targeted treatment of hypoxic tumours** Merabti, A.; Puchán Sánchez, D.; Nocentini, A.; M. A. Ali, L.; Nguyen, C.; Durand, D.; Hamon, K.; Ghanem, T.; Arnoux, P.; Josse, P.; Frochot, C.; Zalubovskis, R.; Richeter, S.; Gary-Bobo, M.; Supuran, C. T.; Cabanetos, C.; Winum, J.-Y.; Clément, S. accepted in *Mater. Adv.* DOI: 10.1039/d3ma00926b

Chapter I

General introduction & thesis outlines

Chapter I: General introduction & thesis Outlines

I. Photodynamic therapy

Cancer represents one of the most leading causes of premature death in the world, responsible for almost 10 million deaths and around 19 million new cases on 2020, according to the World Health Organization (WHO)[1]. According to the French National Cancer Institute (INCa), there will be an estimated 433 136 new cases of cancer in metropolitan France by 2023, including 245 610 in men and 187 526 in women. In contrast to the incidence rate, the mortality rate has been decreasing steadily over the last 25 years thanks to advances in treatment and diagnostic methods, which allow cancers to be detected at an earlier stage and therefore easier to treat.[2]

Chemotherapy, radiotherapy, surgery and immunotherapy are the classical methods adapted in cancer treatment, but they can cause some side effects for the patient. To avoid these complications, to improve prevention and to increase the efforts against this disease, photodynamic therapy (PDT) has emerged as a new alternative treatment to conventional approaches. Its principle is based on the administration of photosensitizer (**PS**) which will be localized in tumoral zone. Then, its irradiation using light produces reactive oxygen species (ROS) able to affect cancer cells due to its highest oxidizing power.

I.1 History of Photodynamic therapy

Since antiquity, light has been an effective tool for curing various skin diseases in ancient Egyptian, Indian and Chinese civilizations.[3] PDT involves the use of light to treat a specific disease and the administration of a photosensitizing agent (PS), which is then accumulated and activated by light in the tissues. This form of therapy also goes back more than 3 000 years, when the Indians and Egyptians employed psoralens derived from natural plants to treat various skin conditions.[4-5]

PDT was proposed as a new therapeutic strategy in the early 1900s. The phenomenon of cell death induced by the combination of light and chemicals was described for the first time by O. Raab.[4] He has shown that the combination of light and acridine red has a lethal effect on protozoa. He has also pointed out that the two factors (light and acridine red) have no effect separately. He proved that the toxicity was induced by the fluorescence resulting from chemical irradiation.[4] In the same year, the French neurologist J. Prime found that the oral administration of eosin intended to epileptic patients induced signs of dermatitis in skin parts that were exposed to the sun. Then in 1903, H. von Tappeiner and A. Jesionek applied topical eosin and white light to skin tumours.[6] One year later, the oxygen was identified as an integral part of photosensitization reactions by H. Von Tappeiner and A. Jodlbauer, and later, in 1907, the term of photodynamic action was introduced to describe this phenomenon.[6]

Chapter I: General introduction & thesis Outlines

Hematoporphyrin was produced for the first time in 1841 by H. Scherer during the investigation of blood nature. Its fluorescence properties were described around 1867 and named hematoporphyrin in 1871. In 1911, W. Hausmann documented the effects of hematoporphyrin and light on protozoa and blood cells, reporting skin reactions in a mouse exposed to light after administration of hematoporphyrin. In 1913, the first human photosensitizer (PS) was reported by F. Meeyer-Betz, when he injected himself with 200 mg of hematoporphyrin to identify if similar effects in human could be induced.[6] He reported that the zones exposed to light showed prolonged pain and swelling. In 1960, the concept of PDT was initiated by R. Lipson and S. Schwartez discovering the diagnostic and therapeutic effects of cancer by administering a derivative of hematoporphyrin (HpD). In 1975, a notable advance in the field of PDT was achieved when T. Dougherty showed that the application of HpD and its activation by red light, eliminated the growth of mammary tumors in mice. In the same year, J. F. Kelly succeed to eliminate bladder carcinoma in mice using HpD activated by light.[3] The application of this procedure in the treatment of pathologies of the gastrointestinal tract was first used in 1984 by J. S. McCaughan, who used PDT to treat patients with esophageal cancer. One year later, Y. Hayata used PDT to treat patients with gastric carcinoma.[7] Dougherty and his team also purified HpD and developed Photofrin®, which was the first photosensitizing agent approved by the US Food and Drug Administration (FDA) in 1995 for cancer treatment.[4]

Thanks to its efficacy, low toxicity and high selectivity, PDT has been approved as an anti-cancer therapeutic modality in some countries to treat malignant tumors.[8-9] The PDT process is based on the dynamic interaction between a PS, light with a specific wavelength irradiation, and molecular oxygen promoting the selective destruction of the target tissue.[10]

PS can be administered to the targeted zone in two different ways, topically, by local application (emulsion, cream, subcutaneous injection) or systemically, by intravenous or oral administration. After a delay following administration, and regardless of the route used, the PS will be accumulated in the tumor tissue, which will then be activated using light of an appropriate wavelength to induce the mechanism of PDT. (**Figure 1**)

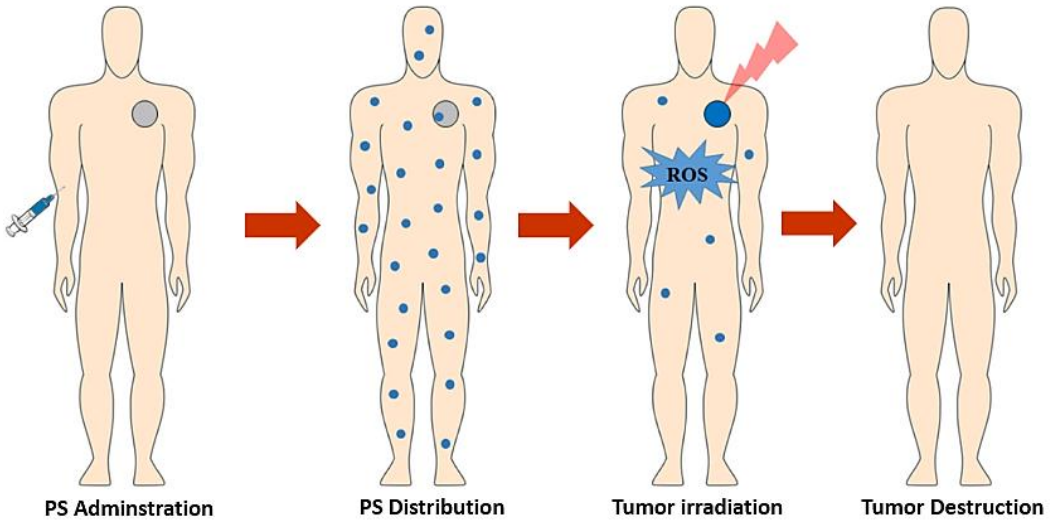


Figure 1. Representation of the clinical application of PDT adapted from.[4]

I.2 Mechanism of PDT:

The photochemical reactions involved in PDT are activated when the **PS** is irradiated by light, in the target tissue. After going from its stable ground state to an unstable state known as the excited singlet state ^{n}**PS*** which will last for a few nanoseconds from this level, the ^{n}**PS*** molecule can return to its fundamental level through various processes. First, it can lose excess energy either through a non-radiative process by emitting heat (through internal conversion) where the PS is stabilized by turning to a low-energy singlet excited state ^{1}**PS*****,** or by emitting a photon (fluorescence). However, the singlet state can undergo intersystem crossing and progress to a more stable, long-lived electronically excited state (triplet, state, ^{3}**PS***), through spin conversion of the electron in the higher-energy orbital. The transition from the triplet state to the ground state is theoretically not allowed and is relatively slow. In this state, PS can return to its ground state by emitting light (phosphorescence), although in the triplet state, PS can undergo two types of reaction: if it interacts directly with a substrate by electron transfer, the reaction is defined as type **I**. Reactive oxygen species (ROS) are formed in the environment inducing oxidative damages leading to cell death. In type **II** reactions, PS transfers its excess energy to molecular oxygen and then returns to its ground state. This step leads to the formation of singlet oxygen $^{1}O_{2}$, which is unstable and highly reactive. It can cause oxidative damage to biomolecules in its environment, such as membrane phospholipids, proteins and even DNA.[11-12]

It was mentioned by Sibata *et al.* that in addition to type **I** and type **II**, there could be a third photosensitive mechanism (type **III**) that works without generation of ROS intermediary. In this type

of PDT, the PS must possess specific targeting property to proteins, nucleic acids, and other cell organs. The PS including targeting-moiety will be able to eliminate the biological-target efficiently and directly. This mechanism avoids perfectly the challenges of oxygen concentration, enhancing the PDT efficiency PDT, and overcome deep-seated problems.[13] The photochemical phenomena involved in PDT are summarized in the schematic Perrin-Jablonski diagram shown in **figure 2.**

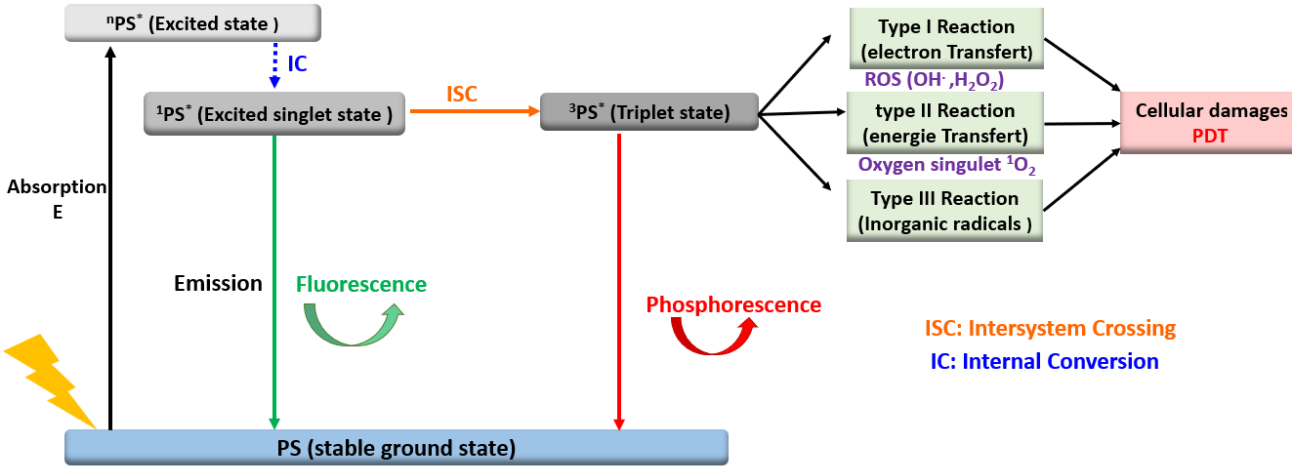


Figure 2. Modified Jablonski diagram of the PDT action mechanism adapted from.[13-14]

I.3 Light Sources:

The choice of light source must be based on several parameters, such as PS absorption, state of tumor (location, lesion size, accessibility and tissue characteristics) and finally, price.[15] The effect of PDT is based on the activation of the PS by light absorption at an ideal wavelength, between 600 nm and 800 nm (**Figure 3**). This range is defined as **therapeutic window**. In this zone, there is sufficient energy to generate singlet oxygen, and endogenous compounds absorb the minimum (blood and tissue constituents absorb in the visible and near-infrared range, while organic constituents such as hemoglobin and melanin absorb strongly around 800 nm).[16]

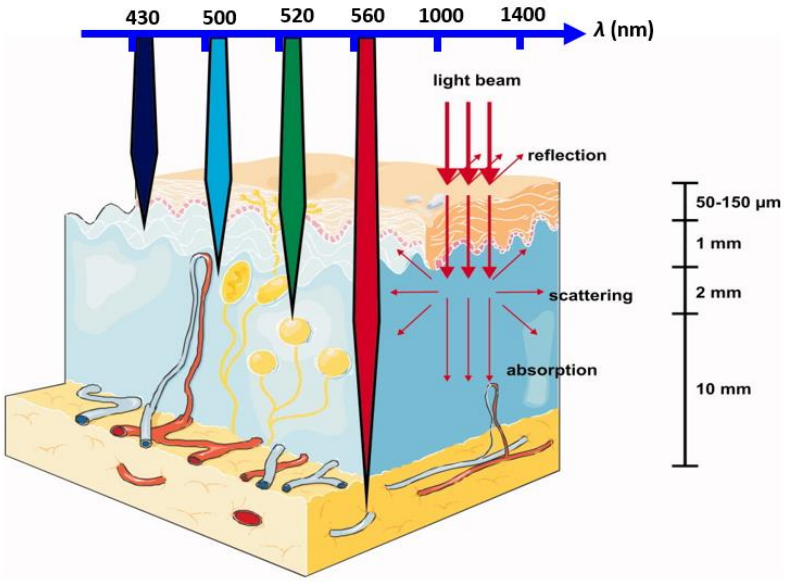


Figure 3. Light Propagation through the tissues adapted from.[15]

I.4 Subcellular localization

The localization of PS depends on several factors such as charge of the PS, degree of aggregation, solubility of the molecule (hydrophilic, hydrophobic, or amphiphilic). Due to its stability and if it is not eliminated within a few hours by the body, PS can be used in both types of targeted PDT, where the first is vascular targeting, and the second is cellular targeting. In this case, the intracellular localization of the PS is essential for efficient PDT. In-depth evaluation of PDT at the cellular level has shown that mitochondria, lysosomes, endoplasmic reticulum, cytoplasm, and cell membranes are among the key organisms that undergo oxidative stress caused by PDT (**Figure 4**).

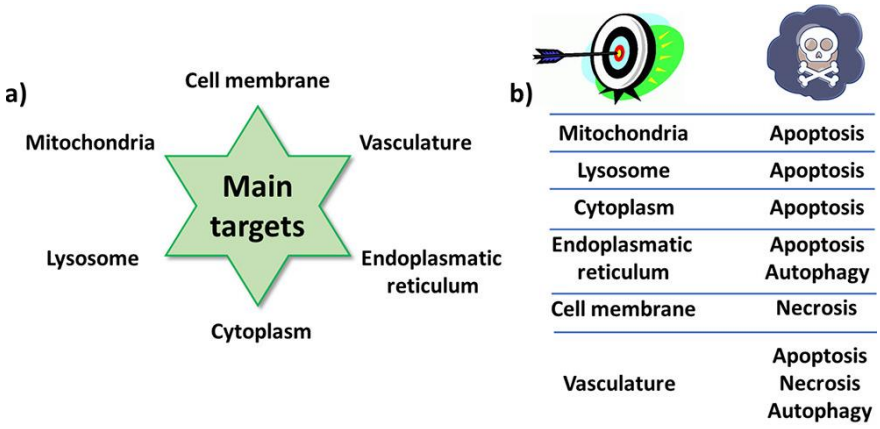


Figure 4. (a) Main targets during PDT and (b) their related effects on cell death adapted from.[17]

Chapter I: General introduction & thesis Outlines

The intracellular distribution pathway and subcellular localization are related to the structural and physicochemical characteristics of the PS (ionic charge, degree of hydrophobicity, and degree of asymmetry present in the molecule). For example, hydrophobic PS can be incorporated into cells through the plasma membrane *via* passive diffusion (and then, move on to other intracellular organelles) or through endocytosis. The interactions of PS with cell membrane and blood transporters, notably LDL (low-density lipoprotein), are also determined to balance the two previous mechanisms. Some PS can be incorporated into various intracellular membranes, such as pyropheophorbide *a*, which was tested on NCI-h446 cells. The molecule was found to be localized in the endoplasmic reticulum, lysosomes, mitochondria and Golgi apparatus.[18]

Many studies have shown that lysosomes can be an important intracellular target for localization of the PS molecule.[19] Kessel *et al*. compared the localization of two *meso*-tetraphenylporphyrin derivatives: 5,10-di[4-*N*-trimethylaminophenyl]-15,20-diphenylporphyrin (DADP-a) or 5,15-di[4-(*N*-trimethylaminophenyl)-10,20-diphenylporphyrin (DADP-o). The presence of a cationic N-$(CH_3)^{3+}$ groups on two of the *para*-phenyl positions of 20-diphenylporphyrin (DADP-o) enables its localization in lysosomal whereas DADP-a localized in mitochondria and led to crucial photodamage after irradiation.[20]

It was proven that some cationic PS could also accumulate in mitochondria[21] due to the influence of mitochondrial membrane potential and the membrane's lipid bilayer.[22] Dumin *et al*. incubated cationic zinc (II) phthalocyanine derivatives bearing lipophilic chains with HeLa cells. They found that these molecules accumulated preferentially in the inner mitochondrial membranes. After irradiation, the mitochondria were completely destroyed, and energy metabolism stopped. Teiten *et al*. also studied the subcellular distribution of Foscan® after incubation in the cells. The fluorescence topographic profiles recorded revealed that Foscan® molecule was weakly localized in lysosomes and mitochondria. However, it was perfectly distributed in the endoplasmic reticulum and Golgi apparatus, and upon irradiation these were the main sites damaged.[23]

All in all, the delivery of photosensitizing molecules to different cell organelles has a crucial role in the photodamages of cancer cells that occurs during PDT.[22]

I.5 Mechanism of Cell Death in Photodynamic Therapy

The main aim of PDT is to induce tumoral cell death, which can occur *via* several pathways, either directly (apoptosis, necrosis), or indirectly by damaging the tumor vasculature supplying oxygen, and nutrition to cancer cells (**Figure 5**). These mechanisms are induced by different signaling pathways

depending on the type of PS and protocol used for its administration, PS dosage and localization, genotype of the cells subjected to PDT, and finally, oxygen level.

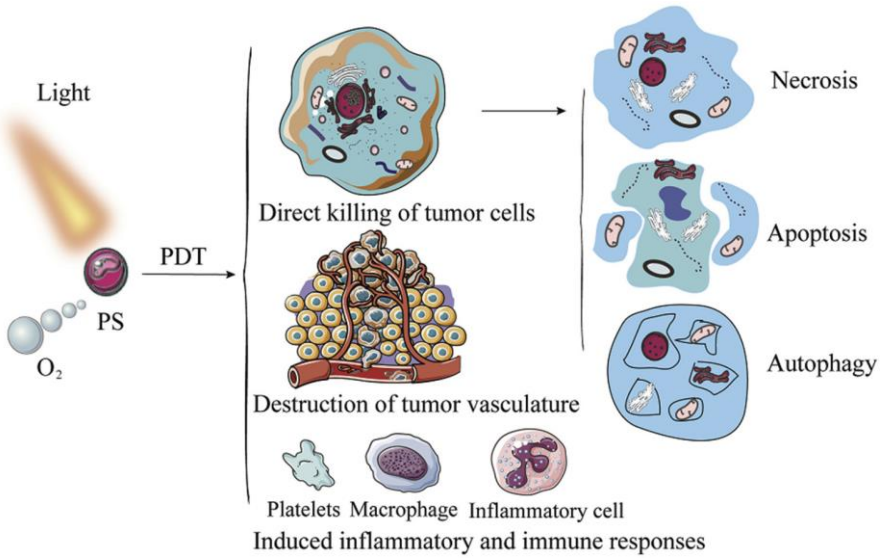


Figure 5. Cytolytic activity of oxygen-consumed PDT adapted from.[24]

I.5.1 Apoptosis

The apoptosis is considered as the main mechanism of cells death in PDT. This process can be activated through two ways either by activation of specific cell death receptors (extrinsic pathway) or by the release of cytochrome c from mitochondrial membrane (intrinsic pathway).[25]

High concentrations of PS have been shown to increase necrotic damage and prevent apoptosis. In addition, PS localized in mitochondria are able to induce apoptosis, while those localized in plasma, membrane and lysosomes induce necrosis.[26]

I.5.2 Necrosis

Necrosis is generally described as a sudden, rapid mechanism that affects many cells and characterized by a pycnotic nucleus, swollen cytoplasm, and progressive disintegration of cytoplasmic membranes, which induce cell fragmentation and release of cellular integrity into the extracellular environment. In contrast to apoptosis, necrosis occurs with high doses of PS. ROS formation is the main cause of this mechanism during the application of PDT. It is considered as the major form of cell death induced by PS localized in the plasma membrane such as Photofrin® and Pc4.[27]

I.5.3 Immunological mechanisms

PDT has been considered as localized treatment for many years, targeting only tumor cells and vascular systems. Recently, various studies have shown that PDT can also affect the adaptive immune response by either stimulation or suppression of the immune response.[28]

Under certain conditions, PDT leads to immunosuppression, which has mainly been related to reactions of topical treatments (local use) with high fluency rates and in large irradiation areas.[4] In contrast, non-topical PDT treatments are often known as immunostimulants. PDT-induced oxidative damage to the tumor stroma will eventually lead to cell death. An immune cascade is also initiated, as PDT induces necrosis of tumors and their vasculature.

I.6 Photosensitizers in PDT

Photosensitizers are the crucial elements in PDT. Ideally, these PSs should accumulate selectively in tumor areas, possess a high $^1O_2$ quantum yield, have low dark toxicity and limited skin photosensitization, be fast and easy to remove by the patient's body, have good solubility in biological media with absorption within the therapeutic window (600 nm- 800 nm). PS must also be inexpensive and require simple synthesis.[29] Among PS, macrocyclic compounds have emerged as a major class of diagnostic and therapeutic agents for the treatment of cancer. These molecules include compounds such as porphyrins, chlorins, bacteriochlorins, phthalocyanines and BODIPY (**Figure 6**).[30]

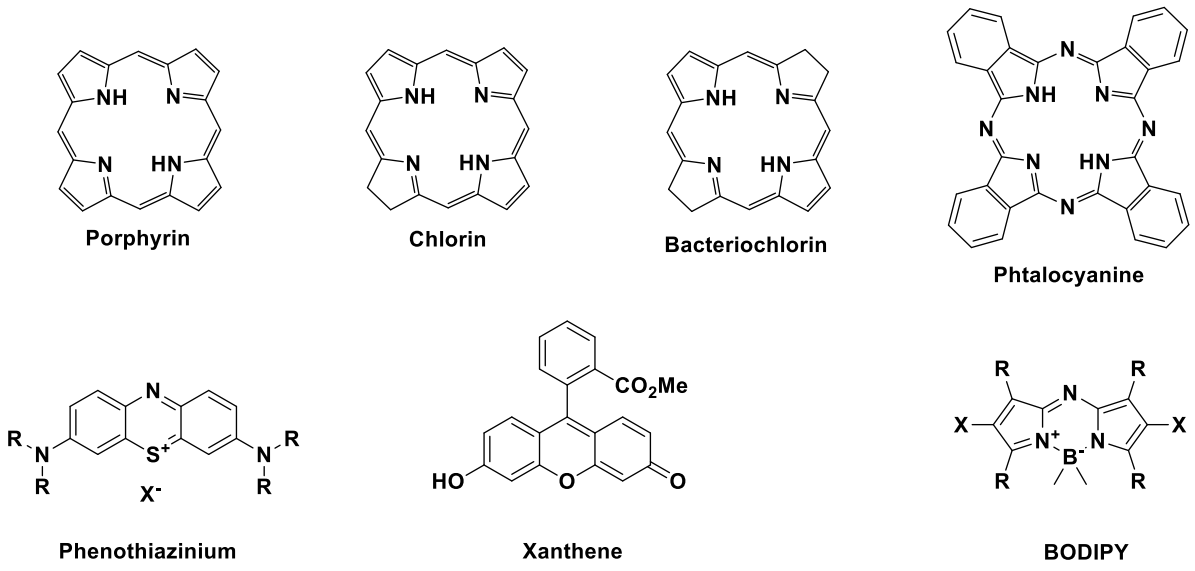


Figure 6. Basic structures of some examples of PS used in PDT, adapted from.[30]

There is a wide range of molecular structures for the PS, which are currently used in PDT. PSs can be classified into three generations.

I.6.1 First generation PS

The first generation of PS involves Photofrin®, which is also known as porfimer sodium, and other water-soluble hematoporphyrin derivatives (**Figure 7**). PS of this generation possess a complex structure making their synthesis difficult in term of cost and time. In addition these compounds exhibit low light absorption rate at 630 nm, which leads to limited penetration into deeper tissues.[31] The most significant drawback is their high accumulation in the skin inducing extended cutaneous photosensitization of up to 2 to 3 months after administration.[32] Therefore, there is an urgent need to develop new PSs.

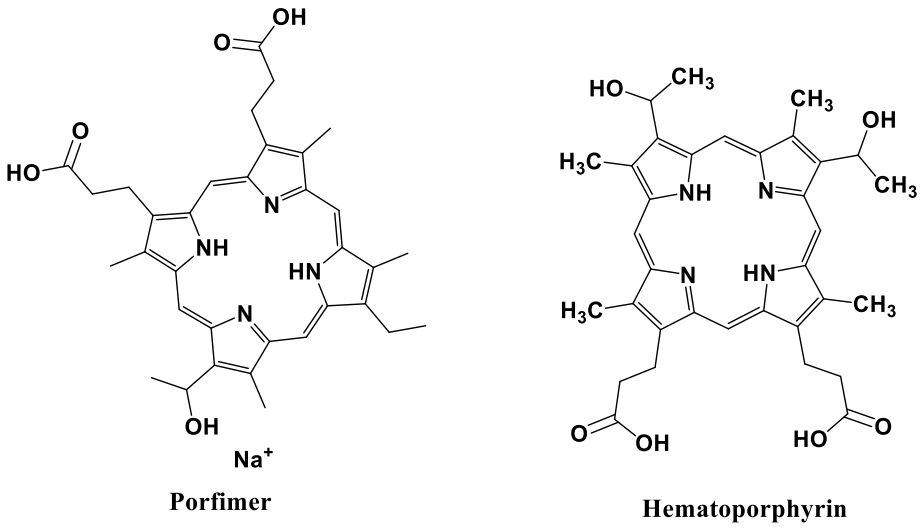


Figure 7. Structures of first generation PS adapted from.[31]

I.6.2 Second generation PS

The drawbacks associated with first-generation PS have led to in-depth studies and research to improve the efficacy of photosensitizing molecules either through direct modification of the porphyrin core[33] or *via* an alteration in the peripheral functionality of porphyrin.[34] After the first-generation of PS were in place, several new non-porphyrinoid PS were introduced (**Figure 8**) including porphycenes,[30] Lutrin® and Lutex®.[35-36]

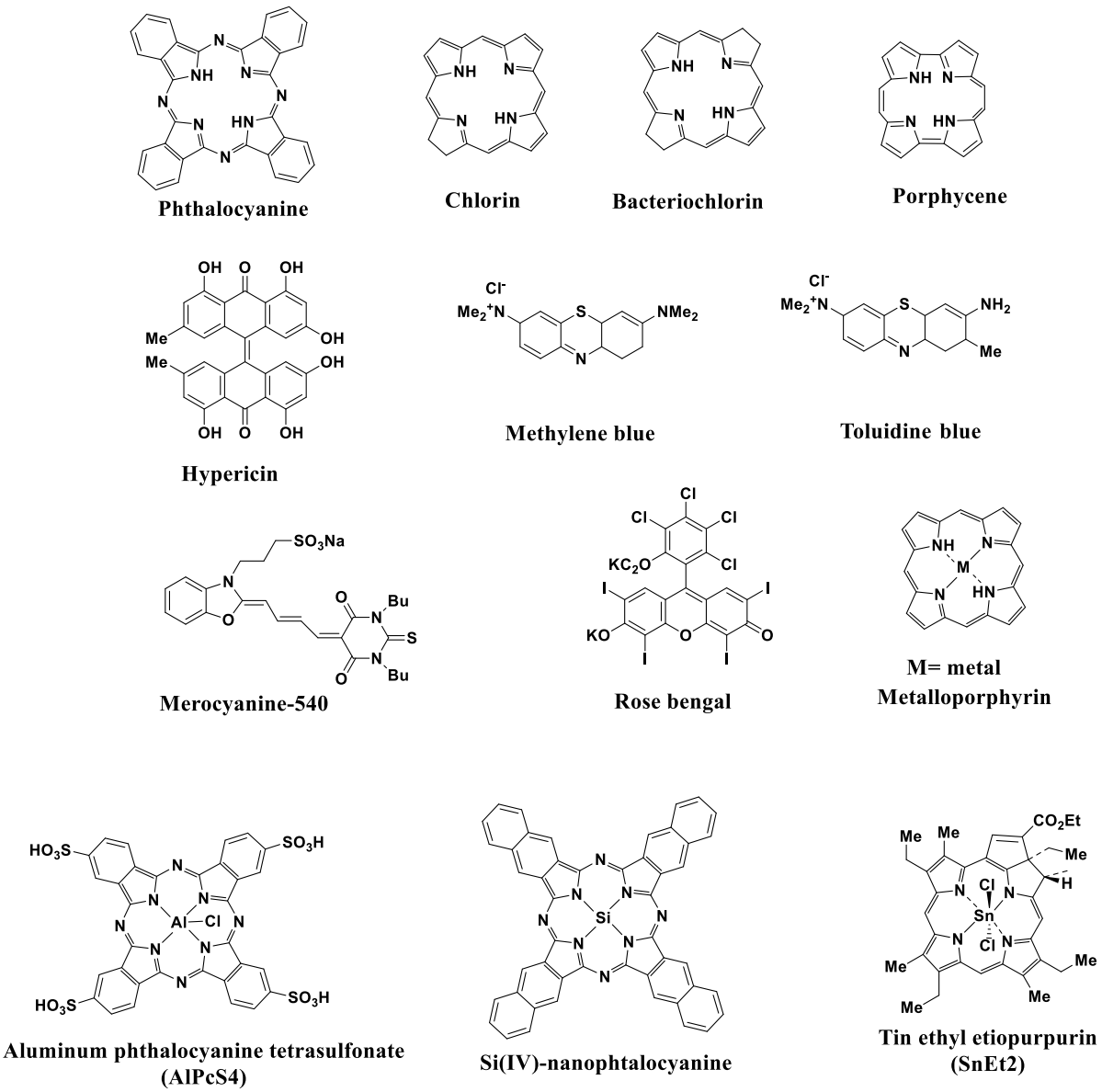


Figure 8. Structures of some second-generation PSs Adapted from. [37]

I.6.3 Third generation PS

Third-generation PS are a further development of second-generation PS because of the clinical problems encountered during the application of PDT, notably, the difficulty of preparing a pharmaceutical procedure that would allow parenteral administration of PSs. New delivery systems have emerged to overcome these problems, effectively increasing the bioavailability and selectivity of PDT (**Figure 9**).[34]

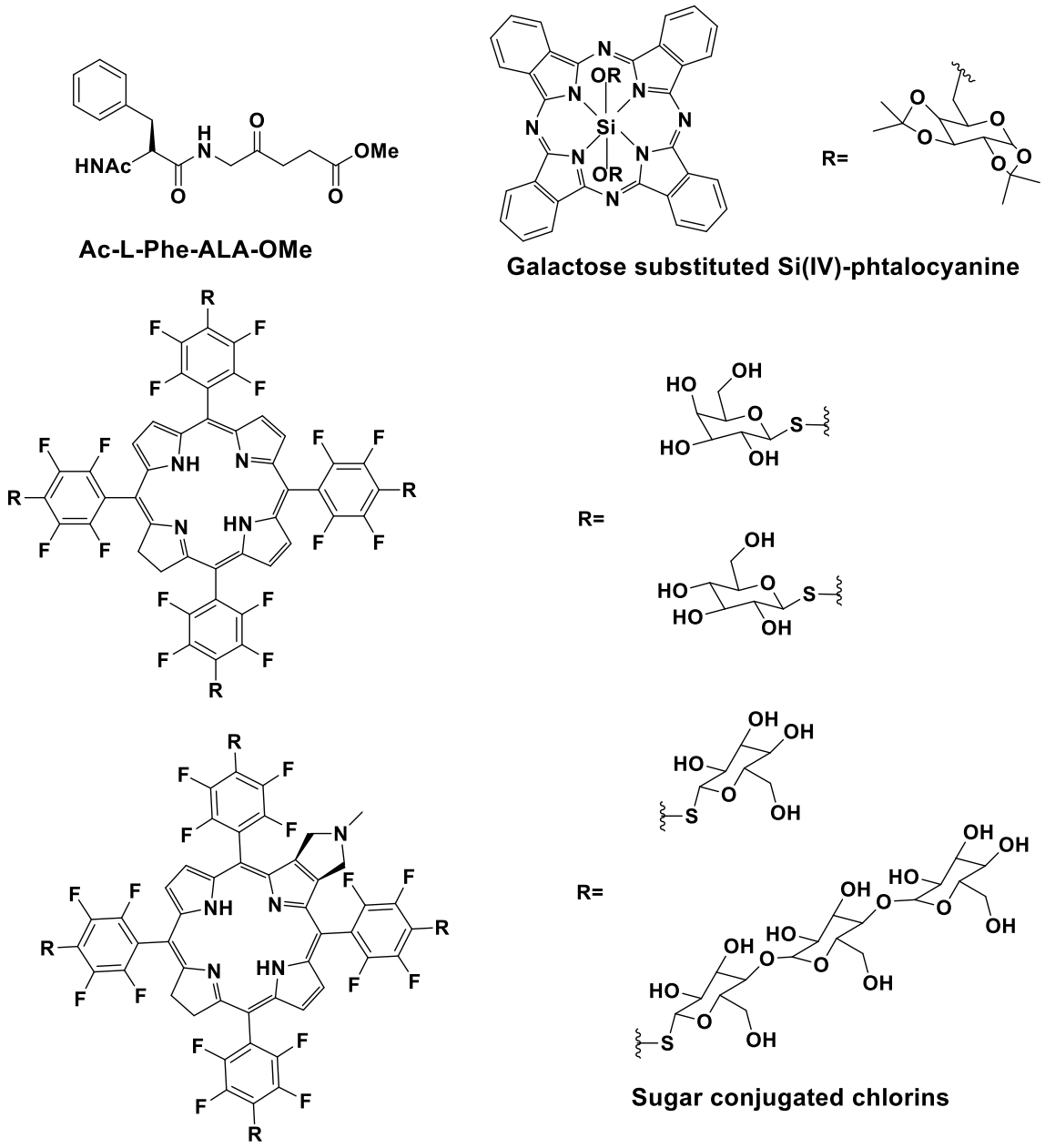


Figure 9. Some examples of third generation PSs (conjugated with targeting agents) adapted from.[37]

In general, 3rd-generation PSs are often obtained by modifying pre-existing systems through association with biological entities to achieve tumor-specific targeting, or by conjugating a PS with an antibody targeting the specific antigens of cancer cells. These solutions make it possible to reduce drug concentrations and doses with highly therapeutic effects,[38-39] and thus, to enhance the selectivity and accumulation of PS in cancer cells (**Table 1**).

PS	λ_{max} (nm)	ε_{max} (M^{-1} cm^{-1})	dose mg/kg	light dose ($J.cm^{-2}$)	DLI (h)	tumors
Photofrin	630	2×10^3	2-5	100-200	24-48	bladder, lung, and esophageal
Foscan	650	$\sim 10^5$	0.15	20	96	head and neck
Talaporfin	675	3×10^4	1	100	0.25-4	lung
Photolon	660	$\sim 10^4$	2.5	50-600	4	skin,breast, mucosal, and rectal
Photodithazine	655	$\sim 10^4$	1	150-450	2	skin, breast, and mucosal
Radachlorin	650	$\sim 10^4$	0.5-2.4	200-300	3	skin and lung
Padeliporfin	762	$\sim 10^5$	4	200	0.25	Prostate
Photosens	675	$\sim 10^5$	0.5-1	150-200	24-72	skin, breast, lung, throat, head, neck, and mucosal

Table 1. PSs Approved for Anticancer PDT adapted from.[17]

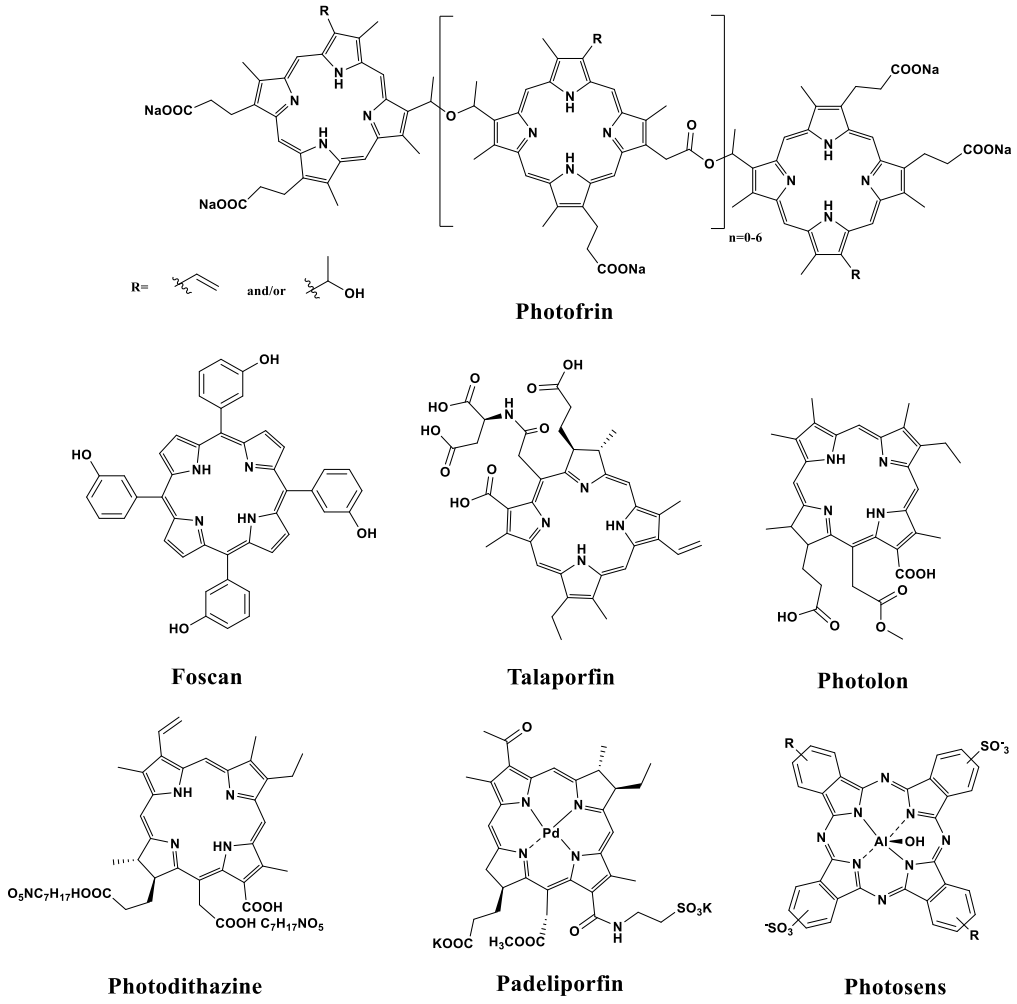


Figure 10. Structure of PSs Approved for Anticancer PDT adapted from.[17]

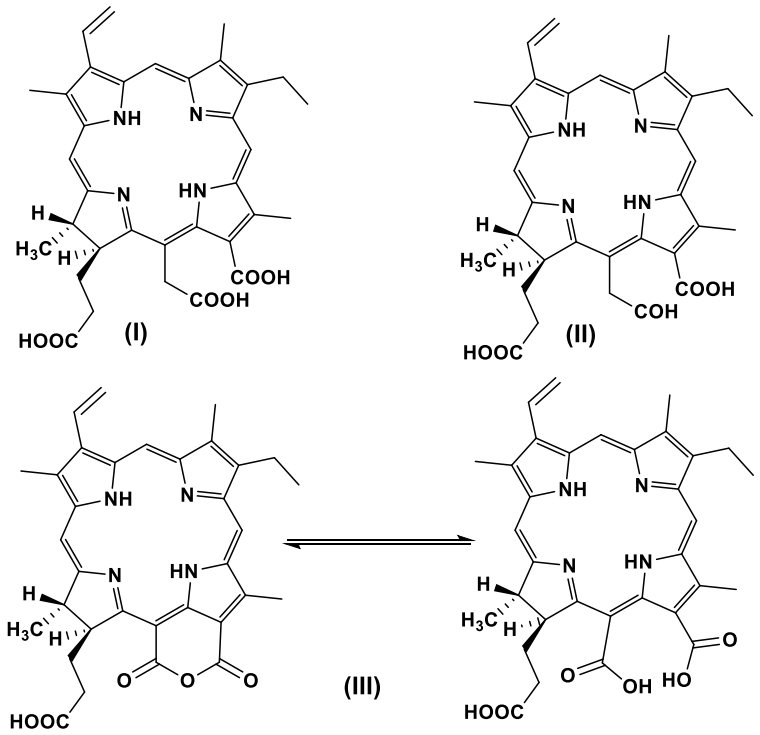


Figure 11. Molecular structure of Radachlorin: chlorin e6 (I), chlorin p6 (II) and purpurin (III) adapted from.[17]

I.7 Molecular Design Strategies for PS

I.7.1 PSs Based on conventional core structures

Among traditional PS, porphyrin, chlorin, and phthalocyanine derivatives have been largely used in PDT applications, thanks to their highest absorption (near-infrared), good fluorescence properties and excellent $^1O_2$ generation. However, due to their difficulty to be synthesized and purified, these systems can also exhibit some drawbacks such as poor solubility and long retention time in the body's patient. Due to their planar structures, they also showed a strong tendency to aggregate in biological media through π-π stacking interactions causing quenching of the excited state. This phenomenon is well known as "aggregation caused quenching (ACQ)" leading to decrease in fluorescence and singlet oxygen generation,[40] rending the PS inactive through self-quenching.

To overcome the aggregation issue and improve their water solubility, several methods have been widely used on porphyrins notably, such as adding some peripheral substituents and axial ligands to the structure of porphyrin resulting in good solubility in water. In addition the use of sulfonation, carboxylation, or *N*-pyridyl-substitution are among the most used strategies to overcome the ACQ issues.[40]

I.7.2 Attaching Heavy Atoms

Introducing heavy atom can also be a strategy used to enhance ISC (inter system crossing) owing SOC (spin-orbital coupling) interactions and $^1O_2$ generation without affecting the conjugation and planarity of the structures. It can also improve PS absorption *via* red-shifting, which is important for good penetration as well as for minimize some drawbacks of PDT.[41-40]

Based on this approach, novel PSs have been synthesized with high fluorescence quantum yield and efficient photosensitization. Gasser *et al.* described the synthesis of homoleptic iodinated bis(dipyrrinato) Zn(II) complexes. The complexes obtained gave triplet excited state lifetimes (τ_T = 207–559 ns) and efficient $^1O_2$ generation for PDT application. The integration of iodine as heavy atom improved SOC significantly leading to an efficient ISC process.[41] In another study, a red metal-free organic phosphor based on bromo-incorporated benzothiadiazole scaffold showed high phosphorescence efficiency (Φ_P = 0.15) and long emission lifetime (τ = 504.6 µs) allowing its application in time-resolved imaging and PDT.[42] Exploiting the same approach, Wang *et al.* described the synthesis of gold nanorods (GNRs) conjugated with Rose Bengal (RB) molecules to improve PDT efficiency. The final nanomaterial exhibits excellent $^1O_2$ generation efficiency upon irradiation at 532 nm as well as high photothermal efficiency upon irradiation at 810 nm. These RB-GNRs also offer excellent cytocompatibility. Thanks to these advantages and good properties shown by these multifunctional drug RB-GNRs, these platforms will have a great potential in cancer therapy applications.[43]

Despite all that, this approach has some drawbacks such as dark toxicity, short triplet-state lifetimes, poor photostability, and the potentially high cost of heavy metals.[44] To address these drawbacks, it is therefore essential to find alternative approaches to improve ISC without using heavy atoms and to reduce dark toxicity. Recent studies have reported that the ISC rate constants could be estimated from the equation below:

$$k_{\mathrm{ISC}} \propto \frac{\left\langle \mathrm{T}_1 \middle| H_{\mathrm{SO}} \middle| \mathrm{S}_1 \right\rangle^2}{\left(\Delta E_{\mathrm{S1\text{-}T1}}\right)}$$

Where:

H_{SO} : Hamiltonien for the spin-orbit perturbations (SOP).

$\Delta E_{S1\text{-}T1}$: energy gap between S_1 and T_1 states.

From this equation, we can summarize that more ΔE_{ST} is smaller, higher will be the ISC rate. This means that ISC can be modeled using SOP. This leads to improved ISC efficiency and subsequent $^1O_2$ generation (**Figure 12**).

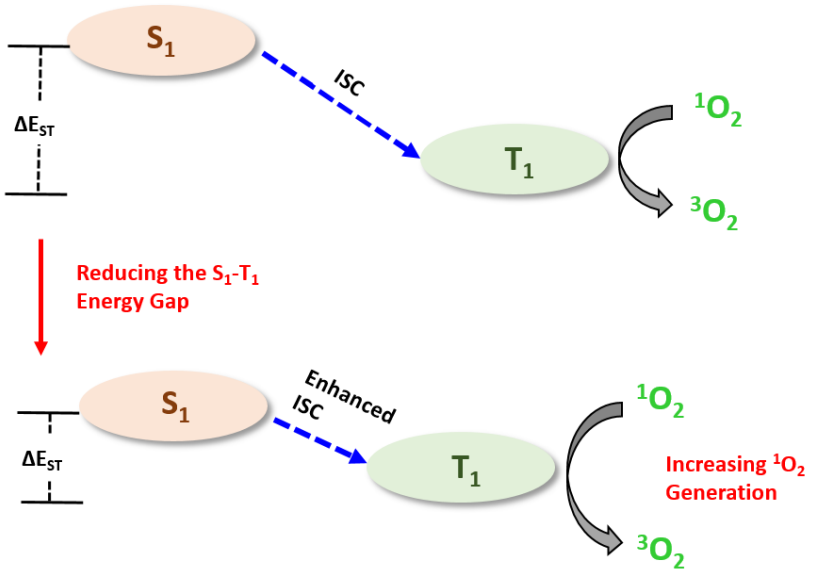


Figure 12. Physical model of $^1O_2$ generation, depicting the S_1–T_1 ISC process and the proposed strategy for increasing $^1O_2$ generation Adapted from.[45]

To reduce the energy gap between Singlet-Triplet states, a novel strategy has been adapted consisting in increasing the size of the chromophores. $\Delta E(S_1\text{-}T_1)$ can also be reduced by donor–acceptor (D-A) approach, requiring the spatial separation of the highest occupied and lowest unoccupied molecular orbitals (HOMO-LUMO). As such, a spatial separation of frontier molecular orbitals can be achieved in a single molecule, as discussed for some molecules such as azulene, or in another strategy based on charge transfer at the interface of D-A materials.[46]

In the same context, Dong *et al.* designed a new D–A–D PS based on the combination of I-BODIPY and DPP moieties *via* a benzene ring as a π-linker with simultaneously enhanced fluorescence and $^1O_2$ generation for tumor imaging-guided PDT treatment (**Figure 13**). The integration of these benzene moieties on the end of DPP able to interact through π-π stacking facilitated end-to-end integration and thus, the promotion of charge transport between adjacent molecules. In particular, the $^1O_2$ generation efficiency was better than the two separate units. A higher photocytotoxicity (IC_{50} = 0.06 µM) was also observed with low dark toxicity when they tested it on HeLa cells. *In vivo* fluorescence imaging showed that this compound could accumulate in the target tumor cells, *via* the EPR effect, and in low doses, it was able to inhibit definitively tumor proliferation after 20 days of PDT application.

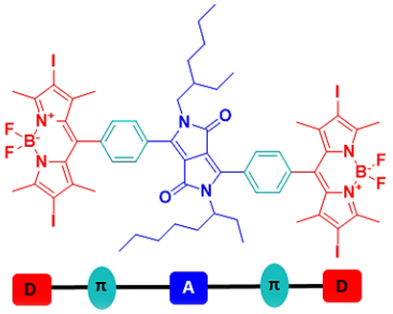


Figure 13. Structure of D–A–D PS obtained adapted from.[41]

I.7.3 AIEgens based PSs

Aggregation-Induced Emission (AIE) can be considered as an opposite phenomenom of the ACQ. Indeed, B. Zhong Tang *et al.* found that 1-methyl-1,2,3,4,5-pentaphenylsilole derivative was not fluorescent in solution (**Figure 14**), while when aggregated or in the solid state, an intense fluorescence was noticed. This phenomenon was considered as novel whereas studies carried out in 1961 by Bray's group reported that 1,1,2,3,4,5-hexaphenylsilole exhibits intense fluorescence in the solid state under ultraviolet irradiation.[47] The phenomenon discovered by Ben Zhong Tang's group was later known as "aggregation-induced emission (AIE)".

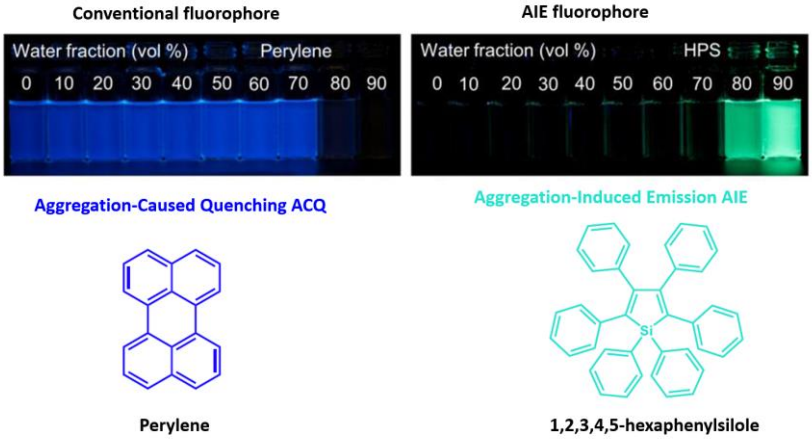


Figure 14. Fluorescence images of solutions or suspensions of perylene and 1,1,2,3,4,5-hexaphenylsilole in THF/water mixtures with different fractions of water (f_w) adapted from.[48]

I.7.3.1 AIE mechanisms

The functional mechanism of these compounds can be the same for all the AEIgens even though they have different structures. To design efficient AIEgens, it is important to understand their luminescence mechanism and the parameters controlling it. Consequently, a lot of research have been carried out to investigate this phenomenon through experiments and theoretical calculations.[48-52] The strategy for activating AIE phenomenon is mainly based on the restriction of intramolecular motion (RIM), which includes the restriction of intramolecular rotations (RIR) and the restriction of intramolecular vibrations (RIV). This mechanism has been proposed and widely verified as a main mechanism for AIE phenomena (**Figure 15**).

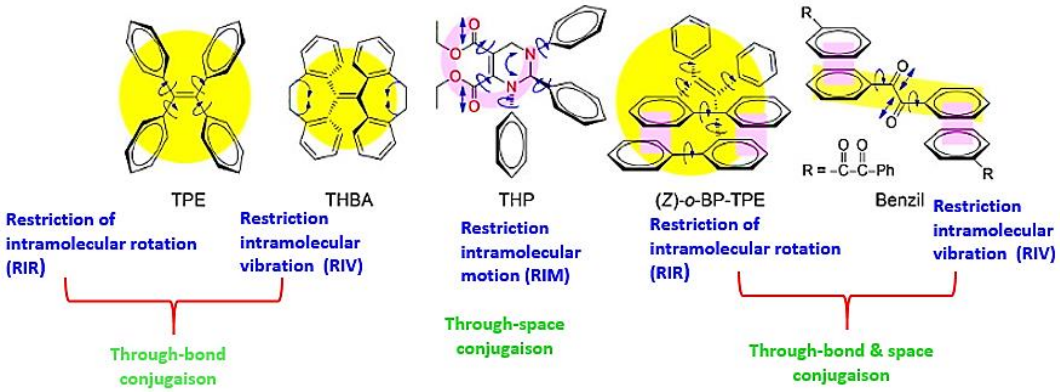


Figure15. Representative examples of AIEgens and their working mechanisms adapted from.[49]

I.7.3.2 Examples of AIEgens based PS

Yuan *et al.* reported for the first time the synthesis of AIE nanoparticles (NPs), that can be used for image-guided PDT,[52] using 2-(2,6-bis((*E*)-4-(phenyl(4'-(1,2,2-triphenylvinyl)-[1,1'-biphenyl]-4-yl)amino)styryl)-4*H*-pyran-4-ylidene)mononitrile (**TTD**) (**Figure 16**). The obtained NPs exhibited significant fluorescence with efficient ROS production as well as selective targeting of cancer cells in the MDA-MB 231 cell line (**Figure 16**).

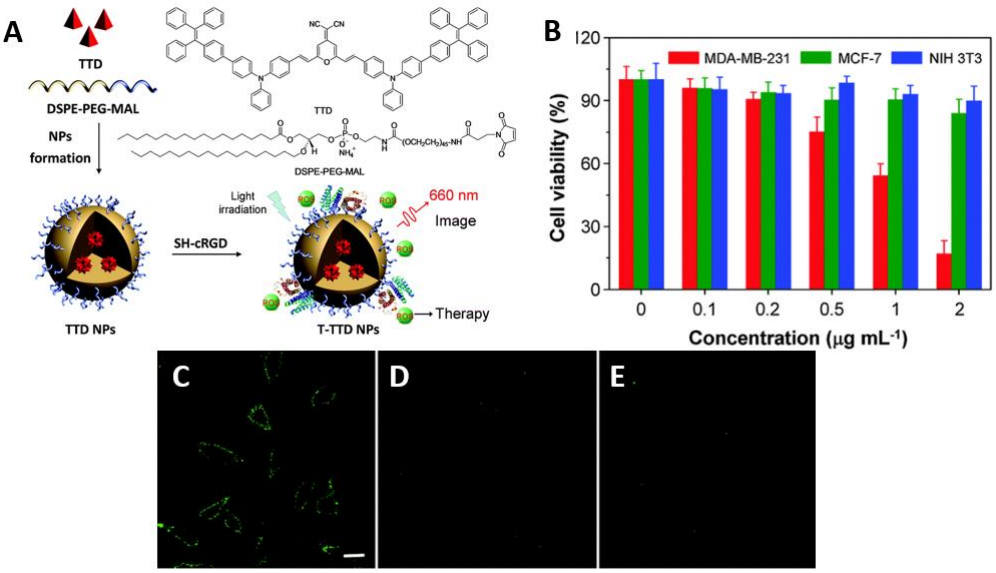


Figure 16. **(A)** Schematic illustration of T-TTD NP formation and surface modification with the target moiety of cRGD, **(B)** Growth inhibition of MDA-MB-231, MCF-7 and NIH 3T3 cells in the presence of different concentrations of T-TTD NPs with light irradiation (0.25 W cm−2, 2 min), Cell apoptosis imaging using FITC-tagged Annexin V in MDA-MB-231. **(C)**, MCF-7. **(D)**, NIH 3T3. **(E)**, cells incubated with T-TTD NPs after light irradiation adapted from.[52]

Another example reported by Liu and his colleagues consists in the preparation of an AIE-based PS (TPE-PyT-CPS) targeting Golgi apparatus (GA). The introduction of pyrene into TPE-Py-CPS, enables reducing ΔE_{ST} and improving $^1O_2$ generation. Upon light irradiation, GA destruction and cleavage of GA proteins (p115/GM130) were observed leading to activation of the apoptotic pathway between GA oxidative stress and mitochondria in HeLa cells. This work provided an innovative strategy for the development of new PS with specific GA targeting and efficient PDT by transferring stress signals from Golgi apparatus to mitochondria.[53]

In 2020, Mao's team proposed a new design of an immunostimulant, which combines an AIE PS **TPEBTPy** with upconversion nanoparticles (UCNPs). This nanomaterial was found to be able to convert NIR light into visible light and ultraviolet light in order to obtain adaptive immune response through the ROS-dependent immune activation mechanism. This approach can overcomes the side-effects of classical immunotherapy and leads to a systemic antitumor immune response and rejection of distant metastases.[54]

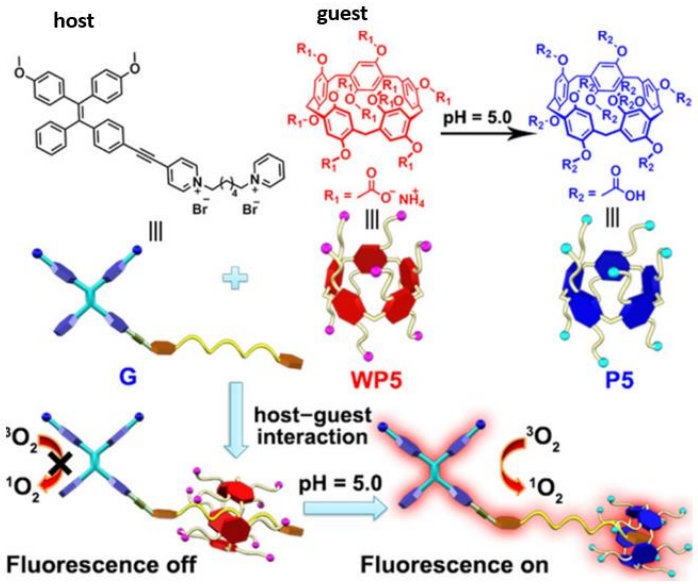


Figure 17. illustration of Chemical structures of WP5, P5 and G. adapted from.[55]

A new strategy has been reported by Shao and his group, to build adaptive photosensitizers *via* a supramolecular modification based on pillararene host-guest interactions. More precisely, they designed and synthesized a supramolecular ROS switch based on a host-guest complex between a water-soluble anionic pillar[5]arene (WP5) host and a photosensitizing guest (G) containing tetraphenylethene (**Figure 17**). This switch produces insignificant fluorescence and ROS in neutral environments, but under acidic conditions, displays bright red fluorescence and high ROS-generating capacity. In view of the fact that tumors are acidic, the supramolecular ROS switch has potential as a precision medicine for cancer treatment.[55] The results of this switch studies demonstrated that it could not produce ROS and lead to fluorescence when it was in its off state under neutral conditions. However, in acidic conditions, it was able to exhibit bright red fluorescence and generate ROS efficiently. It was also found to be able to light lysosomes selectively which confirm its ability to be applied in cancer and imaging therapy.

In the last example, Chen *et al.* reported the synthesis of dimeric BTPE (4,4'-bis(1,2,2-triphenylvinyl)-1,1'-biphenyl) with AIE properties. 1,2-distearoyl-sn-glycero-3-phospho-ethanolamine-N-[methoxy(polyethyleneglycol)$_{-2000}$] (DSPE-PEG$_{-2000}$) coated BTPE can self-assemble to form nanoparticles (NPs) with outstanding disparity in aqueous solution (**Figure 18**). DSPE-PEG$_{-2000}$ coated **BTPE** NPs show enhanced $^1O_2$ generation ability compared to TPE. In addition, BTPE NPs showed best accumulation in HeLa cells with low IC_{50} (8.4 μg mL^{-1}) inducing effective tumor suppression. This study demonstrated that the dimerization of TPE is able to enhance the phototherapy efficacy of BTPE while

simultaneously retains the low dark toxicity. This work may provide a new approach to the design of new PSs.[56]

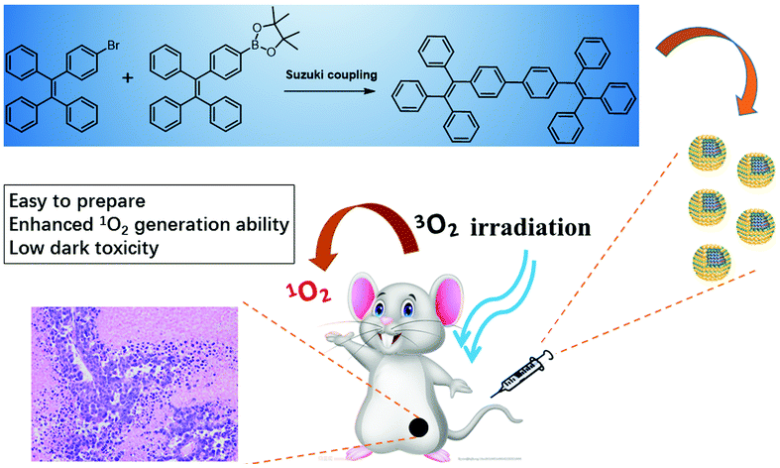


Figure 18. Illustration of synthesis and application of BTPE NPs for improved PDT adapted from.[56]

The development of new molecules is currently in request, although these drugs are available and have been used effectively for several decades due to the low selectivity of accumulation in tumors of current agents used clinically,[57] and the undesirable toxicity to adjacent healthy cells irradiated during treatment. To this end, studies have been performed to improve the biodistribution and known drugs selectivity through combination of PSs with entities designed to eliminate cancer cells, to provide selective tissue distribution and additional chemotherapeutic action, and to treat limited areas during PDT application.[17]

I.8 Combination Therapy

Combination therapy is a promising therapeutic strategy currently used to improve PDT in modern oncology. This combined approach aims to increase the efficacy of the associated approaches through an additive to synergistic effect, and is applied either to eliminate pro-survival signals from PDT-resistant tumor areas, or to weaken tumor cells that will subsequently be treated with PDT.[26]

The combination of PDT with chemotherapy was proven for the first time by Nahabedian *et al.*[58] They have shown that this strategy can induce strong cytotoxic effects.[58] In another hand, Wang *et al.* reported that this strategy was effective in eliminating surviving tumor cells after treatment with cisplatin.[59] Similarly, Antoni *et al*. used cisplatin and zinc porphyrin on human ovarian cancer cells, with high efficiency proving this synergistic effect.[60]

In a recent study, Ding *et al.* reported the construction of novel nanoplatform for a combined chemo-photodynamic synergistic therapy generated by chemiluminescence, called PCL-NP.The

biocompatible macromolecule dextran was selected as the PCL-NP scaffold. It was further decorated with three main components: the ROS-activatable prodrug PTX, the photosensitizer Ce6 and the chemiluminescence agent luminol. H_2O_2 that is overexpressed in tumour tissue is employed as a biochemical driver to achieve chemiluminescence by oxidizing the luminol moiety. *In situ* PDT was triggered by CRET of luminol at Ce6. PCL-NP achieved better therapeutic results by eradicating 4T1 tumors and showed significant safety for non-tumoral tissues. All In all, PCL-NP represents a promising approach for the improvement of synergistic chemo-PDT.[61]

PDT has also been used in combination with other conventional therapies such as radiotherapy RT either simultaneously or as an adjuvant to radiotherapy. Allman *et al*. notably described the use of 5-aminolevulinic acid (ALA) as a PDT agent following gamma irradiation, leading to an additive level of cytotoxicity.[62] In a similar approach, Luksiene *et al*. showed that hematoporphyrin dimethyl ether mediated by PDT and RT inhibited cancer cell proliferation by producing an additive effect.[63]

Umegaki's team used PDT to reduce cutaneous anaplastic large-cell lymphoma prior to RT. In this single-patient study, (ALA), was delivered topically and the tumor was externally irradiated with a halide lamp (λ_{max} = 630-700 nm) 6 h after ALA administration. The patient experienced no significant side effects except for some tolerable pain in the illuminated area.[64]

Cancer immunotherapy has achieved great clinical progress in advanced tumors. It is an innovative therapeutic approach that modulates the immune microenvironment and activates the immune system. It can also produce immunological memory effects in long term without causing damage to surrounding cells.[65] The combination of PDT with immunotherapy had interesting potential in recent years, with promising results. It has been shown that the application of this approach can result in a synergistic effect leading to cell death, tumour regression and ultimately, immune memory.[66-67]

Unfortunately, the PDT efficiency is limited by hypoxic environment of tumor. Therefore, researchers are dedicated to combine PDT with other therapies to obtain effective tumor treatment, particularly with photothermal therapy (PTT), as both PDT and PTT are non-invasive and precision therapy strategies.[68] More importantly, PTT can increase the temperature leading to acceleration blood flow in tissues to improve oxygen delivery to the tumor site which promotes PDT.[69] Meanwhile, the reactive oxygen species (ROS) induced by PDT can kill the heat-resistant tumor cells to obtain synergistic treatment.[70]

Li *et al.* reported the synthesis of three berberine dimers **BD1**–**BD3** and one tetramer **BD4** in which berberine subunits are linked by aromatic rings of varying conjugation sizes (**Figure 19**). Among them, **BD3** featuring a 1,10-phenanthroline-2,9-dimethyl skeleton with the best $^1O_2$ generation ability

was selected to combine with photothermal material AuNSs to form an AuNSs–BD3 hybrid nanocomposite, which was further coated with the hyaluronic acid (HA) to specifically target the CD44 receptor on the surface of tumor cells. After entering the cells with the CD44 mediated endocytosis, the coated HA was diffused *via* the intracellular hyaluronidase (HAase) releasing the AuNSs-BD3 nanosystem. The obtained systems showed excellent therapeutic activity *in vitro* and *in vivo*, thanks to the PTT ability of AuNSs, targeting from HA, and PDT from BD3.[71]

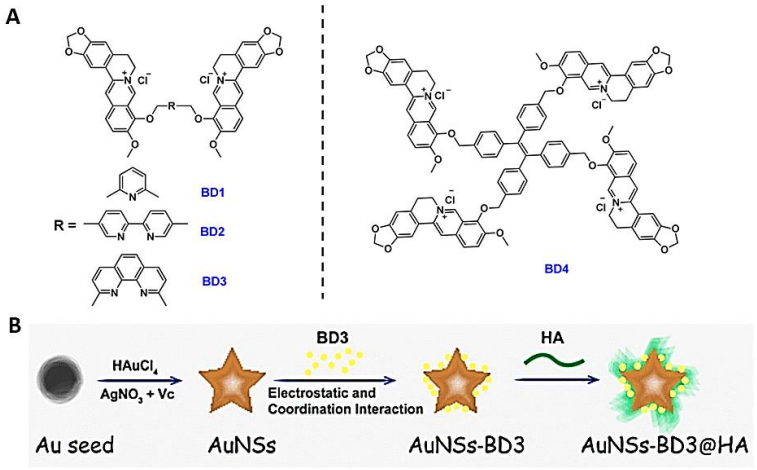


Figure 19. (A) Structures of berberine dimers BD1-BD3 and tetramer BD4,**(B)** Construction de nanocomposites AuNSs-BD3 @HA Adapted from.[71]

I.9 Advantages and applications of PDT

PDT offers several advantages over classical cancer treatment on long term. It has no side effects when it used correctly. It can also be performed in ambulation because it is less invasive than the other surgical procedures. In addition, it can induce cell death by destroying the vascular systems associated with the tumor.[72] Moreover, PDT can be applied directly to targeted areas, notably in the case of topical application, since the PS is applied only to the lesion to be treated, whereas in the case of intravenous application, it must be ensured that the PS is kept in circulation for a long time in order to accumulate in cancer cells. In contrast to radiotherapy, PDT can be used on the same area several times. Finally, this approach is less expensive than other therapeutic modalities.[72]

PDT is a minimally invasive procedure used clinically to treat many oncological diseases such as skin, esophageal, head and neck cancers. However, PDT can be also used in a variety of non-oncological applications.[73] Including the treatment of human non-cancerous diseases, such as dermatological diseases such as acne,[74] warts,[75] photoaging,[76] psoriasis,[77] vascular malformations,[78] hirsutism,[79]

keloid,[80] alopecia,[81] in ophthalmology,[82] cardiovascular,[83] esophageal varices,[84] dental,[85] neurological (Alzheimer's disease),[86] , skeletal (rheumatoid arthritis),[87] and gastrointestinal diseases (Crohn's disease).

I.10 Challenges of PDT

Photodynamic therapy, as a non-invasive therapeutic modality, it is widely studied for cancer treatment. The drawbacks shown by the PS used for PDT applications, such as poor solubility in water, low cell selectivity and poor selectivity in targeted cells, decrease the efficiency and limit the application of PDT.[37]

Among the most notable challenges for PDT are tumor-targeting efficiency, light propagation through tissues, which can lead to incomplete diffusion of light into target areas, and finally, tumor hypoxia.

I.10.1 Tumor- targeting efficiency

Targeting efficacy was always as a crucial challenge related to the poor tumor distribution that many PS tend to exhibit after administration, poor tumor distribution leads to reduced accumulation of PS in the tumor, causing a decrease in active molecules in target areas, and ultimately incomplete destruction of the tumor. This targeting capacity is due to the abnormal physiological properties of tumors. On the other hand, it depends on PS characteristics such as morphology, particles size and surface modulation. For these reasons, research has focused on improving PS targeting in order to enhance efficiency and reduce off-target accumulation. This is usually achieved by using carrier systems, including antibodies, liposomes and nanoparticles (NPs), which can facilitate more favorable biodistribution. Encapsulation in/or association with these carrier systems introduces a degree of control in the distribution of the PS-carrier complex.[88]

I.10.2 Light propagation through Tissues

The attenuation of light in tissues limits the maximum tissue light penetration. This can result in partial illumination of the tumor area if the depth of the tumor goes beyond the maximum light penetration used for PDT leading to an incomplete destruction of tumor cells and its surrounding vasculature.[88] One strategy to overcome this issue is to use PSs that can be excited by NIR light in the therapeutic window area. This strategy can optimize PDT and offer deeper therapy, thus reducing phototoxicity in surrounding healthy tissue .[37]

I.10.3 Tumor Hypoxia

Hypoxia has been known and studied since 1930.[89] It is one of the main feature of most solid tumors (refer to solid tumors area with an oxygen pressure of less than 10 mm Hg) occurring due to disparity between aggressive oxygen consumption by tumor cells and inadequate oxygen supply.[90] The heterogeneous hypoxic environment in different regions of the tumor zone induces multiple tumor progression, including tumor progression, metastasis and angiogenesis, as well as resistance to clinical treatment. It was shown that various enzymes are overexpressed in the hypoxic regions of most solid tumors such as nitroreductase, DT-diaphorase, azoreductase, human carbonic anhydrase IX.[91]

Hypoxia can be caused generally because of the difference in function and morphology between the tumor and physiological vessels, due to the inability of cancer cells to link with angiogenic and anti-angiogenic factors, resulting in an abnormal vascular structure with irregular blood flow[92] and secondly, due to a disorder in the vascular networks induced by the distance between tumor capillaries, which exceeds the oxygen diffusion range.[93] It was observed that cancer cells closer to vessels have better and easier access to nutrient and oxygen than those further away, and in extreme hypoxia such zones can cause the appearance of vast necrotic area within the tumor, they can adapt to hypoxic stress *via* releasing HIF-1α, which can modify more than 60 genes involved in various aspects of cells biology.[94] It was reported that hypoxia could inhibit immune response, which can restricts the PDT efficiency, while enhancing tumor invasion and metastasis. As a consequence, tumor hypoxia represents a major challenge for PDT development and tumor treatment.[24] To overcome the limitations of hypoxia, studies in the context of PDT have proposed PS that consume less oxygen, Fan *et al.* reported the new design of intelligent 2D theranostic nanomaterials based on pH-/H_2O_2-responsive MnO_2 nanosheets anchored with upconversion nanoprobes. These nanoprobes can react with acidic H_2O_2 in order to produce sufficient oxygen, and to improve the synergetic photodynamic therapy efficiency during NIR light/X-ray irradiation.[95] In another study, Chen and his colleagues described the loading photosensitizer into perfluorocarbon nanodroplets to develop a novel oxygen self-enriched photodynamic therapy (Oxy-PDT). They showed in particular that the efficiency of PDT was improved thanks to the higher oxygen capacity and longer $^1O_2$ lifetime.[96]

In another study, a carbon nitride (C_3N_4)-based multifunctional nanocomposite (PCCN) was synthesized by the team of Zheng, the study *in vitro* showed that PCCN could increase the intracellular O_2 concentration and enhance ROS production in both environment (hypoxic and normoxic) upon light irradiation.[97]

In order to improve oxygen diffusion and increase the efficacy of nanomedicine-based PDT, a new approach based on the use of hyaluronidase (HAase), an essential element for perturbing the

extracellular matrix (ECM) in tumors was also described. Treatment with HAase lead to an increase of oxygen content throughout the tumor and allows improving PDT-induced tumor growth inhibition compared with the same treatment without hyaluronidase, indicating the potential of extracellular matrix modeling pre-PDT.[98]

II. Carbonic anhydrases

Carbonic anhydrases (CAs) are metalloenzymes that are omnipresent in nature. They were discovered in 1932 from bovine red blood cells by N.U Meldrum and F.J.W Roughton, to identify the catalytic activity that allows fast transit of bicarbonate from red blood cells to pulmonary capillaries. This research led to the identification of the role of carbonic anhydrases. CAs catalyze the reversible hydration reaction of CO_2 to HCO_3^- and H^+ in all organisms (**Figure 20**).[99]

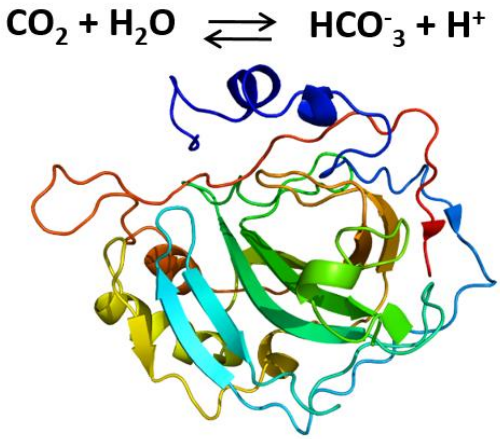


Figure 20. Hydration of CO_2 reaction catalyzed by carbonic anhydrase (hCA II).

In vertebrates, CAs can be found at least 16 isoforms (CA I-XV) related to class α, depending to their distribution (cytosolic, mitochondrial, secreted and membrane associated). They can be classified into four groups in other organisms. Nowadays, they are classified in eight specific genetic unrelated families, namely the α-, β-, γ-, δ-, ζ-, η-, θ- and ι-classes. All human carbonic anhydrases (**hCAs: hCA I**, **hCA II**, **hCA III**, **hCA IV**, **hCA VA**, **hCA VB**, **hCA VI**, **hCA VII**, **hCA VIII**, **hCA XI**, **hCA X**, **hCA XI**, **hCA XII**, **hCA XIII**, **hCA XIV**)[100] are belonging to α class and twelve isoforms (CA I-IV, VA-VB, VI-VII, IX and XII-XIV) exhibit varying degrees of enzymatic activity. These isoforms exhibit different molecular characteristics, cellular localization, distribution in organ and tissue, response to several classes of inhibitors and expression levels. hCA I-III, hCA VII and hCA XIII are cytosolic, hCA IV, hCA IX, hCA XII and hCA XIV are found as membrane-bound, and hCA VA and hCA VB are mitochondrial isoforms.[100-101]

Chapter I: General introduction & thesis Outlines

The extensive expression of CAs is found in a diverse range of human organs and tissues, indicating their important physiological role, they are also implicated in many physiological and pathological processes, notably respiration and transport of CO_2 and bicarbonate between metabolized tissues and lungs, bone resorption, calcification, tumorigenicity and virulence of various pathogens.[102]

II.1 Structure of hCAs

HCA's (human carbonic anhydrases) are metalloenzymes that exhibit catalytic efficiency only when a metal ion (typically Zn^{2+}) is bound within the cavity of the active site. This active site is situated at the base of a large conical cavity, approximately 12 Å wide and 13 Å deep, extending from the protein surface to the molecule's center. The active site features a tetrahedral coordination environment, primarily facilitated by three conserved histidine residues (**His 94, His 96, and His 119**), which serve to anchor the metal ion, along with either a water molecule or a hydroxyl ion (**Figure 21**). The Zn^{2+} bound water molecule/hydroxide ion is involved into a network of hydrogen bonds that contribute improving the hCA nucleophilicity. The hydrogen is bonded to the hydroxyl moiety of a conserved Thr residue (**Thr199**) and to two water molecules, located on opposite sides: the first, called "deep water", is in a hydrophobic cavity delimited by the conserved residues in positions 121, 143, 198 and 209, while the second is in a hydrophilic environment towards the entrance of the active site. (**Figure 22**).[103]

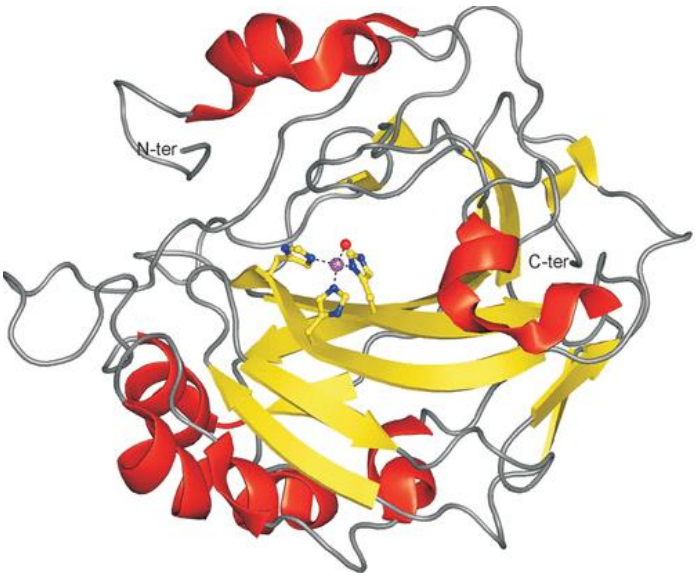


Figure 21. Ribbon diagram of hCA II structure, which has been chosen as representative hCA isoform. The active site Zn^{2+} adapted from.[104]

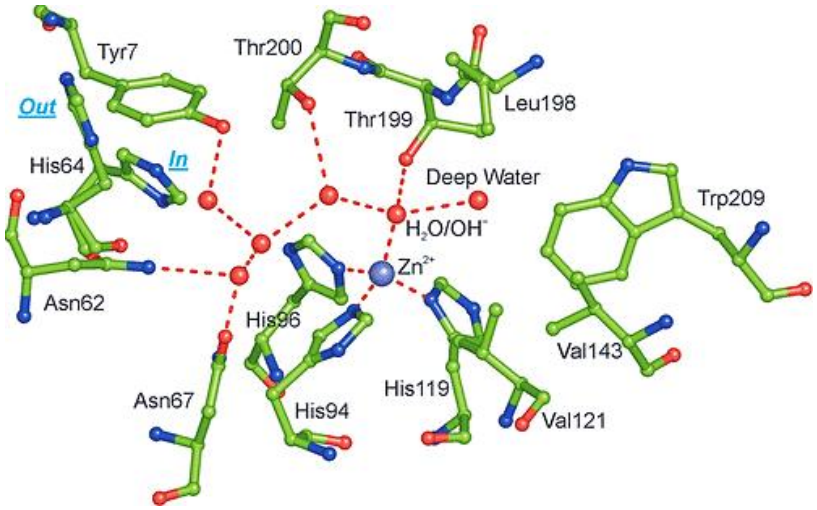


Figure 22. The active site of hCA II, which has been chosen as representative hCA isoform. The Zn^{2+} is tetrahedrally coordinated by three catalytic histidine's and water molecule/hydroxide ion, which is engaged in a well-defined network of hydrogen bonds. Water molecules are indicated as red circles. The side chain of His 64 is shown in both the in and out conformations adapted from.[104]

II.2 Catalytic mechanisms of hCAs

Hydroxide species generated from metal-bounded water is the catalytically active species in all CAs. This is due to the highest nucleophilicity of the hydrophobic environment inside the active site and the coordination of the metal ion.[105] The zinc atom is stabilized by its coordination with three residues of histidine (**Figure 23 A**). The hydroxide ion (HO^-) linked to zinc atom will attack carbon dioxide CO_2, which is bound to a hydrophobic pocket close to zinc ion (**Figure 23 B**) leading to the formation of enzyme-HCO_3^- adduct (**Figure 23 B** to **C**). This intermediate reacts then with water molecule liberating the bicarbonate into solution (**Figure 23 C** to **D**). The enzyme becomes inactive in the acid form. After coordination of zinc atom to water molecules, to return to the activated state and regenerate the hydroxide ion, a proton from the water molecule bound to the zinc will be transferred either to an exogenous proton acceptor or to an active site residue (**Figure 23 D** to **A**). This last step is considered the limiting step in the catalytic cycle.[106]

It was found that in some isoforms such as hCA I, hCA II, hCA IX, the His64 residue situated at the entrance of the active site allowing rapid proton transfer, which can explain the reason behind their better catalytic activity compared with other hCAs isoforms.

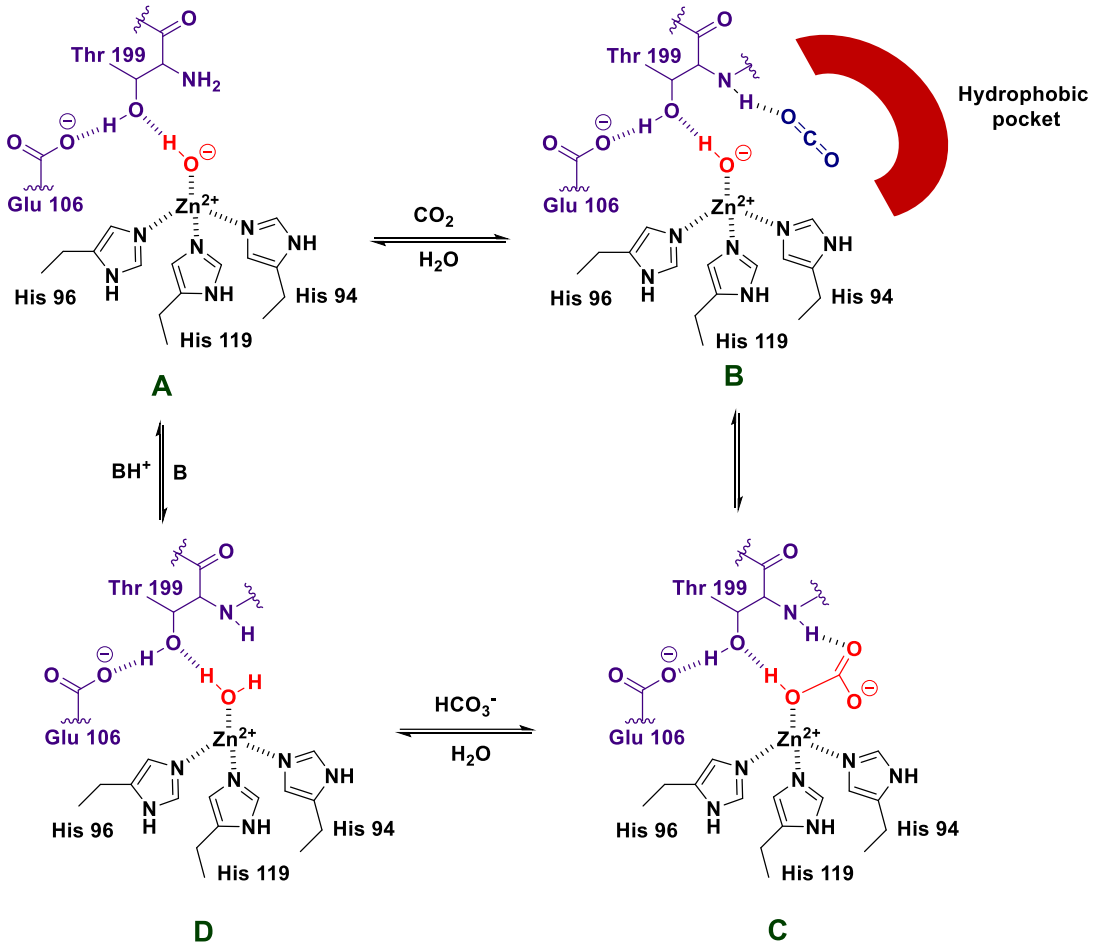


Figure 10. Catalytic mechanism of reversible hydration of CO_2 to HCO_3^- and a proton in the presence of α-CAs Adapted from.[107]

II.3 Expression of hCA IX and hCA XII

Different hCAs isoforms have been implicated in various essential cellular processes, including gas exchange at the air-water interface, CO_2 and HCO_3^- transport across membranes, biosynthetic reactions, acid-base tuning, calcification, oncogenesis, and metastatization.[108]

According to literature, it has been shown that two hCAs isoenzymes, hCA IX and hCA XII have been found to be strongly associated with overexpression in some cancers (the discovery of at least two hCAs isoforms closely connected to tumors, hCA IX in Bratislava by Silvia Pastorekova/Jaromir Postorek in 1992, and hCA XII by Tureci *et al*. in 1998 , and related with tumor progression and resistance to clinical treatment).[109-110] The first hCA IX is strongly overexpressed in cancer cells particularly in solid tumors while hCA XII was found to be coexpressed with hCA IX in some tumor tissues. It was also found to be expressed in normal tissues.[111]

The extracellular environment at the middle of the tumor mass found to be hypoxic. In this case, the cells at the center are far from the blood capillaries supplying them with oxygen and nutrients. These cells respond to hypoxic stress by activating several genes, including the one encoding hCA, by binding the transcription factor HIF-1 (exhibits two subunits: HIF1-α and HIF-1β) to a hypoxia-sensitive element in the gene.[112]

In normoxic conditions, the HIF-1α subunit is hydroxylated and then ubiquitinated by the Von Hippel Lindau protein pVHL, leading to its degradation by the proteasome. In such conditions, transcription is not initiated because the HIF-1α-HIF-1β complex is inactive. In contrast, under hypoxic conditions, and as it is the case in several solid tumors, following inhibition of pVHL binding to HIF-1α, HIF-1α will accumulate and associate with the HIF-1β subunit, leading to stabilization of the HIF-1 complex and transcription of a large number of hypoxia-induced genes, including the gene encoding CA IX (**Figure 24**).[113]

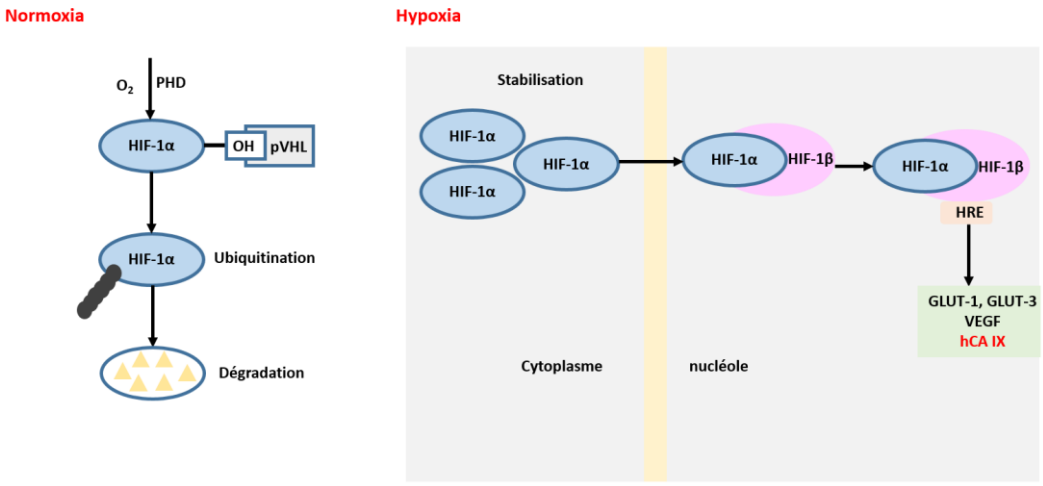


Figure 24. Regulation of hypoxia-induced gene expression mediated by the HIF-1 transcription factor adapted from.[113]

It was documented that hCA XII is also induced by hypoxia.[114] However, hCA XII gene does not include any HRE (hypoxia-responsive element) in the promoter region near the transcription site. The region before the hCA XII gene has several HRE elements estimated with a consensus HIF-binding sequence but their functionality has not been confirmed.[115]

II.4 Pathologies associated to hCAs

Several studies have shown that CAs have crucial roles in different physiological processes due to their wide distribution and diversity in function. When these enzymes are dysfunctional or overexpressed, they lead to a disorder in the physiological process resulting in the appearance of

various severe pathologies such as glaucoma, obesity, osteoporosis, cancer, high altitude sickness, epilepsy, neuropathic pain, and sleep apnea.[104] Therefore, various hCAs isoforms are crucial targets for the design of new inhibitors with clinical applications. hCA I is largely found in many tissues and is implicated in some pathologies such as retinal and cerebral edema. hCA II is also widely presents in several tissues with an important role in many diseases' conditions (*e.g.,* glaucoma, epilepsy, edema, and renal disorders). hCA III is associated to the oxidative stress and to several inflammatory diseases. hCA IV was reported to be as a drug target for glaucoma, stroke, and retinitis pigmentosa. It was mentioned that the mitochondrial isoforms hCA VA and hCA VB are responsible for obesity. hCA VII is well-documented target for epilepsy and it can act together with hCA II and XIV within the brain in cognition-related processes. hCA VIII has been shown to be involved in neurodegenerative troubles and mental retardation. Unfortunately, only limited information is available on the isoforms hCA VIII, hCA X and hCA XI with reference to their actual physiological functions. Both of hCA IX an hCA XII isoforms are known to be overexpressed in solid tumors and responsible for tumor growth, progression, and metastasis. Therefore, these isoforms can be used as drug targets in hypoxic tumors. hCA IX is more studied as a target for anticancer drug than hCA XII. However, several reports have also referred to its role in cancer progression.[100] Table 2 below resumes some pathologies associated to hCAs.

Isoforms	**Diseases in which there are involved**
hCA II, hCA IV, hCA XIV	Edema
hCA II, hCA IV, hCA V, hCA VII et hCA XIV	Hemiplegia, migraine, ataxia, periodic paralysis
hCA IV, hCA XIV	Epilepsy
hCA II, hCA IV, hCA XII	Glaucoma
hCA II, hCA IV,h CA V, hCA XII, hCA XIV	Heart failure, kidney and liver disease, diabetes
hCA IX, hCA XII	**Cancer**
hCA II	Osteoporosis
hCA V, hCA II	Obesity

Table 2. Diseases related to α-hCAs adapted from.[104]

II.5 Inhibitors of hCAs

Inhibition of carbonic anhydrase was clinically exploited for decades. Several studies have described the use of various pharmacological agents that have been developed to inhibit targeted enzyme. The classical family of hCAs inhibitors (hCAIs) is the primary sulfonamides (RSO_2NH_2) discovered for the first time by Mann and Keilin.[116] They are already used in clinic for more than half century as diuretics and antiglaucoma drugs (**Figure 25**) and they still have an important place for the management of these conditions.[117] However, in the last decade, various others applications have emerged the widespread availability of much more selective isoform inhibitors including the use of CAIs such as acetazolamide, topiramate and zonisamide as antiepileptics and anti-obesity agents, anticancer agents, painkillers and anti-infective (**Figure 25)**.

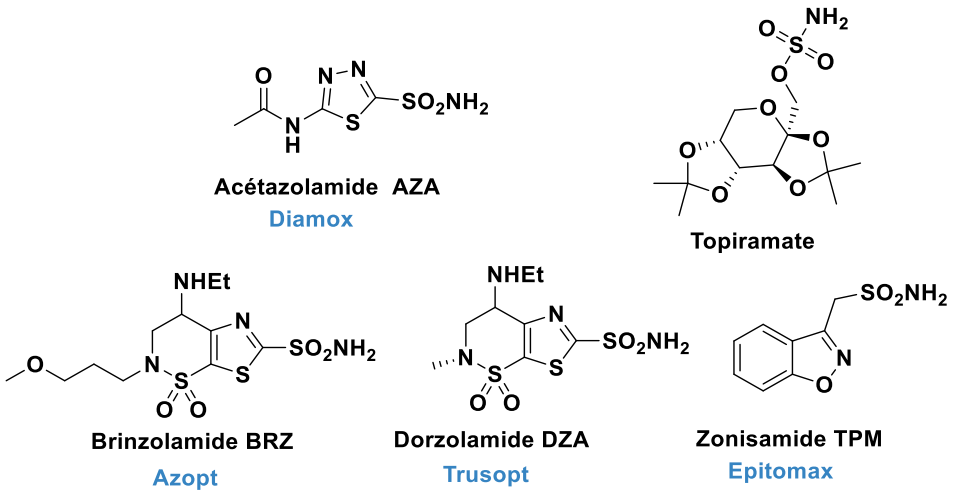


Figure 25. Some hCAIs structures adapted from.[117-118]

II.6 Inhibition mechanism of hCAs

II.6.1 The zinc binders as CAIs

This type of CAs inhibitors are zinc binders including zinc-binding group (ZBG) (SO_2NH^- moieties for the sulfonamides class) that bind directly to the metal ion of the active site which exhibit tetrahedral geometry with three residues of histidine typically (**Figure 26 A**). This presents the classical strategy of carbonic anhydrase inhibition, adapted by several classes of CAIs including inorganic anions, sulfonamides and their isosteres, dithiocarbamates and their derivatives, monothiocarbamates,

xanthates and trithiocarbonates, selenol some carboxylates hydroxamates phosphonamidates, benzoxaboroles, carbamates and ninhydrins.[102-105-119]

II.6.2 CAIs anchoring to the zinc-coordinated water/hydroxide ion

Compounds inhibiting CAs by anchoring mechanism to the water/hydroxide ion molecule bound to the zinc of enzyme's active site (**Figure 26 B**), own anchoring group (AG), that is linked to a scaffold which may include tails that are able to interact with the two halves of the active site as for zinc binders. However, the only difference is the inhibitor which is not in direct contact with the metal ion. Phenol was discovered as the first compound adapting this mechanism, followed by the polyamine spermine. Afterwards this mechanism was also referenced for polyamine, sulfocoumarins, thioxocoumarins and catechols.[102-105-119]

II.6.3 CA inhibition by occlusion of the active site entrance

Figure 26 C illustrates the third CA inhibition mechanism, *i.e.* active site entrance occlusion. In this type, the inhibitor binds at the entrance of the active site cavity, further away from the metal ion compared to other CAIs which bind with zinc of the active site or anchoring to the zinc-linked water molecule. The molecules which possess this mechanism, exhibit a sticky group SG linked to the scaffold which can be aromatic, heterocyclic, or aliphatic. They can also have a tail extending out of the active site. This inhibition strategy has been identified for the first time for the coumarins extracted from the Australian plant *leinema ellipticum*. Thereafter, studies reported that all coumarins related mono-/bicyclic lactones own this kind of inhibition mechanism, which in effect, hydrolyzes the lactone ring to form hydroxy-cinnamic acids (for the coumarins) or aliphatic hydroxy acids in (for 5/6-membered lactones).[102-105-119]

The most interesting aspect of this inhibition mechanism is that the inhibitors binding to a region of the active site is the most variable between the different isoforms. This has an important implication for CAIs drug design. As these compounds bound to this region, they should interact differently with different class of CAIs, and thus, shows CAIs selectivity profiles.

II.6.4 Out of the active site binding

Recently, a fourth mechanism of CA inhibition has also been demonstrated by X-ray crystallography. A benzoic acid derivative was found outside the active site cavity, in a hydrophobic pocket close to the entrance to the active site. Inhibition is achieved by blocking the proton shuttle

residue (His64) in its exit conformation, leading to the collapse of the entire catalytic cycle (**Figure 26 D**).[102-105-119]

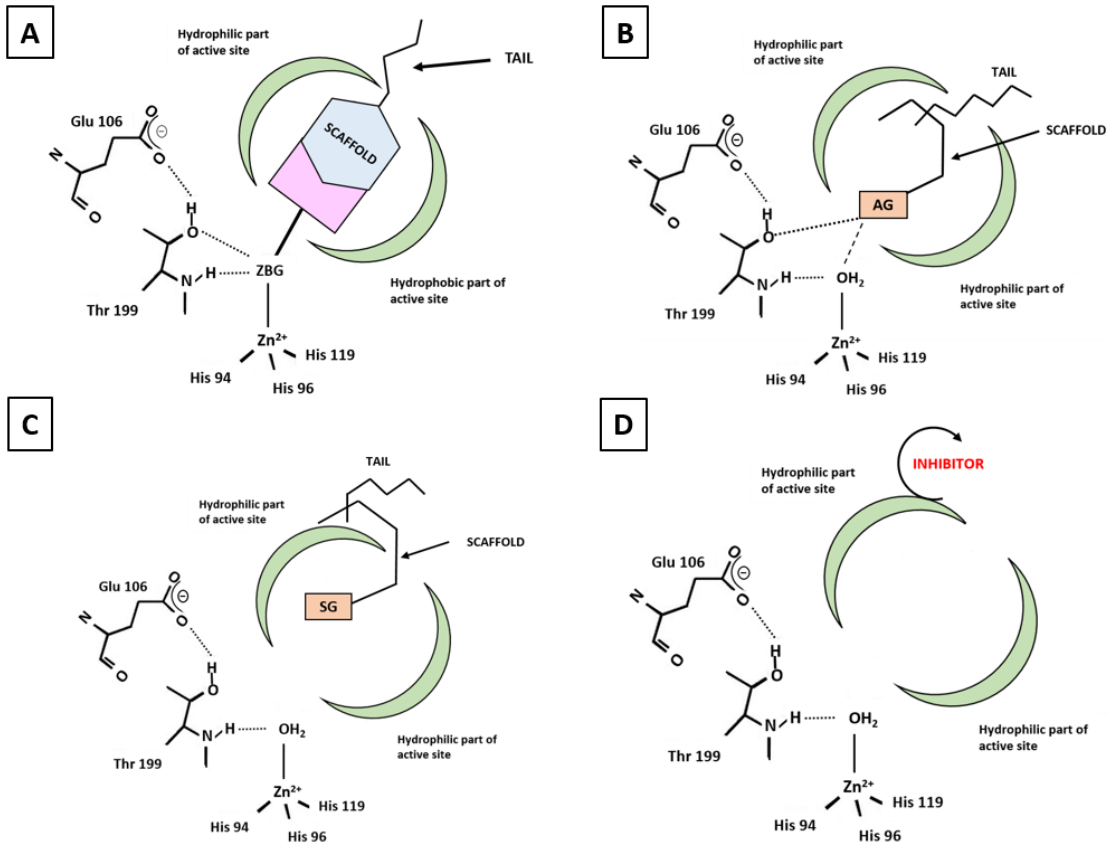


Figure 26. Mechanism of CA inhibition, **A** Zinc binding **B** Anchoring to the zinc-coordinated water/hydroxide ion, **C** Occlusion of the active site entrance, **D** Out of the active site binding adapted from.[102-105-119]

Recent research reported that targeting hCA IX and hCA IIX due to their overexpression in cancer can be one of the innovative strategies which can improve PDT applications leading to efficient therapy. This part will be discussed in more details in the next chapter.

Chapter I: General introduction & thesis Outlines

III. Objectives of thesis

According to statistics from the National Cancer Institute, cancer has major impact on society worldwide over the years. A great deal of research has been carried out to improve the fight against this disease. Today, various types of treatment modalities are available depending on the stage of cancer. PDT is an emerging non-invasive treatment modality and promising alternative to classical approaches based on the combination of three essential components (PS, oxygen, and light) in order to kill cancer cells, by the stress oxidation induced during the photo-activation of the PS. However, the efficiency of PDT can be reduced due to tumoral hypoxia, occurring because of a disparity between intensive oxygen consumption by tumour cells and inadequate oxygen supply. In these conditions, tumoral cells respond to hypoxic stress through activating several genes including the one encoding hCA, *via* binding the transcription factor HIF-1, to a hypoxia-sensitive element in the gene. In response, hCA IX and hCA XII were found to be activated and overexpressed in these zones. The presence of the latest two enzymes in several tumors makes them as valuable targets for cancer treatment. A such, combining targeting, inhibition of hCA IX/XII with PDT has emerged as a potential strategy for developing high-performance PS and overcome hypoxia problems.

Since our work is a part of this context, the main objectives are:

- **Developing several innovative multifunctional systems combining both the targeting and multivalent inhibition of carbonic anhydrase hCA IX and hCA XII with PDT:**
  - **a)** Synthesis of zinc (II) porphyrins platforms combining four peripheral human carbonic anhydrase inhibitors (HCAIs) (sulfonamide and coumarin) through click chemistry reaction. Porphyrins were chosen as photosensitizers for PDT applications thanks to their significant properties reported in literature and the clinical use of their derivatives.
  - **b)** Synthesis of novel PSs based on a thiochromenocarbazole imide (TCI) scaffold linked with hCAIs in coumarin and sulfonamide series. Their very good fluorescence properties and high singlet oxygen generation efficiency enables their use for image-guided PDT.
  - **c)** Design of new AIE-based PS using tetraphenylethene (TPE) as a scaffold to overcome ACQ due to the π-π stacking of porphyrins and BTXI, which may reduce the efficiency of these PSs. Like the two other systems, they were functionalized with hCAIs. We will demonstrate their ability to generate singlet oxygen upon aggregation.
- **Characterizations and studies of their optical properties.**
- **Studies of their biological properties:**

  Including their cytotoxicity, imaging, phototoxicity and inhibition properties.

Chapter I: General introduction & thesis Outlines

IV. Outlines of thesis

Chapter 2 summarizes the latest studies of carbonic anhydrase inhibitors applications, combined with photosensitizing agents used in PDT against solid hypoxic tumors. Its advance, challenges, and future perspectives are also discussed**.**

Chapter 3 is devoted to the synthesis of novel PSs based on tetrafunctionalized zinc (II) porphyrins linked with hCAIs in sulfonamide and coumarin series. This chapter includes characterization, optical characteristic studies, and biological tests (cytotoxicity, inhibitory properties, photocytotoxicity…) of these multifunctional systems.

Chapter 4 deals with the design of new benzothioxanthene-base PSs linked to hCAIs (namely, coumarin, sulfonamide and sulfocoumarine). Their characterization and optical characteristic studies are included. Biological studies including human carbonic anhydrase inhibition, imaging of MDA-MB 231 cell lines, PDT *in vivo* and *in vitro* are also described.

Chapter 5 describes different AIEgen PSs using a TPE scaffold and featuring hCAIs. These PSs will be designed through a Donor-Acceptor (D-A) approach which consists in the separation of the HOMO-LUMO distribution and thus, allows reducing repulsion between valence electrons in the S1 state to achieve smaller ΔEST.[120] To these PSs, were grafted some carbonic anhydrase inhibitors (namely, benzosulfonamide or coumarine). These CAis were either closely linked to the TPE core or separated from the PS with an alkyl side chain. The effect of the number of electrons accepting moieties on the TPE core will also be investigated.

Finally, **Chapter 6** presents a general discussion of the outlined work in this manuscript with outlooks into the future of these PSs as well as the further developments requite to improve their performances.

V. References:

1. https://www.who.int/news-room/fact-sheets/detail/cancer.

2. cancer, F. n. p. l. r. s. l. le cancer en chiffres (France et monde). https://www.fondation-arc.org/cancer/le-cancer-en-chiffres-france-et-monde (accessed 20-07-2023).

3. Ackroyd, R.; Kelty, C.; Brown, N.; Reed, M., The history of photodetection and photodynamic therapy¶. *Photochemistry and photobiology* **2001,** *74* (5), 656-669.

4. Correia, J. H.; Rodrigues, J. A.; Pimenta, S.; Dong, T.; Yang, Z., Photodynamic therapy review: principles, photosensitizers, applications, and future directions. *Pharmaceutics* **2021,** *13* (9), 1332.

5. Jiang, W.; Liang, M.; Lei, Q.; Li, G.; Wu, S. The Current Status of Photodynamic Therapy in Cancer Treatment *Cancers* [Online], 2023.

6. Mitton, D.; Ackroyd, R., A brief overview of photodynamic therapy in Europe. *Photodiagnosis and Photodynamic Therapy* **2008,** *5* (2), 103-111.

7. Hayata, Y.; Kato, H.; Okitsu, H.; Kawaguchi, M.; Konaka, C. In *Photodynamic therapy with hematoporphyrin derivative in cancer of the upper gastrointestinal tract*, Seminars in surgical oncology, Wiley Online Library: 1985; pp 1-11.

8. Wang, Z.; Peng, H.; SHi, W.; Gan, L.; Zhong, L.; He, J.; Xie, L.; Wu, P.; Zhao, Y.; Deng, Z., Application of photodynamic therapy in cancer: Challenges and advancements. *Biocell* **2021,** *45* (3), 489.

9. Merabti, A.; Roger, M.; Nguyen, C.; Nocentini, A.; Gerbier, P.; Richeter, S.; Gary-Bobo, M.; Supuran, C. T.; Clément, S.; Winum, J. Y., Carbonic Anhydrase Inhibitors Featuring a Porphyrin Scaffold: Synthesis, Optical and Biological Properties. *European Journal of Organic Chemistry* **2022**, e202101538.

10. Dos Santos, A. F.; de Almeida, D. Q.; Terra, L. F.; Baptista, M. S.; Labriola, L., Photodynamic therapy in cancer treatment-an update review. *J. Cancer Metastasis Treat* **2019,** *5* (25), 10.20517.

11. Aziz, B.; Aziz, I.; Khurshid, A.; Raoufi, E.; Esfahani, F. N.; Jalilian, Z.; Mozafari, M. R.; Taghavi, E.; Ikram, M. An Overview of Potential Natural Photosensitizers in Cancer Photodynamic Therapy *Biomedicines* [Online], 2023.

12. Kah, G.; Chandran, R.; Abrahamse, H. Curcumin a Natural Phenol and Its Therapeutic Role in Cancer and Photodynamic Therapy: A Review *Pharmaceutics* [Online], 2023.

13. Yao, Q.; Fan, J.; Long, S.; Zhao, X.; Li, H.; Du, J.; Shao, K.; Peng, X., The concept and examples of type-III photosensitizers for cancer photodynamic therapy. *Chem* **2022,** *8* (1), 197-209.

14. Donnelly, R. F.; McCarron, P. A.; Tunney, M. M., Antifungal photodynamic therapy. *Microbiological research* **2008,** *163* (1), 1-12.

15. Agostinis, P.; Berg, K.; Cengel, K. A.; Foster, T. H.; Girotti, A. W.; Gollnick, S. O.; Hahn, S. M.; Hamblin, M. R.; Juzeniene, A.; Kessel, D., Photodynamic therapy of cancer: an update. *CA: a cancer journal for clinicians* **2011,** *61* (4), 250-281.

16. Stallivieri, A. Synthèse de systèmes à base de photosensibilisateurs pour l'amélioration de la sélectivité tumorale en thérapie photodynamique. Université de Lorraine, 2015.

17. Otvagin, V. F.; Kuzmina, N. S.; Kudriashova, E. S.; Nyuchev, A. V.; Gavryushin, A. E.; Fedorov, A. Y., Conjugates of porphyrinoid-based photosensitizers with cytotoxic drugs: current progress and future directions toward selective photodynamic therapy. *Journal of Medicinal Chemistry* **2022,** *65* (3), 1695-1734.

18. Sun, X.; Leung, W. N., Photodynamic Therapy with Pyropheophorbide-a Methyl Ester in Human Lung Carcinoma Cancer Cell: Efficacy, Localization and Apoptosis. *Photochemistry and Photobiology* **2002,** *75* (6), 644-651.

19. Gèze, M.; Morlière, P.; Mazière, J. C.; Smith, K. M.; Santus, R., Lysosomes, a key target of hydrophobic photosensitizers proposed for photochemotherapeutic applications. *Journal of Photochemistry and Photobiology B: Biology* **1993,** *20* (1), 23-35.

20. Kessel, D.; Luguya, R.; Vicente, M. G. H., Localization and Photodynamic Efficacy of Two Cationic Porphyrins Varying in Charge Distribution. *Photochemistry and Photobiology* **2003,** *78* (5), 431-435.

21. Dummin, H.; Cernay, T.; Zimmermann, H. W., Selective photosensitization of mitochondria in HeLa cells by cationic Zn(II)phthalocyanines with lipophilic side-chains. *Journal of Photochemistry and Photobiology B: Biology* **1997,** *37* (3), 219-229.

22. Castano, A. P.; Demidova, T. N.; Hamblin, M. R., Mechanisms in photodynamic therapy: part one—photosensitizers, photochemistry and cellular localization. *Photodiagnosis and photodynamic therapy* **2004,** *1* (4), 279-293.

23. Teiten, M. H.; Bezdetnaya, L.; Morlière, P.; Santus, R.; Guillemin, F., Endoplasmic reticulum and Golgi apparatus are the preferential sites of Foscan® localisation in cultured tumour cells. *British Journal of Cancer* **2003,** *88* (1), 146-152.

24. Sun, Y.; Zhao, D.; Wang, G.; Wang, Y.; Cao, L.; Sun, J.; Jiang, Q.; He, Z., Recent progress of hypoxia-modulated multifunctional nanomedicines to enhance photodynamic therapy: opportunities, challenges, and future development. *Acta Pharmaceutica Sinica B* **2020,** *10* (8), 1382-1396.

25. Rustin, P., Mitochondria, from cell death to proliferation. *Nature genetics* **2002,** *30* (4), 352-353.

26. Chilakamarthi, U.; Giribabu, L., Photodynamic therapy: past, present and future. *The Chemical Record* **2017,** *17* (8), 775-802.

27. Abels, C., Targeting of the vascular system of solid tumours by photodynamic therapy (PDT). *Photochemical & photobiological sciences* **2004,** *3*, 765-771.

28. Rocha, L. G. B. Development of a novel photosensitizer for Photodynamic Therapy of cancer. Universidade de Coimbra (Portugal), 2016.

29. Simões, J. C.; Sarpaki, S.; Papadimitroulas, P.; Therrien, B.; Loudos, G., Conjugated photosensitizers for imaging and PDT in cancer research. *Journal of Medicinal Chemistry* **2020,** *63* (23), 14119-14150.

30. Zhang, J.; Jiang, C.; Longo, J. P. F.; Azevedo, R. B.; Zhang, H.; Muehlmann, L. A., An updated overview on the development of new photosensitizers for anticancer photodynamic therapy. *Acta pharmaceutica sinica B* **2018,** *8* (2), 137-146.

31. Karagianni, A.; Tsierkezos, N. G.; Prato, M.; Terrones, M.; Kordatos, K. V., Application of carbon-based quantum dots in photodynamic therapy. *Carbon* **2023,** *203*, 273-310.

32. Kwiatkowski, S.; Knap, B.; Przystupski, D.; Saczko, J.; Kędzierska, E.; Knap-Czop, K.; Kotlińska, J.; Michel, O.; Kotowski, K.; Kulbacka, J., Photodynamic therapy–mechanisms, photosensitizers and combinations. *Biomedicine & pharmacotherapy* **2018,** *106*, 1098-1107.

33. Wall, M. H.; Basu, P.; Buranda, T.; Wicks, B. S.; Findsen, E. W.; Ondrias, M.; Enemark, J. H.; Kirk, M. L., Photoinduced electron transfer in covalently linked oxomolybdenum (V) porphyrin systems. *Inorganic chemistry* **1997,** *36* (25), 5676-5677.

34. Josefsen, L. B.; Boyle, R. W., Photodynamic therapy: Novel third-generation photosensitizers one step closer? *British journal of pharmacology* **2008,** *154* (1), 1-3.

35. Magda, D.; Miller, R. A. In *Motexafin gadolinium: a novel redox active drug for cancer therapy*, Seminars in cancer biology, Elsevier: 2006; pp 466-476.

36. Young, S.; Woodburn, K.; Wright, M.; Mody, T.; Fan, Q.; Sessler, J.; Dow, W.; Miller, R., Lutetium texaphyrin (PCI-0123): A near-infrared, water-soluble photosensitizer. *Photochemistry and photobiology* **1996,** *63* (6), 892-897.

37. Chen, J.; Fan, T.; Xie, Z.; Zeng, Q.; Xue, P.; Zheng, T.; Chen, Y.; Luo, X.; Zhang, H., Advances in nanomaterials for photodynamic therapy applications: Status and challenges. *Biomaterials* **2020,** *237*, 119827.

38. Kataoka, H.; Nishie, H.; Hayashi, N.; Tanaka, M.; Nomoto, A.; Yano, S.; Joh, T., New photodynamic therapy with next-generation photosensitizers. *Annals of translational medicine* **2017,** *5* (8).

39. Savellano, M. D.; Hasan, T., Targeting cells that overexpress the epidermal growth factor receptor with polyethylene glycolated BPD verteporfin photosensitizer immunoconjugates. *Photochemistry and photobiology* **2003,** *77* (4), 431-439.

40. Hu, F.; Xu, S.; Liu, B., Photosensitizers with aggregation-induced emission: materials and biomedical applications. *Advanced materials* **2018,** *30* (45), 1801350.

41. Pham, T. C.; Nguyen, V.-N.; Choi, Y.; Lee, S.; Yoon, J., Recent strategies to develop innovative photosensitizers for enhanced photodynamic therapy. *Chemical Reviews* **2021,** *121* (21), 13454-13619.

42. Shi, H.; Zou, L.; Huang, K.; Wang, H.; Sun, C.; Wang, S.; Ma, H.; He, Y.; Wang, J.; Yu, H., A highly efficient red metal-free organic phosphor for time-resolved luminescence imaging and photodynamic therapy. *ACS applied materials & interfaces* **2019,** *11* (20), 18103-18110.

43. Wang, B.; Wang, J.-H.; Liu, Q.; Huang, H.; Chen, M.; Li, K.; Li, C.; Yu, X.-F.; Chu, P. K., Rose-bengal-conjugated gold nanorods for in vivo photodynamic and photothermal oral cancer therapies. *Biomaterials* **2014,** *35* (6), 1954-1966.

44. Nguyen, V.-N.; Yan, Y.; Zhao, J.; Yoon, J., Heavy-atom-free photosensitizers: from molecular design to applications in the photodynamic therapy of cancer. *Accounts of chemical research* **2020,** *54* (1), 207-220.

45. Xu, S.; Yuan, Y.; Cai, X.; Zhang, C.-J.; Hu, F.; Liang, J.; Zhang, G.; Zhang, D.; Liu, B., Tuning the singlet-triplet energy gap: a unique approach to efficient photosensitizers with aggregation-induced emission (AIE) characteristics. *Chemical science* **2015,** *6* (10), 5824-5830.

46. Milián-Medina, B.; Gierschner, J., Computational design of low singlet–triplet gap all-organic molecules for OLED application. *Organic Electronics* **2012,** *13* (6), 985-991.

47. Liu, P.; Chen, D.; Wang, Y.; Tang, X.; Li, H.; Shi, J.; Tong, B.; Dong, Y., A highly sensitive “turn-on” fluorescent probe with an aggregation-induced emission characteristic for quantitative detection of γ-globulin. *Biosensors and Bioelectronics* **2017,** *92*, 536-541.

48. Mei, J.; Leung, N. L.; Kwok, R. T.; Lam, J. W.; Tang, B. Z., Aggregation-induced emission: together we shine, united we soar! *Chemical reviews* **2015,** *115* (21), 11718-11940.

49. Wang, H.; Zhao, E.; Lam, J. W.; Tang, B. Z., AIE luminogens: emission brightened by aggregation. *Materials today* **2015,** *18* (7), 365-377.

50. Liang, G.; Lam, J. W.; Qin, W.; Li, J.; Xie, N.; Tang, B. Z., Molecular luminogens based on restriction of intramolecular motions through host–guest inclusion for cell imaging. *Chemical Communications* **2014,** *50* (14), 1725-1727.

51. Zhang, G.-F.; Chen, Z.-Q.; Aldred, M. P.; Hu, Z.; Chen, T.; Huang, Z.; Meng, X.; Zhu, M.-Q., Direct validation of the restriction of intramolecular rotation hypothesis via the synthesis of novel ortho-methyl substituted tetraphenylethenes and their application in cell imaging. *Chemical communications* **2014,** *50* (81), 12058-12060.

52. Yuan, Y.; Feng, G.; Qin, W.; Tang, B. Z.; Liu, B., Targeted and image-guided photodynamic cancer therapy based on organic nanoparticles with aggregation-induced emission characteristics. *Chemical Communications* **2014,** *50* (63), 8757-8760.

53. Liu, M.; Chen, Y.; Guo, Y.; Yuan, H.; Cui, T.; Yao, S.; Jin, S.; Fan, H.; Wang, C.; Xie, R., Golgi apparatus-targeted aggregation-induced emission luminogens for effective cancer photodynamic therapy. *Nature Communications* **2022,** *13* (1), 2179.

54. Mao, D.; Hu, F.; Yi, Z.; Xu, S.; Yan, S.; Luo, Z.; Wu, W.; Wang, Z.; Kong, D.; Liu, X.; Liu, B., AIEgen-coupled upconversion nanoparticles eradicate solid tumors through dual-mode ROS activation. *Science Advances 6* (26), eabb2712.

55. Shao, L.; Pan, Y.; Hua, B.; Xu, S.; Yu, G.; Wang, M.; Liu, B.; Huang, F., Constructing Adaptive Photosensitizers via Supramolecular Modification Based on Pillararene Host–Guest Interactions. *Angewandte Chemie International Edition* **2020,** *59* (29), 11779-11783.

56. Chen, J.; Zou, Z.; Ke, Z.; Zhang, X.; Feng, J.; Jing, Y.; Peng, L.; Yang, J.; Dai, Y.; Zou, D., Dimerization of heavy atom free tetraphenylethylene with aggregation induced emission for boosting photodynamic therapy. *New Journal of Chemistry* **2020,** *44* (17), 7029-7034.

57. Shirasu, N.; Nam, S. O.; Kuroki, M., Tumor-targeted photodynamic therapy. *Anticancer research* **2013,** *33* (7), 2823-2831.

58. Nahabedian, M. Y.; Cohen, R. A.; Contino, M. F.; Terem, T. M.; Wright, W. H.; Berns, M. W.; Wile, A. G., Combination cytotoxic chemotherapy with cisplatin or doxorubicin and photodynamic therapy in murine tumors1. *JNCI: Journal of the National Cancer Institute* **1988,** *80* (10), 739-743.

59. Wang, Z.; Ma, R.; Yan, L.; Chen, X.; Zhu, G., Combined chemotherapy and photodynamic therapy using a nanohybrid based on layered double hydroxides to conquer cisplatin resistance. *Chemical communications* **2015,** *51* (58), 11587-11590.

60. Antoni, P. M.; Naik, A.; Albert, I.; Rubbiani, R.; Gupta, S.; Ruiz-Sanchez, P.; Munikorn, P.; Mateos, J. M.; Luginbuehl, V.; Thamyongkit, P.; Ziegler, U.; Gasser, G.; Jeschke, G.; Spingler, B., (Metallo)porphyrins as Potent Phototoxic Anti-Cancer Agents after Irradiation with Red Light. *Chemistry – A European Journal* **2015,** *21* (3), 1179-1183.

61. Ding, C.; Shi, Z.; Ou, M.; Li, Y.; Huang, L.; Wang, W.; Huang, Q.; Li, M.; Chen, C.; Zeng, X., Dextran-based micelles for combinational chemo-photodynamic therapy of tumors via in vivo chemiluminescence. *Carbohydrate Polymers* **2023,** *319*, 121192.

62. Ayan, S.; Gunaydin, G.; Yesilgul-Mehmetcik, N.; Gedik, M. E.; Seven, O.; Akkaya, E. U., Proof-of-principle for two-stage photodynamic therapy: hypoxia triggered release of singlet oxygen. *Chemical Communications* **2020,** *56* (94), 14793-14796.

63. Nakano, A.; Watanabe, D.; Akita, Y.; Kawamura, T.; Tamada, Y.; Matsumoto, Y., Treatment efficiency of combining photodynamic therapy and ionizing radiation for Bowen's disease. *Journal of the European Academy of Dermatology and Venereology* **2011,** *25* (4), 475-478.

64. Viswanath, D.; Won, Y.-Y., Combining Radiotherapy (RT) and Photodynamic Therapy (PDT): Clinical Studies on Conventional RT-PDT Approaches and Novel Nanoparticle-Based RT-PDT

Approaches under Preclinical Evaluation. *ACS Biomaterials Science & Engineering* **2022,** *8* (9), 3644-3658.

65. Hua, J.; Wu, P.; Gan, L.; Zhang, Z.; He, J.; Zhong, L.; Zhao, Y.; Huang, Y., Current Strategies for Tumor Photodynamic Therapy Combined With Immunotherapy. *Frontiers in Oncology* **2021,** *11*.

66. Canti, G.; Calastretti, A.; Bevilacqua, A.; Reddi, E.; Palumbo, G.; Nicolin, A., Combination of photodynamic therapy + immunotherapy + chemotherapy in murine leukiemia. *Neoplasma* **2010,** *57* (2), 184-188.

67. Lu, Y.; Sun, W.; Du, J.; Fan, J.; Peng, X., Immuno-photodynamic Therapy (IPDT): Organic Photosensitizers and Their Application in Cancer Ablation. *JACS Au* **2023,** *3* (3), 682-699.

68. Li, X.; Wang, X.; Zhao, C.; Shao, L.; Lu, J.; Tong, Y.; Chen, L.; Cui, X.; Sun, H.; Liu, J.; Li, M.; Deng, X.; Wu, Y., From one to all: self-assembled theranostic nanoparticles for tumor-targeted imaging and programmed photoactive therapy. *Journal of Nanobiotechnology* **2019,** *17* (1), 23.

69. You, Q.; Zhang, K.; Liu, J.; Liu, C.; Wang, H.; Wang, M.; Ye, S.; Gao, H.; Lv, L.; Wang, C.; Zhu, L.; Yang, Y., Persistent Regulation of Tumor Hypoxia Microenvironment via a Bioinspired Pt-Based Oxygen Nanogenerator for Multimodal Imaging-Guided Synergistic Phototherapy. *Advanced Science* **2020,** *7* (17), 1903341.

70. Younis, M. R.; Wang, C.; An, R.; Wang, S.; Younis, M. A.; Li, Z.-Q.; Wang, Y.; Ihsan, A.; Ye, D.; Xia, X.-H., Low Power Single Laser Activated Synergistic Cancer Phototherapy Using Photosensitizer Functionalized Dual Plasmonic Photothermal Nanoagents. *ACS Nano* **2019,** *13* (2), 2544-2557.

71. Li, R.-T.; Chen, M.; Yang, Z.-C.; Chen, Y.-J.; Huang, N.-H.; Chen, W.-H.; Chen, J.; Chen, J.-X., AIE-based gold nanostar-berberine dimer nanocomposites for PDT and PTT combination therapy toward breast cancer. *Nanoscale* **2022,** *14* (27), 9818-9831.

72. Calixto, G. M.; Bernegossi, J.; De Freitas, L. M.; Fontana, C. R.; Chorilli, M. Nanotechnology-Based Drug Delivery Systems for Photodynamic Therapy of Cancer: A Review *Molecules* [Online], 2016.

73. Yoo, S. W.; Oh, G.; Ahn, J. C.; Chung, E. Non-Oncologic Applications of Nanomedicine-Based Phototherapy *Biomedicines* [Online], 2021.

74. Calzavara-Pinton, P. G.; Rossi, M. T.; Aronson, E.; Sala, R.; The Italian Group for Photodynamic, T., A retrospective analysis of real-life practice of off-label photodynamic therapy using methyl aminolevulinate (MAL-PDT) in 20 Italian dermatology departments. Part 1: Inflammatory and aesthetic indications. *Photochemical & Photobiological Sciences* **2013,** *12* (1), 148-157.

75. Stender, I.-M.; Na, R.; Fogh, H.; Gluud, C.; Wulf, H. C., Photodynamic therapy with 5-aminolaevulinic acid or placebo for recalcitrant foot and hand warts: randomised double-blind trial. *The Lancet* **2000,** *355* (9208), 963-966.

76. Shin, H. T.; Kim, J. H.; Shim, J.; Lee, J. H.; Lee, D. Y.; Lee, J. H.; Yang, J. M., Photodynamic therapy using a new formulation of 5-aminolevulinic acid for wrinkles in Asian skin: A randomized controlled split face study. *Journal of Dermatological Treatment* **2015,** *26* (3), 246-251.

77. Choi, Y. M.; Adelzadeh, L.; Wu, J. J., Photodynamic therapy for psoriasis. *Journal of Dermatological Treatment* **2015,** *26* (3), 202-207.

78. Jerjes, W.; Upile, T.; Hamdoon, Z.; Mosse, C. A.; Akram, S.; Morley, S.; Hopper, C., Interstitial PDT for vascular anomalies. *Lasers in Surgery and Medicine* **2011,** *43* (5), 357-365.

79. Comacchi, C.; Bencini, P. L.; Galimberti, M. G.; Cappugi, P.; Torchia, D., Topical Photodynamic Therapy for Idiopathic Hirsutism and Hypertrichosis. *Plastic and Reconstructive Surgery* **2012,** *129* (6), 1012e-1014e.

80. Bruscino, N.; Lotti, T.; Rossi, R., Photodynamic therapy for a hypertrophic scarring: a promising choice. *Photodermatology, Photoimmunology & Photomedicine* **2011,** *27* (6), 334-335.

81. Linares-González, L.; Ródenas-Herranz, T.; Sáenz-Guirado, S.; Ruiz-Villaverde, R., Successful response to photodynamic therapy with 5-aminolevulinic acid nanoemulsified gel in a patient with universal alopecia areata refractory to conventional treatment. *Dermatologic Therapy* **2020,** *33* (3), e13416.

82. van Dijk, E. H. C.; Fauser, S.; Breukink, M. B.; Blanco-Garavito, R.; Groenewoud, J. M. M.; Keunen, J. E. E.; Peters, P. J. H.; Dijkman, G.; Souied, E. H.; MacLaren, R. E.; Querques, G.; Downes, S. M.; Hoyng, C. B.; Boon, C. J. F., Half-Dose Photodynamic Therapy versus High-Density Subthreshold Micropulse Laser Treatment in Patients with Chronic Central Serous Chorioretinopathy: The PLACE Trial. *Ophthalmology* **2018,** *125* (10), 1547-1555.

83. Houthoofd, S.; Vuylsteke, M.; Mordon, S.; Fourneau, I., Photodynamic therapy for atherosclerosis. The potential of indocyanine green. *Photodiagnosis and Photodynamic Therapy* **2020,** *29*, 101568.

84. Li, C. Z.; Cheng, L. F.; Wang, Z. Q.; Gu, Y., Attempt of photodynamic therapy on esophageal varices. *Lasers in Medical Science* **2009,** *24* (2), 167-171.

85. Cosgarea, R.; Pollmann, R.; Sharif, J.; Schmidt, T.; Stein, R.; Bodea, A.; Auschill, T.; Sculean, A.; Eming, R.; Greene, B.; Hertl, M.; Arweiler, N., Photodynamic therapy in oral lichen planus: A prospective case-controlled pilot study. *Scientific Reports* **2020,** *10* (1), 1667.

86. Lee, B. I.; Suh, Y. S.; Chung, Y. J.; Yu, K.; Park, C. B., Shedding Light on Alzheimer's β-Amyloidosis: Photosensitized Methylene Blue Inhibits Self-Assembly of β-Amyloid Peptides and Disintegrates Their Aggregates. *Scientific Reports* **2017,** *7* (1), 7523.

87. Gallardo-Villagrán, M.; Leger, D. Y.; Liagre, B.; Therrien, B. Photosensitizers Used in the Photodynamic Therapy of Rheumatoid Arthritis *International Journal of Molecular Sciences* [Online], 2019.

88. Huis in 't Veld, R. V.; Heuts, J.; Ma, S.; Cruz, L. J.; Ossendorp, F. A.; Jager, M. J. Current Challenges and Opportunities of Photodynamic Therapy against Cancer *Pharmaceutics* [Online], 2023.

89. Anduran, E. Bioreductive Activated Prodrugs to Target Tumour Hypoxia. Montpellier university , Maastricht University, 2022.

90. Dutta, D.; Zhou, Q.; Mukerabigwi, J. F.; Lu, N.; Ge, Z., Hypoxia-Responsive Polyprodrug Nanocarriers for Near-Infrared Light-Boosted Photodynamic Chemotherapy. *Biomacromolecules* **2021,** *22* (11), 4857-4870.

91. Wilson, W. R.; Hay, M. P., Targeting hypoxia in cancer therapy. *Nature Reviews Cancer* **2011,** *11* (6), 393-410.

92. Carmeliet, P.; Jain, R. K., Angiogenesis in cancer and other diseases. *Nature* **2000,** *407* (6801), 249-257.

93. Jain, R. K., Normalization of Tumor Vasculature: An Emerging Concept in Antiangiogenic Therapy. *Science* **2005,** *307* (5706), 58-62.

94. Berchem, G. Role of hypoxic stress in the regulation of the anti-tumor immune response mediated by Natural killer lymphocytes

Rôle du stress hypoxique dans la régulation de la réponse immunitaire anti-tumorale des lymphocytes "Natural Killer". Université Paris Sud - Paris XI, 2014.

95. Fan, W.; Bu, W.; Shen, B.; He, Q.; Cui, Z.; Liu, Y.; Zheng, X.; Zhao, K.; Shi, J., Intelligent MnO2 Nanosheets Anchored with Upconversion Nanoprobes for Concurrent pH-/H2O2-Responsive UCL Imaging and Oxygen-Elevated Synergetic Therapy. *Advanced Materials* **2015,** *27* (28), 4155-4161.

96. Cheng, Y.; Cheng, H.; Jiang, C.; Qiu, X.; Wang, K.; Huan, W.; Yuan, A.; Wu, J.; Hu, Y., Perfluorocarbon nanoparticles enhance reactive oxygen levels and tumour growth inhibition in photodynamic therapy. *Nature Communications* **2015,** *6* (1), 8785.

97. Zheng, D.-W.; Li, B.; Li, C.-X.; Fan, J.-X.; Lei, Q.; Li, C.; Xu, Z.; Zhang, X.-Z., Carbon-Dot-Decorated Carbon Nitride Nanoparticles for Enhanced Photodynamic Therapy against Hypoxic Tumor via Water Splitting. *ACS Nano* **2016,** *10* (9), 8715-8722.

98. Gong, H.; Chao, Y.; Xiang, J.; Han, X.; Song, G.; Feng, L.; Liu, J.; Yang, G.; Chen, Q.; Liu, Z., Hyaluronidase To Enhance Nanoparticle-Based Photodynamic Tumor Therapy. *Nano Letters* **2016,** *16* (4), 2512-2521.

99. Aspatwar, A.; Haapanen, S.; Parkkila, S. An Update on the Metabolic Roles of Carbonic Anhydrases in the Model Alga Chlamydomonas reinhardtii *Metabolites* [Online], 2018.

100. Mishra, C. B.; Tiwari, M.; Supuran, C. T., Progress in the development of human carbonic anhydrase inhibitors and their pharmacological applications: Where are we today? *Medicinal Research Reviews* **2020,** *40* (6), 2485-2565.

101. Nocentini, A.; Capasso, C.; Supuran, C. T. Carbonic Anhydrase Inhibitors as Novel Antibacterials in the Era of Antibiotic Resistance: Where Are We Now? *Antibiotics* [Online], 2023.

102. Supuran, C. T., A simple yet multifaceted 90 years old, evergreen enzyme: Carbonic anhydrase, its inhibition and activation. *Bioorganic & Medicinal Chemistry Letters* **2023,** *93*, 129411.

103. Kim, C.-Y.; Whittington, D. A.; Chang, J. S.; Liao, J.; May, J. A.; Christianson, D. W., Structural Aspects of Isozyme Selectivity in the Binding of Inhibitors to Carbonic Anhydrases II and IV. *Journal of Medicinal Chemistry* **2002,** *45* (4), 888-893.

104. Alterio, V.; Di Fiore, A.; D'Ambrosio, K.; Supuran, C. T.; De Simone, G., Multiple Binding Modes of Inhibitors to Carbonic Anhydrases: How to Design Specific Drugs Targeting 15 Different Isoforms? *Chemical Reviews* **2012,** *112* (8), 4421-4468.

105. Supuran, C. T., Structure and function of carbonic anhydrases. *Biochemical Journal* **2016,** *473* (14), 2023-2032.

106. Supuran, C. T., Carbonic anhydrase inhibitors. *Bioorganic & Medicinal Chemistry Letters* **2010,** *20* (12), 3467-3474.

107. Angeli, A.; Carta, F.; Supuran, C. T. Carbonic Anhydrases: Versatile and Useful Biocatalysts in Chemistry and Biochemistry *Catalysts* [Online], 2020.

108. Nocentini, A.; Donald, W. A.; Supuran, C. T., Human carbonic anhydrases: tissue distribution, physiological role, and druggability. In *Carbonic anhydrases*, Elsevier: 2019; pp 151-185.

109. Supuran, C. T., Carbonic anhydrase inhibitors as emerging agents for the treatment and imaging of hypoxic tumors. *Expert Opinion on Investigational Drugs* **2018,** *27* (12), 963-970.

110. Supuran, C. T., Targeting carbonic anhydrases for the management of hypoxic metastatic tumors. *Expert Opinion on Therapeutic Patents* **2023,** (just-accepted).

111. Claudiu T. Supuran , A. S., Janet Conway, *Carbonic Anhydrase Its Inhibitors and Activators*. 2004; Vol. 376, p 376.

112. Höckel, M.; Vaupel, P., Tumor Hypoxia: Definitions and Current Clinical, Biologic, and Molecular Aspects. *JNCI: Journal of the National Cancer Institute* **2001,** *93* (4), 266-276.

113. Thiry, A.; Dogné, J.-M.; Masereel, B.; Supuran, C. T., Targeting tumor-associated carbonic anhydrase IX in cancer therapy. *Trends in Pharmacological Sciences* **2006,** *27* (11), 566-573.

114. Pastorekova, S.; Parkkila, S.; Pastorek, J.; Supuran, C. T., Review Article. *Journal of Enzyme Inhibition and Medicinal Chemistry* **2004,** *19* (3), 199-229.

115. Guler, O.; De Simone, G.; Supuran, C., Drug Design Studies of the Novel Antitumor Targets Carbonic Anhydrase IX and XII. *Current medicinal chemistry* **2010,** *17*, 1516-26.

116. Supuran, C. T.; Scozzafava, A.; Casini, A., Carbonic anhydrase inhibitors. *Medicinal Research Reviews* **2003,** *23* (2), 146-189.

117. Nocentini, A.; Angeli, A.; Carta, F.; Winum, J.-Y.; Zalubovskis, R.; Carradori, S.; Capasso, C.; Donald, W. A.; Supuran, C. T., Reconsidering anion inhibitors in the general context of drug design studies of modulators of activity of the classical enzyme carbonic anhydrase. *Journal of Enzyme Inhibition and Medicinal Chemistry* **2021,** *36* (1), 561-580.

118. Kanfar, N. Multivalent inhibitors of carbonics anhydrases

Synthèse d'inhibiteurs multivalents des anhydrases carboniques. Université Montpellier, 2017.

119. Supuran, C. T., How many carbonic anhydrase inhibition mechanisms exist? *Journal of enzyme inhibition and medicinal chemistry* **2016,** *31* (3), 345-360.

120. Hu, F.; Xu, S.; Liu, B., Photosensitizers with Aggregation-Induced Emission: Materials and Biomedical Applications. *Adv. Mater.* **2018,** *30* (45), e1801350.

Chapter II

Are tumour-associated carbonic anhydrases genuine therapeutic targets for photodynamic therapy?

Merabti, A.; Richeter, S.; Supuran, C. T.; Clement, S.; Winum, J.-Y., Are tumor-associated carbonic anhydrases genuine therapeutic targets for photodynamic therapy? *Expert Opinion on Therapeutic Targets* **2023,** 27(9), 817

Chapter II: Are tumor-associated carbonic anhydrase genuine therapeutic targets for photodynamic therapy?

I. Abstract

Photodynamic therapy (PDT) is a reactive oxygen species (ROS)-dependent treatment modality which has emerged as an alternative cancer therapy strategy. However, in solid tumors, the therapeutic efficacy of PDT is strongly reduced by hypoxia, a typical feature of many such tumors. The tumor-associated carbonic anhydrases IX (hCA IX) and XII (hCA XII), which are overexpressed under hypoxia are attractive, validated anticancer drug targets in solid tumors. Current challenges in therapeutic design of effective PDT systems aim to overcome the limitation of hypoxia by developing synergistic CA-targeted therapies combining photosensitizers and hCA IX/XII inhibitors.

I.1 Area Covered

In this review, the current literature on the use of hCA IX/XII inhibitors (CAi) for targeting photosensitizing chemical systems useful for PDT against hypoxic solid tumors is summarized, along with recent progress, challenges, and prospects.

I.2 Expert Opinion

hCA IX/XII-focused photosensitizers have recently provided new generation of compounds of considerable potential. Proof of concept of *in vivo* efficacy studies suggested enhanced efficacy for CAi-PDT hybrid systems. Further research is needed to deepen our understanding of how hCA IX and/or hCA XII inhibition can enhance PDT and for obtaining more effective such derivatives.

Keywords: drug design, carbonic anhydrase, hCA IX, hCA XII, inhibitor, photodynamic therapy, hypoxia, cancer.

Chapter II: Are tumor-associated carbonic anhydrase genuine therapeutic targets for photodynamic therapy?

I.3 Article highlights

- The use of photosensitizers in photodynamic therapy (PDT), which converts oxygen (O_2) into lethal reactive oxygen species (ROS), has great promise for the treatment of cancer because of its non-invasive aspect, high safety, and low side effects.
- The main drawback of PDT is its application to resistant hypoxic solid tumors which hinders ROS generation due to lack of O_2.
- The membrane-bound zinc metalloenzyme carbonic anhydrase isoforms IX and XII (CA, EC 4.2.1.1), overexpressed under hypoxia in solid tumors *via* the HIF signaling cascade, has been shown to have a crucial role in controlling intracellular and extracellular pH levels as well as invasion and metastatic processes.
- The potential of cancer spread can be drastically reduced thanks to combination of hCA-IX/XII inhibition-mediated pH control with concomitant targeted photodynamic processes.
- The additive of synergistic effect of PDT combined with hCA IX/hCA XII inhibition could be promising to manage and helping to overcome the hypoxia resistant tumours to PDT, but more effective sensitizers are needed.

Chapter II: Are tumor-associated carbonic anhydrase genuine therapeutic targets for photodynamic therapy?

II. Introduction

Intratumoral heterogenety is one of the essential characteristics of solid malignancies and has complex sources including genetic, epigenetic, and microenviromental compounents.[1] Solid human tumors typically have underdeveloped vasculature, which contributes to the significant oxygen concentration gradients within and between tumors. Thus, the tumor microenvironment (TEM) is characterized by hypoxia (*i.e.,* low tissue oxygen content), which is the main driver of this topographic heterogeneity.[2-3]

Hypoxia is a common feature of the tumor microenvironment found in many solid tumors, occurring frequently due to solid tumors imperfect vascularization, which cannot keep with the increased oxygen demand of the fast-growing malignancies. Indeed, tumor cells adapt their microenvironment in hypoxic conditions to sustain survival, stimulate metastasis, invasiveness, and recurrence of tumor cells through a variety of processes controlled, mostly by the transcription factors HIFs (Hypoxia-Inducible Factors 1 and 2 5HIF-1/2)). The treatment of such of solid tumors is consistently hampered by the hypoxic tumor microenvironment, which is one of the most significant factors of poor clinical outcomes for the conventional cancer therapy, due to emergence of resistance to traditional chemo-, radio-, and immunotherapy.[4-8]

Human Carbonic Anhydrase isoforms IX (hCA IX) and XII are under control of HIF transcription factors, which induces their overexpression in hypoxic tumors as a consequence of an activation cascade which upregulates proteins involved in metabolism, pH regulation and angiogenesis (*e.g.*, glucose transporters, CAs, Na^+/H^+ exchangers, the vacuolar ATPase, monocarboxylate transporters (MCTs), sodium bicarbonate co-transporters, vascular endothelial growth factor VEGF, etc.), discoveries for which Ratcliffe, Kaelin and Semenza were awarded the Nobel prize for medicine in 2019.[9-10]

The transmembrane isoforms hCA IX and hCA XII are member of a superfamily of zinc enzymes (CA, EC 4.2.1.1), which are found throughout the body and catalyze the reversible hydration of CO_2 to HCO_3^- with release of a H^+. The druggability of these two isoforms was investigated for more than 20 years, being shown that inhibitors belonging to small molecule classes notably, the sulfonamide CA inhibitor SLC-0111 (presently undergoing Phase Ib/II clinical trials), as well as monoclonal antibodies lead to a significant antiproliferative effect on primary tumors, concomitantly reducing the formation of metastases and decreasing the number of cancer stem cells.[11-16]

Chapter II: Are tumor-associated carbonic anhydrase genuine therapeutic targets for photodynamic therapy?

The overexpression and extracellular location of hCA IX/hCA XII active site on hypoxic cancer cells, allows for the possibility of utilizing it as targets for the delivery of photosensitizers to cancer cells in the context of photodynamic therapy (PDT) expecting to overcome/mitigate the limitations of this treatment strategy.[17-19]

PDT is a promising cancer treatment due to the *in-situ* creation of highly reactive oxygen (ROS) including singlet oxygen ($^1O_2$), superoxide radical ($O_2^{\bullet-}$), hydroxyl radical ($OH^\bullet$) and hydrogen peroxide (H_2O_2) which are harmful to cancer cells. In the PDT process, two types of photo-triggered reactions — type I and type II— occur between both the Ps and the surrounding substances (**Figure 27**). Precisely, the type I reaction proceeds by hydrogen atom abstraction or electron transfer, ultimately resulting in the generation of radicals and H_2O_2. On the other hand, the type II process, which results in the production of $^1O_2$, involves energy transfer from the electronically excited triplet-state Ps to the ground-state molecular oxygen ($^3O_2$). [20]

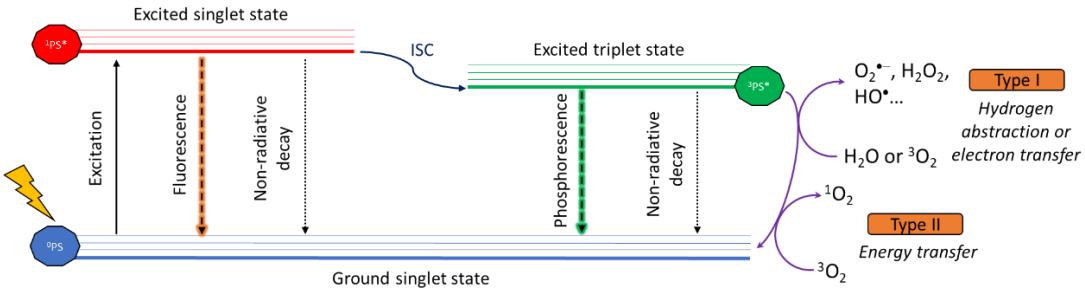


Figure 117. The photochemical reactions involved in type I and type II PDT.

Because of its intrinsic benefits, such as low toxicity, few side effects, and precise target treatment without causing harm to nearby normal tissues, PDT is a minimally invasive therapeutic technique with precise adaptability and strong spatiotemporal precision.[20-21] In addition to directly killing cancer cells by destroying their biological components, ROS can also cause vascular damage and activate both the local and systemic immune systems, which work together to destroy tumors.[21] Nevertheless, its anticancer efficacy is frequently constrained due to its reliance on oxygen concentrations. Since PDT requires a comparatively large oxygen consumption, the hypoxic nature of tumors significantly limits PDT effectiveness and worsens hypoxia at the same time. As a result, the increased tumor hypoxia causes cancer to develop and metastasize, increasing the probability that PDT will not work. Therefore, PDT alone is unable to treat hypoxic tumors in an effective way. To solve this problem, different strategies have been reported in literature to alleviate the tumor hypoxia in PDT.[22]

Chapter II: Are tumor-associated carbonic anhydrase genuine therapeutic targets for photodynamic therapy?

The four main ones are (1) improving tissue oxygenation by modifying the TME, (2) using nanoparticles to transport oxygen to the tumor, (3) breaking down compounds that generate O_2, and (4) taking advantage of hypoxia to facilitate the treatment.[23] Other solutions, such as adjustment of photosensitizer dosage or light irradiation, have also been implemented by several research groups to overcome the hypoxia obstacle.[24-26]

A strategy for exploiting the existing hypoxic microenvironment to deliver therapeutic agents to hypoxic tumor tissues is to target the HIF-mediated signaling cascade. hCA IX and hCA XII are among these membrane proteins particularly upregulated by the HIF pathway and are involved in survival mechanism of tumor cells, as mentioned above.[27-28] Inhibiting hCA IX/XII enzymatic activities was demonstrated to reduce hypoxic-mediated tumor development and restrain the distant metastasis by using a targeted PDT combination .[29-18-19] As a result, on a dual-system (combination of photosensitizer with hCA IX/XII inhibitor), it can be anticipated that hCA IX/XII-related endocytosis would facilitate its selective cellular uptake and its targeted delivery by hypoxic malignant tumors.[30-31] Moreover, the inhibition of hCA IX/XII might further decrease the metastatic phenotype and overcome the hypoxia-induced PDT resistance. (**Figure 28**)

Thus, hCA IX/hCA XII-targeted strategy could result in significant new advances in the field of PDT. Several hCA IX/XII-inhibitor systems have been the focus of numerous studies to precisely target hCA IX/XII and to address hypoxic TME inPDT. In this review, we focus and discuss ongoing efforts related to the different studies reported so far which involve the targeting of Ps conjugated with hCA IX/XII inhibitors, thus addressing the limitations of PDT in hypoxic tumours.

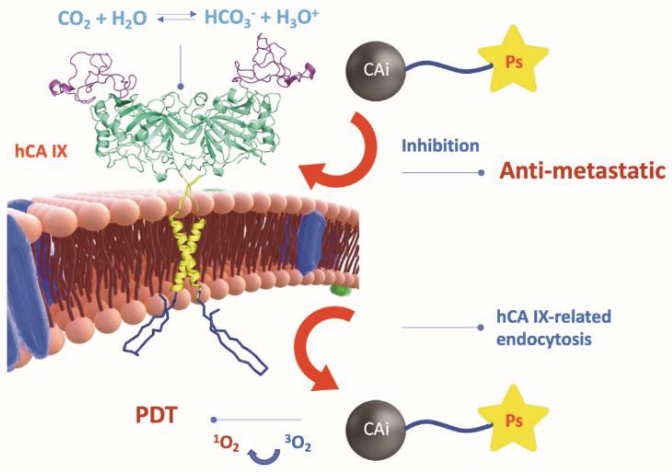


Figure 28. hCA IX-targeted PDT strategy with a conjugate hCA IX inhibitor (CAi) – photosensitizer (Ps).

Chapter II: Are tumor-associated carbonic anhydrase genuine therapeutic targets for photodynamic therapy?

III. Carbonic anhydrase inhibitors with potential applications in photodynamic therapy

Interesting work on using targeted Ps conjugates **1** with associated hCA IX was reported in 2017 by Jung *et al*.[32] (**Figure 29**) The authors described a conjugate of the sulfonamide hCA IX inhibitor acetazolamide (AAZ) with the Ps BODIPY **1** which also enables fluorescence-based tracking of cellular uptake and distribution (**Figure 29**). Studies conducted *in vitro* showed that this conjugate can localize selectively to the mitochondria of cancer cells that overexpress hCA IX. According to TEM images revealing the destruction of mitochondrial structures, this compound also produces $^1O_2$ effectively when exposed to light at 660 nm and causes phototoxicity through mitochondrial failure. This hCA IX targeting Ps displayed tumor reduction *in vivo* on MDA-MB-231-inoculated xenograft mice model and increased efficiently *in vitro* phototoxicity against aggressive human breast cancer MDA-MB-231 cell line and spheroid model.[32]

A multifunctional platform was designed by *Xu et al*. in 2018 based on an iron tetrakis(4-carboxyphenyl)porphyrin nanoscale metal organic framework (NMOF) that has been modified by bovine serum albumin (BSA) and sulfonamide (SA). [33] This nanocomposite targets hypoxic tumor sites by inhibiting hCA IX of tumor cells, also serving as a contrast agent for T1-T2 weighted MRI to direct photodynamic and photothermal therapy. Additionally, it serves as Ps and photothermal agents, which when combined, allow for the death of 95% of 4T1 cells.[33] In 2019, the same group described a similar multifunctional theranostic platform built upon a NMOF also incorporating a tetrakis(4-carboxyphenyl)porphyrin as Ps and Fe^{3+} as metal center, BSA, sulfadiazines (SDs) and MnO_2 nanoparticles.[33] By generating O_2 *in situ* through the catalysis of surrounding H_2O_2 by MnO_2 and down regulating endogenous hCA IX expression, this multifunctional nanoplatform efficiently kills tumors cells (>90% of 4T1 death cells) and inhibits tumor growth which was verified by *in vivo* therapeutic effects.[34] In addition, this platform can also be exploited as positive MRI contrast agent which a higher longitudinal (r_1) at 6.09 $mM^{-1}\,s^{-1}$ than Gd-DTPA, a clinical contrast agent (Gd-DTPA, r1 = 4.33 $mM^{-1}\,s^{-1}$).[34]

Jiang et al. reported in 2019 the first organic semiconducting photodynamic biodegradable nano-inhibitor prepared by nanoprecipitation of a near-IR-absorbing semiconducting polymer B and an amphiphilic linear polymer A with both terminus-grafted sulfonamide-carbonic anhydrase inhibitor (acetazolamide) **2**.[35] (**Figure 29**) The relevance of this hCA IX-targeted nano-system compared to the non-targeted one has been proven on MDA-MB-231 xenograft mouse model showing a selective

targeting of hCA IX expressing tumors, as well as a downregulation of metastasis-related proteins and a total inhibition of tumor growth upon irradiation, with no recurrence observed after 18 days.[35]

Interesting nano-inhibitor self-delivering system, constituted of a hCA IX inhibitor sulfonamide moiety) grafted to the Ps protoporphyrin IX *via* a hydrophilic poly(ethylene glycol) spacer **3**, was reported in 2020 by Fan and Coll.[36] (**Figure 29**) This model exhibited synergistic effect improving cell internalization *via* selective recognition of hCA IX and significant antitumour efficiency *in vivo* against MDA-MB-231 tumors and primary 4T1 tumors under irradiation. Anti-metastasis capability was also evidenced *in vivo* demonstrating the obvious effect of hCA IX inhibition. Moreover, no adverse effects and low systemic toxicity were observed.[36]

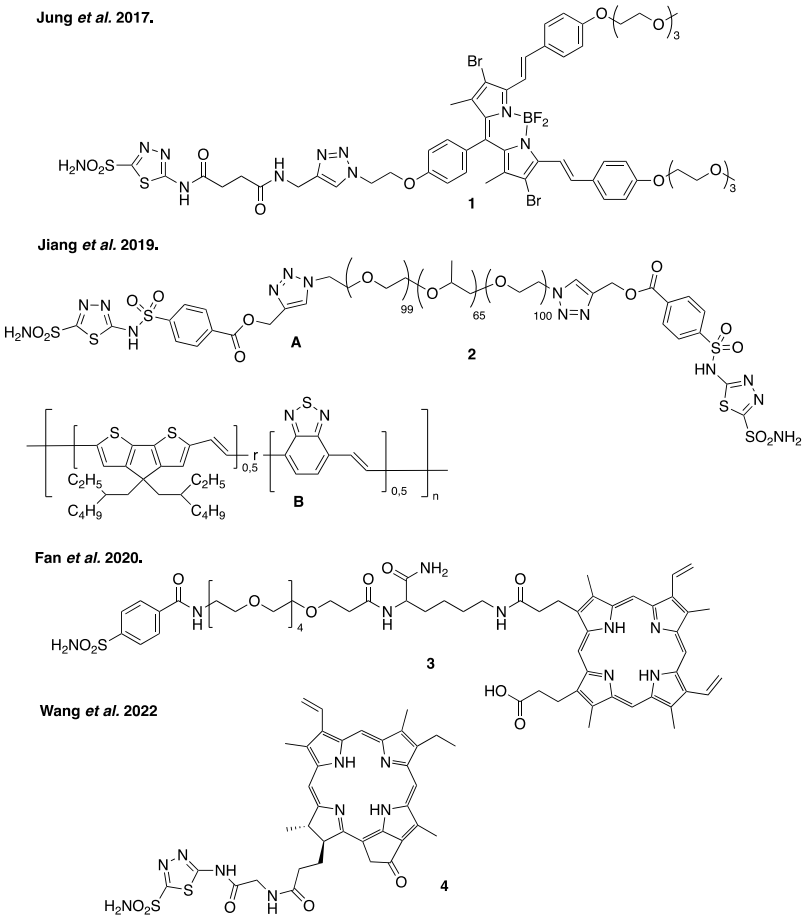


Figure 29. Examples of selected Ps systems conjugated with CA inhibitors.

Based on the same type of Ps scaffold, Wang and coll. reported in 2022 a series of pyropheophorbide a derivatives **4** bearing pendant CA sulfonamide inhibitors such as phenyl sulfonamide or thiadiazol sulfonamide pharmacophoric moiety.[37] Among the five compounds described in this study, the best pyropheophorbide *a* derivative (illustrated in **Figure 29**) was found to

have the best photocytotoxicity against MDA-MB-231 cells with a IC_{50} of 0.17 µM. *In vivo* evaluation on MDA-MB-231 tumor-bearing xenografted mice shed light on the potency of this derivative with a significant inhibition of tumor growth and efficient reduction of tumor volume without affecting the weight of the mice and survival. Moreover, preliminary cell compound distribution experiments showed the interest of the hCA IX targeting moiety, revealing lysosome localization of in MDA-MB-231 cell lines which overexpress hCA IX.

The same year, another group reported the synthesis, the optical properties, and the biological activity of an innovative tetra-functionalized zinc(II) porphyrin with selective hCA IX/XII inhibitors in sulfonamide and coumarin series [38](**Figure 30**). The hybrid molecule with coumarin **5b** was shown to be a low selective nanomolar inhibitor of hCA IX and hCA XII and to specifically target pancreatic cancer cell lines Capan-1 *in vitro*, impairing growth and proliferation at low micromolar concentrations. Moreover, this zinc (II) porphyrin conjugate behave as an efficient photosensitizer for PDT being able to increase Capan-1 cells death *in vitro* when irradiated at 540 nm. Therefore, this study shows the advantageous combination of a Ps and selective CA inhibitors without losing photosensitizing efficiency.[38]

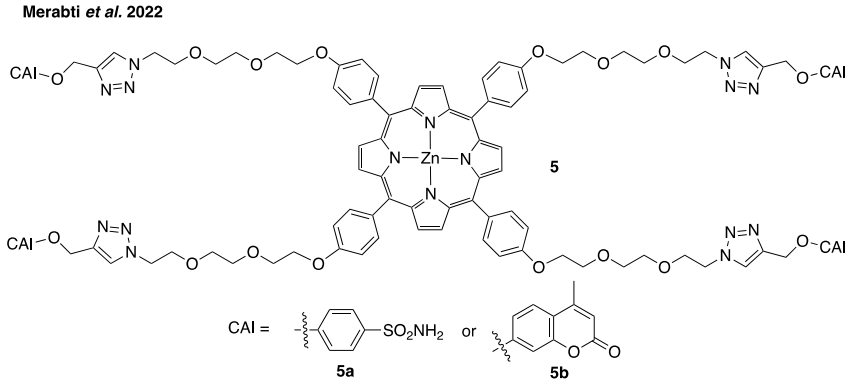


Figure 30. Structure of porphyrin-CA Inhibitor hybrid molecules.

In the field of photoactivated metal complexes, Su *et al*. recently reported a sulfonamide anchored rhenium(I)-based Ps **6** (CAI-Re).[39] (**Figure 31** left) This complex was shown to absorb light in the visible region up to 600 nm with a maximum center at 425 nm and was able to generate $^1O_2$ upon irradiation ($\Phi\Delta$= 16% in CH_3CN) and other ROS. These results indicate that this hCA IX targeted rhenium(I) complex could follow both type-I and type-II PDT. *In vitro* experiments conducted on MDA-MB-231 cells showed that CAI-Re was localized on cell membranes due to its hCA IX binding capacity resulting in a significant inhibition of hCA IX catalytic activity under hypoxic conditions (hCA IX inhibition was evaluated with IC_{50} value of ~3.85 µM). CAI-Re was revealed to be not toxic in the dark

($^{dark}IC_{50}$ > 100 µM), but very toxic under irradiation (λ_{exc} = 425 nm 20 mWcm^{-2}, 10 min: $^{light}IC_{50}$ = 7.3 nm). A very efficient activity under hypoxic conditions with IC_{50} in the nanomolar range (1% O_2, $^{light}IC_{50}$ = 20 nm).[39] More biocompatible irradiation conditions in the green (λ_{exc} = 525 nm), led to ~10 times lower activity. The authors proposed antitumour mechanism resulting from ROS generation such as $^{\bullet}O_2^-$ after irradiation of CAI-Re and leading to oxidation damage of membrane components. Additional studies suggested the existence of a gasdermin D (GSDMD) mediated pyroptotic cell death stimulating tumor immunogenicity after irradiation. Indeed, pyroptosis promotes the maturation of DC cells and activate T cells to eliminate distant tumors at the same time as destroying primary tumors.[39]

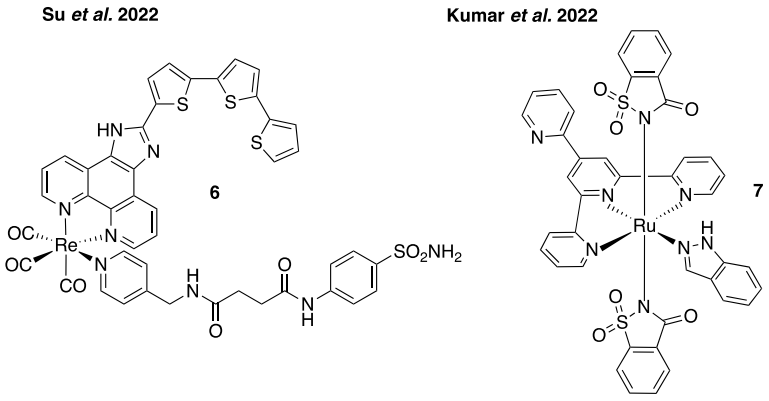


Figure 31. Selected structures of photoactivated metal complexes bearing CA inhibitors.

Kumar *et al*. reported Ru(II) octahedral complexes **7** bearing terpyridines and 1,2-azoles equatorial ligands and two saccharin trans-axial ligands acting as hCA IX inhibitor warheads (**Figure 31**).[40] Interestingly, these complexes undergo photodissociation of monodendate *N*-donor ligands (saccharin or 1,2-azoles) and generation of $^1O_2$ ($\Phi\Delta = 41\%$ for the Ru(II) complex **7** in DMF) upon irradiation with green light (λ_{exc} = 530 nm). Synergistic effects are thus expected for these complexes combining photoactivated chemotherapy (PACT) and PDT. This Ru(II) complex was shown to be particularly toxic for MCF7 cancer cells. Moreover, uptake and localization of the complex in the cytosol and nuclei of MCF7 cancer cells was observed. Increased cytotoxicity observed upon green light irradiation is thought to be due to apoptosis and $^1O_2$ generation and photo-released saccharin ligands are also expected to be potent against aggressive hypoxic tumors via inhibition of hCA IX and modulation of intracellular pH.[40]

Liu *et al*. designed drug delivery nanosystems based on hollow polydopamine (HPDA) on which surface was modified with PEG-NH_2 and 4-(2-aminoethyl) benzene sulfonamide (ABS) a well-known hCA inhibitor model.[41] Surface modified HPDA were then loaded with chlorin e6 (Ce6), a Ps for PDT, and BEZ235, which is an inhibitor targeting phosphatidylinositol-3 kinase (PI3K) and mTOR. Inhibition

of mTOR has a therapeutic effect and reduces hypoxia-inducible factor-1 alpha (HIF-1α) expression in breast cancer. Therefore, both molecules' ABS (on the surface of HPDA) and BEZ235 (within HPDA) can simultaneously mitigate hypoxic adaptation and improve breast cancer treatment. The anticancer effects of the obtained nanoparticles HPDA-ABS/PeG-BEZ235/Ce6, namely H-APBC, were evaluated on 4T1 cells (breast cancer). They showed higher toxicity under hypoxia (38.3% of 4T1 cells showed apoptosis) than normoxia (16.09%) due to the interaction of ABS with hCA IX and the release of BEZ235. Indeed, H-APBC nanoparticles with ABS on the surface interact with transmembrane hCA IX proteins and are endocytosed in cancer cells. Interaction with hCA IX increases intracellular acidity and thus promote acid-responsive release of BEZ235 and Ce6. Released BEZ235 inhibits PI3K/mTOR pathway and reduces HIF-1α expression resulting in decreased angiogenesis. Released Ce6 molecules are used for PDT and generate $^1O_2$ under irradiation (λ_{exc} = 650 nm), while HPDA nanoparticles can be used for photothermal therapy (PTT), (λ_{exc} = 808 nm) consisting in inducing irreversible tissues damage by raising the tumor temperature to achieve thermal ablation. *In vivo* experiments were conducted to evaluate the anticancer properties of H-APBC nanoparticles. A first interesting result is that PTT is efficient after 5 minutes of irradiation at λ_{exc} = 808 nm 12 hours and after injection and the local tumor temperature rose up to 43 °C which is sufficient to kill tumor cells. The strongest tumor growth inhibition was observed when mice treated with H-APBC nanoparticles were submitted to PDT (λ_{exc} = 650 nm) and PTT (λ_{exc} = 808 nm), showing that the nanoplatform combining PDT + PTT exhibited remarkable antitumour efficiency.[41]

Pewklang and coll. reported very recently the synthesis of an aza-BODIPY PS combined with acetazolamide (AAZ) a sulfonamide hCA IX inhibitor **8**.[42] (**Figure 32**) Compared to classical BODIPY, aza-BODIPY can absorb light in the near IR region (λ_{abs} ~ 680 nm) and potentially improve the success of PDT due to better light penetration in tumor tissues compared to BODIPY. The conjugate aza-BODIPY-AAZ was then tested on different cell lines and results obtained showed that it was more efficiently internalized in cells overexpressing hCA IX (MDA-MB-231) compared to cells with low level of hCA IX (MCF-7, HeLa, and A549). The compound did not cause cytotoxicity to any cells in the dark, but the cell viability of all cells decreased significantly upon irradiation (λ_{exc} = 660 nm, power density of 8.7 mW cm^{-2}). For irradiation times of 5-15 minutes, IC_{50} values are 0.23-0.27 µM and 2.28-4.68 µM for MDA-MB-231 and MFC-7 cells, respectively. This result and control experiments clearly highlight the role played by the AAZ moieties in the cellular uptake and the success of PDT. The conjugate aza-BODIPY-AAZ was also evaluated on two murine breast cancer lines, namely 4T1 and 67NR cells, under normoxia and hypoxia conditions. The conjugate was efficiently internalized in 4T1 cells under hypoxia and due to the higher level of hCA IX expressed in 4T1 tumors relative to the 67NR. 4T1 cells under hypoxia are

also more sensitive to light irradiation. Indeed, IC_{50} values after 5-15 minutes of irradiation was 0.25-0.42 µM under hypoxia whereas under normoxia IC_{50} values were significantly higher (2.01-3.30 µM). *In vivo* studies showed that the conjugate aza-BODIPY-AAZ presented no significant toxicity at intravenous administration of 30 mg/kg and when used in the dark. However, applying irradiation on the tumor dramatically lowered tumor mass when compared to mice treated with aza-BODIPY alone or AAZ alone. This clearly shows the therapeutic efficacy of combining PDT with hCA IX - hypoxia targeting agent.[42]

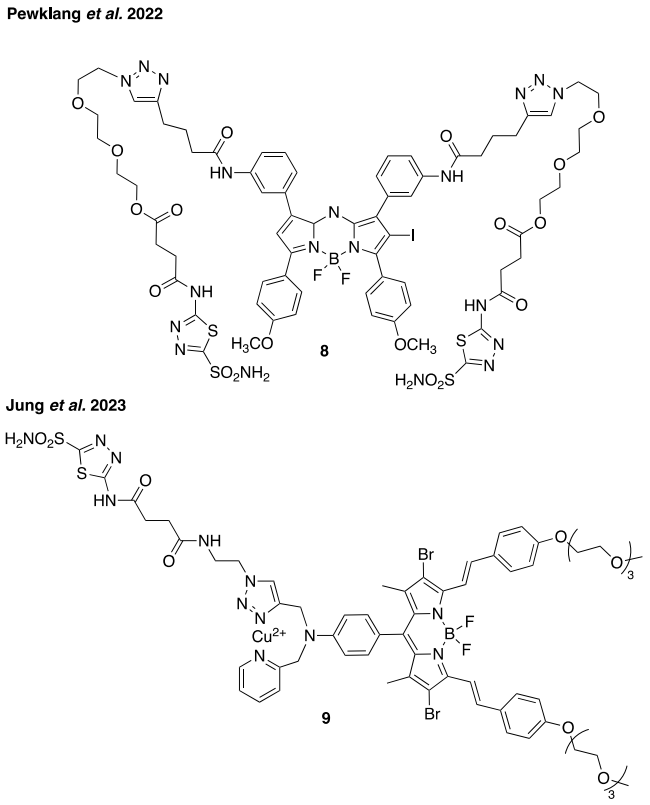


Figure 32. Structures of selected BODIPY based carbonic anhydrase IX inhibitors.

Chemodynamic therapy (CDT) allows ROS production even if local concentration of O_2 is low. One key reaction is the conversion of hydrogen peroxide (H_2O_2) into hydroxyl radicals ($OH^{\bullet}$). This approach is particularly appealing for solid tumors treatments since levels of H_2O_2 is generally high (1-100 µM). Jung *et al*. reported a conjugate **9**, namely CA9-BPS-Cu(II), combining a BODIPY Ps for PDT, a copper complex for CDT and acetazolamide (AAZ) for cancer stem cells targeting *via* hCA IX binding.[43] (**Figure 32**) The rate of $^1O_2$ production of the free ligand CA9-BPS was about 2.5 faster than the copper complex CA9-BPS-Cu(II) (irradiation conditions: λ_{exc} = 660 nm, 2.0 W cm^{-2}, 10 min; 1200 J cm^{-2}).

Under reducing conditions, the Ps CA9-BPS-Cu(II) is able to release Cu(I) ions which can catalyze a Fenton-like reaction to produce $OH^{\bullet}$ in the presence of H_2O_2. *In vitro* experiments conducted on

Chapter II: Are tumor-associated carbonic anhydrase genuine therapeutic targets for photodynamic therapy?

MDA-MB-231 cells showed that CA9-BPS-Cu(II) exhibited higher cytotoxicity upon laser irradiation (λ_{exc} = 660 nm, 100 Mw.cm^{-2}, 5 min; 30 J cm^{-2}). The enhanced ROS production could be attributed to PDT and CDT effects occurring simultaneously, as well as through copper-catalyzed glutathione depletion. The hCA IX-targeting conferred by the AAZ subunit was also evidenced by control experiments where the cytotoxicity of CA9-BPS-Cu(II) was dramatically suppressed in CA9-knockout MDA-MB-231 cells and in MDA-MB-231 cells with high expression of hCA IX pretreated with AAZ. *In vivo* experiments conducted on xenograft mice tumor models also showed that the conjugate CA9-BPS-Cu(II) was efficient to significantly decrease tumor size.[43]

Finally, to allow a comprehensive analysis of all these studies, a table summarizing the different conditions (types of illumination, hCA IX/hCA XII inhibitors, and concentrations used) for all hCA IX/XII-targeted PDT studies are presented below (**Table 3**).

Ref	Concentration	Type of illumination	λ_{exc} (nm)	Power (W.cm^{-2}) of irradiation	Time (min) of irradiation	Cancer cell type	hCA inhibitors
[31]	5 µM	Laser	660	2	30	MCF-7 MDA-MB-231	acetazolamide
[32]	200 µg/mL	Laser	660	0.005	10	4T1	sulfonamides
[33]	10 mg/kg	Laser	660	0.05	15	4T1	sulfadiazines
[34]	250 µg/mL	Laser	680	0.0005	30	MDA-MB-231	acetazolamide
[35]	2.5 mg/kg	Not indicated	Not indicated	0.08	5 (MDA-MB-231) 10 (4T1)	MDA-MB-231, 4T1, COS7	sulfonamide
[36]	0.25 mg/kg	Laser	650	0.0167	4	MDA-MB-231 Eca-109	acetazolamide
[37]	10 µM	Laser	540	0.0306	15	Capan-1	benzene sulfonamide coumarine
[38]	10 µM	Laser	425 525	0.02 0.015	10 60	MDA-MB-231	benzene sulfonamide
[39]	10 µM	Low-energy UV-A Lamp	530	Not indicated	60	MCF-7	saccharin
[40]	50 µg/mL	Laser	650	0.05	2	4T1	Benzene sulfonamide
[41]	0.5 µM	LED Lamp	660	0.0087	5	MDA-MB-231	acetazolamide
[42]	800 µM	Laser	660	2	10	MDA-MB-231	acetazolamide

Table 3. Summary of key conditions used in hCA IX/XII-PDT.

IV. Conclusion

PDT targeting tumor-associated CAs constitutes a promising approach in landscape of novel therapeutic strategies against hypoxic solid tumors. Here, we have reviewed several studies which demonstrate the proof of concept of the approach *in vitro* and *in vivo*, showing that combining a PS with a carbonic anhydrase inhibitor allows a synergistic treatment that enhances the PDT effect against hypoxic cancer cells and reduces resistance.

Nevertheless, on the ten potent systems currently described in literature and reported in this review, only the one reported by a french group has been evaluated *in vivo* for inhibition study against recombinant proteins hCA IX and hCA XII as well as against the cytosolic off-targets hCA I and hCA II.[39] Numerous challenges remain in translation to preclinic, and studies on how the chemical aspects of the carbonic anhydrase inhibitors and of the PS can affect the efficacy of the conjugate as PDT agent, as well as structural informations and understanding of mechanisms of action, will be required.

V. Expert opinion

Hypoxia is an intrinsic feature of a large number of malignant solid tumors due to uncontrollable cell proliferation, altered metabolism, and abnormal tumor blood vessels leading to reduced transport of oxygen and nutrients. This inherent physiologic barrier weakens the therapeutic effect of PDT, especially highly O_2-dependent PDT (Type II). In addition, the consumption of O_2 and the destruction of the tumor blood vessels which blocks the O_2 supply, during PDT process can aggravate this hypoxic tumor environment, leading to the formation of tumor neovascularization and the recurrence and invation of tumor cells through a variety of processes controlled, mostly by the transcription factors HIF. In particular, the high expression of HIF-1 is one of the major obstacles to PDT treatment efficacy, although the half-life of this transcription factor is of the order of 15 min. Numerous strategies consisting in delivering exogenous O_2 to tumor directly or generating oxygen *in situ* have been developed alleviating tumor hypoxia to some extent. Nevertheless, this O_2 supply is not sustainable and these strategies lead to moderate HIF-1 degradation, which can severely impact the PDT efficacy. For that reason, inhibiting HIF-1 signaling pathway has emerged as a promising strategy to relieve tumor hypoxia, mainly by targeting proteins overexpressed as a consequence of HIF activation, among which the tumor-associated CAs.

Ps	Advantages	Drawbacks
1	- Excitation light wavelength appropriate for optimum tissue penetration and for PDT applications - $^1O_2$ quantum yield (ϕ_Δ) (0.52 in DMSO). - Higher cellular uptake in cancerous cellular cells overexpressing hCA IX and hCA XII. - Synergistic treatment.	- Non-specific hCA IX/XII inhibitor. - Light dose quite high (2 W.cm^{-2}, 20 min) compared to other CAi-Ps. - Necessary to dissolve Ps first in DMSO and then, to dilute it in water for biological studies.
2	- Excitation light wavelength suitable for optimum tissue penetration and for PDT applications. - Appropriate light dose. - Higher cellular uptake in cancerous cellular cells overexpressing hCA IX/hCA XII. - Good biodegradation. - Synergistic treatment.	- Non-specific hCA IX/XII inhibitor. - No information about ϕ_Δ - Necessary to prepare organic nanoparticles (NPs and CAi-end-functionalized PEO-PPG-PEO polymer)
3	- Excitation light wavelength appropriate for optimum tissue penetration and for PDT applications. - Appropriate light dose. - Inhibitory effect in cancerous cell migration and invasion. - Synergistic treatment.	- Non-specific hCA IX/XII inhibitor. - Necessary to prepare organic nanoparticles (NPs and CAi-end-functionalized PEO-PPG-PEO polymer). - No information about ϕ_Δ - Irradiation light wavelength not indicated.
4	- Excitation light wavelength appropriate for optimum tissue penetration and for PDT applications. - Appropriate light dose. - $^1O_2$ quantum yield (ϕ_Δ) (0.60 in DMSO). - Acetazolamide makes cellular uptake easier. - Synergistic toxic effect	- Non-specific hCA IX/XII inhibitor.
5a/b	- hCA IX and hCA XII selective inhibitor (coumarine **5b**) proved by hCA inhibition assay. - Appropriate light dose. - Higher singlet oxygen generation than zinc(II) 5,10,15,20-*meso*-tetraphenylporphyrin (ZnTPP) (ϕ_Δ = 0.75 in DMF). - Membrane-localization of Ps in cancerous cellular cells overexpressing hCA IX and hCA XII. - Synergistic toxic effect.	- Excitation light wavelength not optimal for tissue penetration. - Necessary to dissolve Ps first in DMSO and then, to dilute it in water for biological studies.
6	- Excitation light wavelength appropriate for optimum tissue penetration and for PDT applications. - Appropriate light dose. - Type I and Type II PSs - Membrane-localization of Ps in cancerous cellular cells overexpressing hCA IX and hCA XII. - Synergistic toxic effect.	- Non-specific hCA IX/XII inhibitor. - Excitation light wavelength not optimal for tissue penetration. - Low ϕ_Δ (0.16 and 0.06 in aerated acetonitrile and PBS).
7	- $^1O_2$ quantum yield ϕ ($_\Delta$) (0.41 in DMF). - Efficient internalization inside the cell with homogenous distribution within the cytoplasm and nucleus - Synergistic toxic effect	- Non-specific hCA IX/XII inhibitor. - Excitation light wavelength not optimal for tissue penetration. - Light dose quite high compared to other CAi-Ps.
8	- Excitation light wavelength suitable for optimum tissue penetration and for PDT applications. - Appropriate light dose. - High $^1O_2$ quantum yield (ϕ_Δ = 0.88 in DMSO). - Excellent stability in fetal bovine serum (FBS) - Good internalization of Ps in cancerous cellular cells overexpressing hCA IX and hCA XII. - Synergistic cytotoxic effect	- Non-specific hCA IX/XII inhibitor. - Necessary to dissolve Ps first in DMSO and then, to dilute it in water for biological studies.
9	- Combined copper catalyst for chemodynamic therapy (CDT) with Ps. - Excitation light wavelength suitable for optimum tissue penetration and for PDT applications. - Appropriate light dose. - Good cellular uptake in cancerous cellular cells overexpressing hCA IX/hCA XII. - Strong synergistic cytotoxic effect between CDT/PDT (combination index of 1) and hCA IX/XII targeting.	- Non-specific hCA XI/XII inhibitor. - No information about ϕ_Δ - Light dose quite high (2 W.cm^{-2}, 20 min) compared to other CAi-Ps. - High drug dose (800 µM) compared to other CAi-Ps - Necessary to dissolve PS first in DMSO and then, to dilute it in water for biological studies.

Table 4. Advantages and drawbacks of the main selected CAi featuring Ps.

In this respect, hCA IX and/or hCA XII, HIF inducible proteins highly overexpressed in all hypoxic tumors, participating in the complex machinery of pH regulation and thus, contributing to survival, proliferation, invasion, and metastasis of cancer cells, appears to be a very attractive targets for PDT treatment. By targeting hCA IX/XII with small molecule inhibitors linked to Ps, a selective delivery and improved uptake of the Ps into the tumor tissues were generally achieved. In addition, compared to unfunctionalized Ps, hCA IX/XII inhibitor-conjugated Ps offer new opportunities for synergistic treatments because they show enhanced PDT and in the same time additional positive effects by inhibiting significantly tumor growth and decreasing the levels of angiopoieting (ANGPT) and vascular endothelial growth factor A (VEGFA), which are known to promote the initiation of angiogenesis and maturation of new vessels. As described below, promising results were obtained combining hCA IX/XII inhibitors and Ps. A comprehensive analysis of the current progress of this targeted approach was performed by analizing advantages and drawbacks of the main selected CAi featuring Ps described in this review (**Table 4**). To compare all these Ps, different parameters were considered: light and drug dose, excitation wavelength of the Ps compared with the therapeutic window, Ps handling,[44] and selectivity of the CAi.[45] However, the relatively high molecular weight of the CAi- Ps hybrids reported so far may be an obstacle for their effective delivery within the tumor tissues and this factor has poorly been investigated to date. More effective and possibly lower molecular weight such derivatives should be designed in future studies for achieving an enhanced antitumor effect.

Despite the promising results generally obtained from these studies, systematic inhibition studies against recombinant proteins hCA IX, hCA XII and the cytosolic off-targets hCA I and hCA II are still missing as noticed in **Table 4**. Indeed, to our knowledge, except our study, no such inhibition study was performed whereas it is an important key feature that must be considered for a potential therapeutic application of these compounds. Since hCA II is in particular widely distributed in tissue and highly expressed in red blood cells, the sequestrion of nonselective hCA inhibitors-conjugated Ps can be expected, which will reduced their concentrations and their bioavailability for hCA IX and/or hCA XII, and thus, for solid tumor tissues.[46] Consequently, the nature of inhibitor will be important to be selected in view of selectivity for the specific hCA IX and/or hCA XII isoforms. Besides the nature of inhibitor, we point to the following areas of research should be further developed. In the coming years, we anticipate that the molecular diversity of PS will be extended. Up to now, hCA IX/XII inhibitor-conjugated PS have been appointed on the basis of well-etablished Ps. Usually, these Ps used in the biological environment require enough water solubility to avoid their aggregation, which is detrimental to their bioavailability and ROS generation efficiency. To overcome this issue, the Ps can be load/self-assemble onto/into hCA IX-functionalized water-dispersible nanoparticles (NPs). Unfortunaly, once

delivered to the tumor site, the aggregation caused quenching (ACQ) effect would decrease the ROS generation. Hopefully, Aggregation-Induced-Emission (AIE) Ps have emerged as a new class of Ps. Contrary to ACQ Ps, these AIE Ps demonstrate their ability to generate efficiently ROS even in their aggregated states due to the restriction of their molecular motions and thus, the suppression of non-radiative decay.[47] As such, we anticipate an increasing interest for the development of AIE PS able to target hCA IX/XII.[48]

As noted above, most of the Ps used in the design of hCA IX-targeted PDT were built upon a type II-based Ps. Since type II PDT is highly dependent on the oxygen concentration, its therapeutic efficacy is seriously restricted by tumor hypoxia. To address this issue, remodeling oxygen microenvironment either by O_2 replenishing or *in situ* O_2 generation in combination of hCA IX/XII-conjugated Ps has a chance to become a useful strategy for further enhancing PDT efficiency.[18, 48] Besides type II, the exploitation of type I Ps, less affected by O_2 concentrations and able to drive therapy in O_2-deficient environment, is highly desirable.[49] Among these type-I PDT Ps, metal oxide nanomaterials are particularly attractive due to their excellent photostability and ability to generate radicals.[18]

The development of this therapeutic approach combining targeting and inhibition of hCA IX with PDT has expanded the scope of research towards the treatment of hypoxic solid tumors. However, to take the next step towards preclinical and clinical, information regarding mechanism of actions are required allowing to verify hypotheses regarding therapeutic efficacy. The use of the obtained information will allow to: 1) develop a rational in the design of the Ps, 2) develop biomarker for controlling response to therapy, 3) stratify patient in view of precise characterization of therapeutic efficacy and 4) predict and possibly prevent the possible treatment resistance.

Chapter II: Are tumor-associated carbonic anhydrase genuine therapeutic targets for photodynamic therapy?

VI. References:

1. Dagogo-Jack, I.; Shaw, A. T., Tumour heterogeneity and resistance to cancer therapies. *Nature reviews Clinical oncology* **2018,** *15* (2), 81-94.

2. Harris, A. L., Hypoxia—a key regulatory factor in tumour growth. *Nature reviews cancer* **2002,** *2* (1), 38-47.

3. Qian, J.; Rankin, E. B., Hypoxia-induced phenotypes that mediate tumor heterogeneity. *Hypoxia and cancer metastasis* **2019**, 43-55.

4. Luo, W.; Wang, Y., Hypoxia mediates tumor malignancy and therapy resistance. *Hypoxia and Cancer Metastasis* **2019**, 1-18.

5. Petrova, V.; Annicchiarico-Petruzzelli, M.; Melino, G.; Amelio, I., The hypoxic tumour microenvironment. *Oncogenesis* **2018,** *7* (1), 10.

6. Roma-Rodrigues, C.; Mendes, R.; Baptista, P. V.; Fernandes, A. R., Targeting tumor microenvironment for cancer therapy. *International journal of molecular sciences* **2019,** *20* (4), 840.

7. Chen, G.; Wu, K.; Li, H.; Xia, D.; He, T., Role of hypoxia in the tumor microenvironment and targeted therapy. *Frontiers in Oncology* **2022,** *12*, 961637.

8. Jing, X.; Yang, F.; Shao, C.; Wei, K.; Xie, M.; Shen, H.; Shu, Y., Role of hypoxia in cancer therapy by regulating the tumor microenvironment. *Molecular cancer* **2019,** *18*, 1-15.

9. Lee, S.-H.; Griffiths, J. R., How and why are cancers acidic? Carbonic anhydrase IX and the homeostatic control of tumour extracellular pH. *Cancers* **2020,** *12* (6), 1616.

10. Neri, D.; Supuran, C. T., Interfering with pH regulation in tumours as a therapeutic strategy. *Nature reviews Drug discovery* **2011,** *10* (10), 767-777.

11. McDonald, P. C.; Chafe, S. C.; Supuran, C. T.; Dedhar, S., Cancer therapeutic targeting of hypoxia induced carbonic anhydrase IX: from bench to bedside. *Cancers* **2022,** *14* (14), 3297.

12. Angeli, A.; Carta, F.; Nocentini, A.; Winum, J.-Y.; Zalubovskis, R.; Akdemir, A.; Onnis, V.; Eldehna, W. M.; Capasso, C.; Simone, G. D., Carbonic anhydrase inhibitors targeting metabolism and tumor microenvironment. *Metabolites* **2020,** *10* (10), 412.

13. Supuran, C. T., Experimental carbonic anhydrase inhibitors for the treatment of hypoxic tumors. *Journal of Experimental Pharmacology* **2020**, 603-617.

14. Kalinin, S.; Malkova, A.; Sharonova, T.; Sharoyko, V.; Bunev, A.; Supuran, C. T.; Krasavin, M., Carbonic anhydrase IX inhibitors as candidates for combination therapy of solid tumors. *International Journal of Molecular Sciences* **2021,** *22* (24), 13405.

15. Supuran, C. T., Carbonic anhydrase inhibitors: an update on experimental agents for the treatment and imaging of hypoxic tumors. *Expert Opinion on Investigational Drugs* **2021,** *30* (12), 1197-1208.

16. Supuran, C. T., Carbonic anhydrase inhibitors as emerging agents for the treatment and imaging of hypoxic tumors. *Expert Opinion on Investigational Drugs* **2018,** *27* (12), 963-970.

17. Li, R.-T.; Chen, M.; Yang, Z.-C.; Chen, Y.-J.; Huang, N.-H.; Chen, W.-H.; Chen, J.; Chen, J.-X., AIE-based gold nanostar-berberine dimer nanocomposites for PDT and PTT combination therapy toward breast cancer. *Nanoscale* **2022,** *14* (27), 9818-9831.

18. Wan, Y.; Fu, L. H.; Li, C.; Lin, J.; Huang, P., Conquering the hypoxia limitation for photodynamic therapy. *Advanced Materials* **2021,** *33* (48), 2103978.

19. Du, Y.; Han, J.; Jin, F.; Du, Y., Recent strategies to address hypoxic tumor environments in photodynamic therapy. *Pharmaceutics* **2022,** *14* (9), 1763.

20. Celli, J. P.; Spring, B. Q.; Rizvi, I.; Evans, C. L.; Samkoe, K. S.; Verma, S.; Pogue, B. W.; Hasan, T., Imaging and photodynamic therapy: mechanisms, monitoring, and optimization. *Chemical reviews* **2010,** *110* (5), 2795-2838.

21. Zhou, Z.; Song, J.; Nie, L.; Chen, X., Reactive oxygen species generating systems meeting challenges of photodynamic cancer therapy. *Chemical society reviews* **2016,** *45* (23), 6597-6626.

22. Li, X.; Kwon, N.; Guo, T.; Liu, Z.; Yoon, J., Innovative strategies for hypoxic-tumor photodynamic therapy. *Angewandte Chemie International Edition* **2018,** *57* (36), 11522-11531.

23. Zheng, X.; Sun, W.; Ju, M.; Wu, J.; Huang, H.; Shen, B., Chemical Biology Toolbox to Overcome Hypoxic Tumor Microenvironment of Photodynamic Therapy: A Review. *Biomaterials Science* **2022**.

24. Kirino, I.; Fujita, K.; Sakanoue, K.; Sugita, R.; Yamagishi, K.; Takeoka, S.; Fujie, T.; Uemoto, S.; Morimoto, Y., Metronomic photodynamic therapy using an implantable LED device and orally administered 5-aminolevulinic acid. *Scientific reports* **2020,** *10* (1), 22017.

25. Aguilar Cosme, J. R.; Gagui, D. C.; Green, N. H.; Bryant, H. E.; Claeyssens, F., In vitro low-fluence photodynamic therapy parameter screening using 3D tumor spheroids shows that fractionated light treatments enhance phototoxicity. *ACS Biomaterials Science & Engineering* **2021,** *7* (11), 5078-5089.

26. Caverzán, M. D.; Oliveda, P. M.; Beaugé, L.; Palacios, R. E.; Chesta, C. A.; Ibarra, L. E., Metronomic Photodynamic Therapy with Conjugated Polymer Nanoparticles in Glioblastoma Tumor Microenvironment. *Cells* **2023,** *12* (11), 1541.

27. de Keijzer, M. J.; de Klerk, D. J.; de Haan, L. R.; van Kooten, R. T.; Franchi, L. P.; Dias, L. M.; Kleijn, T. G.; van Doorn, D. J.; Heger, M.; Group, P. T. S., Inhibition of the HIF-1 Hypoxia-inducible factor 1 (HIF-1) Survival Pathway as a Strategy to Augment Photodynamic Therapy Photodynamic therapy (PDT) Efficacy. In *Photodynamic Therapy: Methods and Protocols*, Springer: 2022; pp 285-403.

28. Grin, M.; Suvorov, N.; Ostroverkhov, P.; Pogorilyy, V.; Kirin, N.; Popov, A.; Sazonova, A.; Filonenko, E., Advantages of combined photodynamic therapy in the treatment of oncological diseases. *Biophysical Reviews* **2022,** *14* (4), 941-963.

29. Li, M.; Xu, Y.; Peng, X.; Kim, J. S., From low to no O2-dependent hypoxia photodynamic therapy (hPDT): a new perspective. *Accounts of Chemical Research* **2022,** *55* (22), 3253-3264.

30. Bourseau-Guilmain, E.; Menard, J. A.; Lindqvist, E.; Indira Chandran, V.; Christianson, H. C.; Cerezo Magaña, M.; Lidfeldt, J.; Marko-Varga, G.; Welinder, C.; Belting, M., Hypoxia regulates global membrane protein endocytosis through caveolin-1 in cancer cells. *Nature Communications* **2016,** *7* (1), 11371.

31. Christianson, H. C.; Menard, J. A.; Indira Chandran, V.; Bourseau-Guilmain, E.; Shevela, D.; Lidfeldt, J.; Månsson, A.-S.; Pastorekova, S.; Messinger, J.; Belting, M., Tumor antigen glycosaminoglycan modification regulates antibody-drug conjugate delivery and cytotoxicity. *Oncotarget* **2017,** *8* (40).

32. Jung, H. S.; Han, J.; Shi, H.; Koo, S.; Singh, H.; Kim, H.-J.; Sessler, J. L.; Lee, J. Y.; Kim, J.-H.; Kim, J. S., Overcoming the limits of hypoxia in photodynamic therapy: a carbonic anhydrase IX-targeted approach. *Journal of the American Chemical Society* **2017,** *139* (22), 7595-7602.

33. Zhu, W.; Liu, Y.; Yang, Z.; Zhang, L.; Xiao, L.; Liu, P.; Wang, J.; Yi, C.; Xu, Z.; Ren, J., Albumin/sulfonamide stabilized iron porphyrin metal organic framework nanocomposites: targeting tumor hypoxia by carbonic anhydrase IX inhibition and T1–T2 dual mode MRI guided photodynamic/photothermal therapy. *Journal of Materials Chemistry B* **2018,** *6* (2), 265-276.

34. Zhu, W.; Zhang, L.; Yang, Z.; Liu, P.; Wang, J.; Cao, J.; Shen, A.; Xu, Z.; Wang, J., An efficient tumor-inducible nanotheranostics for magnetic resonance imaging and enhanced photodynamic therapy. *Chemical Engineering Journal* **2019,** *358*, 969-979.

35. Jiang, Y.; Li, J.; Zeng, Z.; Xie, C.; Lyu, Y.; Pu, K., Organic photodynamic nanoinhibitor for synergistic cancer therapy. *Angewandte Chemie International Edition* **2019,** *58* (24), 8161-8165.

36. Fan, G.-L.; Yuan, P.; Deng, F.-A.; Liu, L.-S.; Miao, Y.-L.; Wang, C.; Qiu, X.-Z.; Yu, X.-Y.; Cheng, H.; Li, S.-Y., Self-Delivery Photodynamic Nanoinhibitors for Tumor Targeted Therapy and Metastasis Inhibition. *ACS Applied Bio Materials* **2020,** *3* (9), 6124-6130.

37. Wang, F.; Xu, T.; Meerovich, G.; Hong, F.; Chen, Z.-L.; Yan, Y.-J., Synthesis and evaluation of new pyropheophorbide-a derivatives for CAIX-targeted photodynamic therapy. *Dyes and Pigments* **2022,** *203*, 110328.

38. Merabti, A.; Roger, M.; Nguyen, C.; Nocentini, A.; Gerbier, P.; Richeter, S.; Gary-Bobo, M.; Supuran, C. T.; Clément, S.; Winum, J.-Y., Carbonic Anhydrase Inhibitors Featuring a Porphyrin Scaffold:

Synthesis, Optical and Biological Properties. *European Journal of Organic Chemistry* **2022,** *2022* (21), e202101538.

39. Su, X.; Wang, W. J.; Cao, Q.; Zhang, H.; Liu, B.; Ling, Y.; Zhou, X.; Mao, Z. W., A Carbonic Anhydrase IX (CAIX)-Anchored Rhenium (I) Photosensitizer Evokes Pyroptosis for Enhanced Anti-Tumor Immunity. *Angewandte Chemie* **2022,** *134* (8), e202115800.

40. Kumar, P.; Singh, P.; Saren, S.; Sayala, J.; Sivakumar, S.; Patra, A. K., Quaternary Ru(ii) complexes of terpyridines, saccharin and 1,2-azoles: effect of substituents on molecular structure, speciation, photoactivity, and photocytotoxicity. *Dalton Transactions* **2022,** *51* (48), 18416-18437.

41. Liu, J.; Hu, X.; Feng, L.; Lin, Y.; Liang, S.; Zhu, Z.; Shi, S.; Dong, C., Carbonic anhydrase IX-targeted H-APBC nanosystem combined with phototherapy facilitates the efficacy of PI3K/mTOR inhibitor and resists HIF-1α-dependent tumor hypoxia adaptation. *Journal of Nanobiotechnology* **2022,** *20* (1), 187.

42. Pewklang, T.; Chansaenpak, K.; Bakar, S. N.; Lai, R.-Y.; Kue, C. S.; Kamkaew, A., Aza-BODIPY based carbonic anhydrase IX: Strategy to overcome hypoxia limitation in photodynamic therapy. *Frontiers in Chemistry* **2022,** *10*.

43. Jung, H. S.; Koo, S.; Won, M.; An, S.; Park, H.; Sessler, J. L.; Han, J.; Kim, J. S., Cu(ii)-BODIPY photosensitizer for CAIX overexpressed cancer stem cell therapy. *Chemical Science* **2023,** *14* (7), 1808-1819.

44. Gunaydin, G.; Gedik, M. E.; Ayan, S., Photodynamic therapy—current limitations and novel approaches. *Frontiers in Chemistry* **2021,** *9*, 691697.

45. Mishra, C. B.; Tiwari, M.; Supuran, C. T., Progress in the development of human carbonic anhydrase inhibitors and their pharmacological applications: Where are we today? *Medicinal Research Reviews* **2020,** *40* (6), 2485-2565.

46. Lindskog, S., Purification and properties of bovine erythrocyte carbonic anhydrase. *Biochimica et Biophysica Acta* **1960,** *39* (2), 218-226.

47. Hu, F.; Xu, S.; Liu, B., Photosensitizers with aggregation-induced emission: materials and biomedical applications. *Advanced materials* **2018,** *30* (45), 1801350.

48. Chen, H.; Wan, Y.; Cui, X.; Li, S.; Lee, C.-S., Recent Advances in Hypoxia-Overcoming Strategy of Aggregation-Induced Emission Photosensitizers for Efficient Photodynamic Therapy. *Advanced Healthcare Materials* **2021,** *10* (24), 2101607.

49. Lu, B.; Wang, L.; Tang, H.; Cao, D., Recent advances in type I organic photosensitizers for efficient photodynamic therapy for overcoming tumor hypoxia. *Journal of Materials Chemistry B* **2023,** *11* (21), 4600-4618.

Chapter III

Carbonic Anhydrase Inhibitors Featuring a Porphyrin Scaffold: Synthesis, Optical and Biological Properties

Merabti, A.; Roger, M.; Nguyen, C.; Nocentini, A.; Gerbier, P.; Richeter, S.; Gary-Bobo, M.; Supuran, C. T.; Clément, S.; Winum, J. Y., Carbonic anhydrase inhibitors featuring a porphyrin scaffold: synthesis, optical and biological properties. *European Journal of Organic Chemistry* **2022**, *2022* (21), e202101538

Chapter III: Carbonic Anhydrase Featuring a Porphyrin Scaffold: Synthesis, Optical and Biological Properties

I. Abstract:

The synthesis, characterization and study of optical properties of innovative tetrafunctional zinc (II) porphyrins with carbonic anhydrase (CA) inhibitors in sulfonamide and coumarine series are described. The synthetic methodology relies on the preparation of the porphyrin core by condensation of azido triethyleneglycol functionalized benzaldehyde derivative with pyrrole followed by its metalation and inhibitors coupling *via* Huisgen click-reaction. The tetrafunctionalized zinc (II) porphyrin with coumarin moieties showed selective inhibition against tumour-assiated hCA IX and HCA XII *versus* the cytosolic off-targets hCA I and hCA II. This compound was able to accumulate on cell membrane and impair pancreas cancer cells (Capan-1) proliferation in normoxic conditions with LC_{50} of 4.5 µM. Moreover, its optical properties revealed efficient photo-sensitizing properties, leading to cancel cells death under light irradiation, making this compound a suitable candidate for photodynamic therapy.

Keywords: photodynamic therapy, carbonic anhydrases, carbonic anhydrase inhibitors, sulfonamide, coumarin, porphyrin, cancer.

Chapter III: Carbonic Anhydrase Featuring a Porphyrin Scaffold: Synthesis, Optical and Biological Properties

II. Introduction:

Tumors are complex dynamic ecosystems characterized by intratumoral spatial and temporal heterogeneity. Hypoxic zones (intratumoral pO_2 < 10 mmg) are one of the main features that characterizes the intrinsic heterogeneity of most solid tumors.[1] They are critical promoter of tumor hallmarks having important influence on tumor growth, distant metastasis, and invasiveness.[2] Moreover, intratumoral hypoxia is recognized as a factor limiting the response to conventional chemo-,radio- and immune-therapies and is associated with poor patient outcome and aggressive metastatic phenotypes.[3-4]

Photodynamic therapy (PDT) is clinical photochemical-based anticancer therapeutic treatment, which has attracted much enthusiasm due to its minimal invasiveness, implementation, low systematic toxicity and high efficiency. PDT is based on tumoral-specific accumulation of a photosensitizing agent which can be activated by light source at a specific wavelength to produce locally reactive oxygen species (ROS) through two possible process (type I: superoxide anion ($O_2^{\bullet -}$), hydroxyl radical ($OH^{\bullet}$), or hydrogen peroxide (H_2O_2) and type II: singlet oxygen ($^1O_2$)) leading to a cascade of reactions which could trigger cancer cells death by oxidative stress.[5]

PDT suffers from impaired efficacy under hypoxic conditions, as the generation of ROS requires the presence of O_2. Moreover PDT can aggravate hypoxic phenomenon. Thus, many rational strategies have been reported to overcome this limitation either by alleviating hypoxia or by choosing to use it.

Recent comprehensive review papers have in particular highlighted specific aspects to enhance PDT including tumor microenvironment (TME)-responsive photosensitizers (PS), new generation of innovative PSs and their activation strategies, targeted PDT and nanoparticle-targeted PS.[6-11]

To overcome the hypoxia limitation of conventional PDT, the approach of tumor-targeted PDT directed at inhibition of the transmembrane tumor-associated carbonic anhydrase IX (hCA IX) was developed and recently reported in two studies,[12-14] As a result of the transcription factors hypoxia-inducible factor1 and 2 (HIF-1/2) activation pathway, expression of CA IX isoform is strongly upregulated in hypoxic solid tumors participating in PH regulation, especially acidification of the tumor microenvironment, assuring survival and metastatic phenotype of aggressive tumor cells.[15]

hCA IX inhibitors (CAIs) have recently been validated as therapeutic agents hypoxic tumors as illustrated by phase Ib/II study which was initiated in 2014 with the substituted ureidobenzene-sulfonamide derivatives SLC-0111 in combination with other therapeutic agents for the management of pancreatic cancer (ClinicalTrials.gov Identifier: NCT03450018).[16]

Chapter III: Carbonic Anhydrase Featuring a Porphyrin Scaffold: Synthesis, Optical and Biological Properties

The underlying idea of the concept aiming at improving the efficacy of PDT was to combine PS with hCA IX inhibitor and explore whether the combination could give rise to an effective synergistic cancer therapy. In 2007, Jung *et al.* reported a conjugate of CA IX inhibitor acetazolamide (AAZ) with BODIPY photosensitizer (**Figure 33**). This CA IX targeting PS showed enhanced *in vitro* phototoxicity efficacy against aggressive human breast cancer MDA-MB-231 cell line and spheroid model and demonstrated tumor suppression *in vivo* on MDA-MB-231 inoculated xenograft mice model.[12] In 2018, Ren *et al.* developed a multifunctional platform, built upon an iron tetrakis(4-carboxyphenyl)porphyrin nanoscale metal organic framework (NMOF) modified by bovine serum albumin (BSA) and sulfonamide (SA).[13] BSA/SA modification of the NMOF enhanced its blood circulation and allowed to selectivity reach hypoxic location by targeting CA IX of tumor cells while iron-porphyrin NMOF acts both as contrast agent for T_1-T_2 weighted MRI to guide photodynamic and photothermal therapy (PTT) and as PS and photothermal agents allowing to achieve 95% of the 4T1 death cells when combined. More recently, Jiang *et al.* described a biodegradable semiconducting photodynamic nano-inhibitors consisting of amphiphilic polymer with terminating acetazolamide (**AAZ**) (**A**) and near-IR absorbing semiconducting polymer PCVB (**B**) (**Figure 33**). These nanoparticles were able to target selectively tumor and accumulate in MDA-MB-231 xenograft mouse model leading to inhibition of tumor growth downregulation of metastasis related proteins.[14]

These seminal studies shed light on the interest to design CAI-PS conjugates for synergistic cancer therapy and diagnosis to improve the efficacy of PDT in hypoxic tumors and reduce hypoxia-reduced metastasis.

In this context, our objective was to develop multifunctional platform combining both the targeting and multivalent inhibition of carbonic anhydrase IX/XII,[17] and the optical properties of a PS. As such, we report here the synthesis, the optical properties and the biological activity of an innovative tetrafunctionalized zinc (II) porphyrin with selective hCA IX/hCA XII inhibitors in sulfonamide and coumarin series (**Figure 33**).

Chapter III: Carbonic Anhydrase Featuring a Porphyrin Scaffold: Synthesis, Optical and Biological Properties

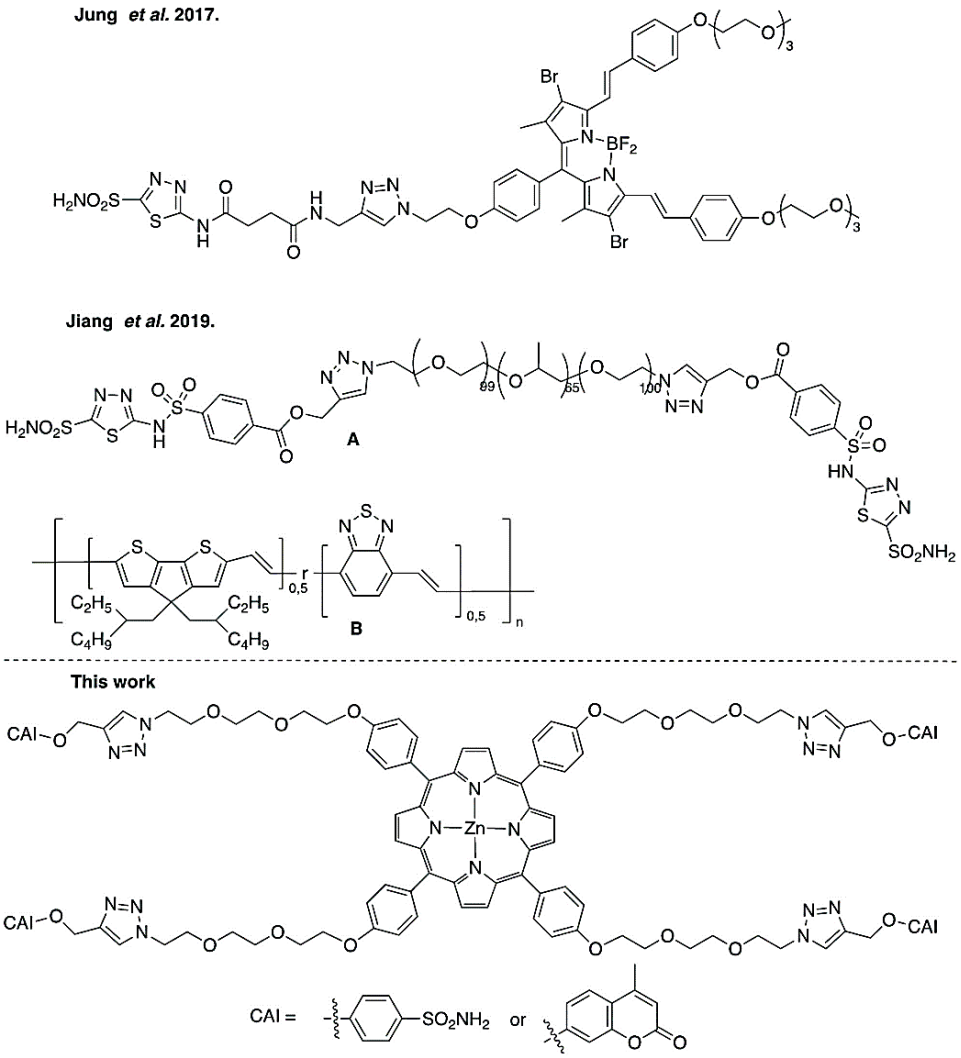


Figure 33. Structure of CAI-PS.

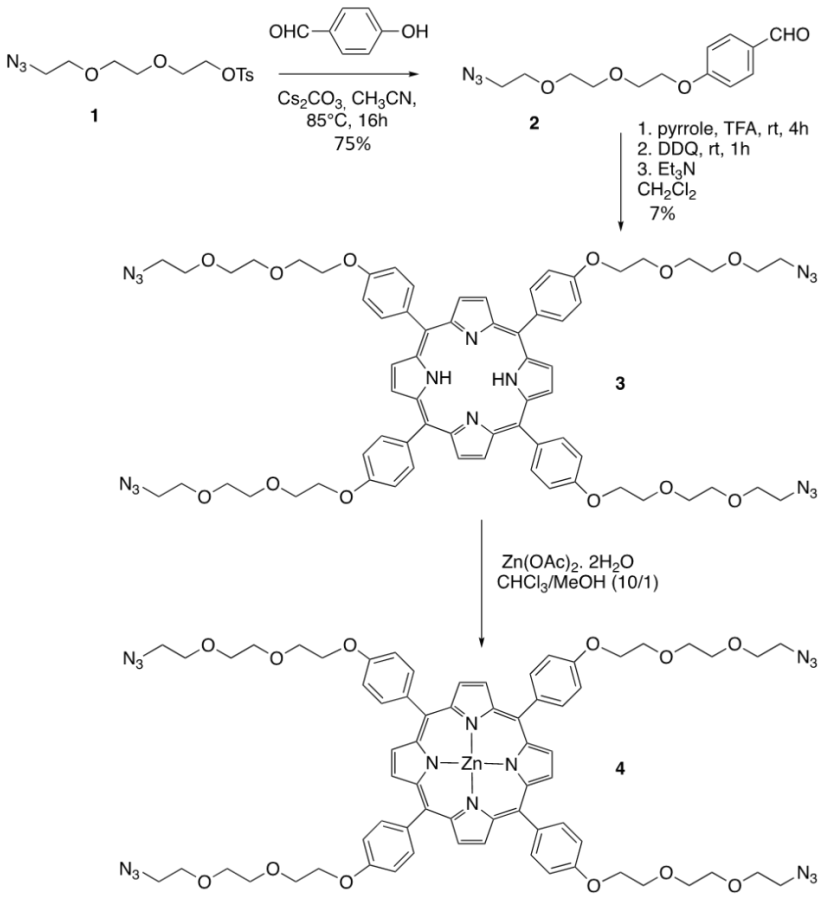
III. Results and Discussion

III.1 Design and synthesis

The design of our platforms is based on the covalent linkage of a zinc (II) porphyrin PS with peripheral sulfonamide or coumarin-based CA IX inhibitors through a "click-chemistry" approach. These systems were obtained *via* a Cu(I)-catalyzed Huisgen 1,3-dipolar cycloaddition between an alkyne-functionalized sulfonamide or coumarin inhibitor and an azido tetrafunctionalized porphyrin (**4**) Leading to the formation of the 1,2,3-triazole bridge. The synthesis of porphyrin **4** is described in **Scheme 1** and first involved the preparation of porphyrin **3** by condensation of 4-[2-[2-(-azidoethoxy)ethoxy]ethoxy]benzaldehyde with pyrrole under mild Lindsey's reaction conditions.

Chapter III: Carbonic Anhydrase Featuring a Porphyrin Scaffold: Synthesis, Optical and Biological Properties

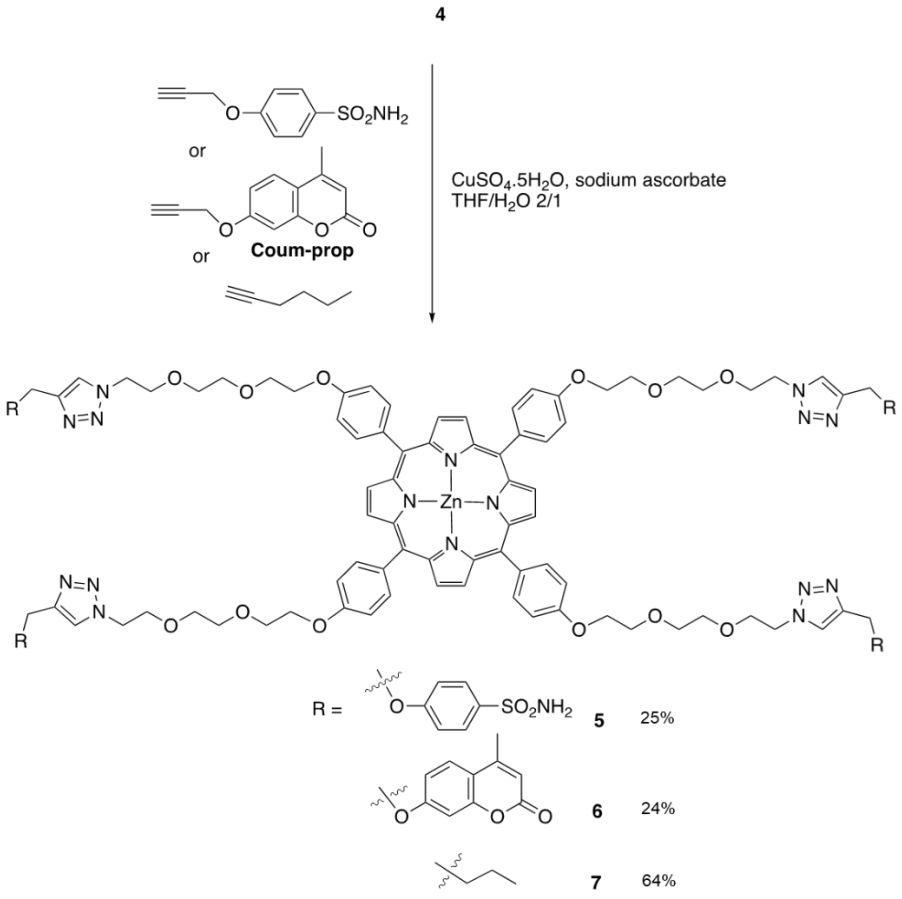
Porphyrin **3** was metalated with $Zn(OAc)_2.2H_2O$ in a mixture of $CHCl_3$/MeOH (10/1, v/v) at room temperature to obtain zinc(II) porphyrin **4** in 88% yield. The structure of the porphyrin **4** was confirmed by IR spectroscopy, ^{1}H NMR spectroscopy and mass spectrometry. The presence of the azido group is characterized by the strong asymmetric stretching frequency at 2094 cm^{-1}, High-resolution ESI-TOF mass spectroscopy (positive mode) showed the pseudo-molecular ion $[M+H]^+$ at *m/z*= 1369.4873 Da in agreement with the calculated one (*m/z*= 1368.4880 Da).



Scheme 1. Synthesis of the tetra-azido based porphyrin platform

"Click" reaction between the azide containing porphyrin **4** and the terminal alkyne containing sulfonamide and coumarin, catalyzed by $CuSO_4.5H_2O$ and sodium ascorbate, in the mixture of THF-H_2O, led to the formation of **5** and **6**, respectively. A porphyrin analog without CA IX inhibitor **7** was also synthesized hex-1-ne to serve as control system (**Scheme 2**). The ATR-FTIR spectrum of the disappearance of the strong asymmetric stretching frequency in the region of 2160-2090 cm^{-1}.[18] The ^{1}H NMR spectra of these compounds showed the presence of a characteristic singlet at δ ~ 8.30 ppm indicating the successful formation of the 1, 2, 3-triazole ring. The structure of porphyrins **5**, **6** and **7**

were also confirmed by high-resolution ESI-TOF mass spectrometry (positive mode) through the presence of the dication $[M+2H]^{2+}$ for **5** and **6** and monocation $[M+H]^{+}$ for **7**.



Scheme 2. Synthesis of the tetra-CAI based porphyrins.

III.2 Optical properties

The UV-visible absorption spectra in DMSO of sulfonamide, coumarin-functionalized zinc (II) porphyrin **5** (Figure S74 in the Supporting information) and **6** (**Figure 34**) as well as control system **7** (Figure S75 in the Supporting information) showed the presence of a typical Soret absorption band at 431 nm and two Q bands at ~560 nm and ~ 600 nm.

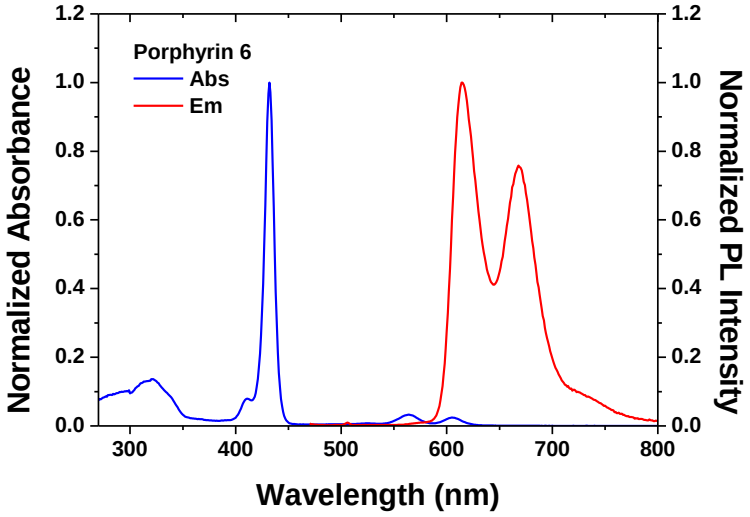


Figure 34. UV-Visible absorption (blue) and emission (red) spectra of porphyrin 6 in DMSO (C = 10^{-6} M, λ_{ex} = 440 nm).

Besides the Soret and Q bands in the UV-Visible absorption spectrum of **6**, an additional broad absorption band was also observed at ~320 nm, which could be assigned to the presence of coumarin peripheral moieties when compared to the native propargyl-functionalized coumarin (**Coum-prop**) (Figure S76 in the Supporting Information). Since the UV-Visible absorption spectrum of **6** is the linear combination of the alkyne-substituted coumarin and porphyrin **7**, it could be concluded that there is no or negligible electron interaction between the porphyrin and coumarin moieties in the ground state.[19-20]

	λ_{ex} [nm]	λ_{em}[nm]	φ (%)	log ε
5	431, 561, 604	615, 665	3	7.3, 4.16, 4.04
6	320, 431, 562, 605	615, 668	3	6.3, 4.38, 4.06
7	431, 563, 604	615, 667	4	5.41, 4.37, 3.93

Table 5. Photophysical data of porphyrins **5**-**7** in DMSO solutions.

The steady-state emission studies of the porphyrins **5-7** were then carried out. The spectral characteristics including emission maxima and quantum yields are summarized in **Table 5**. The emission spectra zinc (II) porphyrins **5-7** showed two bands at ~ 615 and ~ 665 nm when excited at 440 nm (Figure S76-S77 in the Supporting Information and Figure 35). When excited at 320 nm, an additional emission bans is also observed at ~ 380 nm, corresponding to the coumarin emission (**Figure 35**). Compared to the starting alkyne **Coum-prop** and porphyrin **7**, the intensity of this fluorescence

band decreased while those relative to the emission of porphyrin subunits increased after introduction of the coumarin subunits. The excitation spectra of porphyrin **6** obtained at 615 nm emission wavelength exhibited a high excitation intensity at 320 nm, indicating significant contribution of coumarin subunits in the emission of porphyrin (Figure S79 in the Supporting Information). Such findings indicate that an energy transfer occurs from the coumarins to the porphyrins core but is not quantitave in the system.[19] [20-22] The significant overlapping of the fluorescence spectrum of **Coum-prop** with the UV-visible absorption spectrum of porphyrin **6** (Figure S80 in the Supporting Information) meets the requirements for FRET. Fréchet *et al.* have notably studied the FRET in porphyrin dendrimers with coumarin end-functionalized poly(ε-caprolactone) arms.[21] They demonstrated in particular that as chain length of poly (ε-caprolactone) increases, more the distance between the donor and acceptor chromophores increases leading to a reduced probability of FRET this explains why in our system, an incomplete FRET is observed probably due to the long distance separating the coumarin donor and the porphyrin acceptor.

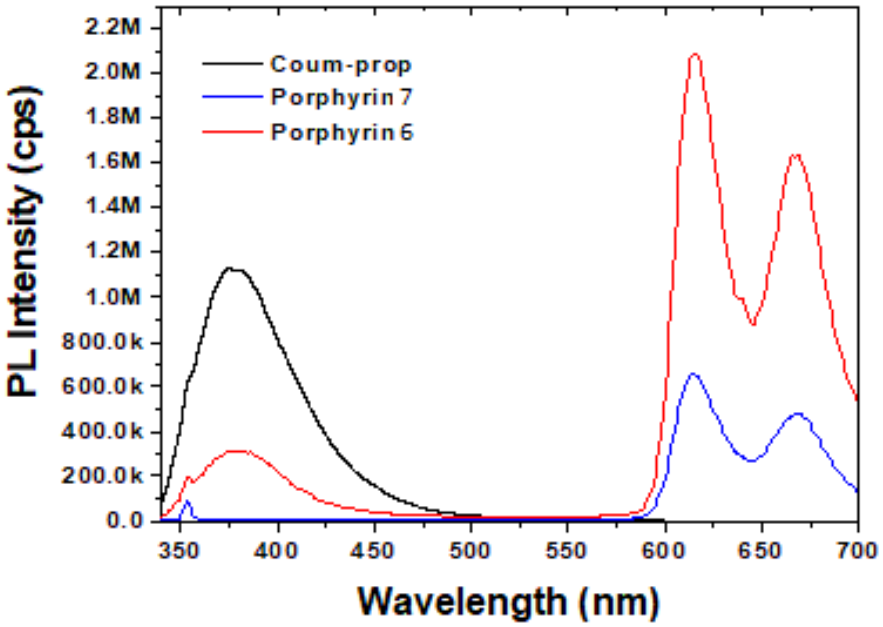


Figure 35. Emission spectra of **Coum-prop (**2×10^{-5} M, black)**,** porphyrin **6** (5×10^{-6} M, red), and porphyrin **7** (5×10^{-6} M,blue), in DMSO (λ_{ex} = 320 nm).

III.3 Singlet oxygen ($^1O_2$) generation

In view of PDT applications , we first evaluated the ability of the porphyrins **5**,**6** and **7** to generate $^1O_2$ compared to the reference PS zinc (II) 5,10,15,20-*mes*-tetraphenylporphyrin (ZnTPP, $^1O_2$ quantum yield $\Phi\Delta$= 75% in DMF).[23] The 9,10-dimethylanthracene (DMA, λ_{max} = 379 nm) was used as $^1O_2$ quencher.

DMA and $^1O_2$ react through a [4+2] cycloaddition resulting in the formation of the corresponding 9, 10-endoperoxide. Therefore, by following the decrease of the absorption at $\lambda = 379$ nm, the $^1O_2$ generation can be monitored. Plots of $\ln(A_0/A)$ *vs*. irradiation time are depicted in **Figure 36** (A_0 and A were measured at λ = 379 nm). These plots are linear and consistent with first order kinetics and show that porphyrins **5-7** and **ZnTTP** are able to photooxidize DMA upon irradiation with green light (λ_{exc} = 525 nm). Both porphyrins **5** and **7** are slightly less efficient PS compared to **ZnTPP** because their efficiency to generate $^1O_2$ are ~87% and ~72% of **ZnTPP**, respectively. On the contrary, porphyrin **6** with coumarin moieties seems to be more efficient (~1.2 times better compared to **ZnTPP**) to generate $^1O_2$.

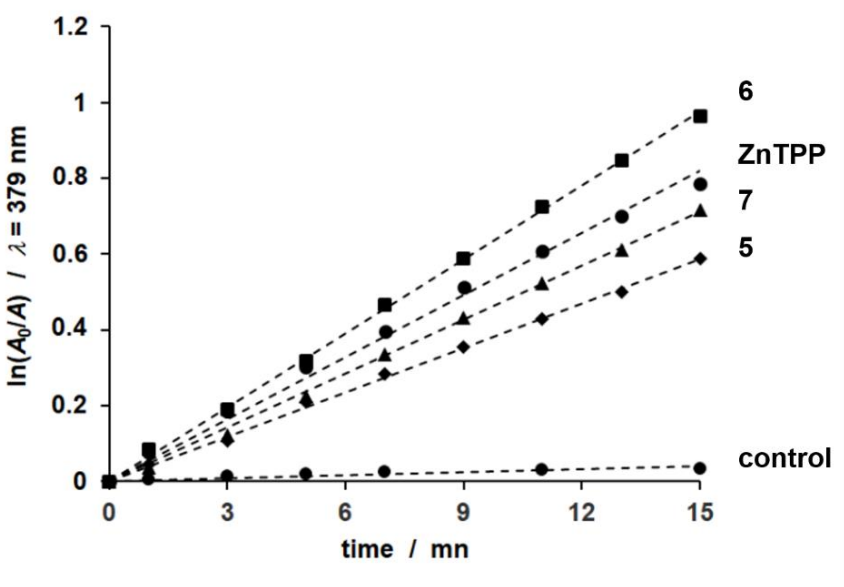


Figure 36. Time dependent photodecomposition of DMA photosensitized by porphyrins **5**, **6**, **7** and **ZnTPP** (final concentration of porphyrins and DMA are 0.25 and 100 µM in anhydrous DMF, respectively) upon irradiation with green light (λ_{exc} = 525 nm, led irradiation). Control experiment was performed without porphyrin.

III.4 Carbonic anhydrase inhibition assays

The newly synthesized molecules **4**-**7** were then evaluated for their CA-inhibitory activities against four clinically relevant human isoforms, that is the two cytosolic off-targets hCA I and hCA II as well as the two tumor-associated membrane bound hCA IX and hCA XII (**Table 6**), by using a stopped-flow assay method.

As expected, the two negative controls **4** and **7**, which do not harbored pharmacophoric scaffold able to inhibit CA, were not active on the four tested isoforms (K_I>50000 nM). The tetra-phenylsulfonamide based porphyrin **5** exhibited nanomolar activity against the four isoforms, with inhibition constants ranging from 16.9 to 98.7 nM. Moreover, **5** showed to be more effective than clinically used acetazolamide AAZ against hCA I (K_I = 98.7 vs 250 nM).

The tetra-coumarin based porphyrin **6** was found to be hCA IX and hCA XII selective with inhibition constant K_I = 652.1 and 92.4 nM respectively compared to the cytosolic hCA I and hCA II (K_I>50000 nM). The selectivity against the tumors-associated isoforms can be explained by the hydrolysis of the coumarin scaffolds in substituted 2-hydroxycinnamic acid form, which bind at the entrance of the active site, this region being the most variable region among the different human isoforms.[24]

Cmpds	K_i (nM)[a]			
	hCA I	hCA II	hCA IX	hCA XII
4	>50000	>50000	>50000	>50000
5	98.7	35.5	48.6	16.9
6	>50000	>50000	652.1	92.4
7	>50000	>50000	>50000	>50000
AAZ	250	12	25	5.7

Table 6. Inhibitory activity of compounds **4**-**7** against **hCA I**, **hCA II**, **hCA IX** and **hCA XII** using acetazolamide **AAZ** as reference drug. **[a]** Mean from 3 different measurements by a stopped flow technique (errors were in the range of ± 5-10 % of the reported values).

III.5 Biological assays

As zinc porphyrins were grafted with inhibitors of CA, we have studied their properties to inhibit the proliferation of Capan-1 cells, human pancreatic cancer cells strongly aggressive and known to express high level of CAs even in normoxic conditions as those used for cell culture conditions.[25-26] For this, Capan-1 cells were incubated three days with increasing concentrations of zinc porphyrins, and at the end of the incubation time, a colorimetric assay (MTT test) was performed to determine the

ratio of living cells in comparison with control. **Figure 37** shows that porphyrin **6** exhibited the higher efficiency to inhibit cancer cells proliferation with a LC_{50} ~ 4.5 µM. The two others porphyrins **5** and **7** are less cytotoxic with a LC_{50} ~ 11.2 µM.

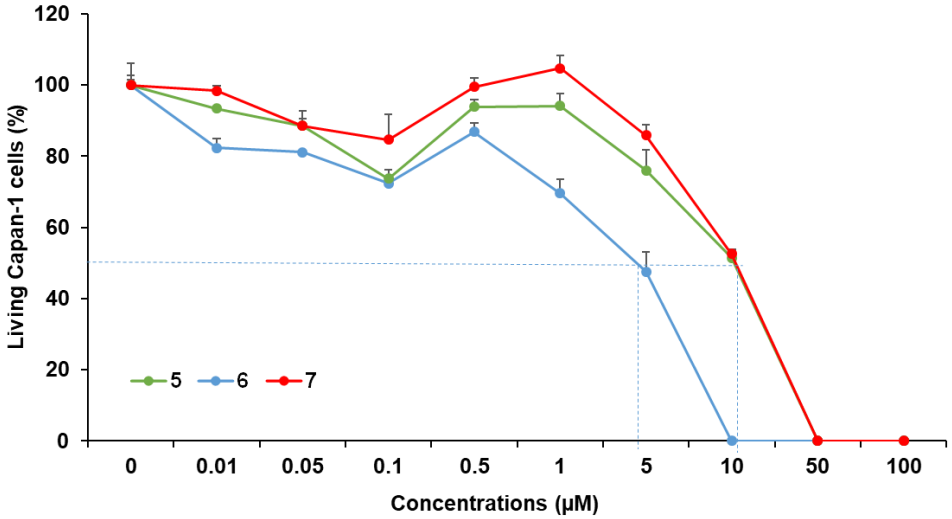


Figure 37. Cytotoxic study of compounds incubated at increasing concentrations (from 0.01 to 100 µM) with Capan-1 cells for 72 h. Values are means ± SD of three experiments.

These data highlight the interest to inhibit CAs expressed at the cell membrane to impair the proliferation of pancreatic cancer. Thanks to the photophysical properties of zinc porphyrins and their luminescence, we studied their localization in the Capan-1 cells to determine if they could act at the membrane of the cancer cells. For this, we performed imaging analyses using confocal microscope and **Figure 38** shows that porphyrin **5** is located inside the cell and also, outside stuck to the cell membrane and porphyrin **6** are clearly concentrated at the membrane of cells, while the aggregation of porphyrin **7** in aqueous medium, prevents the determining of its localization. As already shown in **Table 6**, these data are in accordance with expected results since sulfonamide presents in porphyrin **5** targets cytosolic hCA I and hCA II as well as membrane-associated hCA IX and hCA XII and coumarin grafted to porphyrin core **6** is specific of CA IX and CA XII exclusively localized on the cell membrane.

PDT efficiency was then studied in order to Know if these molecules could act (i) as inhibitors of CAs and inhibitors of cancer cells proliferation and also, (ii) as efficient photosensitizers to kill cancer cells under light irradiation. PDT experiments were performed by incubating 24h Capan-1 cells with 10 µM of porphyrin **5**, **6** and **7** and irradiate the with green light (λ_{exc} = 540 nm, 15 min, 34 J cm^{-2}).

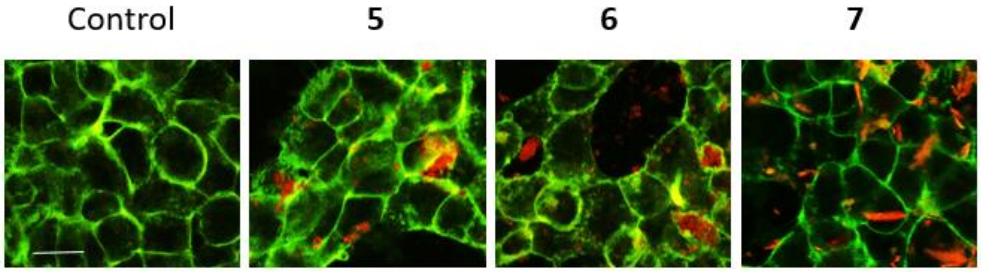


Figure 38. Fluorescence imaging of pancreas cancer cells (Capan-1) incubated for 24 h with or without (Control) compounds at 10 µM. Cells were imaged with confocal microscope LSM880 Fast Airyscan (7% power). Cell membranes were stained with CellMask and revealed under λ_{exc} = 561 nm (green) and porphyrins **5**, **6** and **7** appeared in red (λ_{exc} = 488 nm). Scale bar:10 µm.

Figure 39 shows that all zinc-porphyrins are efficient for PDT on Capan-1 cells when irradiated at 540 nm. The fact that porphyrin grafted with a small molecule does not reduce the PDT effect is a crucial point. Indeed, it's not rare that a very efficient porphyrin lost its PDT potential when grafted with a molecule in order to bring a dual effect.[27] In addition, porphyrin **6** was as efficient as porphyrin **7** and because porphyrin **6** is targeted on CA IX and CA XII, this suggests a biomedical application for this compound for cancer treatment by impairing cancer cell proliferation and killing them by PDT. Importantly, the accumulation of porphyrin **6** at cell membrane do not impair the PDT efficiency as already demonstrated.[28]

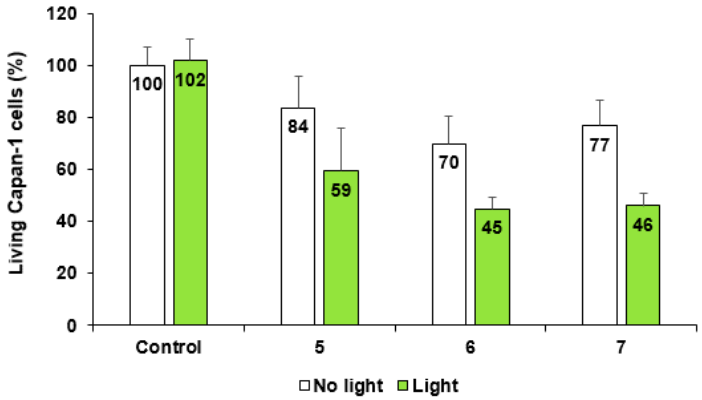


Figure 39. Analysis of PDT efficiency. Capan-1 cells were incubated 24 h with compounds at 10 µM and submitted or not to light irradiation (λ_{exc} = 540 nm, 15 min, 34 J.cm^{-2}). Values are means ± SD of three experiments.

III.6 Conclusion

This work describes for the first time the preparation of zinc porphyrin tetrafunctionalized with carbonic anhydrase inhibitors in sulfonamide or coumarin series. The synthesis was achieved in a four steps procedure consisting in the preparation of the key azido porphyrin platform **4** which was then coupled with two types of inhibitors using copper(I)-catalyzed azide alkyne cycloaddition methodology.

This study shows the advantageous combination of a photosensitizer and selective carbonic anhydrase inhibitors without losing photosensitizing efficiency. More specifically, introduction of specific membrane-bound CA IX / CA XII inhibitors such as coumarin, confers the porphyrin with the possibility to specifically target pancreatic cancer cell membrane and to impair cell proliferation at low micromolar range. Moreover, the efficient photosensitizing properties make this hybrid molecule **6** a potential good candidate for photodynamic therapy. Perform tests on integrated models such as small animals bearing human pancreatic tumors will be the next step to confirm this hypothesis.

III.7 Experimental Section

Full details, including starting material synthesis procedures, supporting spectra, CA inhibition assay procedure and biological assay procedures can be found in the Supporting Information.

4-[2-[2-(2-Azidoethoxy)ethoxy]ethoxy]benzaldehyde 2: a mixture of 4-hydroxybenzaldehyde (2 g, 16.39 mmol, 1 equiv), compound 1 (6.19 g, 18.84 mmol 1.25 equiv) and Cs_2CO_3 (0.41 g, 17.96 mmol, 1.09 equiv) in acetonitrile (90 mL) was prepared and stirred at reflux for about 16 hours until the reaction was complete. After evaporation of acetonitrile, dichloromethane was added and the mixture was washed with water. The organic phase was dried over anhydrous $MgSO_4$, filtered and evaporated to dryness. The residue was subjected to silica gel column chromatography (eluent: cyclohexane/ethyl acetate 60:40) to obtain compound 2 (3.45 g, 75 %). **^{1}H NMR** (400 MHz, $CDCl_3$) δ 9.80 (s, 1H, CHO), 7.75 (d, $^3J_{H-H}$ = 8.8 Hz, 2H, Ar), 6.95 (d, $^3J_{H-H}$ = 8.8 Hz, 2H, Ar), 4,16 (t, $^3J_{H-H}$ = 4,7 Hz, 2H), 3.84 (t, $^3J_{H-H}$ = 4,7 Hz, 2H, CH_2), 3.71 – 3.66 (m, 2H, CH_2), 3.64 – 3.59 (m, 4H, CH_2), 3,32 (t, $^3J_{H-H}$ = 5,0 Hz, 2H, CH_2). **^{13}C{^{1}H}NMR** (126 MHz, $CDCl_3$) δ 190.5, 163.9, 132.0, 130.1, 114.9, 71.0, 70.8, 70.1, 69.6, 67.8, 50.7. **ATR-FTIR**: $\tilde{\nu}$(cm^{-1}) = 2094 (ν_{N3}). **HRMS (ESI$^+$) m/z** calcd for $C_{13}H_{18}N_3O_4$ $[M+H]^+$ = 280.1292; found: 280.1294.

Porphyrin 3: Pyrrole (250 mg, 3.79 mmol, 1.05 equiv) and compound **2** (1 g, 3.58 mmol, 1 equiv) were dissolved in 200 mL of freshly distilled dichloromethane in a dried 1000 mL three-necked round-bottom flask that was protected from light with aluminium foil. The solution was degassed with argon

for 10 min and TFA (0.273 mL, 1.49 mmol, 1 equiv) was added dropwise into the flask. The solution was stirred for 4 h at room temperature. Then, DDQ (610 mg, 2.69 mmol, 0.75 equiv) was added and the mixture was stirred for one hour. Finally, triethylamine (0.485 mL 3.47mmol, 1 equiv) was added to the dark mixture, which was stirred for 15 minutes. The solvent was removed under reduced pressure and the dark residue was purified on alumina column chromatography using CH_2Cl_2/MeOH 95:5, as eluent. The residue was purified as second time on silica gel column of chromatography using the same eluent.

Porphyrin 3 was obtained as purple crystals (330 mg, 7%).**^{1}H NMR** (400 MHz, CDCl3) δ 8.85 (s, 8H, β-pyrr), 8.11 (d, $^3J_{H-H}$ = 8.6 Hz, 8H, Ar), 7.30 (d, $^3J_{H-H}$ = 8.6 Hz, 8H, Ar), 4.43 (t, $^3J_{H-H}$ = 4.8 Hz, 8H, CH_2), 4.07 (t, $^3J_{H-H}$ = 4.8 Hz, 8H, CH_2), 3.93 – 3.86 (m, 8H, CH_2), 3.84 – 3.75 (m, 16H, CH_2), 3.47 (t, $^3J_{H-H}$ = 5.0 Hz, 8H, CH_2), -2.76 (s, 2H, NH). $^{13}C\{^1H\}$ NMR (126 MHz, $CDCl_3$) δ 158.7, 135.7, 134.9, 119.9, 112.9, 71.1, 71.0, 70.7, 70.3, 67.8, 50.9. ATR-FTIR : $\tilde{\nu}$(cm-^{1}) = 2095 (ν_{N3}). **HRMS (ESI+) m/z** calcd for $C_{68}H_{75}N_{16}O_{12}$ $[M+H]^+$ = 1307.5745 found 1307.5730. **UV-Vis** (DMSO): λ_{max}(log ε): 421 (5.28), 519 (4.38), 553 (3.97), 593 (3.70), 651 (3.65).

Porphyrin 4: Porphyrin 3 (250 mg, 0.19 mmol, 1equiv) was dissolved in $CHCl_3$ (30 mL). A solution of $Zn(OAc)_2.2H_2O$ (45 mg, 0.228 mmol, 1.2 equiv) in methanol (3 mL) was prepared and added to the solution of porphyrin **3** in $CHCl_3$. After stirring overnight at room temperature under inert atmosphere, the solvent was evaporated to give compound **4** (230 mg, 88%) as a purple solid. **^{1}H NMR** (400 MHz, $CDCl_3$) δ 8.96 (s, 8H, β-pyrr), 8.11 (d, $^3J_{H-H}$ = 8.6 Hz, 8H, Ar), 7.30 (d, $^3J_{H-H}$ = 8.6 Hz, 8H, Ar), 4.44 (t, $^3J_{H-H}$ = 4.7 Hz, 8H, CH_2), 4.07 (t, $^3J_{H-H}$ = 4.7 Hz, 8H), 3.91 – 3.86 (m, 8H, CH_2), 3.82 – 3.75 (m, 16H, CH_2), 3.45 (t, $^3J_{H-H}$ = 5,0 Hz, 8H, CH2). **$^{13}C\{^1H\}$ NMR** (126 MHz, $CDCl_3$) δ 158.6, 135.8, 135.5, 132.0, 120.8, 119.9, 71.1, 70.9, 70.2, 70.1, 67.8, 50.8. **ATR-FTIR**: $\tilde{\nu}$(cm^{-1}) = 2094 (ν_{N3}). **HRMS (ESI)** m/z calcd for $C_{68}H_{73}N_{16}O_{12}Zn$ $[M+H]^+$= 1369.4880; found 1368.4873. **UV-Vis** (DMSO): λ_{max}(log ε): 421(5.82), 551(4.38), 590(4.06).

General procedure for the azide-alkyne Huisgen cycloaddition: In a 50 mL two-necked round-bottom flask, porphyrin **4** (0.050 g, 0.0365 mmol, 1 equiv) and the corresponding alkyne (6 equiv) were dissolved in THF (10 mL). In a Schlenk tube, $CuSO_4.5H_2O$ (0.547 g, 0.219 mmol, 6 equiv) and sodium ascorbate (0.434 g, 0.219 mmol, 1 equiv) were dissolved in H_2O (5 mL) and this mixture was added to the solution of porphyrin **4** and alkyne in THF. The reaction was allowed to proceed for 48 hours at room temperature under argon. The mixture was then diluted with dichloromethane and washed with water. The organic layer was dried over anhydrous $MgSO_4$, filtered and evaporated under vacuum. The residue was then dissolved in 10 mL of a solution of $CHCl_3$ and then, washed with an aqueous solution

of EDTA (0.1 M) (3 x 10 mL). The organic layer was dried under $MgSO_4$ and then, the solvent was removed under reduced pressure to give the expected compound.

Compound 5: yield: 25%; **^{1}H NMR** (400 MHz, DMSO-d_6) δ 8.79 (s, 8H), 8.32 (s, 4H), 8.06 (d, $^3J_{H-H}$ = 8.3 Hz, 8H), 7.74 (d, $^3J_{H-H}$ = 8.8 Hz, 4H), 7.33 (d, $^3J_{H-H}$ = 8.3 Hz, 8H), 7.24 – 7.18 (m, 16H), 5.26 (s, 8H), 4.62 (t, $^3J_{H-H}$ = 5.1 Hz, 8H), 4.36 (s, 8H), 3.91 (m, 16H), 3.68 (d, $^3J_{H-H}$ = 4.1 Hz, 16H). **^{13}C{^{1}H} NMR** (126 MHz, $CDCl_3$) δ 160.4, 158.0, 149.5, 142.0, 136.5, 135.2, 135.1, 131.1, 127.6, 125.2, 119.9, 114.8, 112.6, 69.9, 69.7, 69.1, 68.8, 67.4, 61.4, 49.5. **HRMS (ESI$^+$) m/z** calcd for $C_{104}H_{110}N_{20}O_{24}S_4Zn$ $[M+2H]^{2+}$ = 1107.3083, found 1107.3064. **UV-Vis** (DMSO): λ_{max}(log ε): 431(7.3), 562(4.16), 605(4.04).

Compound 6: yield: 24%; **^{1}H NMR** (400 MHz, $CDCl_3$) δ 8.86 (s, 8H), 8.06 (d, $^3J_{H-H}$ = 8.1 Hz, 8H), 7.77 (s, 4H), 7.21 (d, $^3J_{H-H}$ = 8.1 Hz, 8H), 7.10 (d, $^3J_{H-H}$ = 8.5 Hz, 4H), 6.67 (m, 8H), 5.69 (s, 4H), 4.89 (s, 8H), 4.48 (s, 8H), 4.32 (s, 8H), 3.91 (s, 8H), 3.85 (s, 8H), 3.71 (s, 8H), 3.63 (s, 8H), 1.97 (s, 12H). **^{13}C{^{1}H} NMR** (126 MHz, $CDCl_3$: δ 161.1, 160.9, 158.4, 154.8, 152.3, 150.4, 142.6, 136.0, 135.8, 131.8, 125.5, 124.4, 120.4, 113.7, 112.8, 112.4, 111.9, 102.0, 70.8, 70.8, 70.0, 69.5, 67.8, 53.6, 50.5, 18.4 **HRMS (ESI$^+$) m/z** calcd for $C_{120}H_{114}N_{16}O_{24}Zn$ $[M+2H]^{2+}$ = 1113.3736, found 1113.3704; **UV-Vis** (DMSO): λ_{max}(log ε): 431(6.3), 562(4.38), 605(4.06).

Compound 7: yield: 64%; **^{1}H NMR** (400 MHz, $CDCl_3$) δ 8.79 (s, 8 H), 8.06 (d, $^3J_{H-H}$ = 8.5 Hz, 8H), 7.89 (s, 4H), 7.34 (d, $^3J_{H-H}$ = 8.5 Hz, 8H), 4.53 (t, $^3J_{H-H}$ = 5.2 Hz, 8H), 4.40 – 4.29 (m, 8H), 3.89 (q, 3JH-H = 5.1 Hz, 16H), 3.73 – 3.62 (m, 16H), 2.63 (t, $^3J_{H-H}$ = 7.4 Hz, 8H), 1.59 (quint, $^3J_{H-H}$ = 7.4 Hz, 8H), 1.32 (sx, $^3J_{H-H}$ = 7.4 Hz, 8H), 0.88 (t, $^3J_{H-H}$ = 7.4 Hz, 12H). **^{13}C{^{1}H} NMR** (126 MHz, $CDCl_3$) δ 148.1, 131.8, 127.8, 121.8, 114.7, 112.7, 71.0, 70.8, 70.7, 70.0, 69.9, 69.7, 67.8, 50.2, 31.8, 31.8, 25.1, 22.4, 14.0. **HRMS (ESI) m/z** calcd for $C_{92}H_{113}N_{16}O_{12}Zn$ $[M+H]^+$ = 1697.8010, found 1696.8014; **UV-Vis** (DMSO): λ_{max}(log ε): 431(5.41), 562(4.37), 605(3.93).

IV. References

1. Dagogo-Jack, I.; Shaw, A. T., Tumour heterogeneity and resistance to cancer therapies. *Nature reviews Clinical oncology* **2018,** *15* (2), 81-94.

2. Gillies, R. J., Cancer heterogeneity and metastasis: life at the edge. *Clinical & Experimental Metastasis* **2022,** *39* (1), 15-19.

3. Harris, A. L., Hypoxia—a key regulatory factor in tumour growth. *Nature reviews cancer* **2002,** *2* (1), 38-47.

4. Jing, X.; Yang, F.; Shao, C.; Wei, K.; Xie, M.; Shen, H.; Shu, Y., Role of hypoxia in cancer therapy by regulating the tumor microenvironment. *Molecular cancer* **2019,** *18*, 1-15.

5. Chilakamarthi, U.; Giribabu, L., Photodynamic therapy: past, present and future. *The Chemical Record* **2017,** *17* (8), 775-802.

6. Zhao, X.; Liu, J.; Fan, J.; Chao, H.; Peng, X., Recent progress in photosensitizers for overcoming the challenges of photodynamic therapy: from molecular design to application. *Chemical Society Reviews* **2021,** *50* (6), 4185-4219.

7. Pham, T. C.; Nguyen, V.-N.; Choi, Y.; Lee, S.; Yoon, J., Recent strategies to develop innovative photosensitizers for enhanced photodynamic therapy. *Chemical Reviews* **2021,** *121* (21), 13454-13619.

8. Wan, Y.; Fu, L. H.; Li, C.; Lin, J.; Huang, P., Conquering the hypoxia limitation for photodynamic therapy. *Advanced Materials* **2021,** *33* (48), 2103978.

9. Li, G.; Wang, Q.; Liu, J.; Wu, M.; Ji, H.; Qin, Y.; Zhou, X.; Wu, L., Innovative strategies for enhanced tumor photodynamic therapy. *Journal of Materials Chemistry B* **2021,** *9* (36), 7347-7370.

10. Hu, T.; Wang, Z.; Shen, W.; Liang, R.; Yan, D.; Wei, M., Recent advances in innovative strategies for enhanced cancer photodynamic therapy. *Theranostics* **2021,** *11* (7), 3278.

11. Pucelik, B.; Sułek, A.; Barzowska, A.; Dąbrowski, J. M., Recent advances in strategies for overcoming hypoxia in photodynamic therapy of cancer. *Cancer Letters* **2020,** *492*, 116-135.

12. Jung, H. S.; Han, J.; Shi, H.; Koo, S.; Singh, H.; Kim, H.-J.; Sessler, J. L.; Lee, J. Y.; Kim, J.-H.; Kim, J. S., Overcoming the limits of hypoxia in photodynamic therapy: a carbonic anhydrase IX-targeted approach. *Journal of the American Chemical Society* **2017,** *139* (22), 7595-7602.

13. Zhu, W.; Liu, Y.; Yang, Z.; Zhang, L.; Xiao, L.; Liu, P.; Wang, J.; Yi, C.; Xu, Z.; Ren, J., Albumin/sulfonamide stabilized iron porphyrin metal organic framework nanocomposites: targeting tumor hypoxia by carbonic anhydrase IX inhibition and T1–T2 dual mode MRI guided photodynamic/photothermal therapy. *Journal of Materials Chemistry B* **2018,** *6* (2), 265-276.

14. Jiang, Y.; Li, J.; Zeng, Z.; Xie, C.; Lyu, Y.; Pu, K., Organic photodynamic nanoinhibitor for synergistic cancer therapy. *Angewandte Chemie International Edition* **2019,** *58* (24), 8161-8165.

15. Angeli, A.; Carta, F.; Nocentini, A.; Winum, J.-Y.; Zalubovskis, R.; Akdemir, A.; Onnis, V.; Eldehna, W. M.; Capasso, C.; Simone, G. D., Carbonic anhydrase inhibitors targeting metabolism and tumor microenvironment. *Metabolites* **2020,** *10* (10), 412.

16. Supuran, C. T., Experimental carbonic anhydrase inhibitors for the treatment of hypoxic tumors. *Journal of Experimental Pharmacology* **2020**, 603-617.

17. Carta, F.; Dumy, P.; Supuran, C. T.; Winum, J.-Y., Multivalent carbonic anhydrases inhibitors. *International Journal of Molecular Sciences* **2019,** *20* (21), 5352.

18. Lieber, E.; Rao, C.; Thomas, A.; Oftedahl, E.; Minnis, R.; Nambury, C., Infrared spectra of acid azides, carbamyl azides and other azido derivatives: Anomalous splittings of the N3 stretching bands. *Spectrochimica Acta* **1963,** *19* (7), 1135-1144.

19. Singh, D. K.; Nath, M., Synthesis and photophysical properties of β-triazole bridged porphyrin–coumarin dyads. *RSC advances* **2015,** *5* (83), 68209-68217.

20. Cheng, F.; Wang, H.-H.; Kandhadi, J.; Zhao, F.; Zhang, L.; Ali, A.; Wang, H.; Liu, H.-Y., Porphyrin–Coumarin Dyads: Investigation of Photophysical Properties and DNA Interactions. *The Journal of Physical Chemistry B* **2018,** *122* (32), 7797-7810.

21. Hecht, S.; Vladimirov, N.; Fréchet, J. M. J., Encapsulation of Functional Moieties within Branched Star Polymers: Effect of Chain Length and Solvent on Site Isolation. *Journal of the American Chemical Society* **2001,** *123* (1), 18-25.

22. Cerqueira, A. F. R.; Almodôvar, V. A. S.; Neves, M. G. P. M. S.; Tomé, A. C. Coumarin–Tetrapyrrolic Macrocycle Conjugates: Synthesis and Applications *Molecules* [Online], 2017.

23. Röder, B.; Büchner, M.; Rückmann, I.; Senge, M. O., Correlation of photophysical parameters with macrocycle distortion in porphyrins with graded degree of saddle distortion. *Photochemical & Photobiological Sciences* **2010,** *9* (8), 1152-1158.

24. Supuran, C. T., Exploring the multiple binding modes of inhibitors to carbonic anhydrases for novel drug discovery. *Expert Opinion on Drug Discovery* **2020,** *15* (6), 671-686.

25. Fanjul, M.; Alvarez, L.; Hollande, E., Expression and subcellular localization of a 35-kDa carbonic anhydrase IV in a human pancreatic ductal cell line (Capan-1). *Journal of Histochemistry & Cytochemistry* **2007**, 55 (8), 783-794.

26. Xu, P.-l.; Cheng, C.-s.; Jiao, J.-y.; Chen, H.; Chen, Z.; Li, P., Matrine injection inhibits pancreatic cancer growth via modulating carbonic anhydrases- a network pharmacology-based study with in vitro validation. Journal of Ethnopharmacology 2022, 287, 114691.

27. Toubia, I.; Nguyen, C.; Diring, S.; Pays, M.; Mattana, E.; Arnoux, P.; Frochot, C.; Gary-Bobo, M.; Kobeissi, M.; Odobel, F. Study of Cytotoxic and Photodynamic Activities of Dyads Composed of a Zinc Phthalocyanine Appended to an Organotin *Pharmaceuticals* [Online], 2021.

28. Su, X.; Wang, W. J.; Cao, Q.; Zhang, H.; Liu, B.; Ling, Y.; Zhou, X.; Mao, Z. W., A Carbonic Anhydrase IX (CAIX)-Anchored Rhenium (I) Photosensitizer Evokes Pyroptosis for Enhanced Anti-Tumor Immunity. *Angewandte Chemie* **2022,** *134* (8), e202115800.

Chapter III: Carbonic Anhydrase Featuring a Porphyrin Scaffold: Synthesis, Optical and Biological Properties

VI. Supplementary data

IV.1 Chemistry

IV.1.1 Materials

Reactions needing inert atmosphere were performed under argon using oven-dried glassware and Schlenk techniques. All solvents were obtained from commercial suppliers and used as received. 4-hydroxybenzaldehyde (TCI, 98%), caesium carbonate (Cs_2CO_3, Fluorochem, 99%), pyrrole (Fluorochem, 99%), tifluoroacetic acid (TFA, Alfa Aesar, 99%), 2,3-dichloro-5,6-dicyano-1,4-benzoquinone (DDQ, Acros Organics, 98%), triethylamine (Fluorochem, 99%), zinc(II) acetate dihydrate ($Zn(OAc)_2.2H_2O$, Sigma-Aldrich, >98%), copper (II) sulfate pentahydrate ($CuSO_4.5H_2O$, Fluorochem, 98%), sodium ascorbate (Fluorochem, 99%), Ethylenediaminetetraacetic acid disodium salt dihydrate EDTA (Sigma-Aldrich, 99%), hexyne (Sigma-Aldrich, 98%) were used as received. Compound **1**, **Sulfo-prop** and **Coum-prop** were prepared according to literature procedure.[1-2] TLC were carried out on Merck DC Kieselgel 60 F-254 aluminium sheets and spots were visualized with UV-lamp (λ = 254/365 nm) if necessary. Preparative purifications were performed by silica gel column chromatography (Merck 40–60 µM).

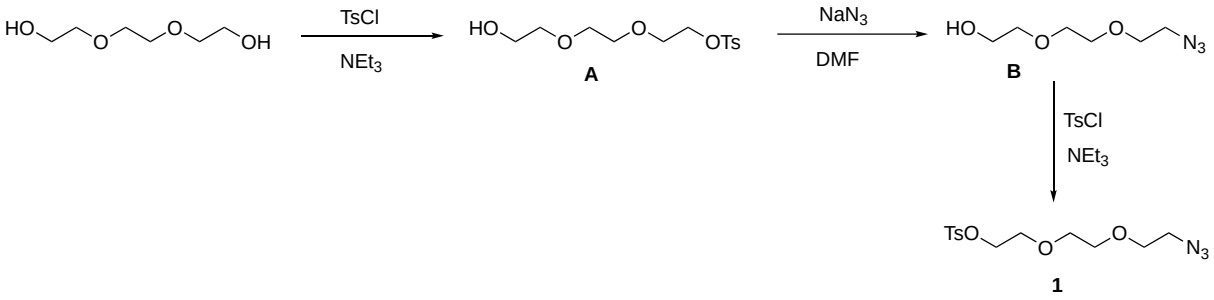
IV.1.2 Instruments and methods

NMR spectroscopy and MS spectrometry were performed at the Laboratoire de Mesures Physiques (LMP) of the University of Montpellier (UM). ^1H and $^{13}C\{^1H\}$ NMR spectra were recorded on Bruker 400 MHz Avance III HD and 500 MHz Avance III spectrometers at 298 K. Deuterated solvents DMSO-d_6, and $CDCl_3$ were used as received (purchased from Sigma-Aldrich). ^1H and $^{13}C\{^1H\}$ NMR spectra were calibrated to TMS on the basis of the relative chemical shift of the residual non-deuterated solvent as an internal standard. Chemical shifts (δ) are expressed in ppm and coupling constants values (nJ) are expressed in Hz. Abbreviations used for NMR spectra are as follows: s, singlet; d, doublet; t, triplet; q: quadruplet; quint, quintuplet; sx, sextuplet and m, multiplet. High Resolution Mass spectra (HRMS) were recorded on a Bruker MicroTof QII instrument in positive/negative modes (ESI). UV-Visible absorption spectra were recorded in DMSO with a JASCO V-750 UV-Visible-NIR spectrophotometer in 10 mm quartz cells (Hellma); molar extinction coefficients ε ($L.mol^{-1}.cm^{-1}$) are expressed as log ε. The extinction coefficients were determined by preparing solutions of porphyrin derivatives at different concentrations in DMSO. The concentration range was chosen to remain in the linear range of the Beer–Lambert relationship (A ca. 0.2–0.8). The emission spectra were recorded at 25°C on a fluorescence spectrophotometer (FS920, Edinburgh Instrument), equipped with a calibrated photomultiplier in a Peltier (air cooled) housing (R928P, Hamamatsu), with a 450 W continuous xenon

arc lamp as the excitation source for steadystate photoluminescence measurement using a 10 mm quartz cell (Hellma) with excitation path length.

IV.1.3 Synthesis

Synthesis of compound 1:



Scheme 3: Synthesis of compound **1**.

2-[2-(2-Hydroxyethoxy)ethoxy]ethyl 4-methylbenzenesulfonate (A)

Triethylene glycol (20 g, 133.2 mmol, 2 equiv.) and dry CH_2Cl_2 (150 mL) were added in a 500 mL two-necked round-bottom flask and then, NEt_3 (8.1 mL, 80.0 mmol, 1.2 equiv.) was added to the flask. The solution was cooled to -78°C followed by the portionwise addition of *p*-toluenesulfonyl chloride (12.7 g, 66.6 mmol, 1 equiv.). The solution was allowed to warm to room temperature and stirred for 16 hours. A white precipitate was then formed. The reaction mixture was washed with HCl (2M) (2 x 50 mL) and then, with brine (2 x 50 mL). The combined organic layers were dried over anhydrous $MgSO_4$ and concentrated under vacuum. The residue was purified by flash silica gel column chromatography (8/2, cyclohexane/ethyl acetate) to give compound **A** as a colorless oil (5.02 g, 25%). **^{1}H NMR** (400MHz, $CDCl_3$): δ 7.79 (d, $^3J_{H\text{-}H}$ = 8.2 Hz, 2H), 7.34 (d, $^3J_{H\text{-}H}$ = 8.0 Hz, 2H), 4.16 (t, 2H, $^3J_{H\text{-}H}$ = 4.8 Hz), 3.73 – 3.65 (m, 4H), 3.60 (s, 4H), 3.57 (t, 2H, $^3J_{H\text{-}H}$ = 4.8 Hz), 2.44 (s, 3H). **^{13}C{^{1}H} NMR** (126 MHz, $CDCl_3$) δ 144.8, 132.7, 129.7, 127.7, 72.3, 70.5, 70.0, 69.1, 68.4, 61.4, 21.4. **ATR-FTIR**: $\tilde{\nu}$ (cm^{-1}) = 3443 (ν_{OH})**. HRMS (ESI$^+$)** m/z calcd for $C_{13}H_{21}O_6S$ $[M+H]^+$ = 305.1059, found: $[M+H]^+$ = 305.1053.

2-(2-(2-azidoethoxy)ethoxy)ethanol (B)

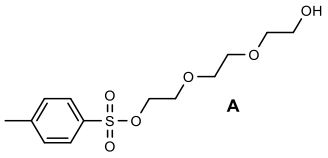
In a 100 mL two-necked round-bottom flask under inert atmosphere, compound **A** (13.65 g, 65.5 mmol, 1 equiv) and NaN_3 (7.34 g, 113.0 mmol, 2 equiv) were dissolved in DMF (40 mL). The reaction mixture was stirred for 24 h at 65°C. After cooling to room temperature, water (50 mL) was added and the

solution was extracted with ethyl acetate (2 x 100 mL). The organic layer was washed with water (2 x 100 mL) and cold brine (30 mL). The organic phase was then dried over anhydrous $MgSO_4$, filtered and evaporated under vacuum. The residue was then purified by flash silica gel chromatography (6/4 cyclohexane/ ethyl acetate) to give compound **B** (6.3 g, 64%). **^{1}H NMR** (400 MHz, $CDCl_3$) δ 3.65 (t, $^3J_{H-H}$ = 4,4 Hz, 2H), 3.61 (m, 6H), 3,53 (t, $^3J_{H-H}$ = 4.9 Hz, 2H), 3.33 (t, $^3J_{H-H}$ = 4.9 Hz, 2H), 2.86 (s, OH). **^{13}C{^{1}H} NMR** (126 MHz, $CDCl_3$) δ 72.4, 70.3, 70.1, 69.7, 61.3, 50.4. **ATR-FTIR**: $\tilde{\nu}$ (cm^{-1}) = 3400 (ν_{OH}), 2094 (ν_{N3}). **HRMS (ESI$^+$)** calcd for $C_6H_{13}N_3O_3$ $[M+H]^+$= 176.1035, found: $[M+H]^+$= 176.1030.

2-(2-(2-Azidoethoxy) ethoxy) ethyl 4-methylbenzenesulfonate (1)

Compound **B** (2.31 g, 13.2 mmol, 1 equiv) and dry CH_2Cl_2 (20 mL) were added to a two-necked round bottom flask and then, NEt_3 (3.67 mL, 26.4 mmol, 2 equiv) was added. The solution was cooled to -78°C followed by the portionwise addition of *p*-toluenesulfonyl chloride (3.76 g, 19.78 mmol, 2 equiv). The solution was allowed to warm to room temperature and stirred for 16 hours. The reaction mixture was then washed by HCl 2M (2 x 50 mL) and with brine (2 x 50 mL). The combined organic layers were then dried over anhydrous $MgSO_4$ and concentrated under vacuum. The residue was purified by flash silica gel chromatography (8/2, cyclohexane/ ethyl acetate) to give compound **1** as a colorless oil (6.3 g, 43%). **^{1}H NMR** (400 MHz, $CDCl_3$) δ 7.75 (d, $^3J_{H-H}$ = 8.1 Hz, 2H), 7.31 (d, $^3J_{H-H}$ = 8.1 Hz, 2H), 4.12 (t, $^3J_{H-H}$ = 4.8 Hz, 2H), 3.65 (t, $^3J_{H-H}$ = 4.8 Hz, 2H), 3.60 (t, $^3J_{H-H}$ = 5.0 Hz, 2H), 3.55 (s, 4H), 3.32 (t, $^3J_{H-H}$ = 5.0 Hz, 2H), 2.40 (s, 3H). **^{13}C{^{1}H} NMR** (151 MHz, $CDCl_3$) δ 144.8, 133.0, 129.8, 127.9, 70.7, 70.5, 70.0, 69.3, 68.7, 50.6, 21.6. **(ATR-FTIR)**: $\tilde{\nu}$ (cm^{-1}) = 2294 (ν_{N3}). **MS (ESI)** calcd for $C_{13}H_{19}N_3O_5S$ $[M+H]^+$ = 330.1124 found: $[M+H]^+$ = 330.1118.

IV.2 Characterization



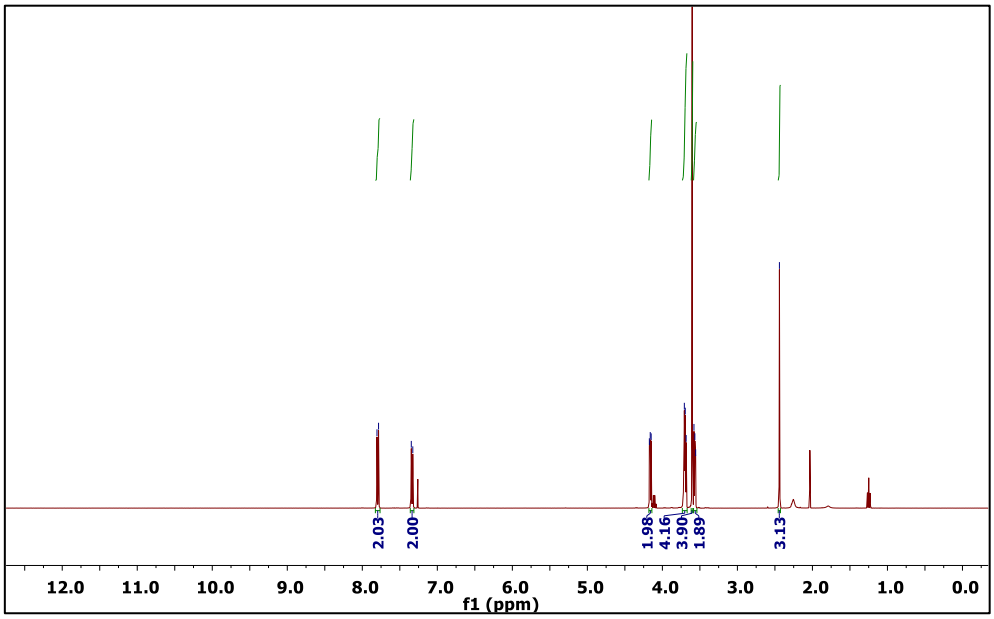


Figure 40. ^{1}H NMR spectrum (400 MHz, $CDCl_3$, 298K) of compound **(2-[2-(2-Hydroxyethoxy)ethoxy]ethyl 4-methylbenzenesulfonate) (A)**.

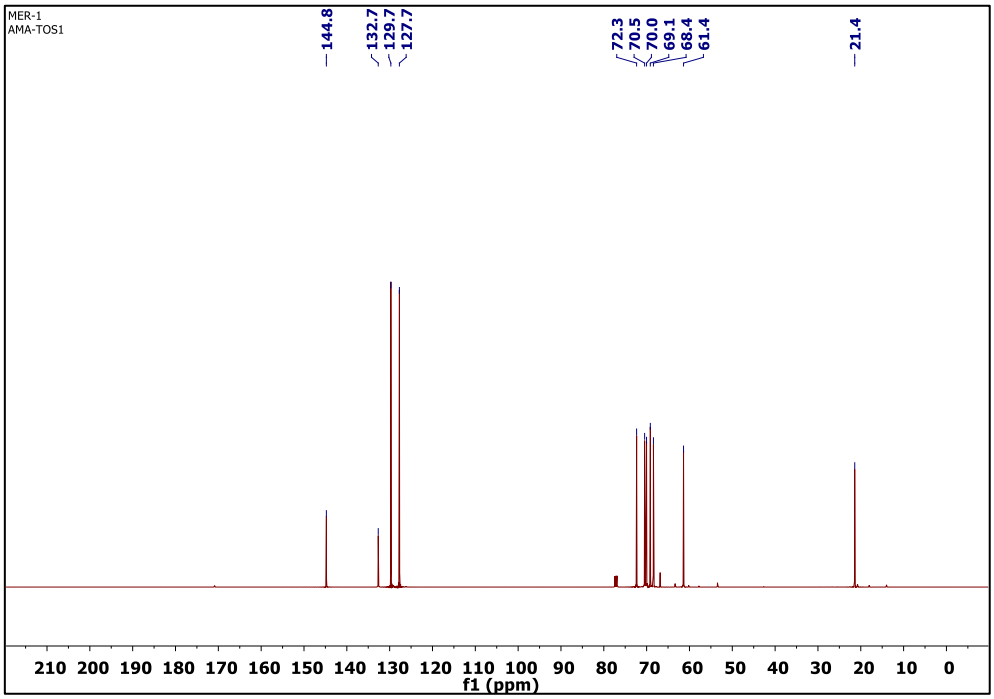


Figure 41. $^{13}C\{^{1}H\}$ NMR (126 MHz, $CDCl_3$, 298K) spectrum of compound **(2-[2-(2-Hydroxyethoxy)ethoxy]ethyl 4-methylbenzenesulfonate) (A)**.

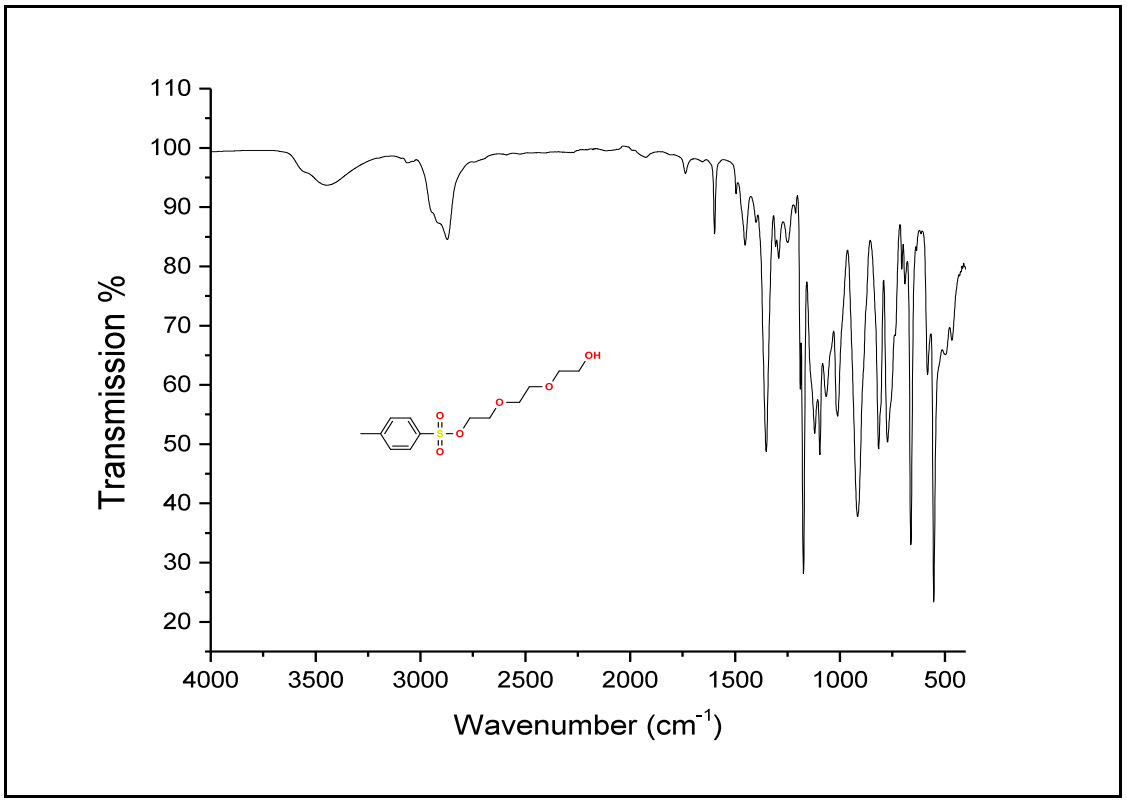


Figure 42. ATR-FTIR spectrum of compound **(2-[2-(2-Hydroxyethoxy)ethoxy]ethyl 4-methylbenzenesulfonate) (A).**

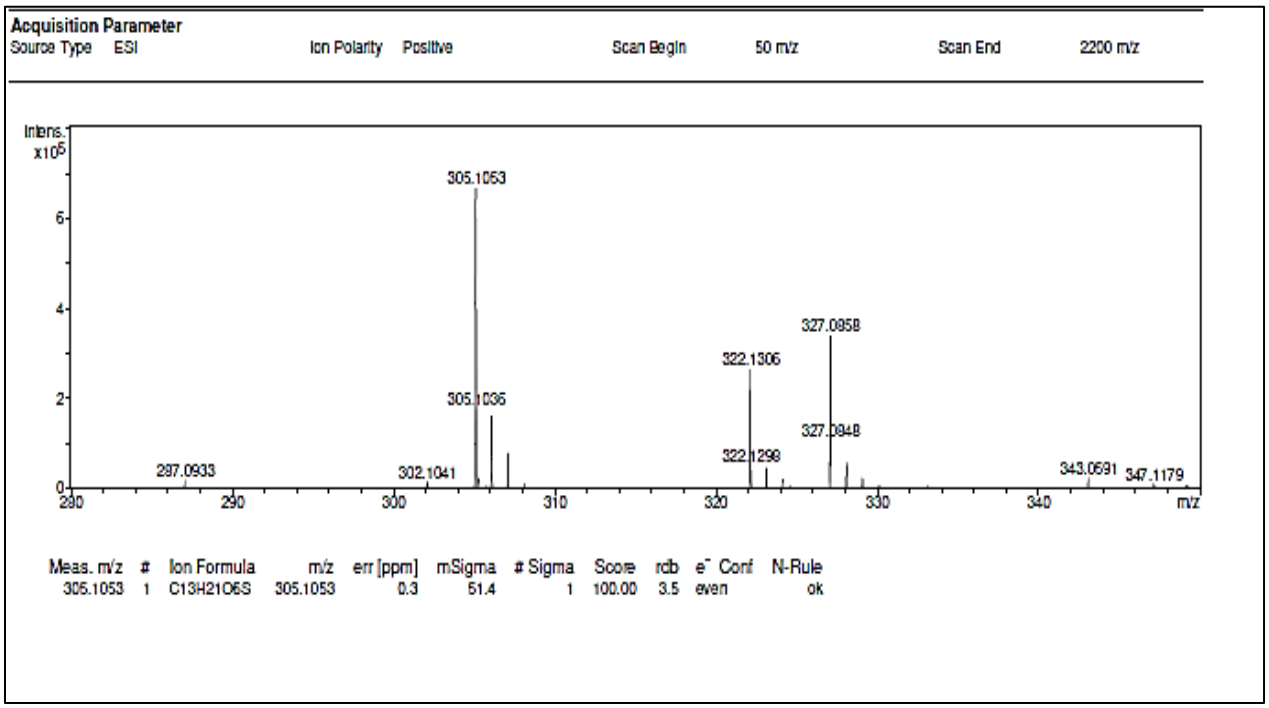


Figure 43. High resolution ESI-TOF (positive mode) mass spectrum of compound **(2-[2-(2-hydroxyethoxy)ethoxy]ethyl 4-methylbenzenesulfonate) (A).**

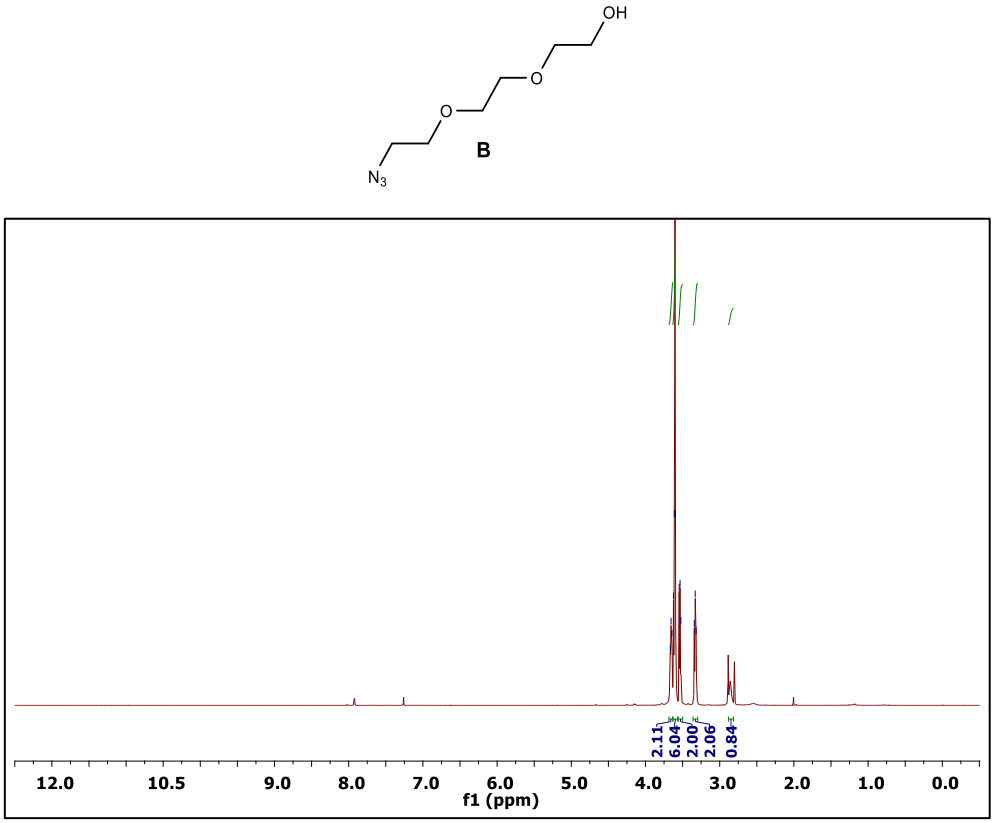


Figure 44. ^{1}H NMR spectrum (400 MHz, $CDCl_3$, 298K) of compound **2 (2-(2-(2-azidoethoxy)ethoxy)ethanol) (B).**

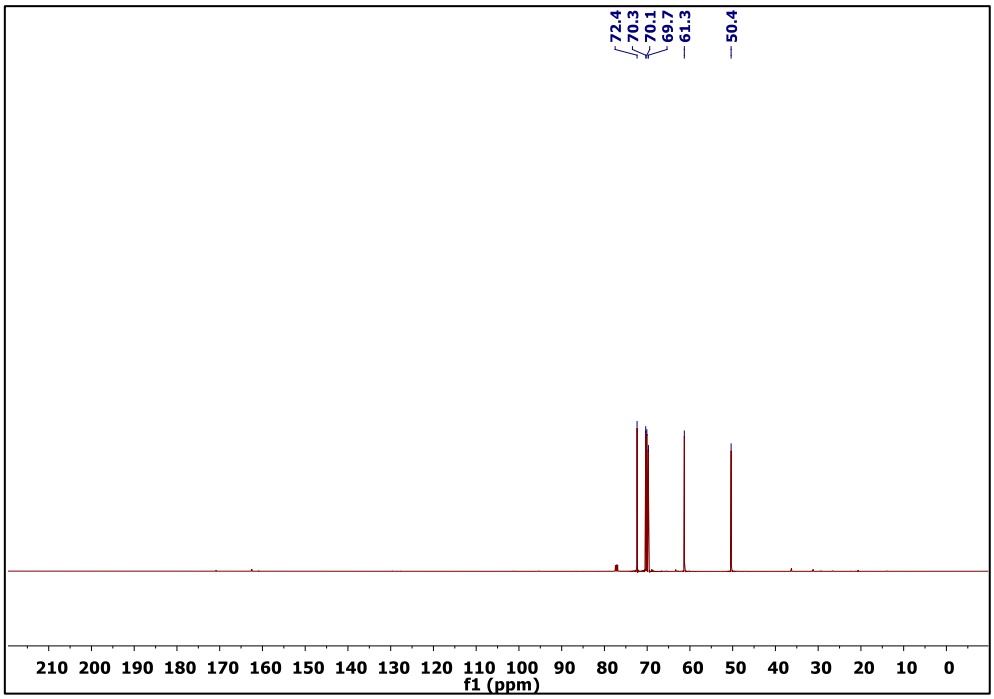


Figure 45. $^{13}C\{^{1}H\}$ NMR spectrum (126 MHz, $CDCl_3$, 298K) of compound **2 (2-(2-(2-azidoethoxy)ethoxy)ethanol) (B).**

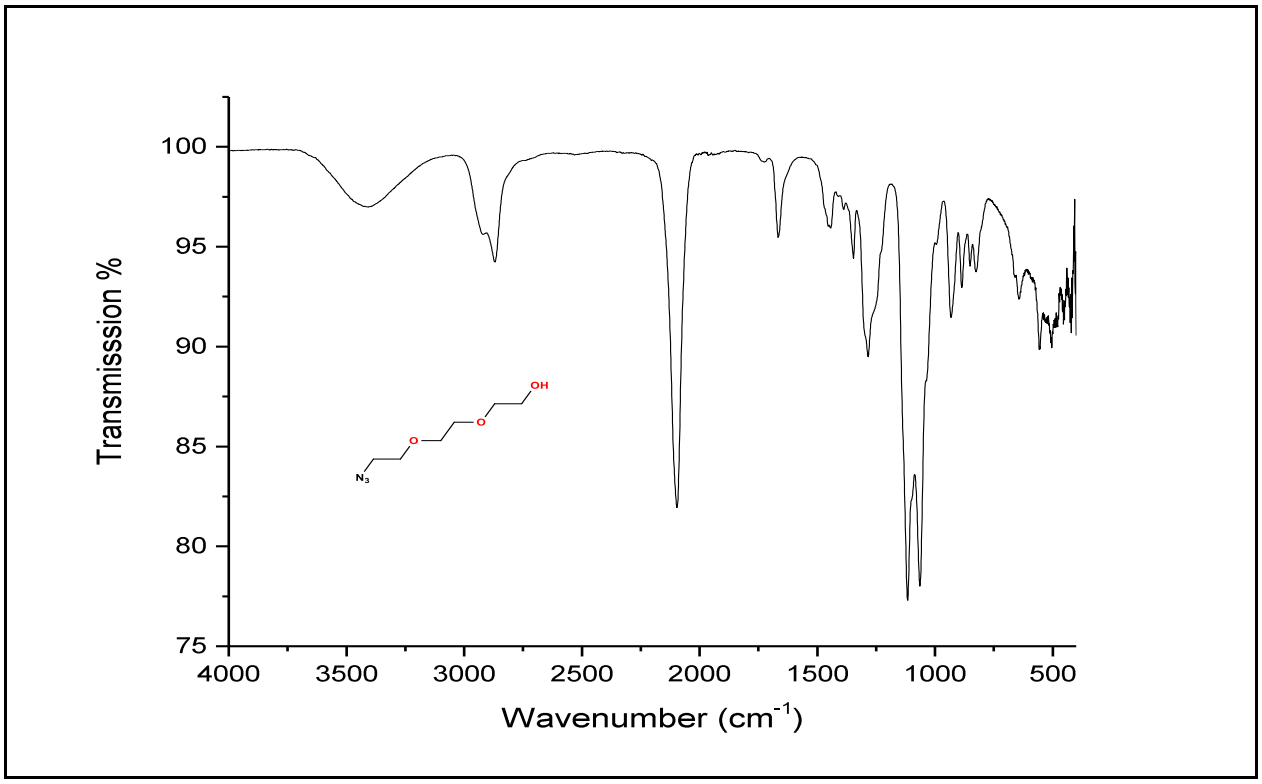


Figure 46. ATR-FTIR spectrum of compound **(2-(2-(2-azidoethoxy)ethoxy)ethanol) (B).**

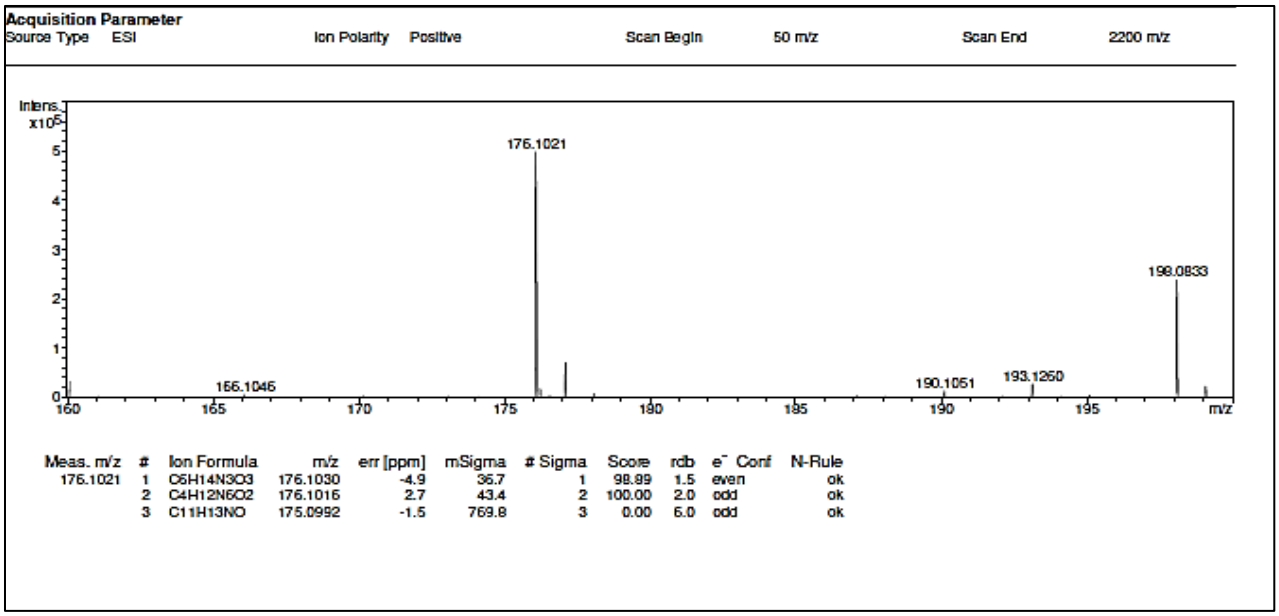
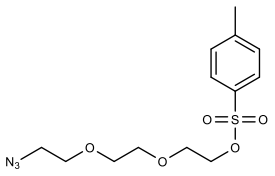


Figure 47. High resolution ESI-TOF (positive mode) mass spectrum of compound **(2-(2-(2-azidoethoxy)ethoxy)ethanol) (B).**



1

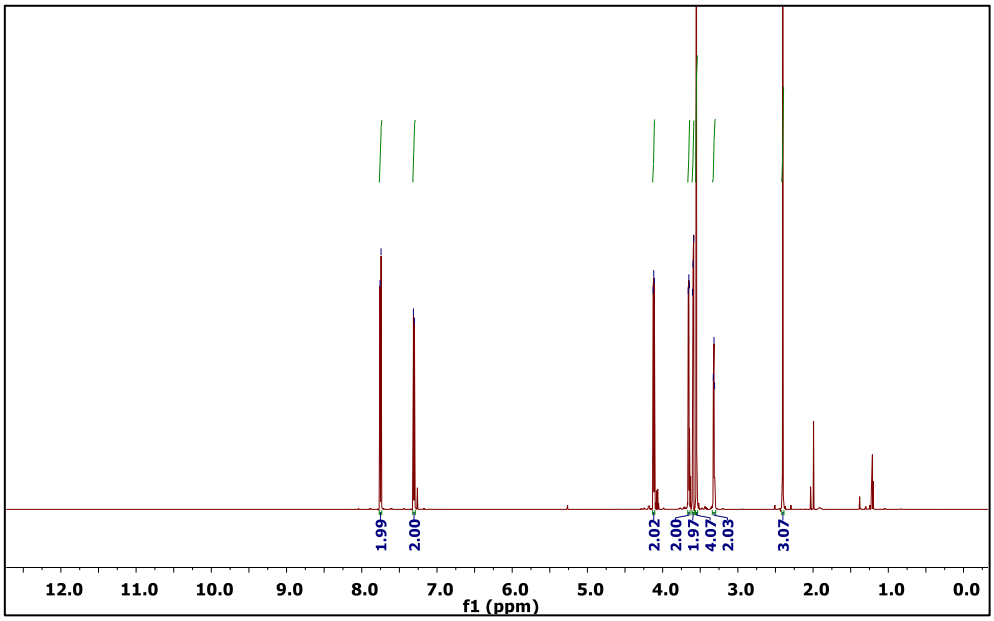


Figure 48. ^{1}H NMR spectrum (400 MHz, $CDCl_3$, 298K) of compound **(2-(2-(2-Azidoethoxy)ethoxy)ethyl 4-methylbenzenesulfonate) (1).**

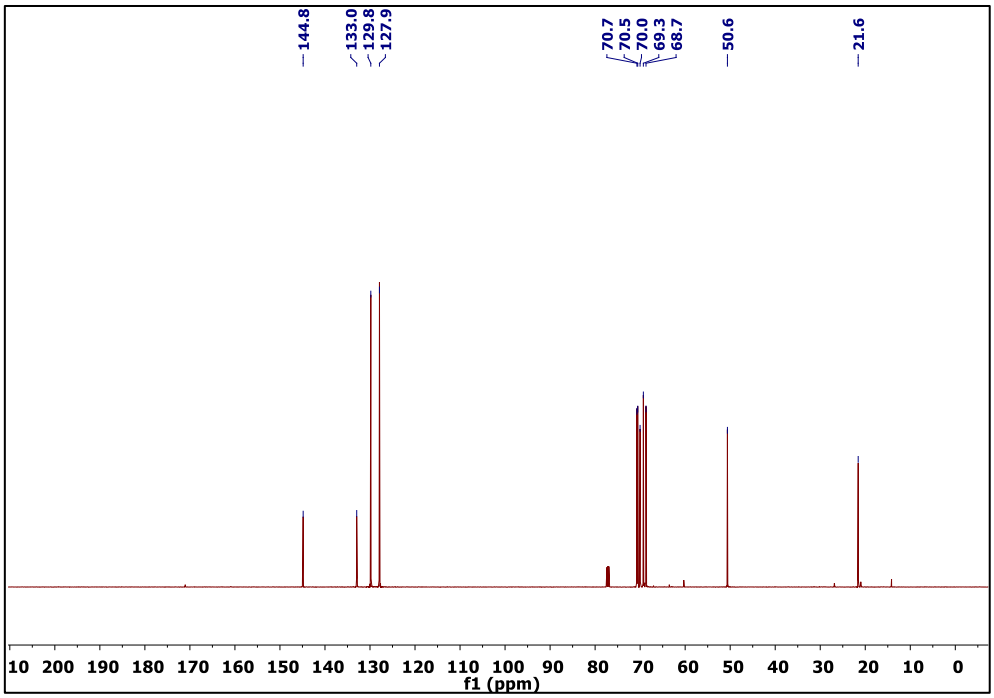


Figure 49. $^{13}C\{^{1}H\}$ NMR spectrum (126 MHz, $CDCl_3$, 298K) of compound **(2-(2-(2-azidoethoxy)ethoxy)ethyl 4-methylbenzenesulfonate) (1).**

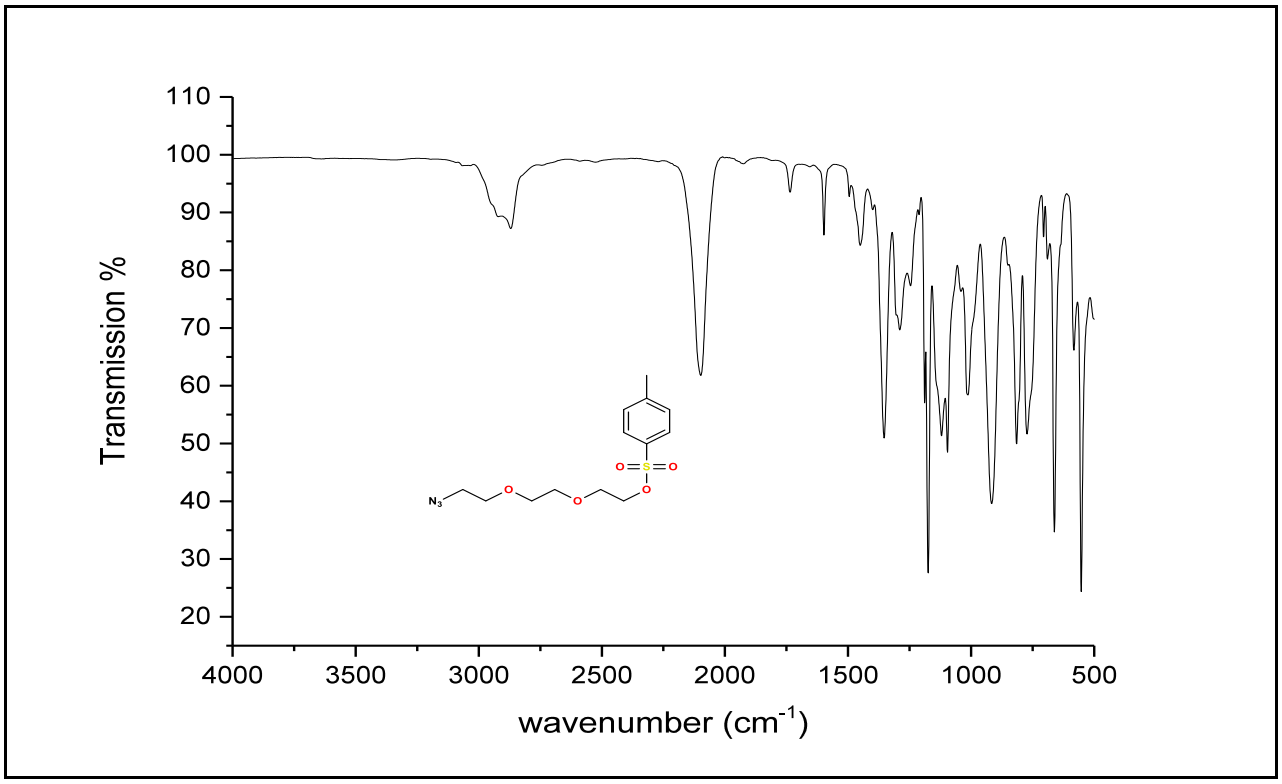


Figure 50. ATR-FTIR spectrum of compound **(2-(2-(2-azidoethoxy)ethoxy)ethyl 4-methylbenzenesulfonate) (1).**

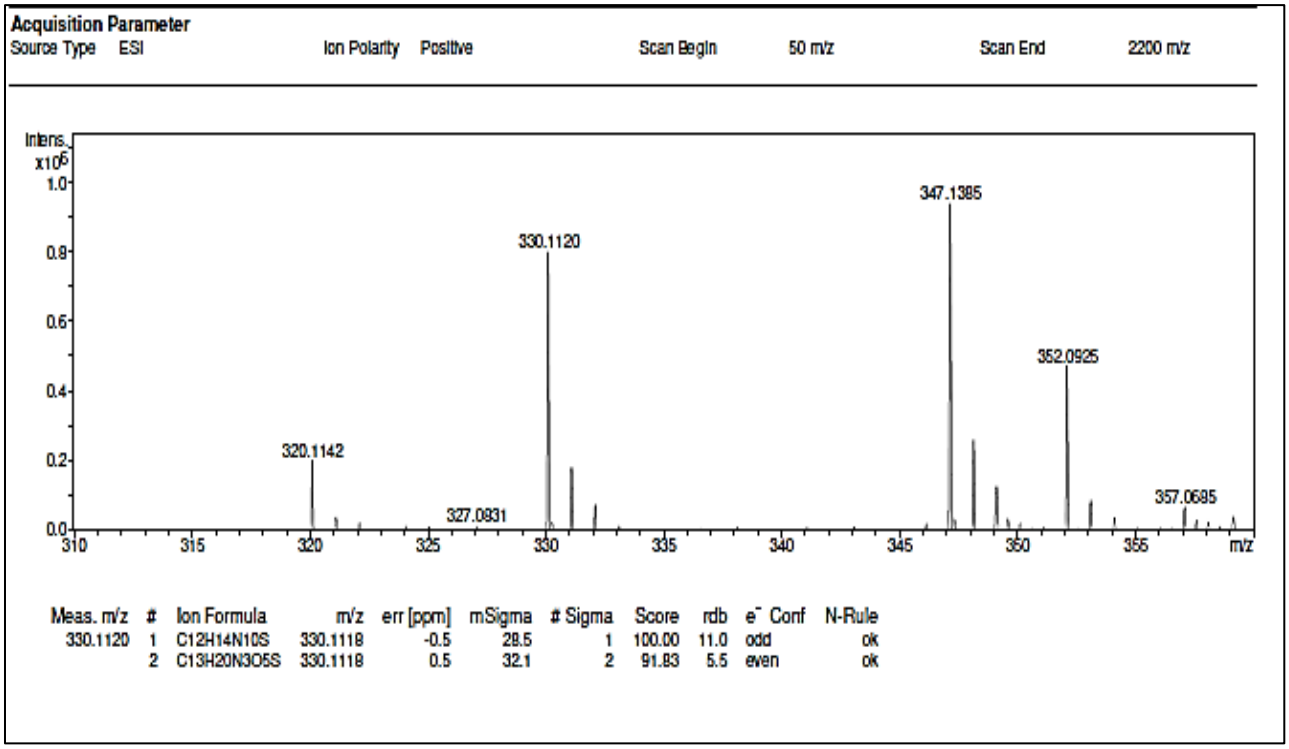
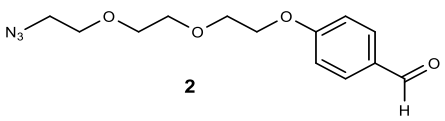


Figure 51. High resolution ESI-TOF (positive mode) mass spectrum of compound **1 (2-(2-(2-azidoethoxy)ethoxy)ethyl 4-methylbenzenesulfonate) (1).**



2

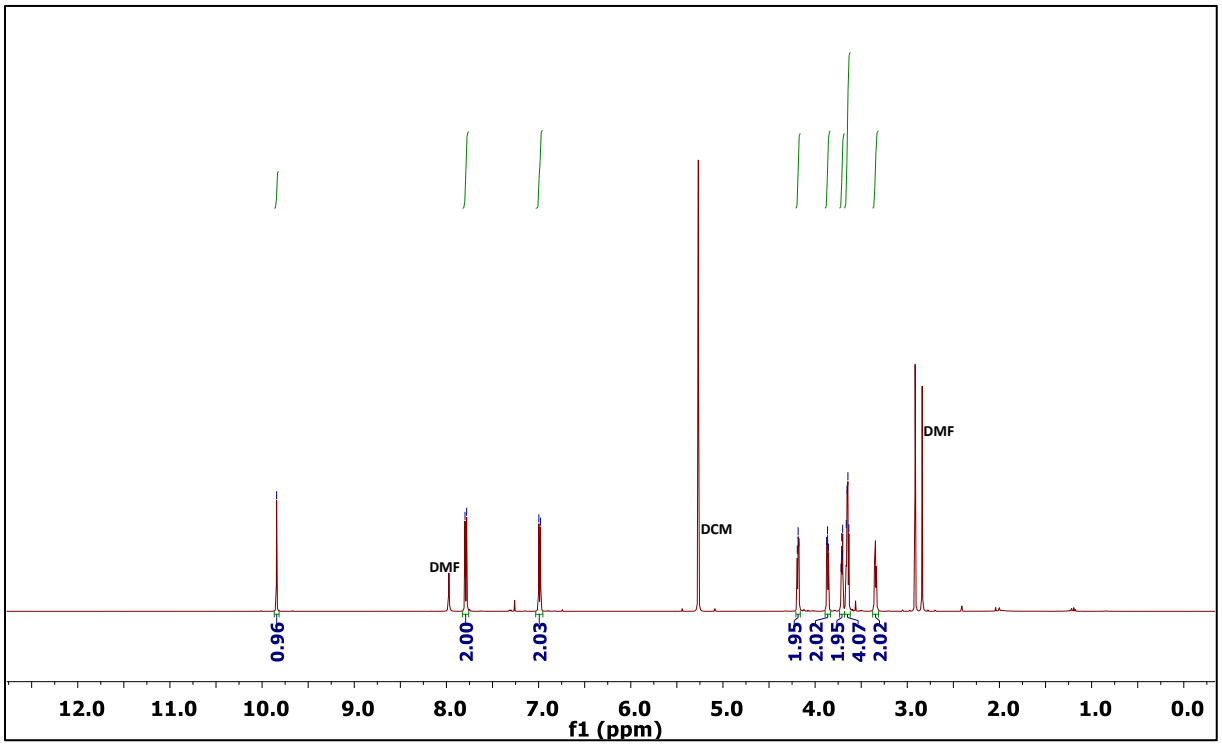


Figure 52. ^{1}H NMR spectrum (400 MHz, $CDCl_3$, 298K) of compound **4 (4-[2-[2-(2-Azidoethoxy)ethoxy]ethoxy]benzaldehyde) (2).**

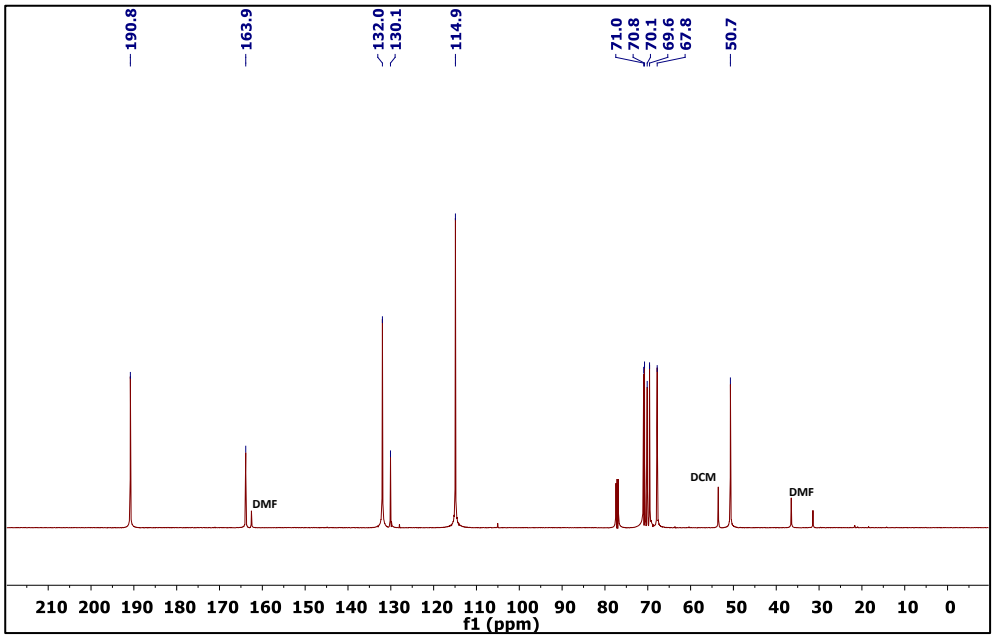


Figure 53. $^{13}C\{^{1}H\}$ NMR spectrum (400 MHz, $CDCl_3$, 298K) of compound **4 (4-[2-[2-(2-Azidoethoxy)ethoxy]ethoxy]benzaldehyde) (2).**

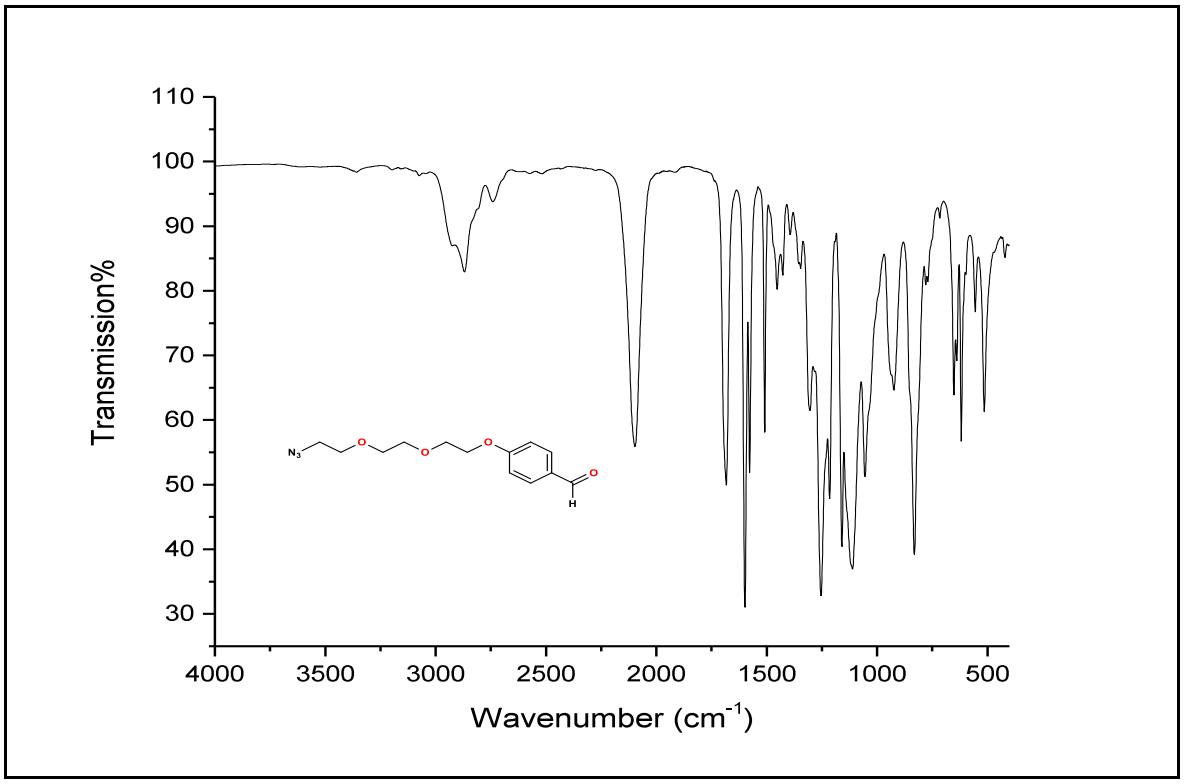


Figure 54. FTIR-ATR spectrum of **4 (4-[2-[2-(2-Azidoethoxy)ethoxy]ethoxy]benzaldehyde) (2).**

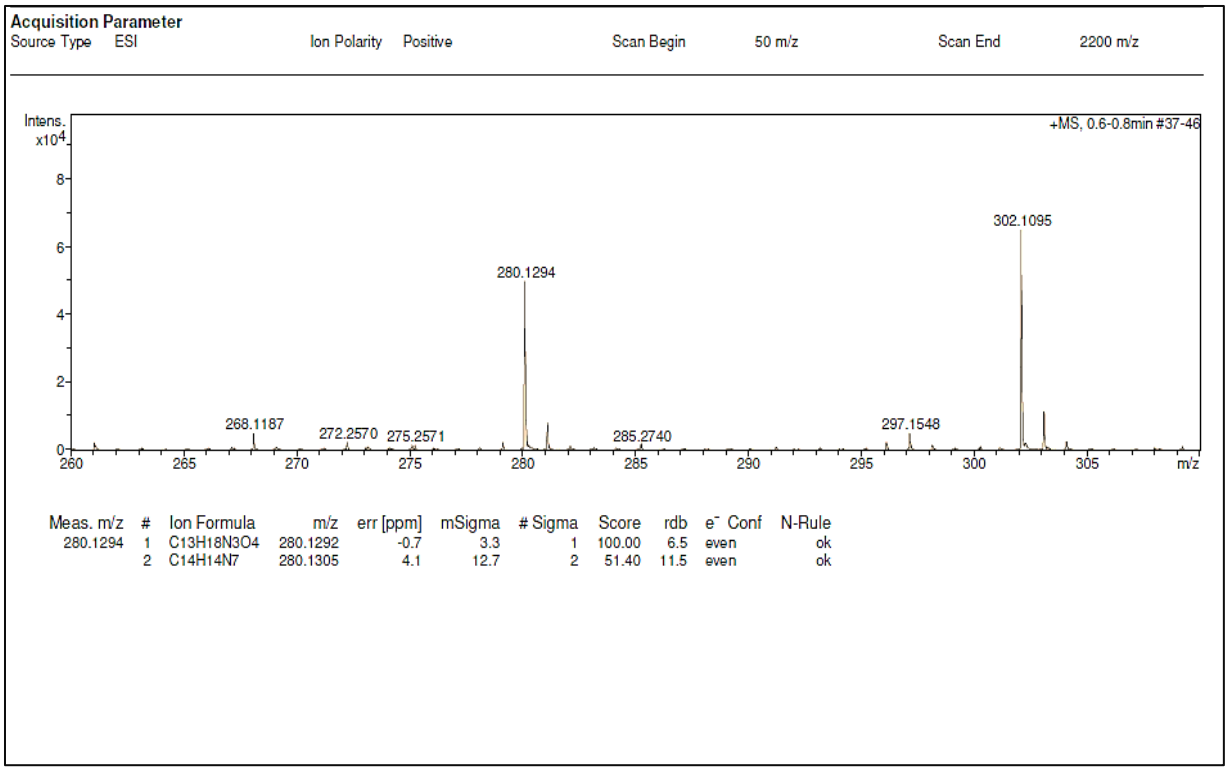


Figure 55. High resolution ESI-TOF (positive mode) mass spectrum of **compound 4 (4-[2-[2-(2-Azidoethoxy)ethoxy]ethoxy]benzaldehyde) (2).**

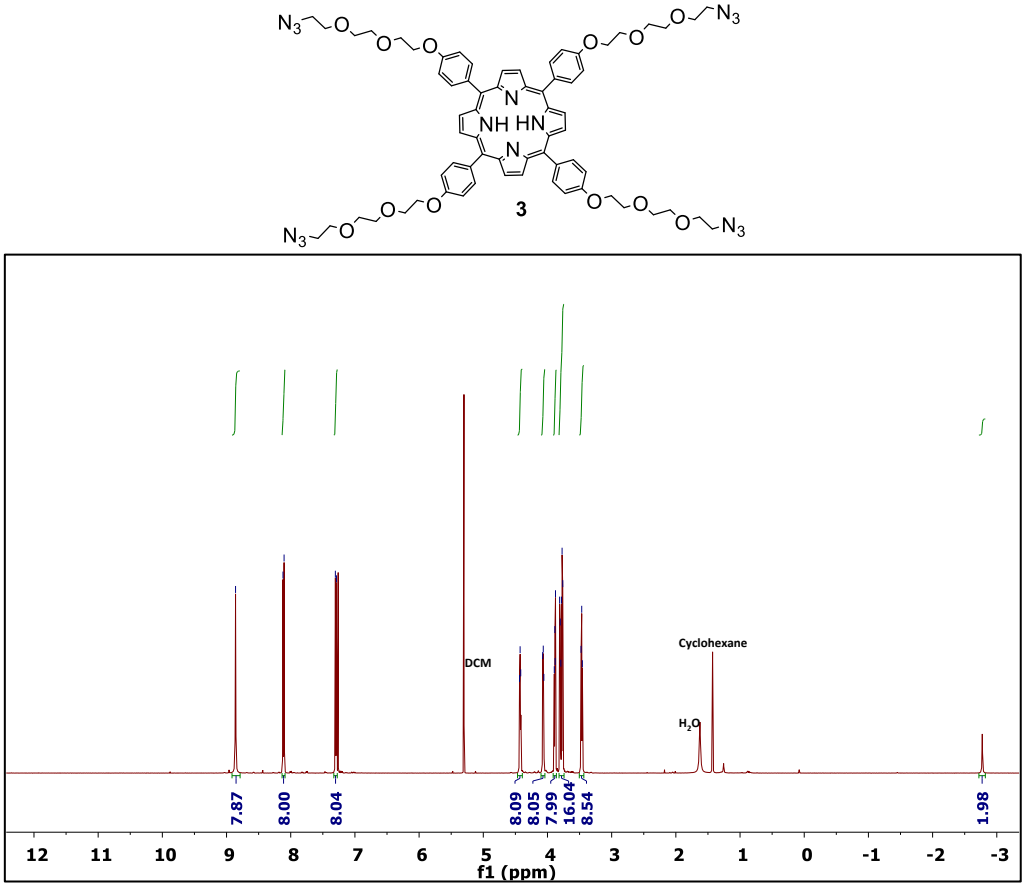


Figure 56. ^{1}H NMR spectrum (400 MHz, $CDCl_3$, 298K) of porphyrin **3.**

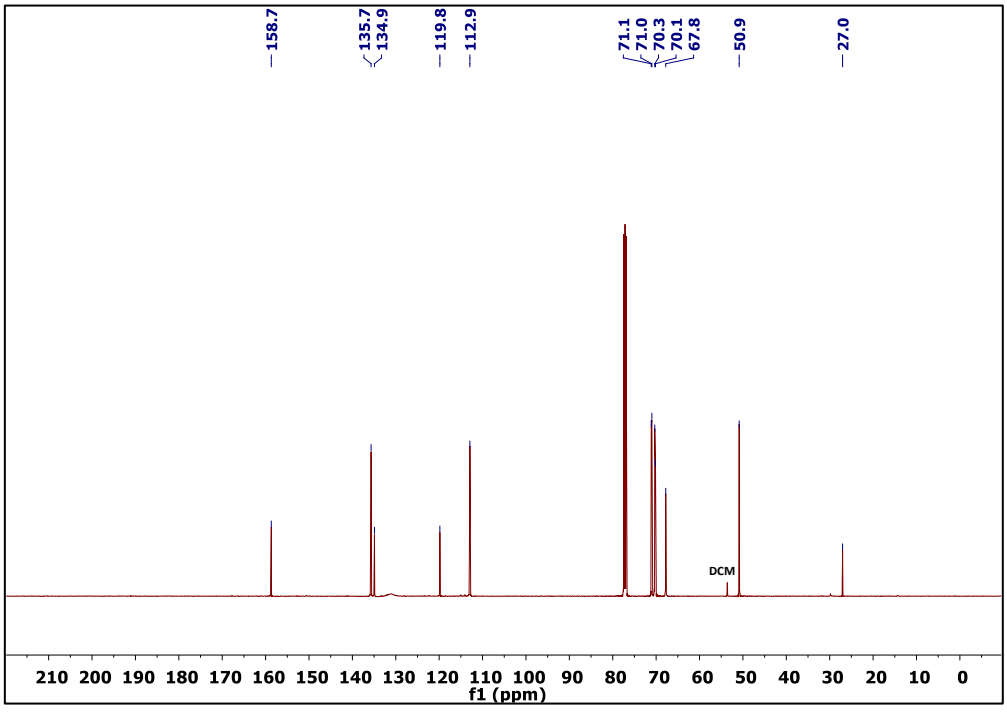


Figure 57. $^{13}C\{^{1}H\}$ NMR spectrum (126 MHz, $CDCl_3$, 298K) of porphyrin **3.**

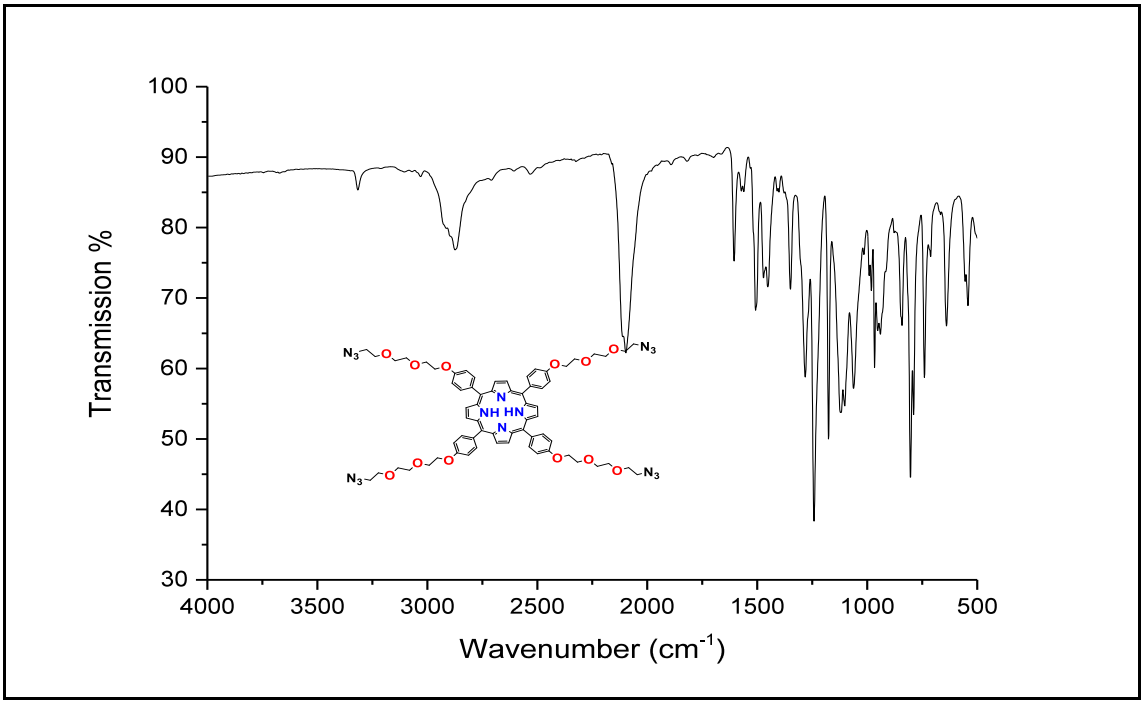
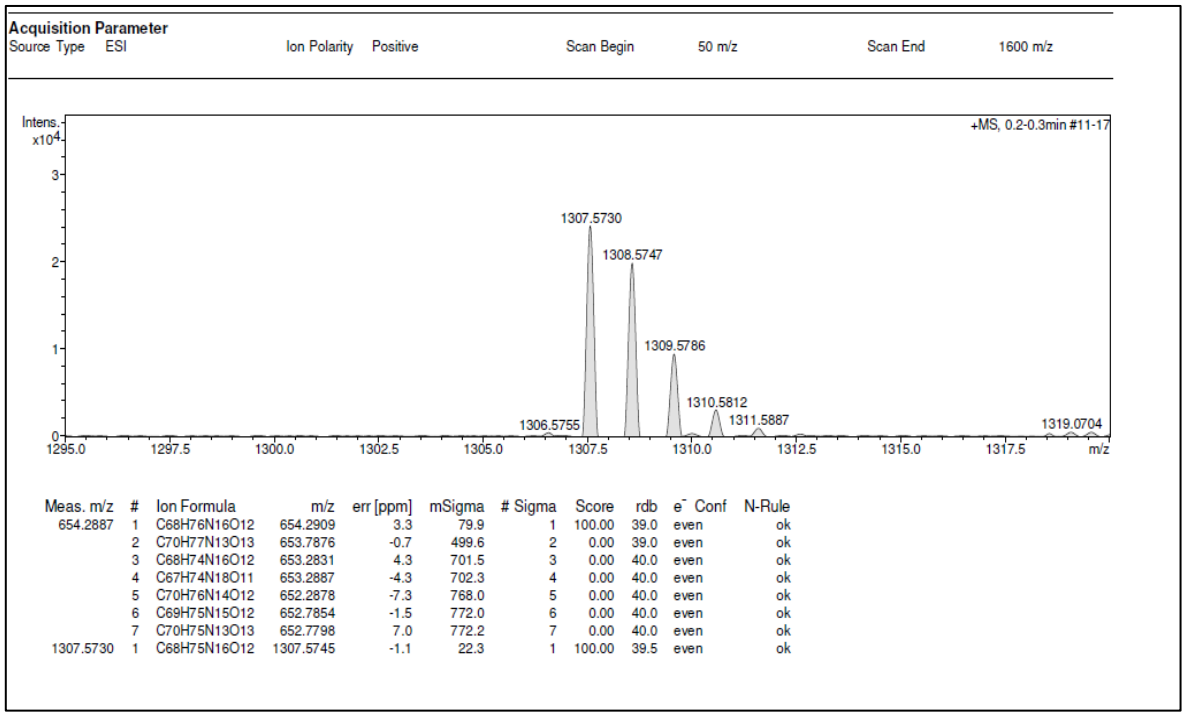
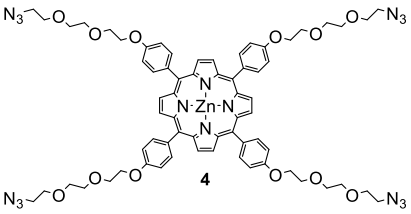


Figure 58. ATR-FTIR spectrum of porphyrin **3.**



Meas. m/z	#	Ion Formula	m/z	err [ppm]	mSigma	# Sigma	Score	rdb	e⁻ Conf	N-Rule
654.2887	1	C68H76N16O12	654.2909	3.3	79.9	1	100.00	39.0	even	ok
	2	C70H77N13O13	653.7876	-0.7	499.6	2	0.00	39.0	even	ok
	3	C68H74N16O12	653.2831	4.3	701.5	3	0.00	40.0	even	ok
	4	C67H74N18O11	653.2887	-4.3	702.3	4	0.00	40.0	even	ok
	5	C70H76N14O12	652.2878	-7.3	768.0	5	0.00	40.0	even	ok
	6	C69H75N15O12	652.7854	-1.5	772.0	6	0.00	40.0	even	ok
	7	C70H75N13O13	652.7798	7.0	772.2	7	0.00	40.0	even	ok
1307.5730	1	C68H75N16O12	1307.5745	-1.1	22.3	1	100.00	39.5	even	ok

Figure 59. High resolution ESI-TOF (positive mode) mass spectrum of porphyrin **3.**



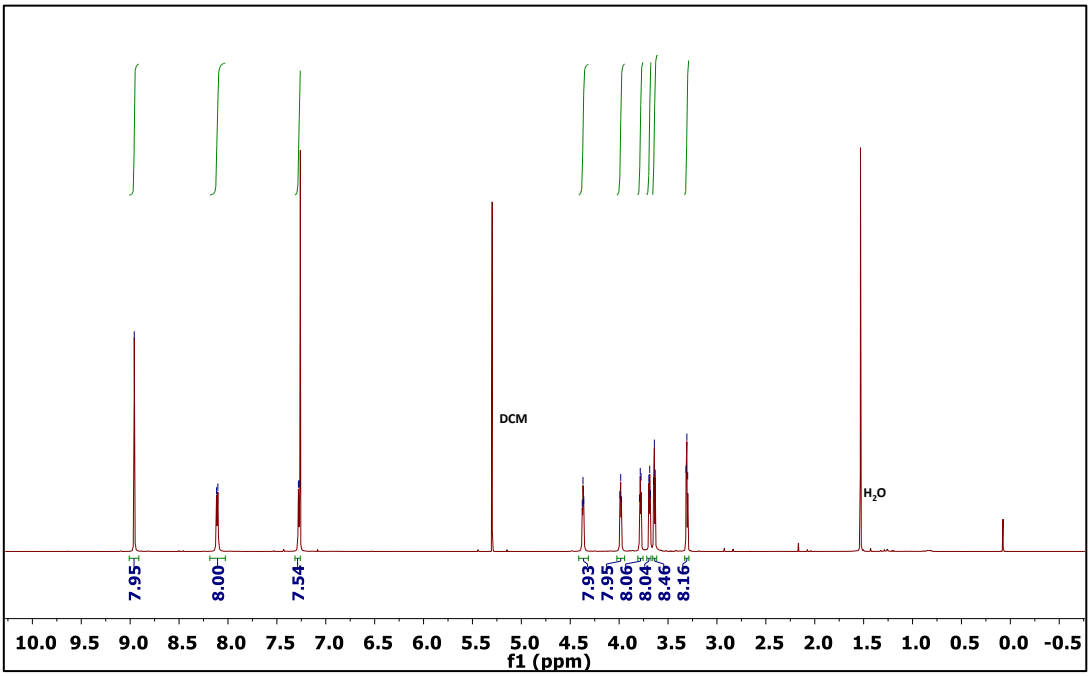


Figure 60. ^{1}H NMR spectrum (400 MHz, $CDCl_3$, 298K) of porphyrin **4**.

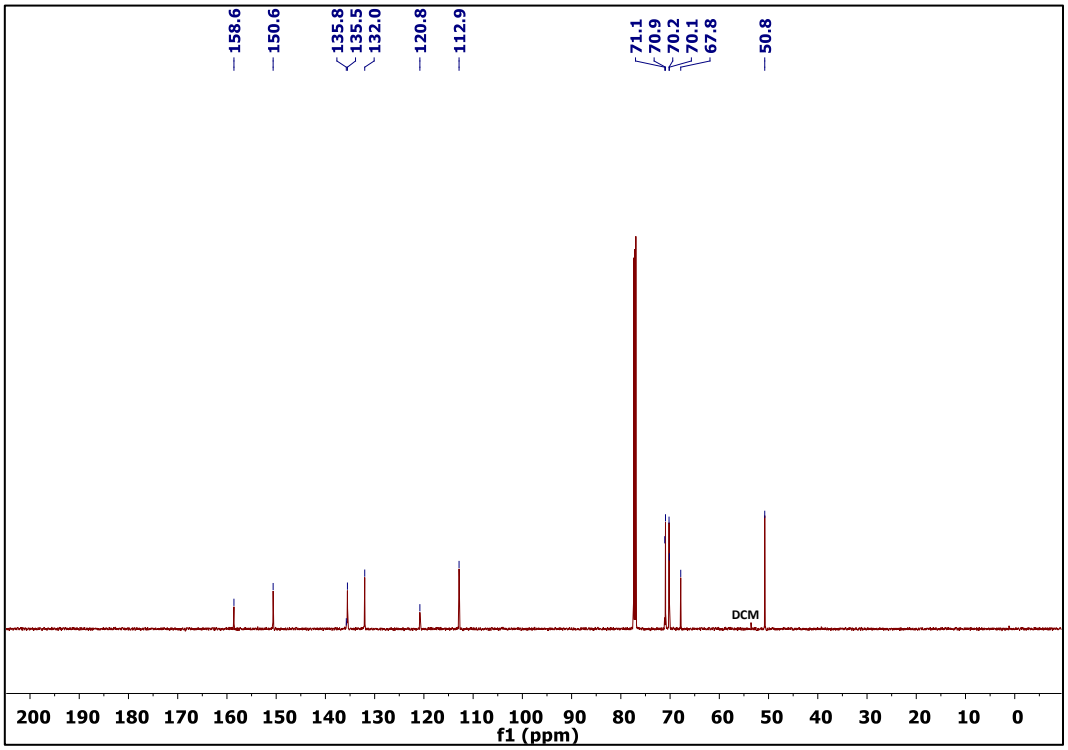


Figure 61. $^{13}C\{^{1}H\}$ NMR spectrum (126 MHz, $CDCl_3$, 298K) of porphyrin **4.**

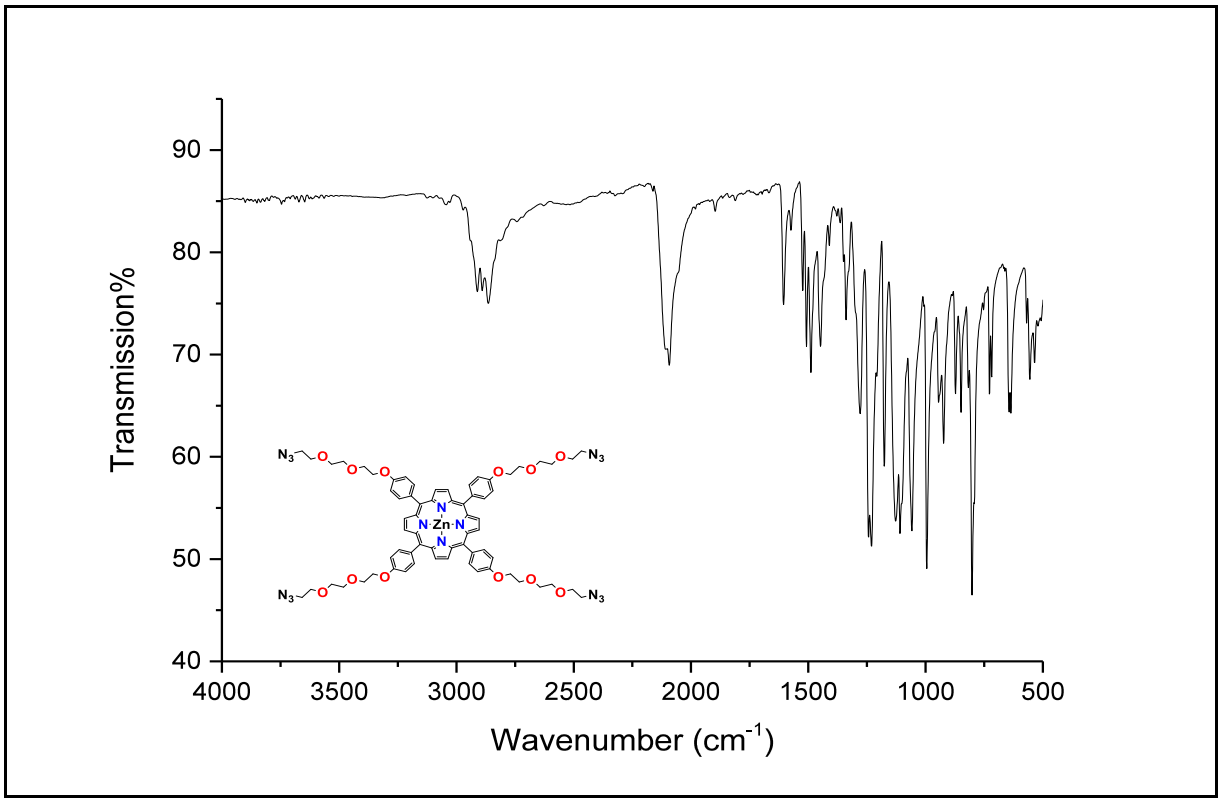
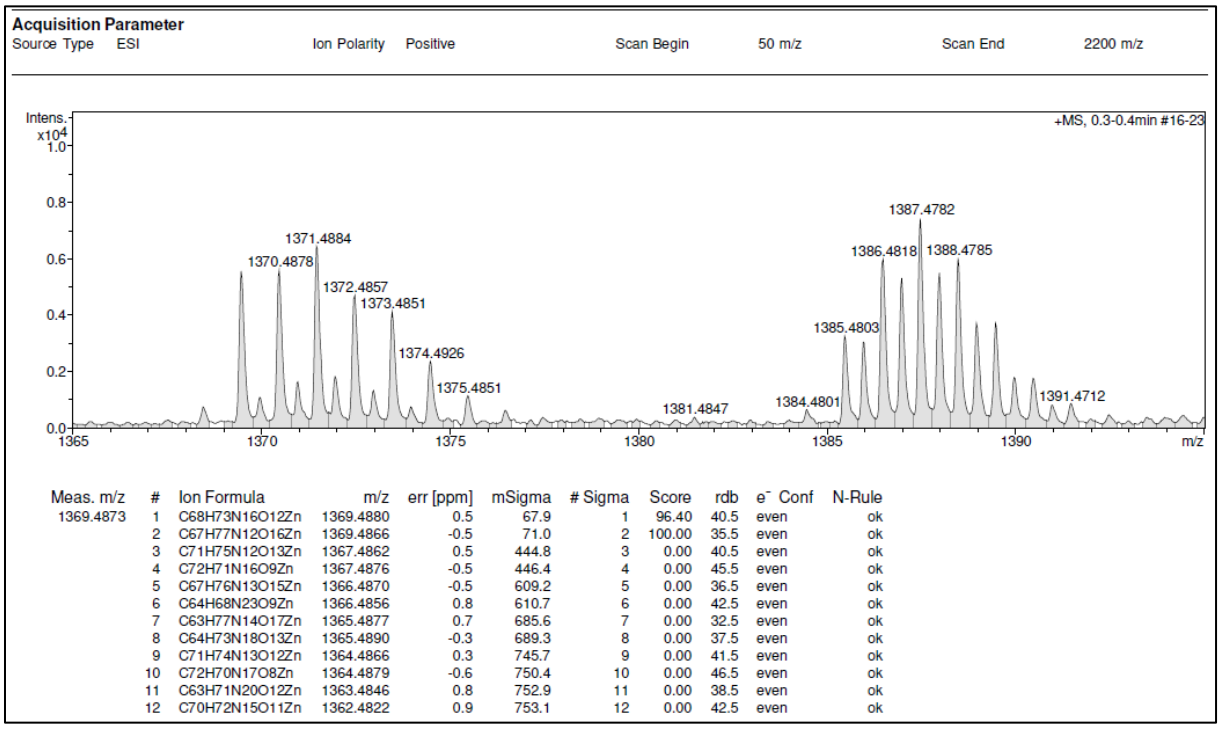


Figure 62. ATR-FTIR spectrum of porphyrin **4.**



Meas. m/z	#	Ion Formula	m/z	err [ppm]	mSigma	# Sigma	Score	rdb	e⁻ Conf	N-Rule
1369.4873	1	C68H73N16O12Zn	1369.4880	0.5	67.9	1	96.40	40.5	even	ok
	2	C67H77N12O16Zn	1369.4866	-0.5	71.0	2	100.00	35.5	even	ok
	3	C71H75N12O13Zn	1367.4862	0.5	444.8	3	0.00	40.5	even	ok
	4	C72H71N16O9Zn	1367.4876	-0.5	446.4	4	0.00	45.5	even	ok
	5	C67H76N13O15Zn	1366.4870	-0.5	609.2	5	0.00	36.5	even	ok
	6	C64H68N23O9Zn	1366.4856	0.8	610.7	6	0.00	42.5	even	ok
	7	C63H77N14O17Zn	1365.4877	0.7	685.6	7	0.00	32.5	even	ok
	8	C64H73N18O13Zn	1365.4890	-0.3	689.3	8	0.00	37.5	even	ok
	9	C71H74N13O12Zn	1364.4866	0.3	745.7	9	0.00	41.5	even	ok
	10	C72H70N17O8Zn	1364.4879	-0.6	750.4	10	0.00	46.5	even	ok
	11	C63H71N20O12Zn	1363.4846	0.8	752.9	11	0.00	38.5	even	ok
	12	C70H72N15O11Zn	1362.4822	0.9	753.1	12	0.00	42.5	even	ok

Figure 63. High resolution ESI-TOF (positive mode) mass spectrum of porphyrin **4.**

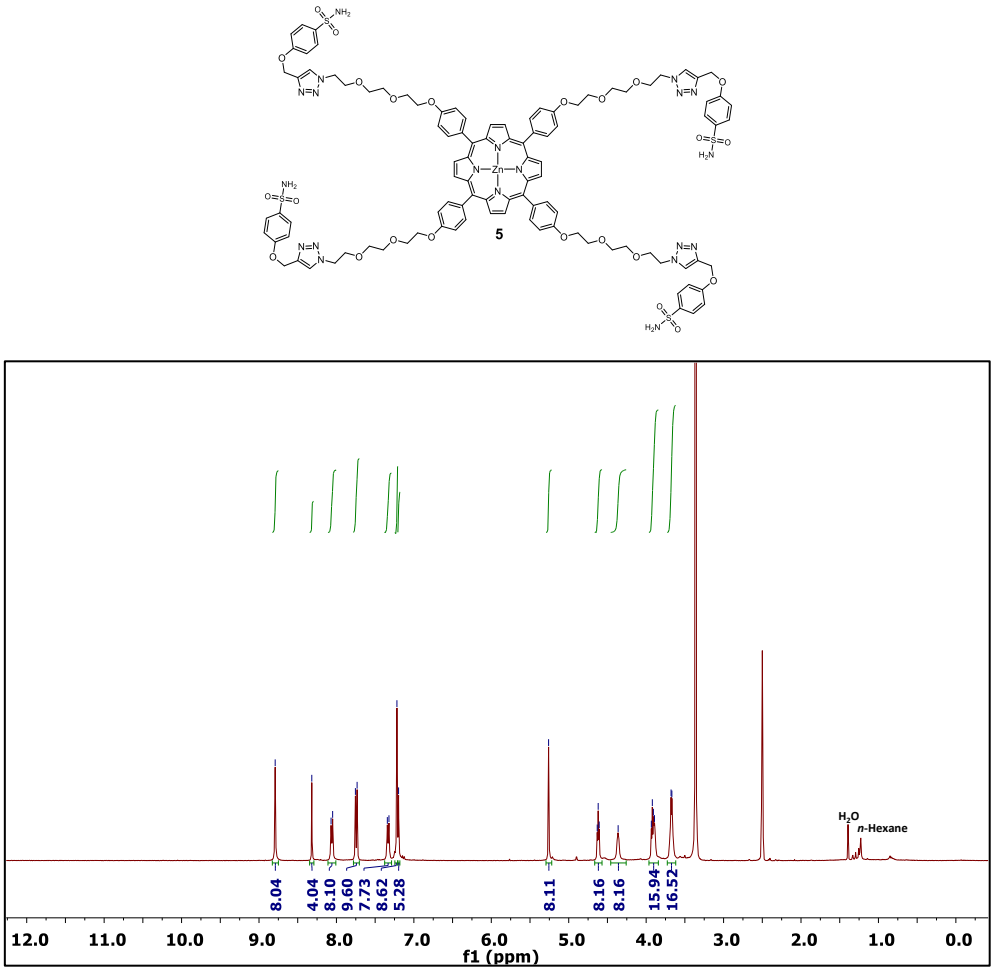


Figure 64. ^{1}H NMR spectrum (400 MHz, [D$_6$]DMSO, 298K) of porphyrin **5.**

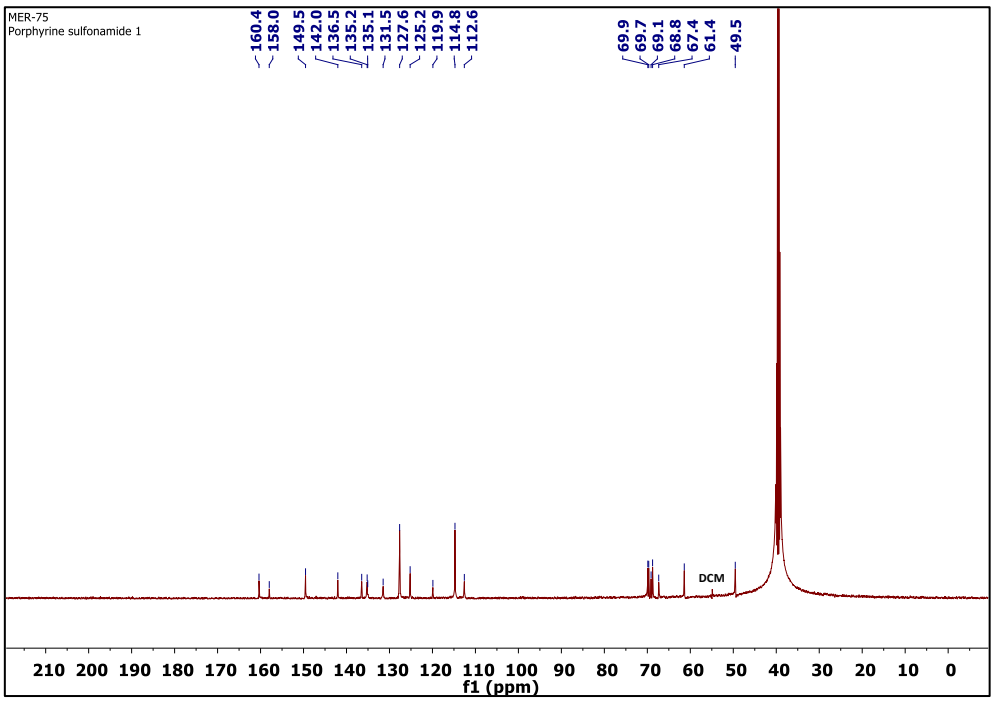


Figure 65. ^{13}C{^{1}H} NMR spectrum (126 MHz, [D$_6$]DMSO, 298K) of porphyrin **5**.

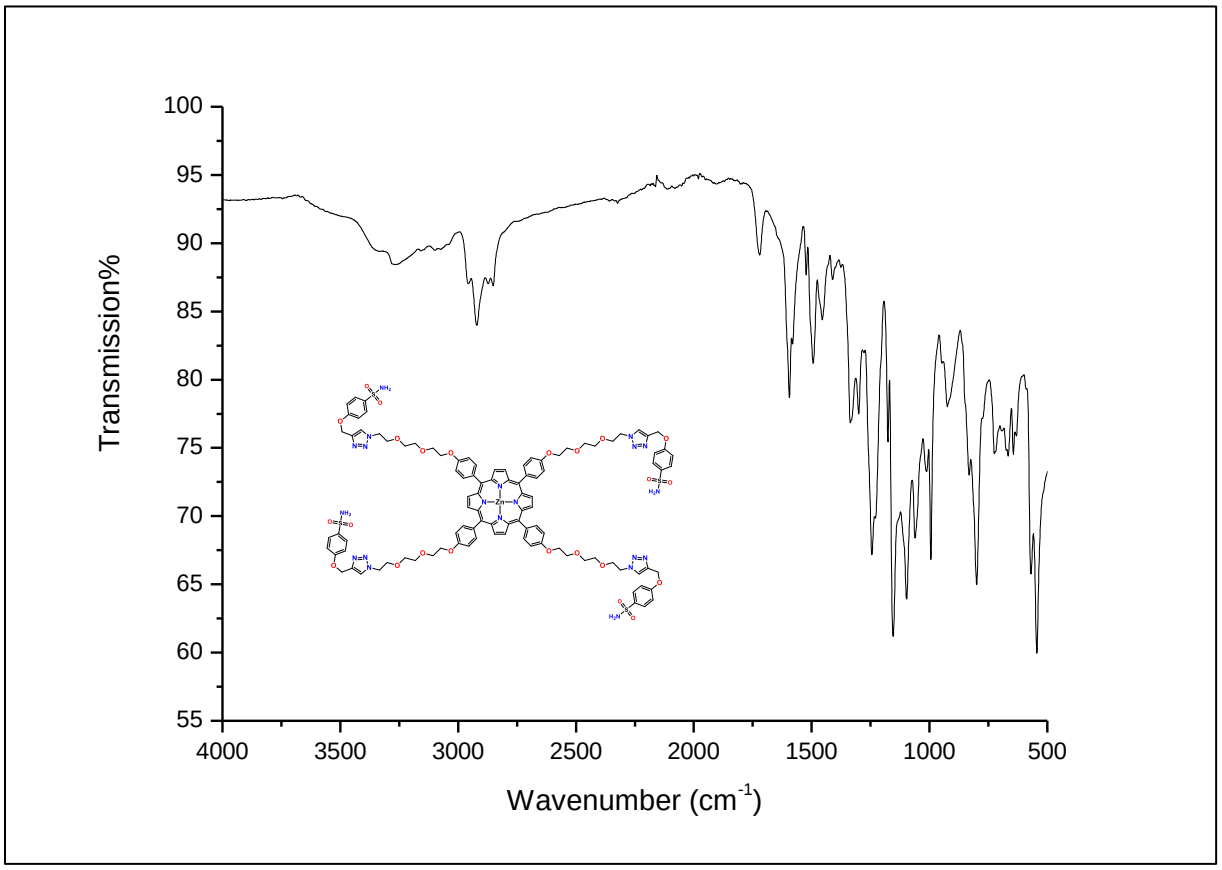


Figure 66. ATR-FTIR spectrum of porphyrin **5.**

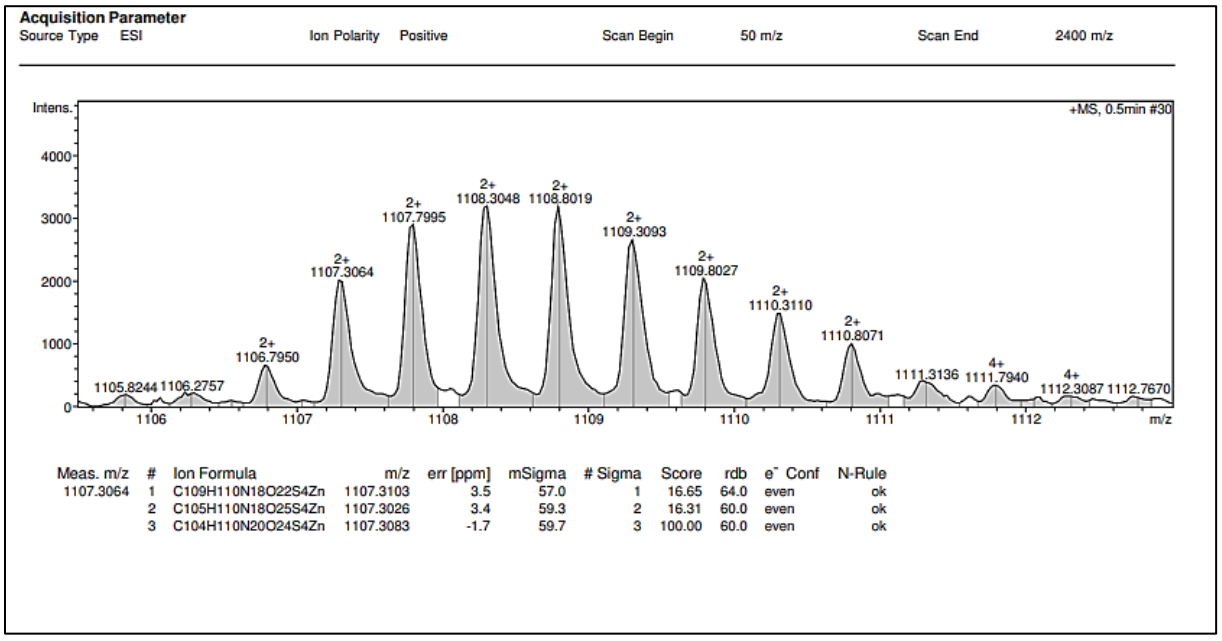
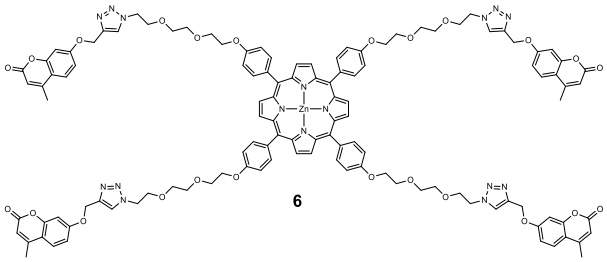


Figure 67. High resolution ESI-TOF (positive mode) mass spectrum of porphyrin **5.**



6

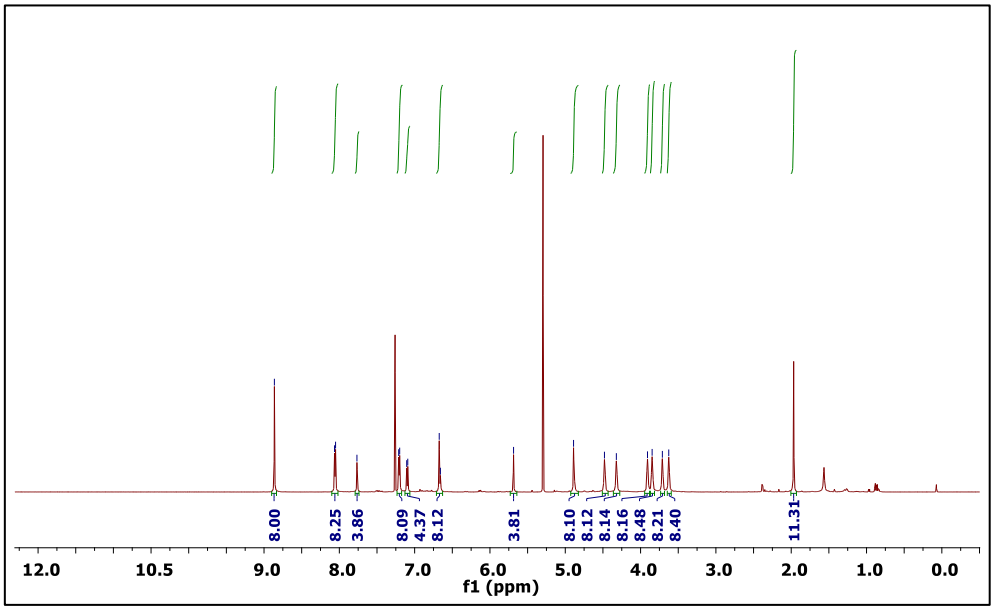


Figure 68. ^{1}H NMR spectrum (400 MHz, $CDCl_3$, 298K) of porphyrin **6.**

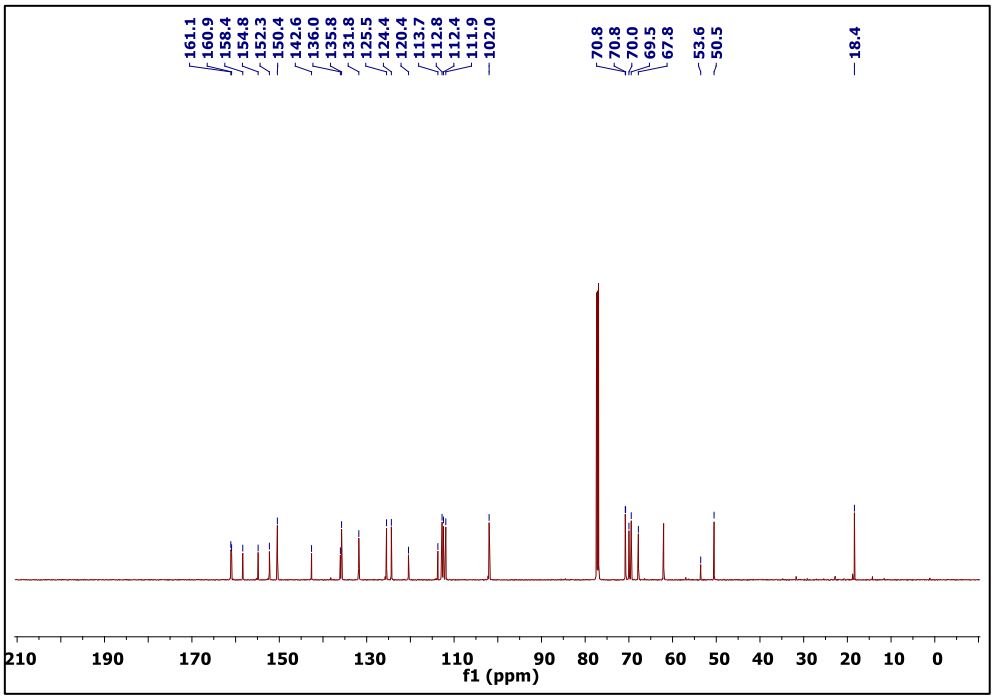


Figure 69. $^{13}C\{^{1}H\}$ NMR spectrum (126 MHz, $CDCl_3$, 298K) of porphyrin **6.**

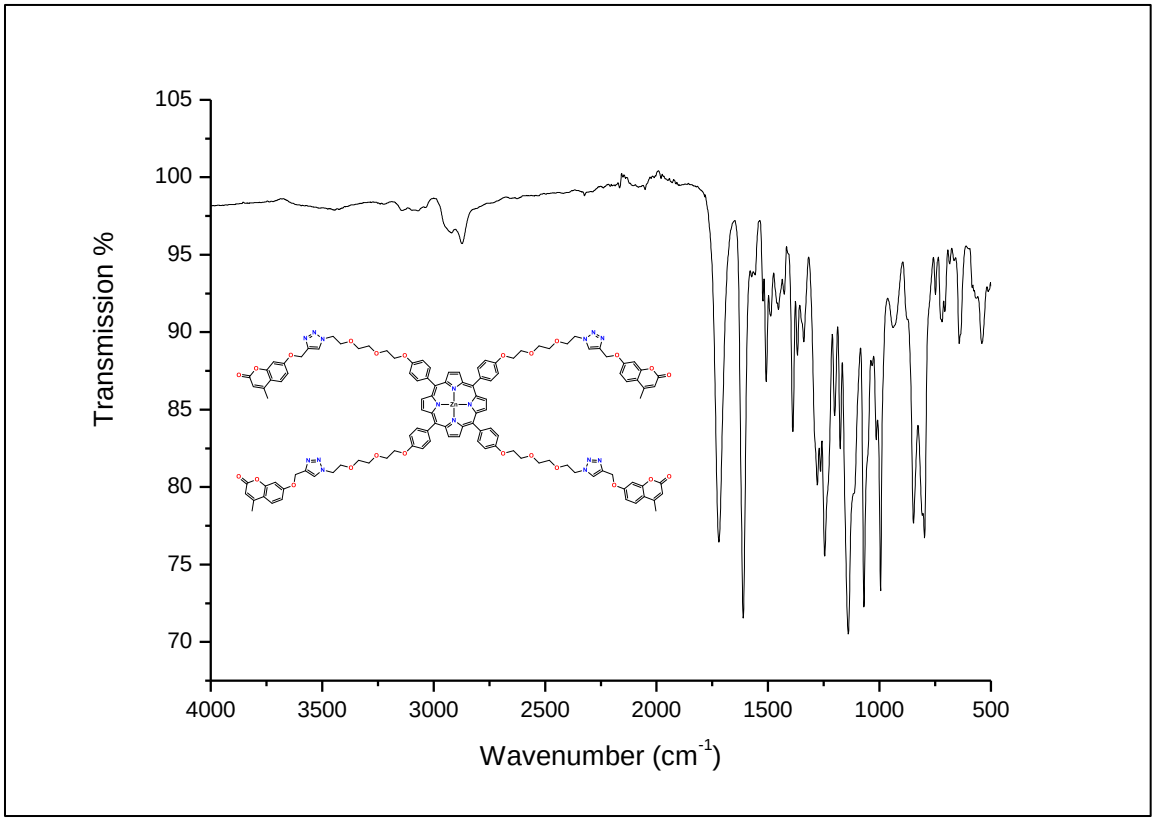


Figure 70. ATR-FTIR spectrum of porphyrin **6.**

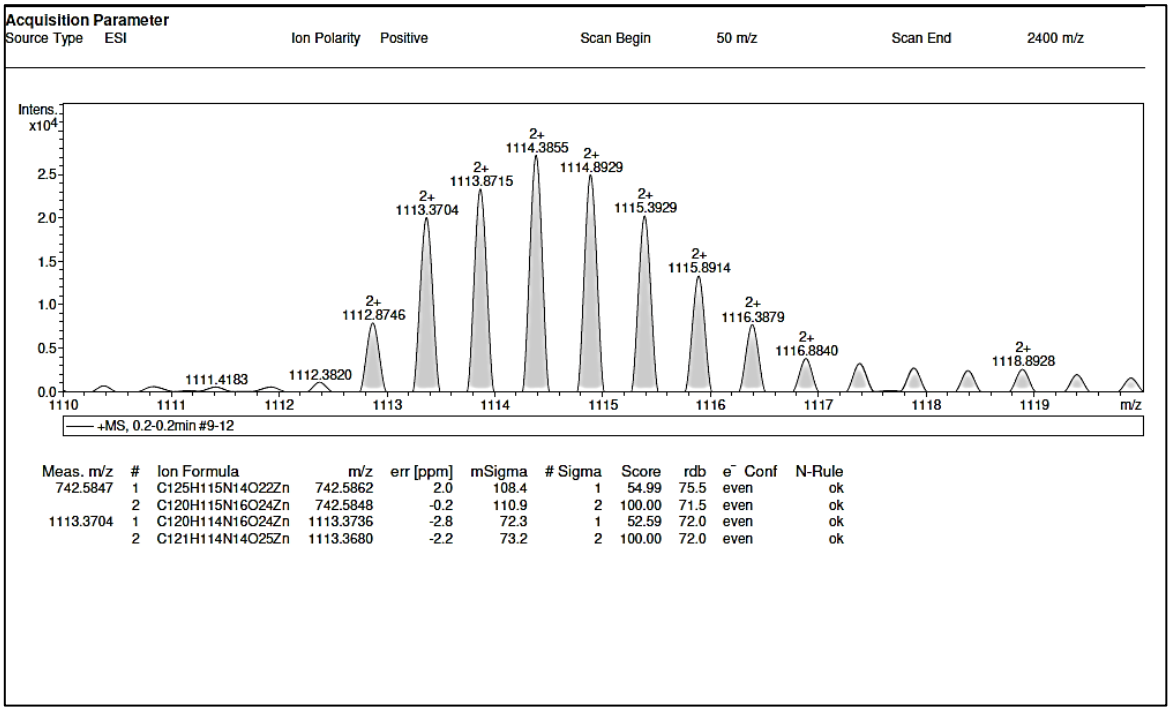
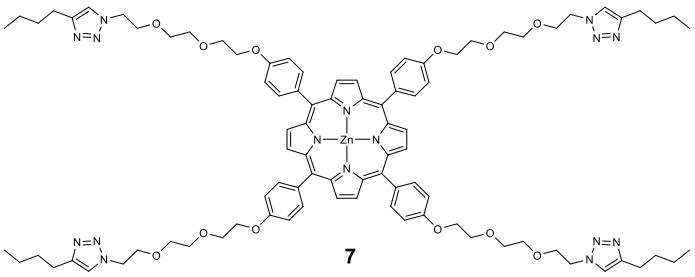


Figure 71. High resolution ESI-TOF (positive) mass spectrum of porphyrin **6.**



7

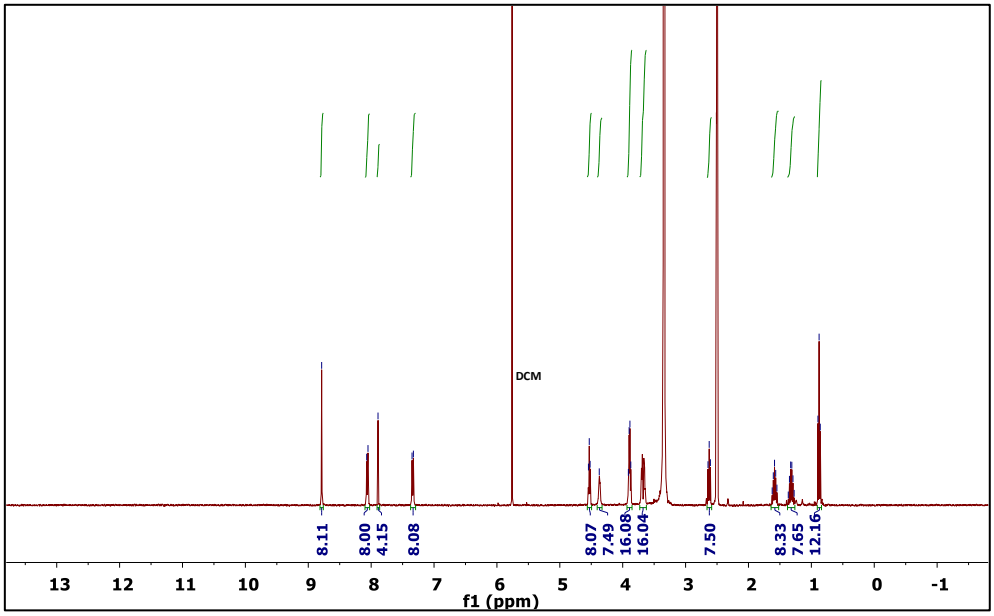


Figure 72. ^{1}H NMR spectrum (400 MHz, $[D_6]$DMSO, 298K) of porphyrin **7.**

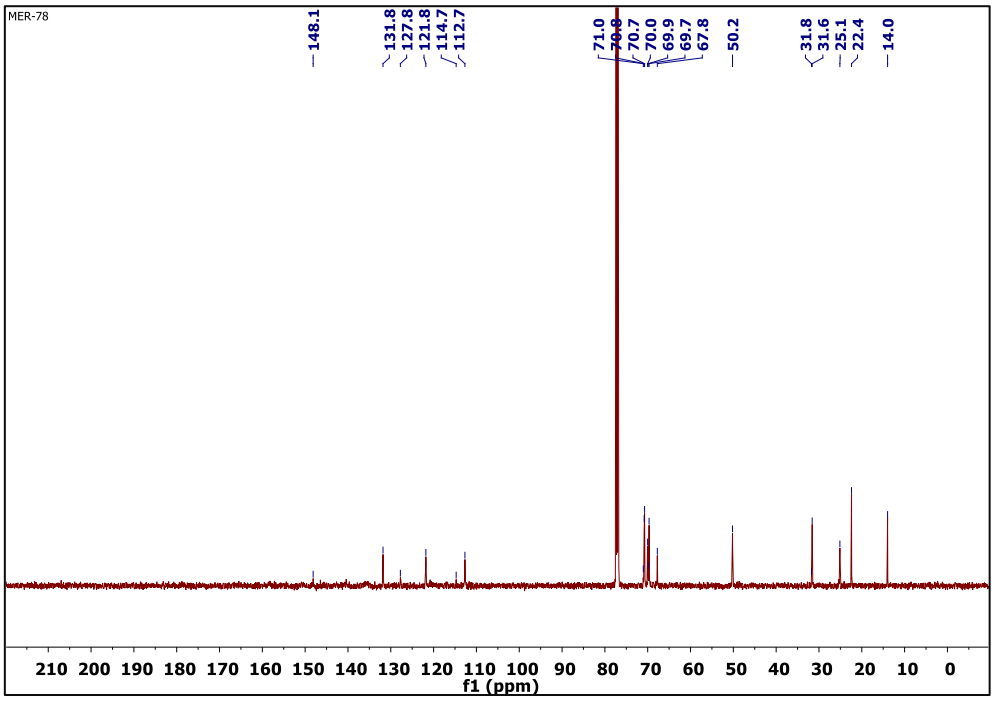


Figure 73. $^{13}C\{^{1}H\}$ NMR spectrum (126 MHz, $[D_6]$DMSO, 298K) of porphyrin **7**.

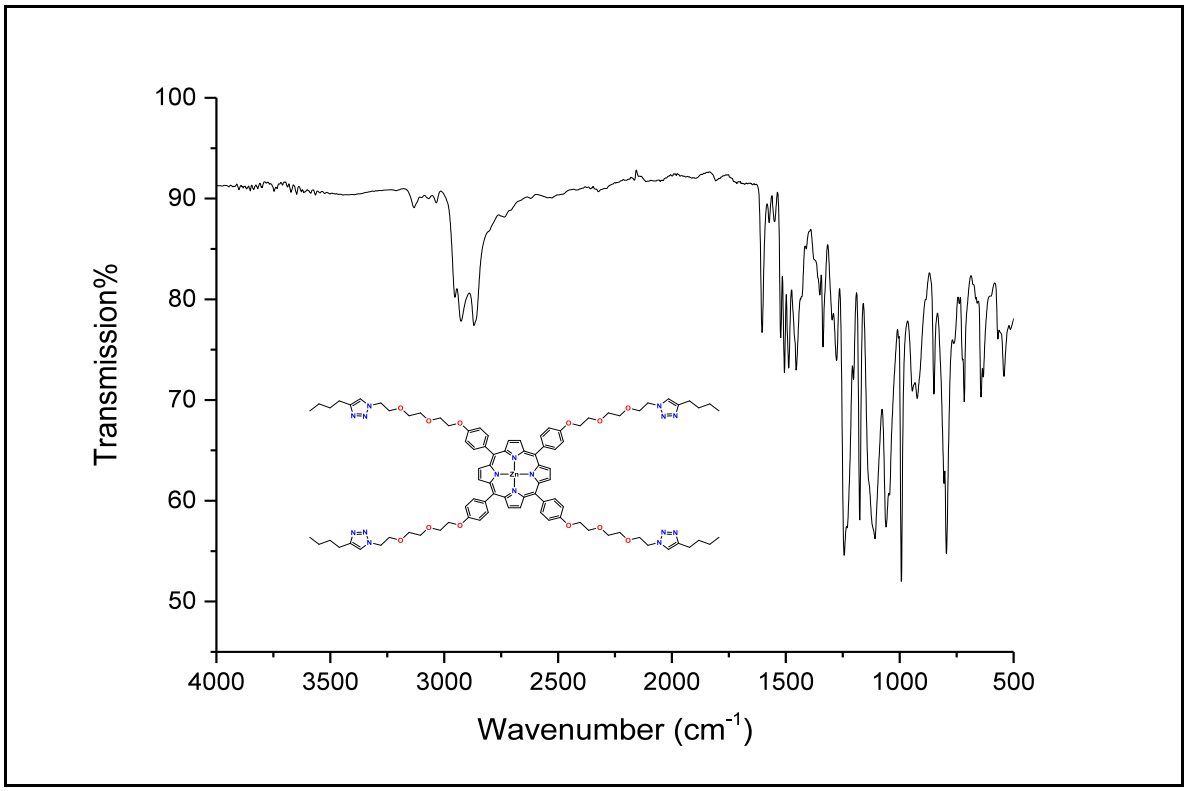
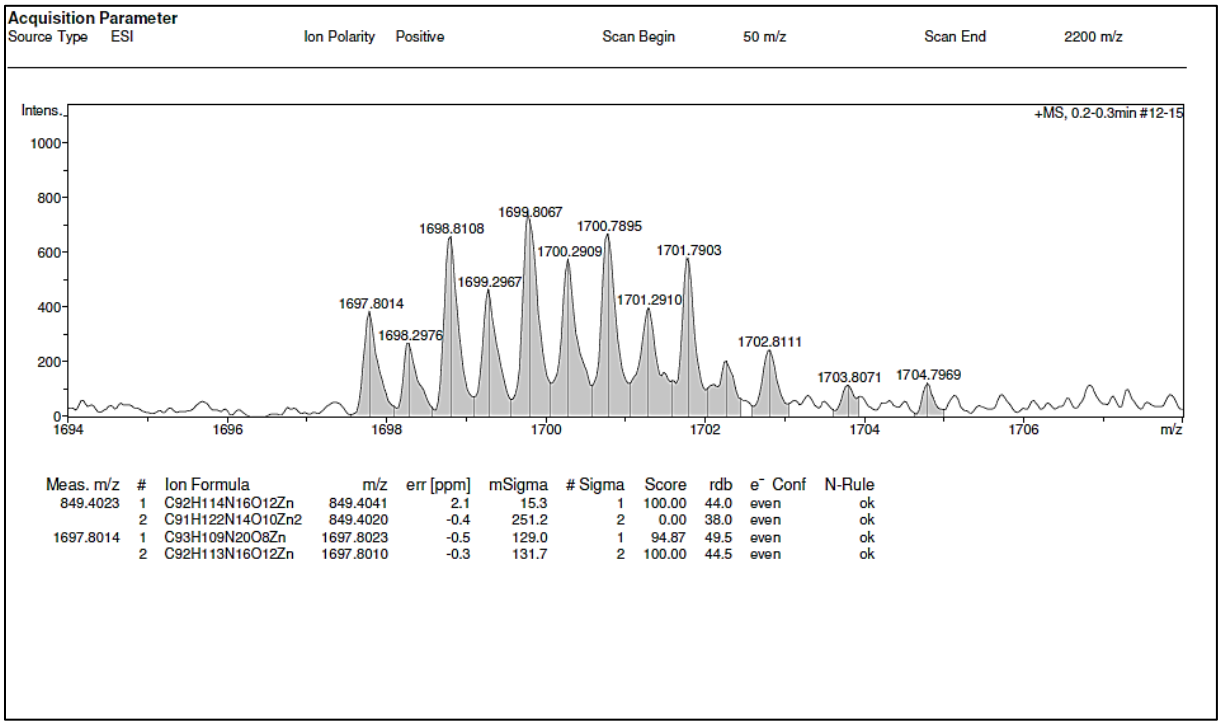


Figure 74. ATR-FTIR spectrum of porphyrin **7.**



Meas. m/z	#	Ion Formula	m/z	err [ppm]	mSigma	# Sigma	Score	rdb	e⁻ Conf	N-Rule
849.4023	1	C92H114N16O12Zn	849.4041	2.1	15.3	1	100.00	44.0	even	ok
	2	C91H122N14O10Zn2	849.4020	-0.4	251.2	2	0.00	38.0	even	ok
1697.8014	1	C93H109N20O8Zn	1697.8023	-0.5	129.0	1	94.87	49.5	even	ok
	2	C92H113N16O12Zn	1697.8010	-0.3	131.7	2	100.00	44.5	even	ok

Figure 75. High resolution ESI-TOF (positive mode) mass spectrum of porphyrin **7**.

IV.3 Optical properties

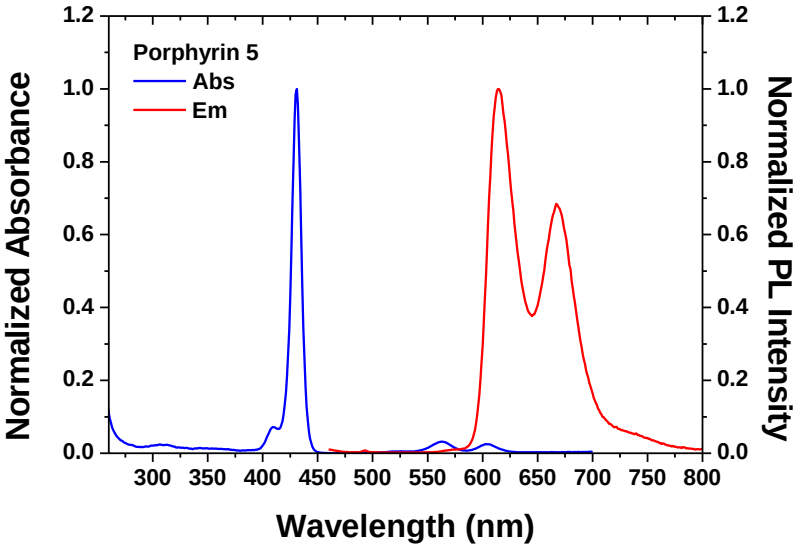


Figure 76. UV-Visible (blue) and emission (red) spectra of porphyrin **5** (10^{-6} M) in DMSO (λ_{exc} = 440 nm).

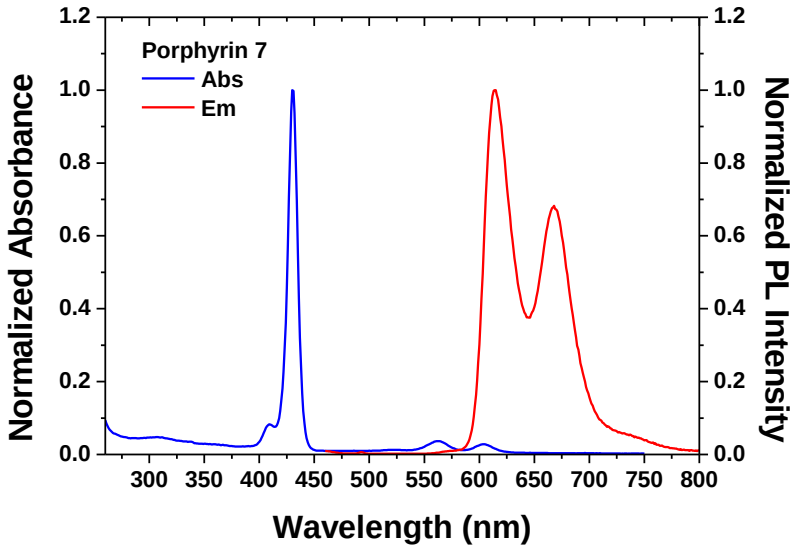


Figure 77. UV-Visible absorption (blue) and emission (red) spectra of porphyrin **7** (10^{-6} M) in DMSO (λ_{exc} = 440 nm).

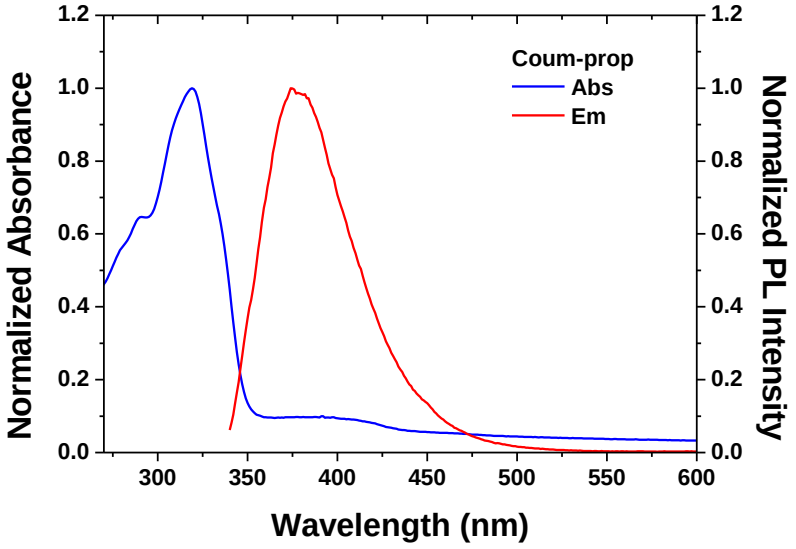


Figure 78. UV-Visible absorption (blue) and emission (red) spectra of Coum-prop (2 x 10^{-5} M) in DMSO (λ_{exc} = 320 nm).

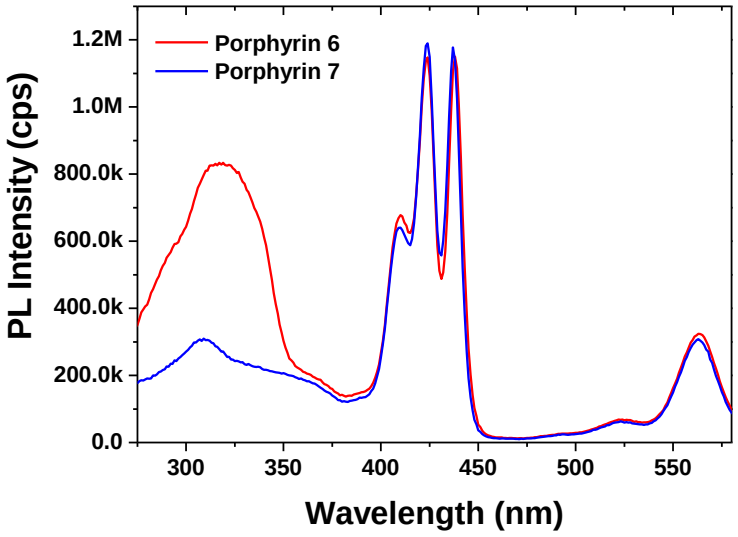


Figure 79. Excitation spectra of porphyrins **6** (red) and **7** (blue) at 5 x 10^{-6} M in DMSO (λ_{em} = 615 nm).

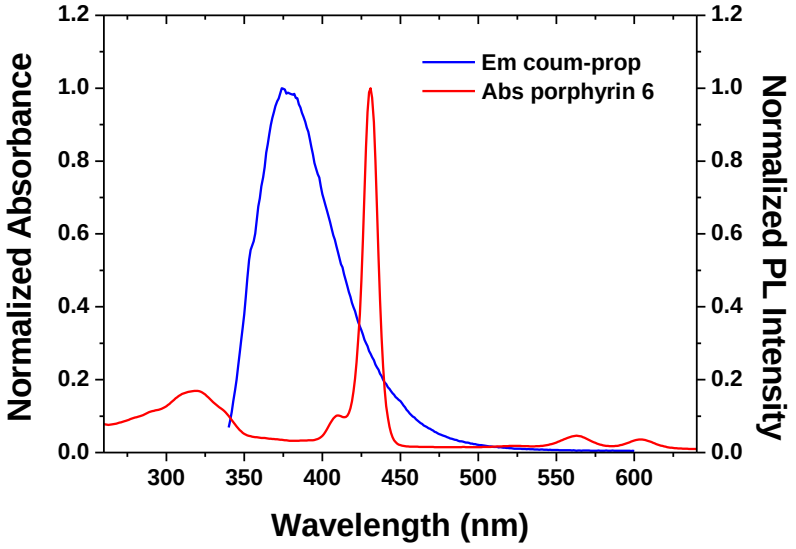


Figure 80. UV-Visible absorption spectrum of porphyrin **6** (C= 5 x 10^{-6} M, red) and emission spectrum of Coum-prop (C = 2 x 10^{-5} M)(blue, λ_{exc} = 320 nm) **5** in DMSO.

IV.4 CA inhibition assays

An SX.18V-R Applied Photophysics (Oxford, UK) stopped flow instrument was used to assay the catalytic/inhibition of various CA isozymes.[2] Phenol Red (at a concentration of 0.2 mM) has been used as an indicator, working at an absorbance maximum of 557 nm, with 10 mM HEPES (pH 7.4) as a buffer, 0.1 M Na_2SO_4 or $NaClO_4$ (for maintaining constant the ionic strength; these anions are not inhibitory in the used concentration), following the CA-catalyzed CO_2 hydration reaction for a period of 5–10 s. Saturated CO_2 solutions in water at 25 °C were used as substrate. Stock solutions of inhibitors were prepared at a concentration of 10 mM (in DMSO/water 1:1, v/v) and dilutions up to 0.01 nM done with the assay buffer mentioned above. At least 7 different inhibitor concentrations have been used for measuring the inhibition constant. Inhibitor and enzyme solutions were pre-incubated together for 6h at 4 °C prior to assay, in order to allow for the formation of the E-I complex. Triplicate experiments were done for each inhibitor concentration, and the values are reported throughout the paper is the mean of such results. The inhibition constants were obtained by nonlinear least squares methods using the Cheng-Prusoff equation, as reported earlier, and represent the mean from at least three different determinations. All CA isozymes used here were recombinant proteins obtained as reported earlier by our groupand their concentration in the assay system was of 6–12 nM. [3-6]

Chapter III: Carbonic Anhydrase Featuring a Porphyrin Scaffold: Synthesis, Optical and Biological Properties

IV.5 Biological assays

Cell culture conditions. Pancreas cancer cell line (Capan-1) were purchased from ATCC (American Type Culture Collection, Manassas, VA, USA). They were routinely maintained in Dulbecco's Modified Eagle Medium (DMEM) supplemented with 10% fetal bovine serum (FBS) and 1% penicillin/streptomycin (P/S). Cells were grown in a humidified atmosphere at 37 °C under 5% CO_2.

Cytotoxicity study. Capan-1 cells were seeded in 96-well plates and incubated for 3 days with increasing concentrations of compounds (from 0.01 to 100 µM). At the end of incubation time, a quantification of living cells was performed using 3-(4,5-dimethylthiazol-2-yl)-2,5-diphenyltetrazolium bromide; Promega (MTT) assay. Briefly, cells were incubated with 0.5 $mg{\cdot}mL^{-1}$ MTT for 4 h to determine mitochondrial enzyme activity. Then, MTT precipitates were dissolved in 150 µl ethanol/DMSO solution (in proportion 1/1) and absorbance was read at 540 nm.

Photodynamic therapy (PDT). For *in vitro* PDT experiments, cells were seeded into 96-well plates, 1000 cells per well in 100 µL of culture medium, and let grow for 24 h. Then, cells were incubated with 10 µM **5**, **6** and **7** for 24 h. After incubation, cells were submitted (or not) to light irradiation (Mercury lamp of Leica DM.IRB fluorescence microscope, λ_{exc} = 545 nm, 15 min, 34 $J.cm^{-2}$). Two days after irradiation, living cells quantification was performed.

Confocal fluorescence imaging. The cellular uptake experiment was performed using confocal fluorescence microscope Zeiss 880 FastAiryscan on living cells. Capan-1 cells were seeded (10^6 $cells{\cdot}cm^{-2}$) on 8-well on cover glass II (Sarstedt). After seeding, cells were incubated with 10 µM of compounds for 24 h. Then, cells were loaded with CellMask (Invitrogen, Cergy Pontoise, France) at 5 $\mu g{\cdot}mL^{-1}$, for 15 min, for membrane staining. At the end of incubation times, cells were washed and visualized at λ_{exc} = 488 nm for compounds and λ_{exc} = 561 nm for cell membranes. All images were obtained with a high magnification (63x/1.4 OIL DIC Plan-Apo).

References

1. **a)** Roberson, M. G.; Duncan, J. M.; Flieth, K. J.; Geary, L. M.; Tucker, M. J., Photo-initiated rupture of azobenzene micelles to enable the spectroscopic analysis of antimicrobial peptide dynamics. *RSC advances* **2020,** *10* (36), 21464-21472. **b)** Walker, J. A.; Bohn, J.J; Ledesma, F; Sorkin, M.R; Kabaria, S.R; Thornlow, D.N; Alabi, C. A., *Bioconjugate Chemistry* **2019**, 30, 2452−2457; **c)** Lossouarn, A.; Renault, K.; Bailly, L.; Frisby, A.; Le Nahenec-Martel, P.; Renard, P.Y.; Sabot, C., *Organic & Biomolecular Chemistry* **2020**, 18, 3874-3887

2. Khalifah, R. G., The carbon dioxide hydration activity of carbonic anhydrase: I. Stop-flow kinetic studies on the native human isoenzymes B and C. *Journal of Biological Chemistry* **1971**, 246 (8), 2561-2573.

3. Küçükbay, H.; Gönül, Z.; Küçükbay, F. Z.; Angeli, A.; Bartolucci, G.; Supuran, C. T., Preparation, carbonic anhydrase enzyme inhibition and antioxidant activity of novel 7-amino-3, 4-dihydroquinolin-2 (1H)-one derivatives incorporating mono or dipeptide moiety. Journal of Enzyme Inhibition and Medicinal Chemistry **2020**, 35 (1), 1021-1026.

4. Awadallah, F. M.; Bua, S.; Mahmoud, W. R.; Nada, H. H.; Nocentini, A.; Supuran, C. T., Inhibition studies on a panel of human carbonic anhydrases with N 1-substituted secondary sulfonamides incorporating thiazolinone or imidazolone-indole tails. Journal of enzyme inhibition and medicinal chemistry 2018, 33 (1), 629-638.

5. Supuran, C. T., Carbon-versus sulphur-based zinc binding groups for carbonic anhydrase inhibitors? Journal of enzyme inhibition and medicinal chemistry 2018, 33 (1), 485-495.

6. Di Fiore, A.; De Simone, G.; Alterio, V.; Riccio, V.; Winum, J.-Y.; Carta, F.; Supuran, C. T., The anticonvulsant sulfamide JNJ-26990990 and its S, S-dioxide analog strongly inhibit carbonic anhydrases: solution and X-ray crystallographic studies. Organic & Biomolecular Chemistry 2016, 14 (21), 4853-4858.

Chapter IV

Thiochromenocarbazole imide-based photosensitizers decorated with carbonic anhydrase inhibitors for synergistic treatment of hypoxic tumours

Thiochromenocarbazole imide-based photosensitizers decorated with carbonic anhydrase inhibitors for the targeted treatment of hypoxic tumours Merabti, A.; Puchán Sánchez, D.; Nocentini, A.; M. A. Ali, L.; Nguyen, C.; Durand, D.; Hamon, K.; Ghanem, T.; Arnoux, P.; Josse, P.; Frochot, C.; Zalubovskis, R.; Richeter, S.; Gary-Bobo, M.; Supuran, C. T.; Cabanetos, C.; Winum, J.-Y.; Clément, S. accepted in Mater. Adv. DOI: 10.1039/d3ma00926b

Chapter IV: Thiochromenocarbazole imide-based photosensitizers decorated with carbonic anhydrase inhibitors for synergistic treatment of hypoxic tumours

I. Abstract

Hypoxia PDT has gained growing interest as a prospective approach for cancer therapy, thanks to its minimal invasiveness and low systemic toxicity, making it a promising therapeutic option. Nevertheless, type II PDT is significantly influenced by the oxygen levels in the tumoral microenvironment. Consequently, the weak oxygen pressure encountered in hypoxic regions of solid tumours poses a significant challenge in cancer treatment. In this case, PDT efficiency is reduced and the existing hypoxia is intensified by oxygen consumption and vascular closure, activating the angiogenic factors and thus, potentially leading to cancer recurrence and progression. We describe here a series of thiochromenocarbazole imide (TCI) photosensitizers featuring carbonic anhydrase inhibitors (CAi) of the sulfonamide, coumarin and sulfocoumarine type, designed to alleviate the consequences of PDT-induced hypoxia by merging the advantages of hCA IX knockdowns with PDT. TCIs with coumarin and sulfocoumarin moieties showed selective inhibition against tumour-associated hCA IX and hCA XII, while TCI incorporating benzenesulfonamide moieties also showed activity against the off-target hCA II. In biological assays, theTCI photosensitizer incorporating coumarin-based CAi demonstrated minimal dark toxicity and showcased strong imaging and photodynamic therapy (PDT) effects in both *in vitro* and *in vivo* settings.

Chapter IV: Thiochromenocarbazole imide-based photosensitizers decorated with carbonic anhydrase inhibitors for synergistic treatment of hypoxic tumours

II. Introduction

Photodynamic therapy (PDT) has emerged as a promising therapeutic approach for solid cancer treatment, due to its minimal invasiveness, high safety, and low systemic toxicity.[1-2] A typical PDT process involves the *in situ* formation of cytotoxic reactive oxygen species (ROS) such as singlet oxygen ($^1O_2$), peroxide (O_2^-), superoxide ($O_2^{\bullet-}$), and the hydroxyl radical ($HO^\bullet$) through the photoexcitation of a photosensitizer (PS), accumulated in the tumour, under appropriate light irradiation.[3-4] PDT process can be categorized into type **I** and type **II** depending on the photo-triggered reactions occurring between PS and the substances in its vicinity.[3-4] Specifically, the type **I** reaction involves either hydrogen atom abstraction or electron transfer, ultimately leading to the formation of radicals and hydrogen peroxide (H_2O_2) while type **II** leads to the generation singlet oxygen ($^1O_2$) by energy transfer from the electronically excited triplet-state PS to the ground-state molecular oxygen ($^3O_2$).[3-4] Type **II** PDT is the dominant mechanism since most of PS are type **II**.[3-4] Unfortunately, this dependency on the surrounding oxygen contradicts the inherent properties of tumour hypoxia.

Hypoxia is a salient and important feature of the tumour microenvironment found in solid tumours due to the fast tumour cell proliferation and the irregular vascular system within the tumour.[5] The oxygen pressure typically falls below 10 mmHg in the hypoxic regions of the tumour in contrast to the 40-60 mmHg range found in most healthy tissues.[6] Consequently, since type II PDT is highly dependent on oxygen concentrations, the hypoxic tumour microenvironment not only hampers the PDT efficiency but also, exacerbate the existing hypoxia by consuming oxygen and vascular closure.[7] Hypoxic cells respond to PDT-induced damages by activating signaling cascades mostly regulated by transcription factors HIFs (Hypoxia-Inducible Factors 1 and 2, HIF-1/2) and by releasing pro-angiogenic growth factors which sustain survival, stimulate metastasis, invasiveness, and recurrence of tumour cells.[8-9] Several strategies, including the direct delivery of exogenous oxygen to the tumour or the generation of oxygen *in situ*, have been developed to partially alleviate tumour hypoxia. [10-12] However, these methods provide only temporary oxygen supply and often result in modest degradation of HIF-1, which can significantly compromise PDT effectiveness. Consequently, the inhibition of the HIF-1 signaling pathway has emerged as a promising approach to mitigate tumour hypoxia.[10-12]

Human Carbonic Anhydrase IX (hCA IX) and another related isoform, hCA XII, are transmembrane proteins regulated by hypoxia-inducible factor (HIF) transcription factors, leading to their overexpression under hypoxic conditions.[13] These transmembrane isoforms hCA IX and hCA XII are member of the hCA family of zinc enzymes (CA, EC 4.2.1.1) which play a crucial role in regulating

the pH balance within tumours, thereby contributing to the survival, proliferation, invasion, and metastasis of cancer cells.[14] The overexpression and extracellular location of the active site of hCA IX/hCA XII in hypoxic cancer cells offer potential as a target for delivering PS to cancer cells in PDT, with the aim of addressing the limitations associated with this treatment approach. In 2017, Jung *et al.* described the synthesis of a BODIPY-based PS featuring hCA IX inhibitor (CAi) acetazolamide (AAZ).[15] This PS, designed to specifically target hCA IX, exhibited significantly improved effectiveness in causing phototoxicity *in vitro* against the aggressive human breast cancer MDA-MB-231 cell line, both in standard culture and in a spheroid model. Moreover, its ability to suppress tumour growth *in vivo* was also demonstrated when tested on xenograft mice inoculated with MDA-MB-231 cells. Since this pioneering work, series of CAi-PS systems including conjugated polymer,[16] metal organic framework,[17-18] porphyrins,[19-21] and metal complexes were developped.[22-25] We recently reviewed all these systems highlighting that a synergistic treatment that enhances the PDT effect against hypoxic cancer cells and reduces resistance can be achieved by combining a PS with a CAi.[26] Nevertheless, although these studies have yielded promising results thus far, it is worth noting that comprehensive inhibition studies against recombinant proteins such as hCA IX, hCA XII, as well as the cytosolic off-targets hCA I and hCA II, have only rarely been carried out.[26]

Herein, we design a series of CAi-PS hybrid system incorporating as CAi either a classical benzenesulfonamide chemotype, known to strongly inhibit hCA isoforms with high potency, or coumarin and sulfocoumarin-based moieties more selective for hCA IX and XII.[27-29] Considering PS, we exploit a metal-free PS, the thiochromenocarbazole imide (TCI) block due to its moderate synthetic cost and its synthetic versatility allowing to fine tune the photophysical properties (fluorescence quantum yield, singlet oxygen generation…).[30-31] We describe here the synthesis, optical properties as well as detailed biological and PDT studies on the human breast adenocarcinoma (MDA-MB-231) cell line of this innovative CAi-TCI hybrid system.

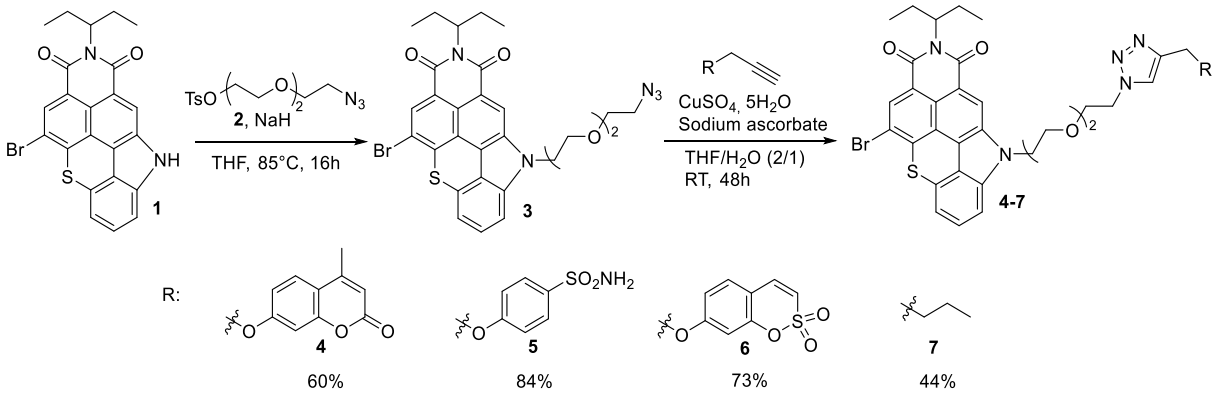
III. Results and discussion

III.1 Design and synthesis

The synthetic route to a series of TCI PS featuring CAIs is illustrated in **Scheme 4**. This series of PSs was achieved by formation of a 1,2,3-triazole bridge between a carbonic anhydrase inhibitor (coumarin, benzenesulfonamide and sulfocoumarin) and TCI-based PS through a Cu(I)-catalyzed 1,3-dipolar cycloaddition. A TCI PS without hCA IX inhibitor **7** was also prepared from hex-1-yne serving as

control system (**Scheme 4**). Azido-functionalized TCI PS **3** was prepared in 68% yield by *N*-alkylation of CTI **1** with 2-[2-(2-azidoethoxy)ethoxy]ethyl 4-methylbenzenesulfonate **2** in THF at 85°C in the presence of sodium hydride. The structure of TCI **3** was confirmed by IR spectroscopy by the strong asymmetric stretching frequency at 2111 cm^{-1} related to the azido group. High-resolution ESI-TOF mass spectrometry (positive mode) also revealed the presence of pseudo-molecular ion $[M+H]^+$ at *m/z* = 622.1105 Da in agreement with the calculated one (calcd *m/z* = 622.1118 Da).

Alkyne-substituted carbonic anhydrase inhibitors were then grafted to azido-functionalized TCI **3** via copper catalyzed azide alkyne cycloaddition reaction in a mixture of THF-H_2O, affording the TCI-CAi-based PS **4**-**6** with yields ranging from 60 % to 84 %. A control system without CA inhibitor was also elaborated through the reaction of TCI **3** with hex-1-yne (**Scheme 4**). The disappearance of the strong N_3 stretching bands in the ATR-FTIR of the TCI **4**-**7** confirmed that the cycloaddition occurred. The formation of the triazole ring was also corroborated by ^{1}H NMR spectroscopy and the presence of an additional singlet between 7.20 and 7.90 ppm. Finally, the presence of monocation $[M+H]^+$ was also observed in the high-resolution ESI-TOF mass spectra (positive mode) of all CAi-TCI PSs **4**-**6** as well as control PS **7**



Scheme 4. Synthetic route to CAi-based TCIs.

III.2 Optical properties

All molecules were studied in diluted DMF solutions and their absorption, maximum emission wavelength, fluorescence quantum yield and lifetime were systematically studied. The absorption and emission spectra of CAi-TCI **4** are depicted in **Figure 81** as an example. All the CAi-TCI hybrid systems exhibit two broad absorption bands centered at around 410 nm and 480 nm corresponding to the absorption of the TCI central core. These CAi-TCI hybrid systems exhibit a broad emission band at

532 nm with moderate Stokes shift (~50 nm) and fluorescence quantum yields between 0.13 and 0.20 using rose bengal as a reference (ΦF = 0.11 in EtOH).[32]

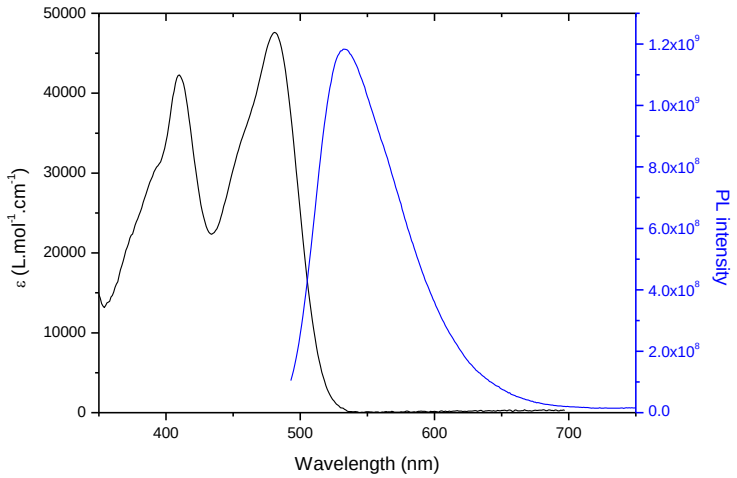


Figure 81. UV-visible absorption (black) and emission spectra (blue) of CAi-TCI **4** in DMF (C= 10^{-5} mol.L^{-1}, λ_{exc} = 435 nm).

The ability of CAi-TCI hydrid systems **4**-**7** to generate $^1O_2$ was then evaluated by monitoring its photoluminescence (PL) at 1270 nm in aerated DMF using rose bengal as a reference (Φ_Δ = 0.40).[33] As shown in **Table 7**, the nature of CAi had very little effect on the production of $^1O_2$ with $^1O_2$ yield between 0.3-0.4 for all TCIs **4**, **6**, **7** whereas in the case of **5**, a little lower $^1O_2$ yield is noticed. These yields are in the same range as that of rose bengal.[33] Indeed, the presence of a halogen substituent, namely bromine, on TCI core enables efficient $^1O_2$ generation due to increased singlet-to-triplet Inter-System Crossing (ISC) owing to the so-called heavy atom effect.[30]

Compounds	λ_{abs} (nm)	λ_{em} (nm)	ϕ_F	τ_{obs}	$\phi\Delta$
4	410, 481	532	0.20	7.6	0.36
5	412, 483	532	0.18	7	0.25
6	410, 480	532	0.13	9.8	0.31
7	410, 480	532	0.18	6.7	0.39

Rose bengal was used as reference both for determining fluorescence quantum yields[a] and singlet oxygen generation efficiency[b]

Table 7. Summary of the main spectroscopic and photophysical data for all studied CAi-TCI hybrid systems.

Chapter IV: Thiochromenocarbazole imide-based photosensitizers decorated with carbonic anhydrase inhibitors for synergistic treatment of hypoxic tumours

III.3 Carbonic anhydrase inhibition assays

The CAi-TCI hybrid systems **4**-**7** were subsequently assessed for their inhibitory activity against carbonic anhydrases, using a stopped-flow assay method. Four clinically relevant human isoforms were investigated including the two cytosolic off-targets, hCA I and hCA II, along with two tumor-associated membrane-bound isoforms, hCA IX and hCA XII. The clinically used acetazolamide (AAZ) served as a reference drug (**Table 8**).

Compounds	K_I **(nM)**[a]			
	Cytosolic		**Membrane-bound**	
	hCA I	hCA II	hCA IX	hCA XII
4	>100 µM	>100 µM	86.2	45.3
5	89.5	28.7	42.9	21.3
6	>100 µM	>100 µM	76.9	48.2
7	>100 µM	>100 µM	>100 µM	>100 µM
AAZ	250	12	25	5.7

[a] Mean from 3 different measurements by a stopped flow technique (errors were in the range of 5-10% of the reported values).

Table 8. Inhibitory activity of CAi-TCI **4**–**7** against **hCA I**, **hCA II**, **hCA IX** and **hCA XII** using acetazolamide (AAZ) as reference drug.

As anticipated, the negative control **7**, which lacks a pharmacophoric CA inhibitory moiety, exhibited no inhibitory activity (*Ki*>100 µM) against the four tested isoforms. When compared to the standard drug **AAZ**, which effectively inhibits all four CA isoforms considered in this study, analogues **4**, **5** and **6** exhibited lower effectiveness as hCA IX and XII inhibitors. However, derivatives **4** and **6** displayed strong selectivity, as neither of them inhibited the cytosolic off-targets hCA I and hCA II. Specifically, coumarin derivative **4** and sulfocoumarin derivative **6** demonstrated identical activity profiles against the membrane-bound isoforms, with inhibitory activity against hCA IX at 86.2 and 76.9 nM, respectively, and slightly improved inhibitory activity against hCA XII, with Ki values of 45.3 and 48.2 nM, respectively. Although compound **5** displayed one of the best inhibition values against hCA IX and hCA XII, with inhibition constants of 42.9 and 21.3 nM, respectively, it exhibited the same inhibitory

profile against hCA I and hCA II. Given the absence of selectivity exhibited by compound **5**, we will only consider the selective inhibitors **4** and **6**, along with the negative control **7**, in the biological studies.

III.4 Biological studies *in vitro*

The biological potential of **4**, **6** and **7** was studied both in vitro and *in vivo*. First, human breast cancer cell line (MDA-MB-231) was used to establish the dark cytotoxicity of these three compounds. **Figure 82A** describes the cell viability after 72 h of incubation with increasing concentrations of **4**, **6** and **7** (from 0.1 to 100 µg.mL^{-1}). As observed, **4** and **6** exhibit relatively low toxicity in the studied condition while **7** is strongly toxic from 5 µg.mL^{-1}. In order to clearly demonstrate a PDT effect without any dark toxicity background, we performed the PDT experiments by incubating cells with only 0.5 µg.mL^{-1} (**Figure 82B**).

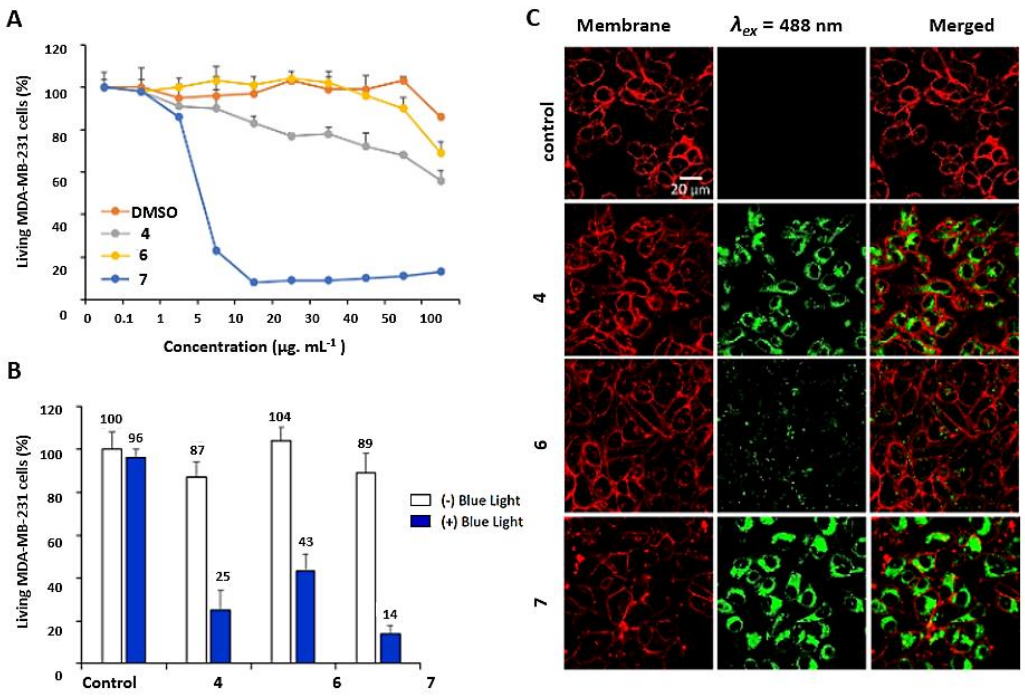


Figure 82. (A) Toxicity study in human breast cancer cell line (MDA-MB 231) incubated 3 days with increasing concentrations of **4**, **6**, **7** and the corresponding volume of the vehicle (DMSO). Values are mean ± SEM of three experiments. **(B)** Phototoxic effect of **4**, **6**, **7** on MDA-MB 231 cells incubated with 0.5 µg.mL^{-1} of compounds for 24 h then exposed to blue light at 469-494 nm for 30 seconds using EVOS. Cell viability was quantified after 48 h. Results are presented as mean ± SEM of three experiments. **(C)** Confocal microscopy imaging of living MDA-MB-231 cells incubated with 10 µg.mL^{-1} of **4**, **6**, **7** for 24 h using confocal microscopy LSM780.

For this, MDA-MB-231 cells were incubated 24 h with 0.5 µg.mL^{-1} and excited during 30 s with a blue LED source (470 ± 22 nm). Two days after, living cells were quantified and **Figure 82B** showed that compounds **4**, **6** and **7** are very efficient to kill cancer cells by PDT with 75%, 57 % and 86% of cell death induced by light excitation, respectively. Then, we decided to analyze the imaging potential of such compounds by incubating cells with 10 µg.mL^{-1} for 24 h. **Figure 82C** highlights the strong fluorescence of compounds **4** and **7** and the localisation inside the cells, which suggests their potential for imaging of living cells.

These data demonstrate that **4** exhibits a low toxic level without specific excitation, a strong PDT and imaging potential. The compound **6** is not toxic in the studied conditions without excitation, but it is the less efficient in PDT and particularly, in imaging. Finally, while compound **7** may be deemed the most effective choice for imaging and PDT, its notable high toxicity above **5** µg.mL^{-1} stems from its lack of specificity, as it can be internalized by all cells owing to its lipophilic properties.

III.5 Biological studies *in vivo*

These highly encouraging results on cells led us to test their effectiveness in vivo, on zebrafish embryos. This is a particularly well-suited substitute animal model for small mammals to study biocompatibility, PDT and imaging.[34-35] We first injected the three compounds in the intravenous system of embryos. More precisely, 10 nL of **4**, **6** and **7** at a concentration of 1 mg.mL^{-1} in 5% glucose were injected in the tail vein of embryos at 72 hours post-fertilization (hpf) in order to reach a final concentration around 14 µg.mL^{-1} (**Figure 83**). As observed *in vitro*, at a first sight, all compounds were luminescent and very well dispersed in the embryos, suggesting a good bioavailability, but analogue **6** was the least fluorescent. **4** was also well-dispersed and particularly luminescent when observed in the same condition as **6**, that is 3 hours after injection and using a laser power of 30 %.

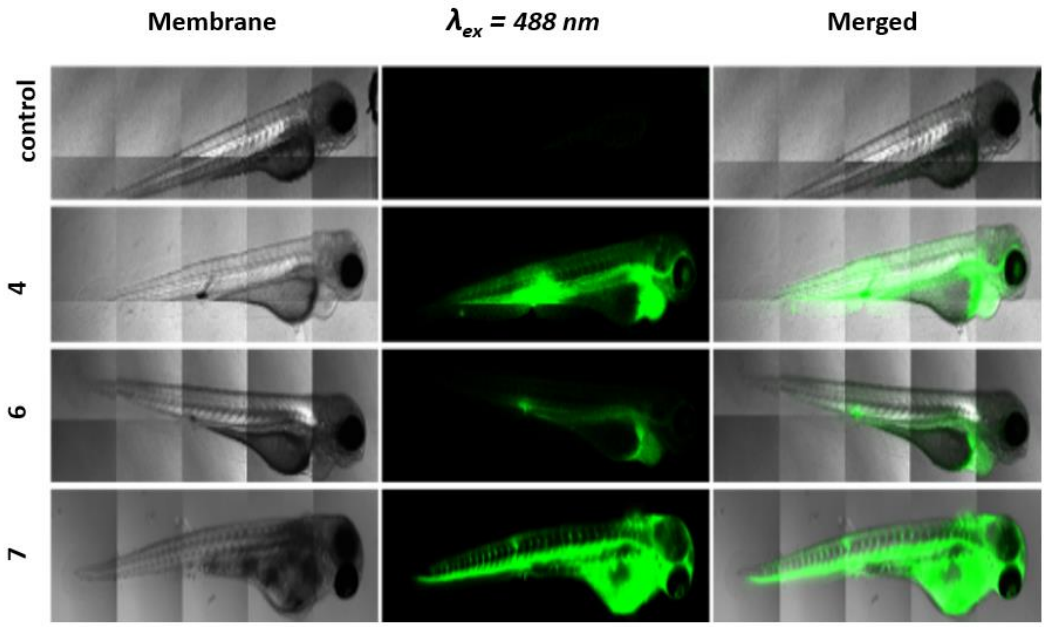


Figure 83. Casper zebrafish embryos at 72 hours post-fertilization (hpf) were injected with 10 nL of **4**, **6**, **7** at a concentration of 1 mg.mL^{-1} in 5% glucose (Final concentration ~ 14 µg.mL^{-1}). Embryos injected with **4** and **6** were observed with LSM880 (Laser power 30%) 3 h post-injection. Embryos injected with **7** were observed with LSM880 (Laser power 1%) immediately after injection

Finally, negative control **7** exhibiting a tremendous brightness is visualized at only 1% laser power and immediately after injection because embryos died in the minutes following the injection. Taking all these results into account, we concluded that compound **4** was the most effective in terms of imaging and PDT, while maintaining a high level of safety.

So, we decided to study its PDT activity *in vivo*. For this, MDA-MB-231 cells stably expressing red fluorescent protein were injected in the yolk of 30 hpf embryos. These MDA-MB-231 cells were previously treated (or not) with 10 µg.mL^{-1} of compound **4** for 24 h (**Figure 84**).Twenty-four hours after cell injection, embryos were imaged then, exposed to blue light for 2 min. One day later, embryos were imaged again in order to monitor the xenograft growth. By quantifying the fluorescence intensity of the xenograft before and after light exposure, results (**Figure 84**) show the high efficiency of compound **4** to eradicate the tumours.

Chapter IV: Thiochromenocarbazole imide-based photosensitizers decorated with carbonic anhydrase inhibitors for synergistic treatment of hypoxic tumours

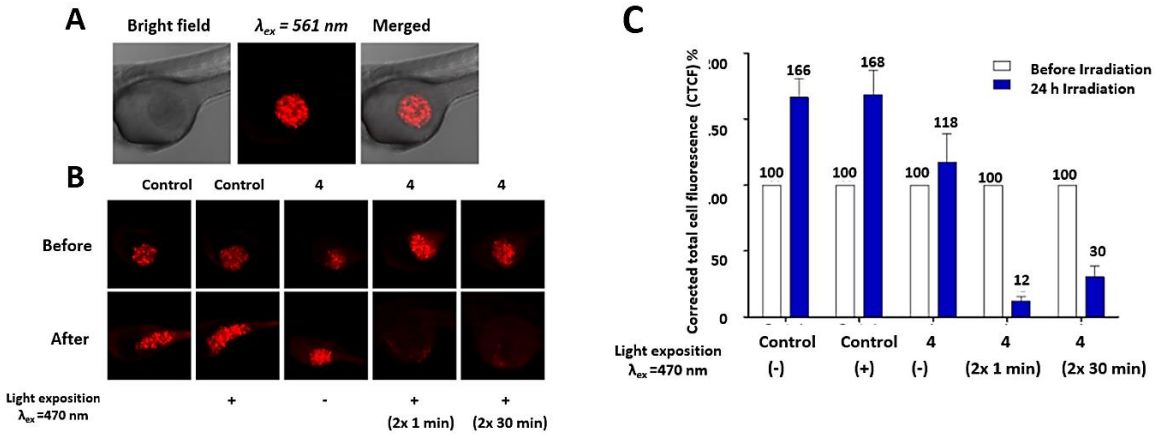


Figure 84. **(A)** Casper zebrafish embryos at 30 hpf were used for the microinjection of red fluorescent cells (MDA-MB-231-Luc-RFP) previously incubated (or not) with **4**. Each embryo received 10 nL of cell suspension in the yolk. Injected Casper embryos with cells without **4** were used as the control. **(B)** Twenty-four hours after injection, the embryos were exposed or not to light excitation (470 nm) (n=10/group) during 2 or 1 min (λ_{ex} = 470 ± 22 nm, 9.41 J cm^{-2}). **(C)** The fluorescence intensity of the xenografts before and 24 h after irradiation were quantified using ImageJ program. The corrected total cell fluorescence (CTCF) was calculated as CTCF = Integrated Density – (Area of selected cell X Mean fluorescence of background readings) and the tumour regression (%) was calculated by considering the fluorescence intensity value of each embryo before irradiation is 100%.

III.6 Conclusions

In summary, we have successfully designed and synthesized thiochromenocarbazole imide derivatives incorporating carbonic anhydrase inhibitor moiety. Among the three CAi-TCI hybrid systems that were subject to biological assays, compound **4**, featuring the selective hCA IX / h CA XII coumarin inhibitor, displayed low dark toxicity and exhibited robust imaging and PDT effects both *in vitro* and *in vivo*. Interestingly, the negative-control compound **7**, lacking pharmacophoric scaffold able to inhibit CA, surprisingly demonstrated significant imaging and PDT effects, albeit with high toxicity. The high lipophilicity of this non-targeted photosensitizer may account for its effectiveness, as it can readily penetrate various cell types, thereby explaining its significant toxicity. This underscores the importance of focusing on therapeutic targets, such as relevant carbonic anhydrase isoforms, to address this issue. Altogether, this study provides a valuable resource for the study of innovative photosensitizers linked to selective carbonic anhydrase inhibitors, with potential applications in imaging and PDT.

Chapter IV: Thiochromenocarbazole imide-based photosensitizers decorated with carbonic anhydrase inhibitors for synergistic treatment of hypoxic tumours

IV. References

1. Jiang, W.; Liang, M.; Lei, Q.; Li, G.; Wu, S., The Current Status of Photodynamic Therapy in Cancer Treatment. *Cancers* **2023,** *15* (3), 585.

2. Alsaab, H. O.; Alghamdi, M. S.; Alotaibi, A. S.; Alzhrani, R.; Alwuthaynani, F.; Althobaiti, Y. S.; Almalki, A. H.; Sau, S.; Iyer, A. K., Progress in clinical trials of photodynamic therapy for solid tumors and the role of nanomedicine. *Cancers* **2020,** *12* (10), 2793.

3. Celli, J. P.; Spring, B. Q.; Rizvi, I.; Evans, C. L.; Samkoe, K. S.; Verma, S.; Pogue, B. W.; Hasan, T., Imaging and Photodynamic Therapy: Mechanisms, Monitoring, and Optimization. *Chem. Rev.* **2010,** *110* (5), 2795-2838.

4. Kwiatkowski, S.; Knap, B.; Przystupski, D.; Saczko, J.; Kędzierska, E.; Knap-Czop, K.; Kotlińska, J.; Michel, O.; Kotowski, K.; Kulbacka, J., Photodynamic therapy–mechanisms, photosensitizers and combinations. *Biomedicine & pharmacotherapy* **2018,** *106*, 1098-1107.

5. Challapalli, A.; Carroll, L.; Aboagye, E. O., Molecular mechanisms of hypoxia in cancer. *Clinical and translational imaging* **2017,** *5*, 225-253.

6. Brown, J. M.; Wilson, W. R., Exploiting tumour hypoxia in cancer treatment. *Nature Reviews Cancer* **2004,** *4* (6), 437-447.

7. Atkuri, K. R.; Herzenberg, L. A.; Niemi, A.-K.; Cowan, T.; Herzenberg, L. A., Importance of culturing primary lymphocytes at physiological oxygen levels. *Proceedings of the National Academy of Sciences* **2007,** *104* (11), 4547-4552.

8. Petrova, V.; Annicchiarico-Petruzzelli, M.; Melino, G.; Amelio, I., The hypoxic tumour microenvironment. *Oncogenesis* **2018,** *7* (1), 10.

9. Chen, G.; Wu, K.; Li, H.; Xia, D.; He, T., Role of hypoxia in the tumor microenvironment and targeted therapy. *Frontiers in Oncology* **2022,** *12*, 961637.

10. Larue, L.; Myrzakhmetov, B.; Ben-Mihoub, A.; Moussaron, A.; Thomas, N.; Arnoux, P.; Baros, F.; Vanderesse, R.; Acherar, S.; Frochot, C., Fighting hypoxia to improve PDT. *Pharmaceuticals* **2019,** *12* (4), 163.

11. Wan, Y.; Fu, L. H.; Li, C.; Lin, J.; Huang, P., Conquering the hypoxia limitation for photodynamic therapy. *Advanced Materials* **2021,** *33* (48), 2103978.

12. Shen, R.; Li, P.; Wang, D.; Jiang, Q.; Yu, C.; Hu, F.; Ji, J.; Yuan, H., Polymer-Modified Lipid Nanoparticles with Microenvironment-Responsive Graded Release for Amplified Photodynamic Therapy Through Tumor Vascular Normalization. *ACS Applied Nano Materials* **2023,** *6* (14), 13352-13362.

13. Supuran, C. T., A simple yet multifaceted 90 years old, evergreen enzyme: Carbonic anhydrase, its inhibition and activation. *Bioorganic & Medicinal Chemistry Letters* **2023**, 129411.

14. Kalinin, S.; Malkova, A.; Sharonova, T.; Sharoyko, V.; Bunev, A.; Supuran, C. T.; Krasavin, M., Carbonic anhydrase IX inhibitors as candidates for combination therapy of solid tumors. *International Journal of Molecular Sciences* **2021,** *22* (24), 13405.

15. Jung, H. S.; Han, J.; Shi, H.; Koo, S.; Singh, H.; Kim, H.-J.; Sessler, J. L.; Lee, J. Y.; Kim, J.-H.; Kim, J. S., Overcoming the limits of hypoxia in photodynamic therapy: a carbonic anhydrase IX-targeted approach. *Journal of the American Chemical Society* **2017,** *139* (22), 7595-7602.

16. Jiang, Y.; Li, J.; Zeng, Z.; Xie, C.; Lyu, Y.; Pu, K., Organic photodynamic nanoinhibitor for synergistic cancer therapy. *Angewandte Chemie International Edition* **2019,** *58* (24), 8161-8165.

17. Zhu, W.; Liu, Y.; Yang, Z.; Zhang, L.; Xiao, L.; Liu, P.; Wang, J.; Yi, C.; Xu, Z.; Ren, J., Albumin/sulfonamide stabilized iron porphyrin metal organic framework nanocomposites: Targeting tumor hypoxia by carbonic anhydrase IX inhibition and T 1–T 2 dual mode MRI guided photodynamic/photothermal therapy. *Journal of Materials Chemistry B* **2018,** *6* (2), 265-276.

18. Zhu, W.; Zhang, L.; Yang, Z.; Liu, P.; Wang, J.; Cao, J.; Shen, A.; Xu, Z., An efficient tumor-inducible nanotheranostics for magnetic resonance imaging and enhanced photodynamic therapy. *Chemical Engineering Journal* **2019,** *358*, 969-979.

19. Fan, G.-L.; Yuan, P.; Deng, F.-A.; Liu, L.-S.; Miao, Y.-L.; Wang, C.; Qiu, X.-Z.; Yu, X.-Y.; Cheng, H.; Li, S.-Y., Self-delivery photodynamic nanoinhibitors for tumor targeted therapy and metastasis inhibition. *ACS Applied Bio Materials* **2020,** *3* (9), 6124-6130.

20. Wang, F.; Xu, T.; Meerovich, G.; Hong, F.; Chen, Z.-L.; Yan, Y.-J., Synthesis and evaluation of new pyropheophorbide-a derivatives for CAIX-targeted photodynamic therapy. *Dyes and Pigments* **2022,** *203*, 110328.

21. Merabti, A.; Roger, M.; Nguyen, C.; Nocentini, A.; Gerbier, P.; Richeter, S.; Gary-Bobo, M.; Supuran, C. T.; Clément, S.; Winum, J. Y., Carbonic anhydrase inhibitors featuring a porphyrin scaffold: synthesis, optical and biological properties. *European Journal of Organic Chemistry* **2022,** *2022* (21), e202101538.

22. Su, X.; Wang, W. J.; Cao, Q.; Zhang, H.; Liu, B.; Ling, Y.; Zhou, X.; Mao, Z. W., A carbonic anhydrase IX (CAIX)-anchored rhenium (I) photosensitizer evokes pyroptosis for enhanced anti-tumor immunity. *Angewandte Chemie International Edition* **2022,** *61* (8), e202115800.

23. Kumar, P.; Singh, P.; Saren, S.; Sayala, J.; Sivakumar, S.; Patra, A. K., Quaternary Ru (ii) complexes of terpyridines, saccharin and 1, 2-azoles: effect of substituents on molecular structure, speciation, photoactivity, and photocytotoxicity. *Dalton Transactions* **2022,** *51* (48), 18416-18437.

24. Hao, L.; Wang, J.; Pan, Z.-Y.; Mao, Z.-W.; Tan, C.-P., Photodegradation of carbonic anhydrase IX via a binding-enhanced ruthenium-based photosensitizer. *Chemical Communications* **2022,** *58* (58), 8069-8072.

25. Jung, H. S.; Koo, S.; Won, M.; An, S.; Park, H.; Sessler, J. L.; Han, J.; Kim, J. S., Cu (ii)-BODIPY photosensitizer for CAIX overexpressed cancer stem cell therapy. *Chemical Science* **2023,** *14* (7), 1808-1819.

26. Merabti, A.; Richeter, S.; Supuran, C. T.; Clement, S.; Winum, J.-Y., Are tumor-associated carbonic anhydrases genuine therapeutic targets for photodynamic therapy? *Expert Opinion on Therapeutic Targets* **2023,** (just-accepted).

27. Angeli, A.; Carta, F.; Nocentini, A.; Winum, J.-Y.; Zalubovskis, R.; Akdemir, A.; Onnis, V.; Eldehna, W. M.; Capasso, C.; Simone, G. D., Carbonic anhydrase inhibitors targeting metabolism and tumor microenvironment. *Metabolites* **2020,** *10* (10), 412.

28. Mishra, C. B.; Tiwari, M.; Supuran, C. T., Progress in the development of human carbonic anhydrase inhibitors and their pharmacological applications: Where are we today? *Medicinal Research Reviews* **2020,** *40* (6), 2485-2565.

29. Supuran, C. T., Targeting carbonic anhydrases for the management of hypoxic metastatic tumors. *Expert Opinion on Therapeutic Patents* **2023**, 1-20.

30. Galán, L. A.; Castán, J. M. A.; Dalinot, C.; Marqués, P. S.; Blanchard, P.; Maury, O.; Cabanetos, C.; Le Bahers, T.; Monnereau, C., Theoretical and experimental investigation on the intersystem crossing kinetics in benzothioxanthene imide luminophores, and their dependence on substituent effects. *Physical Chemistry Chemical Physics* **2020,** *22* (22), 12373-12381.

31. Castán, J. M. A.; Amruth, C.; Josse, P.; Galan, L. A.; Marqués, P. S.; Allain, M.; Maury, O.; Le Bahers, T.; Blanchard, P.; Monnereau, C., Thiochromenocarbazole imide: a new organic dye with first utility in large area flexible electroluminescent devices. *Materials Chemistry Frontiers* **2022,** *6* (14), 1912-1919.

32. SEYBOLD, P. G.; GOUTERMAN, M.; CALLIS, J., Calorimetric, photometric and lifetime determinations of fluorescence yields of fluorescein dyes. *Photochemistry and photobiology* **1969,** *9* (3), 229-242.

33. Redmond, R. W.; Gamlin, J. N., A compilation of singlet oxygen yields from biologically relevant molecules. *Photochemistry and photobiology* **1999,** *70* (4), 391-475.

34. Chen, Z.; Pascal, S.; Daurat, M.; Lichon, L.; Nguyen, C.; Godefroy, A.; Durand, D.; Ali, L. M.; Bettache, N.; Gary-Bobo, M., Modified Indulines: From Dyestuffs to In Vivo Theranostic Agents. *ACS Applied Materials & Interfaces* **2021,** *13* (26), 30337-30349.

35. Hamon, N.; Roux, A.; Beyler, M.; Mulatier, J.-C.; Andraud, C.; Nguyen, C.; Maynadier, M.; Bettache, N.; Duperray, A.; Grichine, A., Pyclen-based Ln (III) complexes as highly luminescent bioprobes for in vitro and in vivo one-and two-photon bioimaging applications. *Journal of the American Chemical Society* **2020,** *142* (22), 10184-10197.

36. Roberson, M. G.; Duncan, J. M.; Flieth, K. J.; Geary, L. M.; Tucker, M. J., Photo-initiated rupture of azobenzene micelles to enable the spectroscopic analysis of antimicrobial peptide dynamics. *RSC advances* **2020,** *10* (36), 21464-21472.

37. Khalifah, R. G., The carbon dioxide hydration activity of carbonic anhydrase: I. Stop-flow kinetic studies on the native human isoenzymes B and C. *Journal of Biological Chemistry* **1971,** *246* (8), 2561-2573.

38. Küçükbay, H.; Gönül, Z.; Küçükbay, F. Z.; Angeli, A.; Bartolucci, G.; Supuran, C. T., Preparation, carbonic anhydrase enzyme inhibition and antioxidant activity of novel 7-amino-3, 4-dihydroquinolin-2 (1H)-one derivatives incorporating mono or dipeptide moiety. *Journal of Enzyme Inhibition and Medicinal Chemistry* **2020,** *35* (1), 1021-1026.

39. Awadallah, F. M.; Bua, S.; Mahmoud, W. R.; Nada, H. H.; Nocentini, A.; Supuran, C. T., Inhibition studies on a panel of human carbonic anhydrases with N 1-substituted secondary sulfonamides incorporating thiazolinone or imidazolone-indole tails. *Journal of enzyme inhibition and medicinal chemistry* **2018,** *33* (1), 629-638.

40. Supuran, C. T., Carbon-versus sulphur-based zinc binding groups for carbonic anhydrase inhibitors? *Journal of enzyme inhibition and medicinal chemistry* **2018,** *33* (1), 485-495.

41. Di Fiore, A.; De Simone, G.; Alterio, V.; Riccio, V.; Winum, J.-Y.; Carta, F.; Supuran, C. T., The anticonvulsant sulfamide JNJ-26990990 and its S, S-dioxide analog strongly inhibit carbonic anhydrases: solution and X-ray crystallographic studies. *Organic & Biomolecular Chemistry* **2016,** *14* (21), 4853-4858.

Chapter IV: Thiochromenocarbazole imide-based photosensitizers decorated with carbonic anhydrase inhibitors for synergistic treatment of hypoxic tumours

V. Supplementary data

V.1 Chemistry

V.1.1 Materials

Reactions needing inert atmosphere were performed under argon using oven-dried glassware and Schlenk techniques. All solvents were obtained from commercial suppliers and used as received. 4-hydroxybenzaldehyde (TCI, 98%), caesium carbonate (Cs_2CO_3, Fluorochem, 99%), pyrrole (Fluorochem, 99%), tifluoroacetic acid (TFA, Alfa Aesar, 99%), 2,3-dichloro-5,6-dicyano-1,4-benzoquinone (DDQ, Acros Organics, 98%), triethylamine (Fluorochem, 99%), zinc(II) acetate dihydrate ($Zn(OAc)_2.2H_2O$, Sigma-Aldrich, >98%), copper (II) sulfate pentahydrate ($CuSO_4.5H_2O$, Fluorochem, 98%), sodium ascorbate (Fluorochem, 99%), Ethylenediaminetetraacetic acid disodium salt dihydrate EDTA (Sigma-Aldrich, 99%), hexyne (Sigma-Aldrich, 98%) were used as received. Compound **1**, **Sulfo-prop** and **Coum-prop** were prepared according to literature procedure.[1] TLC were carried out on Merck DC Kieselgel 60 F-254 aluminium sheets and spots were visualized with UV-lamp (λ = 254/365 nm) if necessary. Preparative purifications were performed by silica gel column chromatography (Merck 40−60 μM).

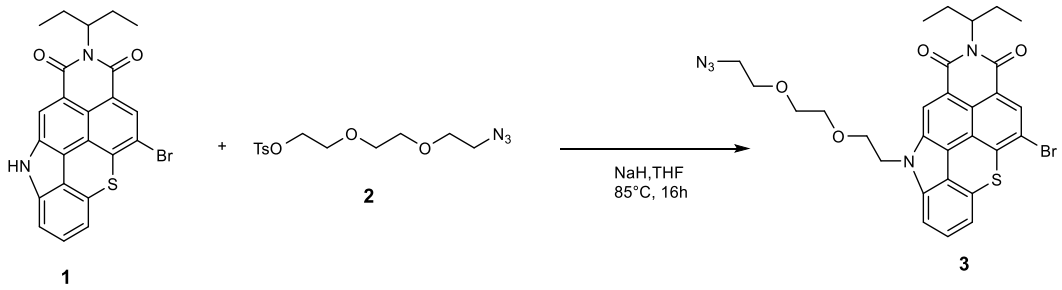
V.2 General instruments

IR spectra were carried out on a Perkin Elmer Spectrum 2 FT-IR instrument using the attenuated total reflectance (ATR) measurement mode (diamond crystal). The wavenumber range analyzed was 500-4000 cm^{-1} and the optical resolution of the instrument was 4 cm^{-1}. NMR spectroscopy and mass spectrometry were performed at the Laboratoire de Mesures Physiques (LMP) of the University of Montpellier (UM). ^1H and $^{13}C\{^1H\}$ NMR spectra were recorded either on Bruker 400 MHz Avance III HD or 500 MHz Avance III spectrometers at 298 K. Deuterated solvents $CDCl_3$ was used as received (purchased from Sigma-Aldrich). ^1H and $^{13}C\{^1H\}$ NMR spectra were calibrated to TMS based on the relative chemical shift of the residual non-deuterated solvent as an internal standard. Chemical shifts (δ) are expressed in ppm and coupling constants values (^nJ) are expressed in Hz. Abbreviations used for NMR spectra are as follows: s: singlet; d: doublet, t: triplet, q: quadruplet; quint: quintuplet, sx: sextuplet and m: multiplet. High Resolution Mass spectra (HRMS) were recorded on a Bruker MicroTof QII instrument in positive modes (ESI). UV-Visible absorption spectra were recorded in DMF with a JASCO V-750 UV-Visible-NIR spectrophotometer in 10 mm quartz cells (Hellma); molar extinction coefficients ε ($L.mol^{-1}.cm^{-1}$) are expressed as log ε. The extinction coefficients were determined by

preparing solutions of BTXI derivatives at different concentrations in DMF. The concentration range was chosen to remain in the linear range of the Beer–Lambert relationship (*A ca*. 0.2– 0.8).

V.3 Synthesis and characterization

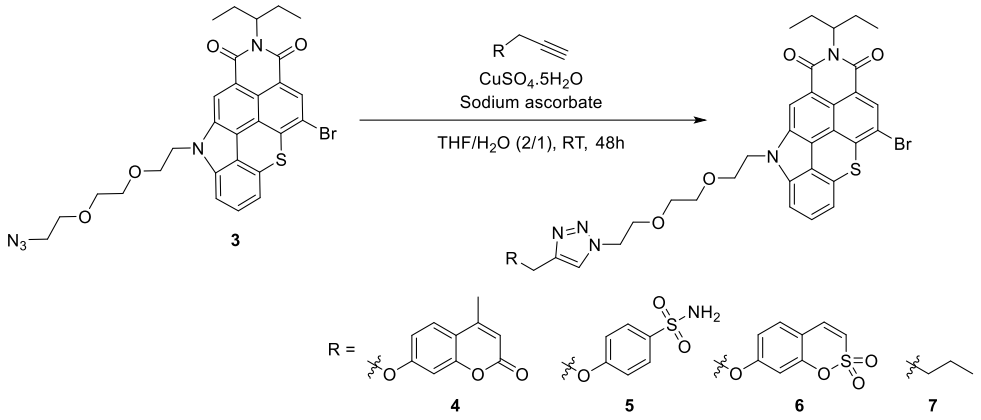
Synthesis of compound 3



Scheme 5: Synthesis of compound 3.[2]

A solution of compound **1** (50 mg, 0.107 mmol) and sodium hydride 60 % (22 mg, 0.535 mmol, 5 equiv.) in THF (10 mL) was stirred for 15 minutes at room temperature under inert atmosphere. Compound **2**[2] (44 mg, 0.133 mmol, 1.25 equiv) was then added to the resulting solution and the mixture was stirred under reflux overnight. The *N*-alkylation was followed by TLC (6/4, cyclohexane/ ethyl acetate). When it was judged finished, the solvent was evaporated under reduced pressure and the residue was diluted with CH_2Cl_2. The organic layer was washed several times with 200 mL of water, dried over anhydrous $MgSO_4$, filtered, and concentrated. The residue was purified by column chromatography on silica gel (6/4, cyclohexane/ ethyl acetate, R_F= 0.34) to obtain compound **3** as an orange solid (45 mg, yield: 68 %). ATR-FTIR: $\tilde{\nu}$ (cm^{-1}) =2111 (ν_{N3}), 1630 (ν_{CO}). **^{1}H NMR** (400 MHz, $CDCl_3$) δ 8.69 (s, 1H), 8.40 (s, 1H), 7.47 (t, $^3J_{H\text{-}H}$ = 7.91 Hz, 1H), 7.23 (d, $^3J_{H\text{-}H}$ = 7.53 Hz, 1H), 7.10 (d, $^3J_{H\text{-}H}$ = 7.53 Hz, 1H), 5.09 (m, 1H), 4.58 (t, $^3J_{H\text{-}H}$ = 5.34 Hz, 2H), 3.94 (t, $^3J_{H\text{-}H}$ = 5.34 Hz, 2H), 3.53 (m, 6H), 3.25 (t, 2H, $^3J_{H\text{-}H}$ = 5.00 Hz), 2.26 (m, 2H), 1.93 (m, 2H), 0.90 (t, $^3J_{H\text{-}H}$ = 7.5 Hz, 6H). **^{13}C{^{1}H} NMR** (126 MHz, $CDCl_3$): δ 144.9, 141.3, 134.6, 133.4, 130.0 , 129.8, 123.0, 122.0, 119.0, 114.1, 107.8, 71.2, 71.1, 70.3, 69.4, 69.0, 57.7, 50.8, 45.2, 25.2, 21.8, 11.5. **HRMS (ESI$^+$)** ***m/z*** calcd for $C_{29}H_{29}BrN_5O_4S$ $[M+H]^+$ = 622.1118, found: 622.1105.

Chapter IV: Thiochromenocarbazole imide-based photosensitizers decorated with carbonic anhydrase inhibitors for synergistic treatment of hypoxic tumours



Scheme 6: Synthesis of CAi-based BTIs.

General procedure for the azide-alkyne Huisgen cycloaddition. In a 50 mL two-necked round-bottom flask, compound **3** (40 mg, 0.064 mmol, 1 equiv.) and the corresponding alkyne (1 equiv.) were dissolved in THF (10 mL). In a Schlenk tube, $CuSO_4.5H_2O$ (2 mg, 0.019 mmol, 0.3 equiv.) and sodium ascorbate (15 mg, 0.081 mmol, 1 equiv.) were dissolved in H_2O (5 mL) and this mixture was added to the solution of compound **3** and alkyne in THF. The reaction was allowed to proceed for 48 hours at room temperature. The reaction was monitored by TLC (6/4, cyclohexane/ ethyl acetate). After reaction completion, the mixture was then diluted with dichloromethane (50 mL) and washed with water (50 mL). The organic layer was dried over anhydrous $MgSO_4$, filtered and evaporated under vacuum. The crude product was purified by column chromatography on silica gel using cyclohexane/ethyl acetate mixture (8/2 to 6/4) as eluents to give the expected compound.

Compound 4: Yield 60%. R_F= 0.25. ATR-FTIR: $\tilde{\nu}$ (cm^{-1}) =2920 (ν_{CH3}), 1610(ν_{CO}). **^{1}H NMR** (400 MHz, $CDCl_3$): δ 8.67 (s, 1H), 8.39 (s, 1H), 7.83 (s, 1H), 7.53 (d, $^3J_{H\text{-}H}$ = 8.8 Hz, 2H), 7.46 (t, $^3J_{H\text{-}H}$ = 7.9 Hz, 1H), 7.19 (d, $^3J_{H\text{-}H}$ = 8.2 Hz, 1H), 7.09 (d, $^3J_{H\text{-}H}$ = 7.5 Hz, 1H), 6.93 (m, 2H), 6.18 (d, $^3J_{H\text{-}H}$ = 7.9 Hz, 1H), 5.12 (m, 3H), 4.76 (d, $^3J_{H\text{-}H}$ = 3.6 Hz, 3H), 4.52 (m, 3H), 3.87 (m, 2H), 3.81 (m, 2H), 3.52 (s, 4H), 2.41 (d, $^3J_{H\text{-}H}$ = 1.0 Hz, 3H), 2.26 (m, 2H), 1.91 (m, 2H), 0.89 (t, $^3J_{H\text{-}H}$ = 7.5 Hz, 6H).**^{13}C{^{1}H} NMR** (126 MHz, $CDCl_3$): δ 161.0, 155.1, 152.2 , 142.9, 141.2, 134.7 , 129.9, 125.6, 124.4, 123.0, 122.0, 119.0, 114.3, 114.2, 114.1, 112.4, 112.1, 107.7, 102.2, 71.1, 70.6, 69.5,

62.4, 57.8, 50.6 , 45.3, 25.2, 18.7, 11.5. **HRMS (ESI$^+$) *m/z*** calcd for $C_{42}H_{39}BrN_5O_7S$ $[M+H]^+$: 836.1748, found: 836.1748. UV-Vis (DMF): λ_{max}(log ε): 410(4.63), 481(4.68).

Compound 5: Yield 84 %. R_F= 0.25. ATR-FTIR: $\tilde{\nu}$ (cm^{-1}) = 1150(ν_{SO}). **^{1}H NMR** (400 MHz, $CDCl_3$) δ 8.72 (s, 1H), 8.36 (s, 1H), 7.79 (d, $^3J_{H-H}$ = 8.4 Hz, 2H), 7.58 (s, 1H), 7.46 (t, $^3J_{H-H}$ = 7.8 Hz, 1H), 7.22 (d, $^3J_{H-H}$ = 8.3 Hz, 1H), 7.09 (d, $^3J_{H-H}$ = 8.0 Hz, 1H), 6.95 (d, $^3J_{H-H}$ = 8.5 Hz, 2H), 5.15 (s, 2H), 5.09 (m, 1H), 4.86 (s, 2H), 4.54 (t, $^3J_{H-H}$ = 5.1 Hz, 2H), 4.43 (t, $^3J_{H-H}$ = 5.0 Hz, 2H), 3.85 (t, $^3J_{H-H}$ = 5.1 Hz, 2H), 3.73 (t, $^3J_{H-H}$ = 5.0 Hz, 2H), 3.43 (s, 4H), 2.25 (m, , 2H), 1.91 (m, 2H), 0.89 (t, $^3J_{H-H}$ = 7.4 Hz, 6H).**^{13}C{^{1}H} NMR**(126 MHz, $CDCl_3$) δ 161.3, 160.8, 141.1, 134.3, 129.9, 128.7, 125.6, 122.7, 121.8, 118.6, 115.3, 114.1, 114.0, 107.9, 77.1, 76.9, 71.0, 70.6, 70.2, 69.4, 57.7, 56.1, 45.3, 34.2, 30.4, 29.8, 25.1, 22.4, 14.2, 11.5. **HRMS (ESI$^+$) *m/z*** calcd for $C_{38}H_{38}BrN_6O_7S_2$ $[M+H]^+$: 833.1421, found: $[M+H]^+$= 833.1413. UV-Vis (DMF): λ_{max}(log ε): 412(4.65), 483(4.69)

Compound 6: Yield 73%. R_F= 0.25. ATR-FTIR: $\tilde{\nu}$ (cm^{-1}) = 1168(ν_{SO}). **^{1}H NMR** (400MHz, $CDCl_3$): δ 8.69 (s, 1H), 8.41 (s, 1H), 7.69 (s, 1H), 7.46 (t, $^3J_{H-H}$ = 7.8 Hz, 1H), 7.20 (m, 2H), 7.10 (m, 2H), 6.99 (m, 2H), 6.77 (m, 1H), 5.11 (s, 2H), 4.72 (s, 1H), 4.53 (m, 2H), 4.46 (m, 2H), 3.86 (m, 2H), 3.77 (m, 2H), 3.47 (s, 4H), 2.26 (m, 2H), 1.92 (m, 2H), 0.89 (t, $^3J_{H-H}$ = 7.3 Hz, 6H). **^{13}C{^{1}H}** NMR (126 MHz, $CDCl_3$): δ 155.7, 145.6, 141.1, 135.7, 134.5, 130.1, 129.8, 123.0, 122.8, 121.9, 120.1, 119.9, 119.6, 119.2, 119.0, 118.8, 114.7, 114.2, 107.6, 77.4, 77.1, 76.9, 71.0, 70.6, 70.1, 69.4, 62.6, 57.7, 56.5, 50.5, 45.1, 31.7, 30.4, 29.8, 25.1, 14.2, 11.5. **HRMS (ESI$^+$) *m/z*** calcd for $C_{40}H_{37}BrN_5O_8S$ $[M+H]^+$: 858.1261, found: 858.1260. UV-Vis (DMF): λ_{max}(log ε): 410(4.61), 480(4.65)

Compound 7: Yield 44 %. R_F= 0.3. ATR-FTIR: $\tilde{\nu}$ (cm^{-1}) =2917 (ν_{CH3}). **^{1}H NMR** (400 MHz, $CDCl_3$): δ 8.63 (s, 1H), 8.35 (s, 1H), 7.42 (t, $^3J_{H-H}$ = 7.9 Hz, 1H), 7.28 (s, 1H), 7.17 (d, $^3J_{H-H}$ = 8.1 Hz, 1H), 7.03 (d, $^3J_{H-H}$ = 7.5 Hz, 1H), 5.09 (m, 1H), 4.52 (t, $^3J_{H-H}$ = 5.3 Hz, 2H), 4.38 (t, $^3J_{H-H}$ = 5.1 Hz, 2H), 3.86 (t, $^3J_{H-H}$ = 5.2 Hz, 2H), 3.72 (t, $^3J_{H-H}$ = 5.2 Hz, 2H), 3.46 (m, 4H), 2.64 (m, 2H), 2.26 (m, 2H), 1.92 (m, 2H), 1.58 (m, 2H), 1.33 (m, 2H), 0.90 (t, $^3J_{H-H}$ = 7.4, Hz, 6H), 0.88 (t, $^3J_{H-H}$ = 7.3 Hz, 3H).**^{13}C{^{1}H} NMR** (126 MHz, $CDCl_3$) : δ 148.3, 141.1, 134.4, 132.8, 131.0, 130.0, 129.8, 128.1, 122.9, 122.0 (x2), 121.7, 118.8, 114.2, 114.0, 107.7, 77.1, 71.1, 70.6, 70.1, 69.8, 57.7, 50.1, 45.1, 31.7, 29.8, 25.5, 25.1, 22.4, 14.0, 11.5. **HRMS (ESI$^+$) *m/z*** calcd for $C_{35}H_{39}BrN_5O_4S$ $[M+H]^+$ = 704.1901. found: $[M+H]^+$ = 704.1905. UV-Vis (DMF): λ_{max}(log ε): 410(4.61), 480(4.65).

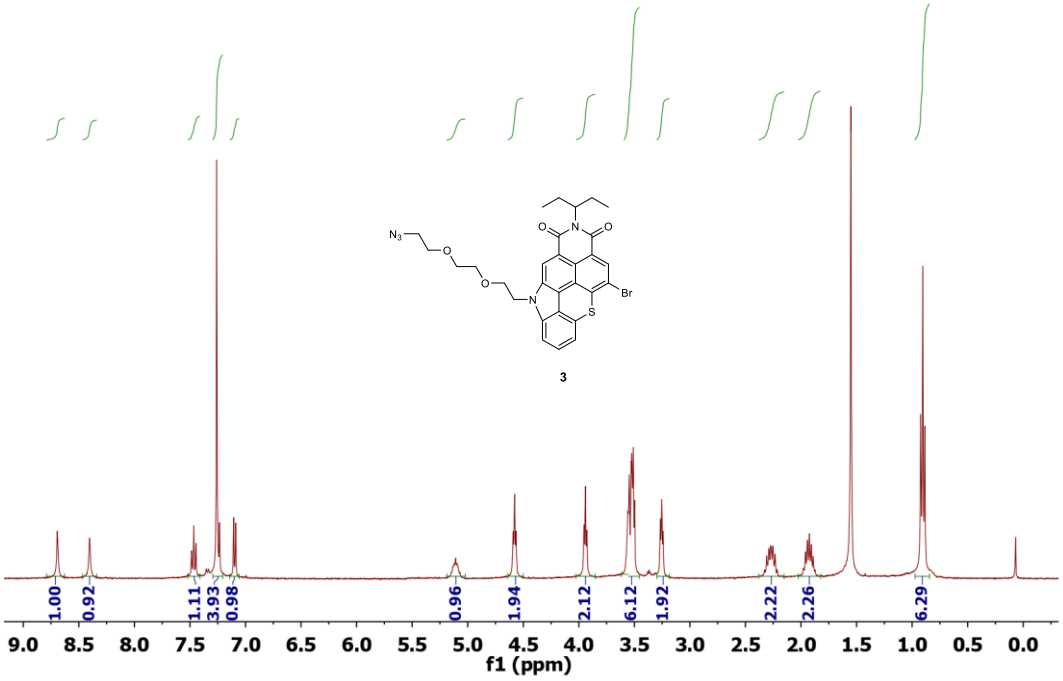


Figure 85. ^{1}H NMR spectrum (400 MHz, $CDCl_3$, 298K) of compound **3**.

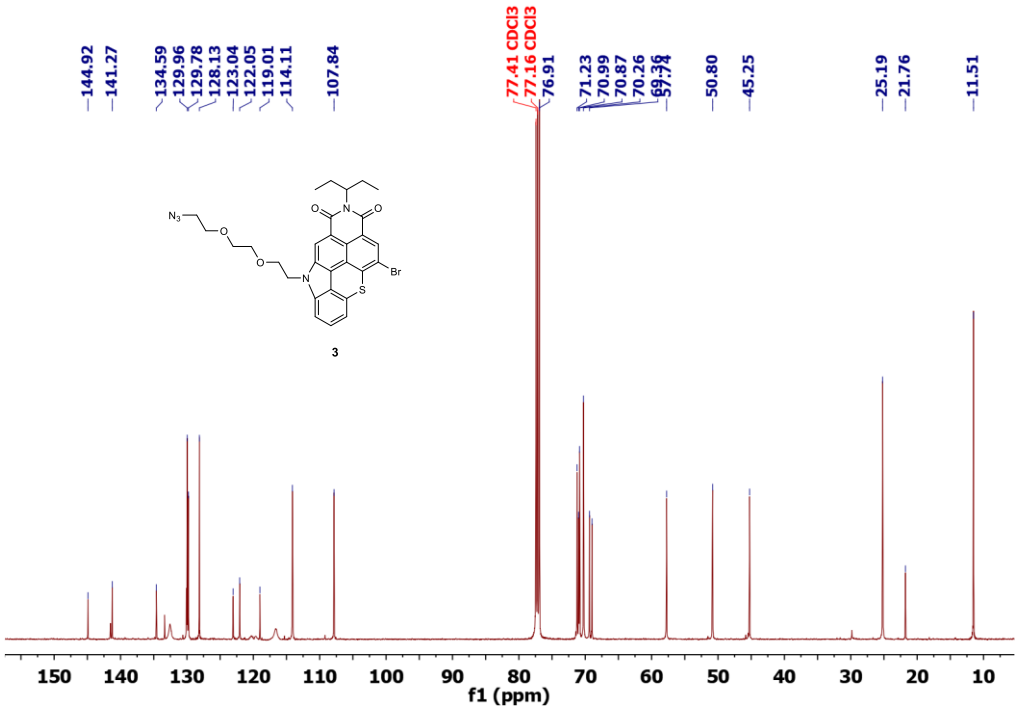


Figure 86. $^{13}C\{^{1}H\}$ NMR spectrum (126 MHz, $CDCl_3$, 298K) of compound **3**.

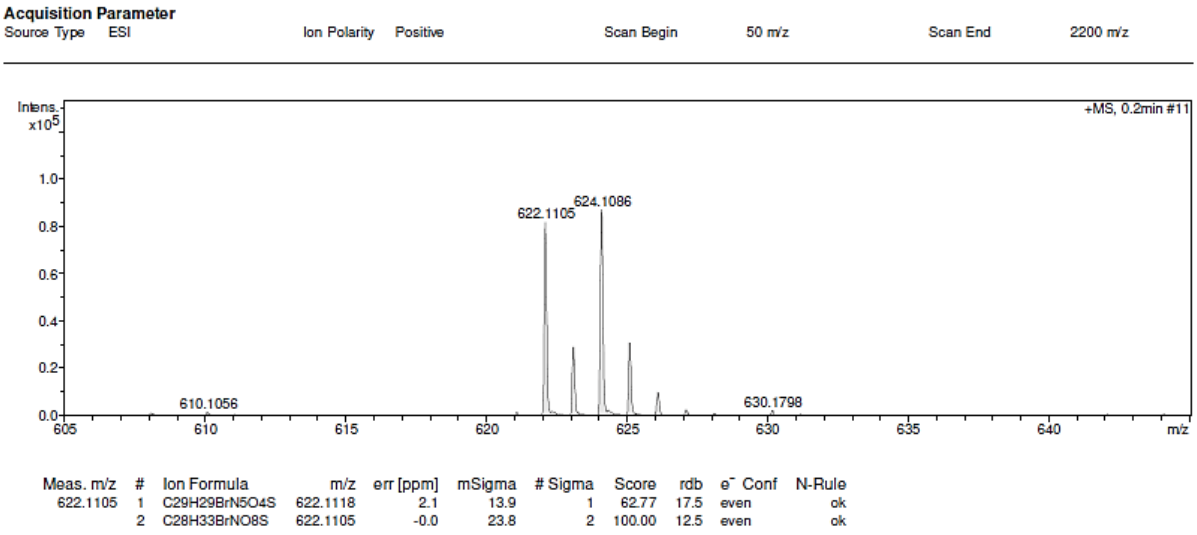


Figure 87. High resolution ESI-TOF (positive mode) mass spectrum of compound **3**.

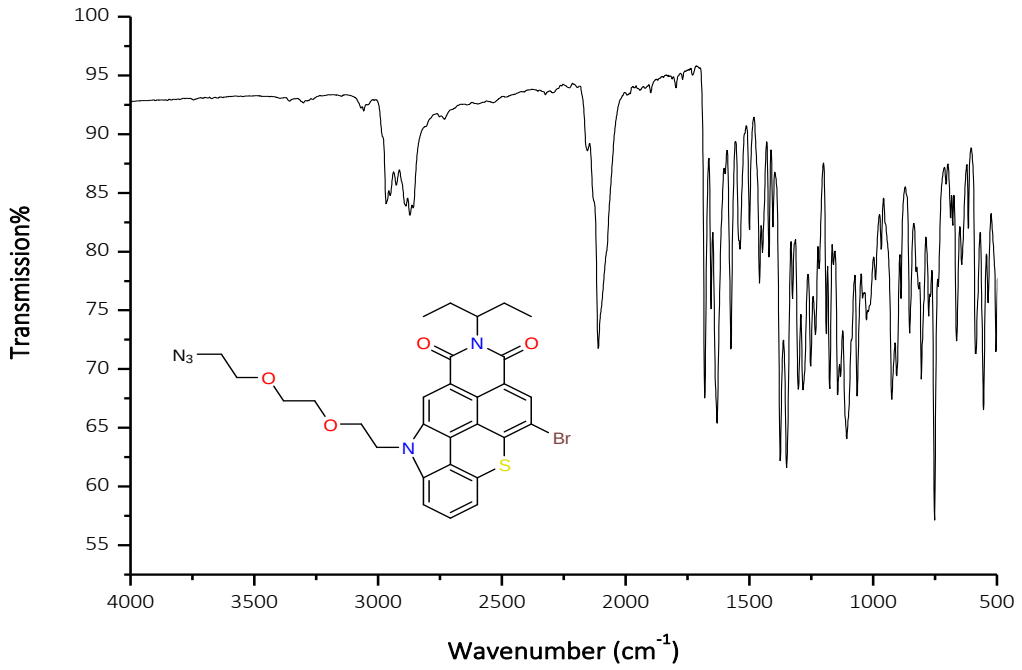


Figure 88. ATR-FTIR spectrum of compound **3.**

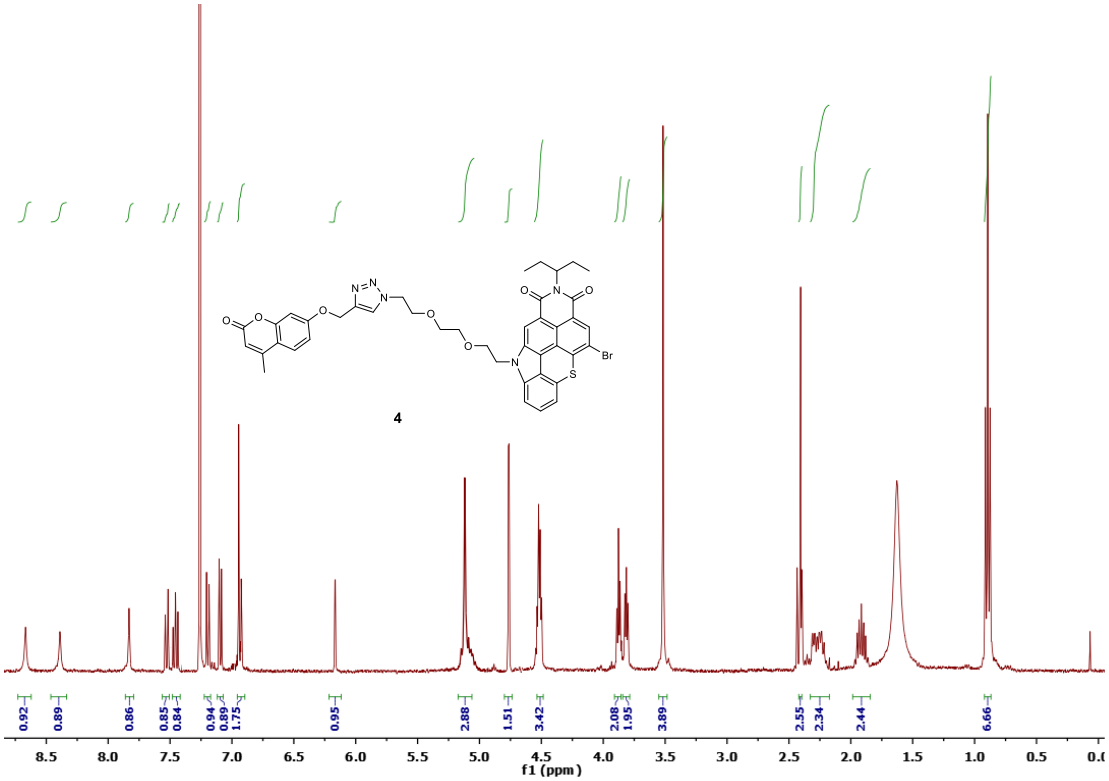


Figure 89. ^{1}H NMR spectrum (400 MHz, $CDCl_3$, 298K) of compound **4**.

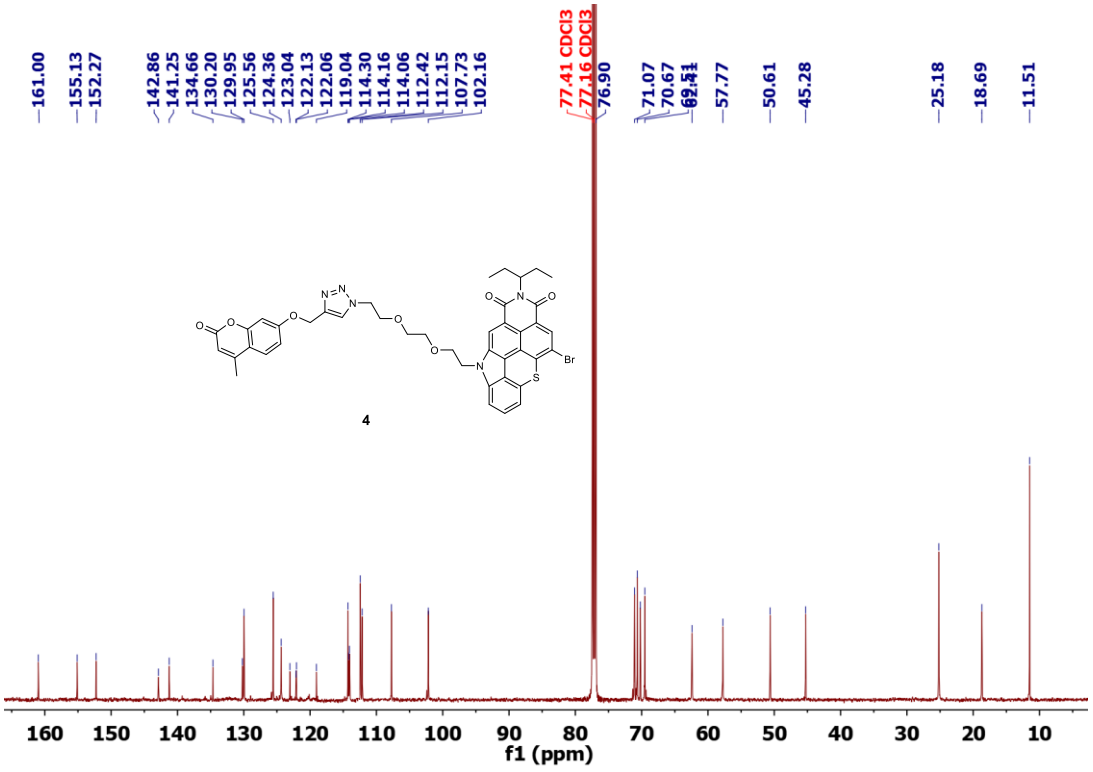
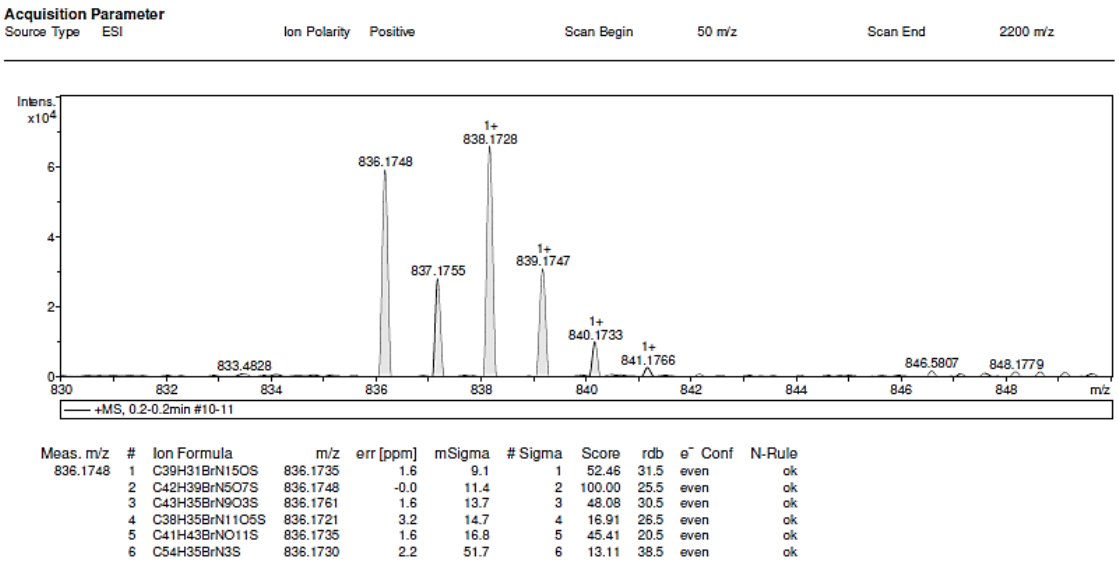


Figure 90. $^{13}C\{^{1}H\}$ NMR spectrum (126 MHz, $CDCl_3$, 298K) of compound **4**.

Chapter IV: Thiochromenocarbazole imide-based photosensitizers decorated with carbonic anhydrase inhibitors for synergistic treatment of hypoxic tumours



Meas. m/z	#	Ion Formula	m/z	err [ppm]	mSigma	# Sigma	Score	rdb	e⁻ Conf	N-Rule
836.1748	1	C39H31BrN15OS	836.1735	1.6	9.1	1	52.46	31.5	even	ok
	2	C42H39BrN5O7S	836.1748	-0.0	11.4	2	100.00	25.5	even	ok
	3	C43H35BrN9O3S	836.1761	1.6	13.7	3	48.08	30.5	even	ok
	4	C38H35BrN11O5S	836.1721	3.2	14.7	4	16.91	26.5	even	ok
	5	C41H43BrNO11S	836.1735	1.6	16.8	5	45.41	20.5	even	ok
	6	C54H35BrN3S	836.1730	2.2	51.7	6	13.11	38.5	even	ok

Figure 91. High resolution ESI-TOF (positive mode) mass spectrum of compound **4**.

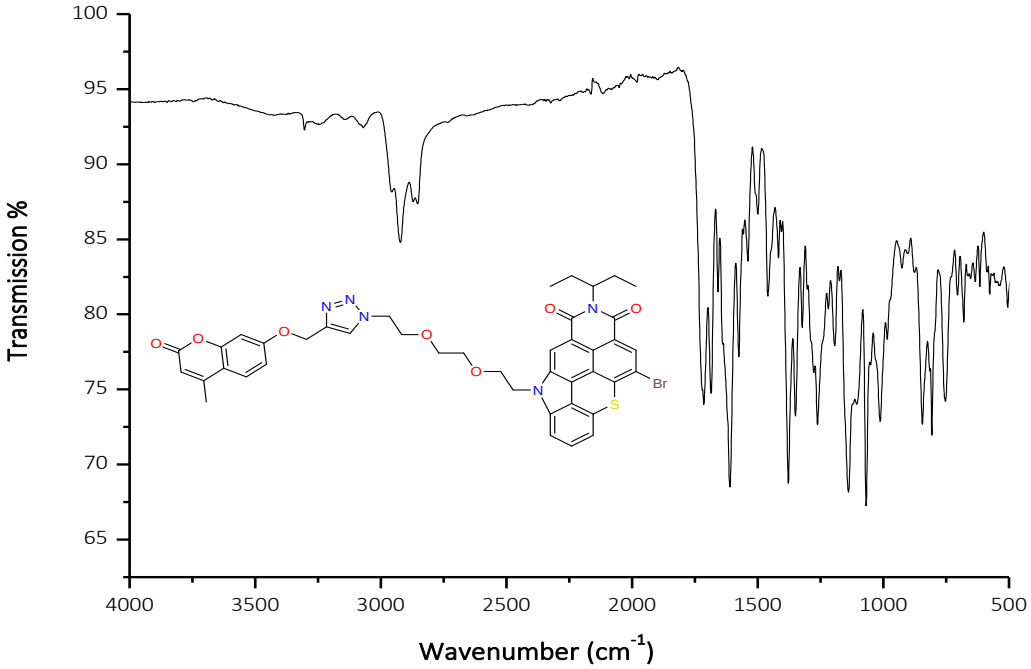


Figure 92. ATR-FTIR spectrum of compound **4**.

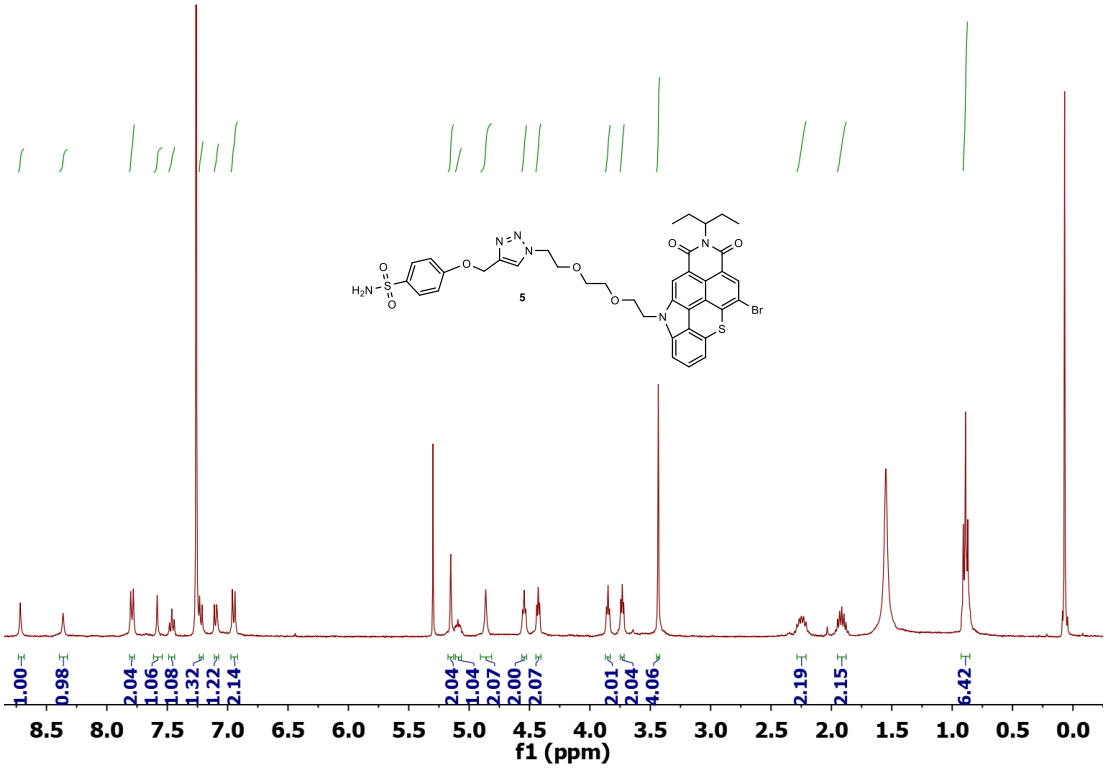


Figure 93. ^{1}H NMR spectrum (400 MHz,$CDCl_3$, 298K) of compound **5**.

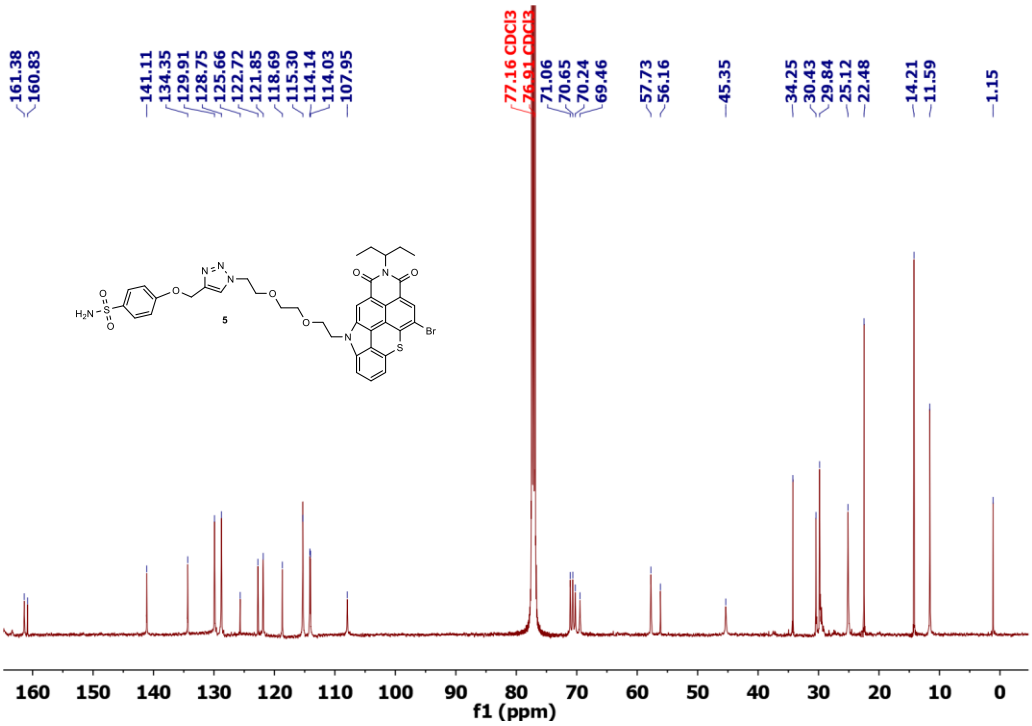
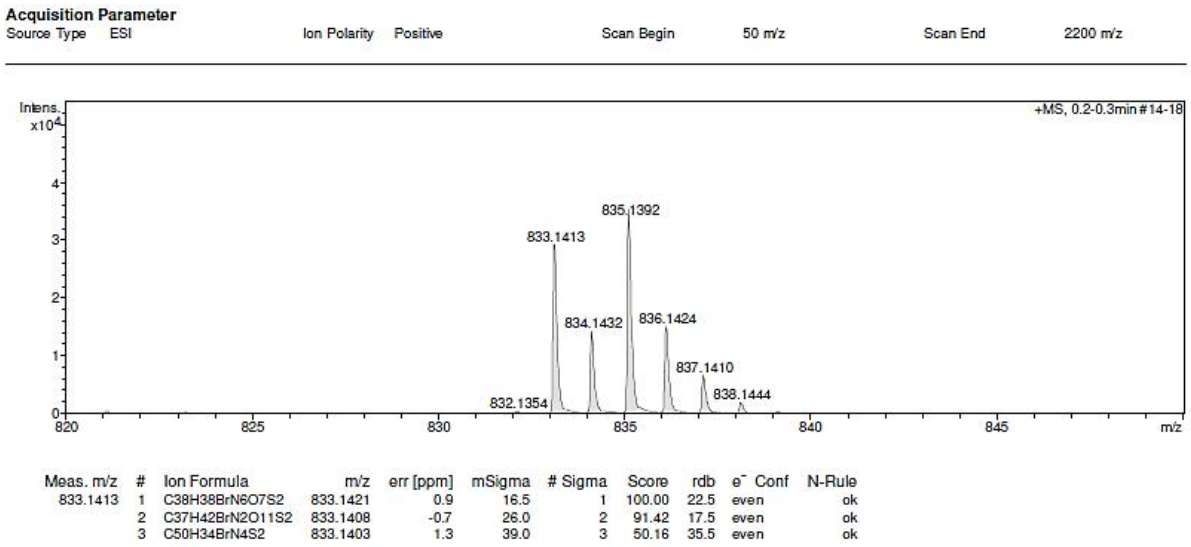


Figure 94. $^{13}C\{^{1}H\}$ NMR spectrum (126 MHz, $CDCl_3$, 298K) of compound **5**.



Meas. m/z	#	Ion Formula	m/z	err [ppm]	mSigma	# Sigma	Score	rdb	e⁻ Conf	N-Rule
833.1413	1	C38H38BrN6O7S2	833.1421	0.9	16.5	1	100.00	22.5	even	ok
	2	C37H42BrN2O11S2	833.1408	-0.7	26.0	2	91.42	17.5	even	ok
	3	C50H34BrN4S2	833.1403	1.3	39.0	3	50.16	35.5	even	ok

Figure 95. High resolution ESI-TOF (positive mode) mass spectrum of compound **5**.

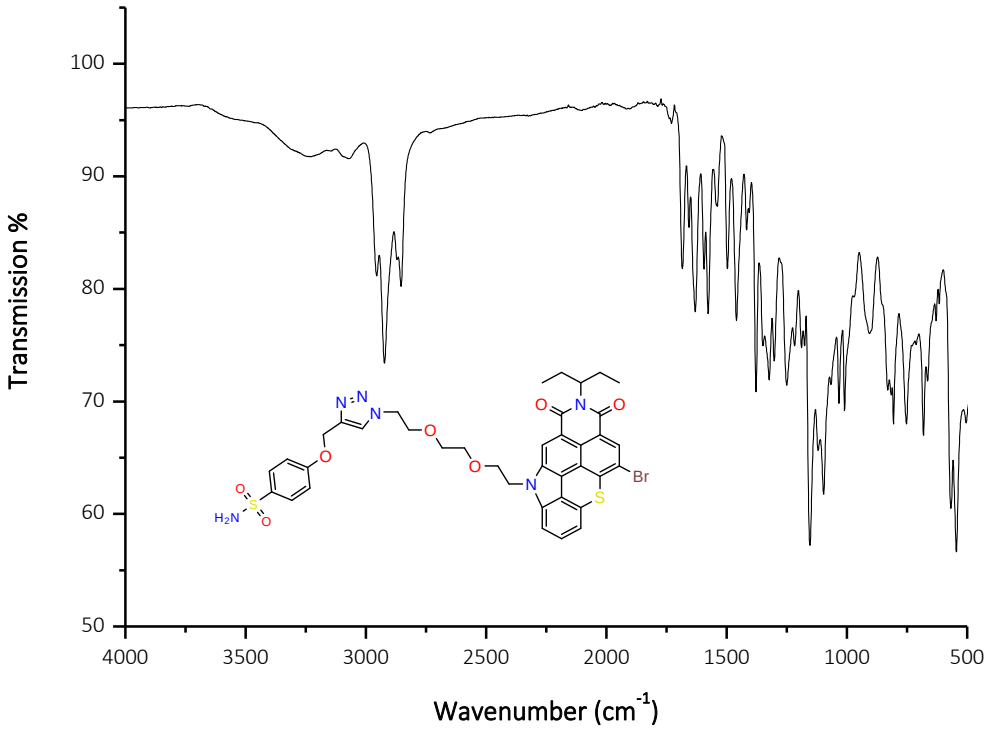


Figure 96. ATR-FTIR spectrum of compound **5**.

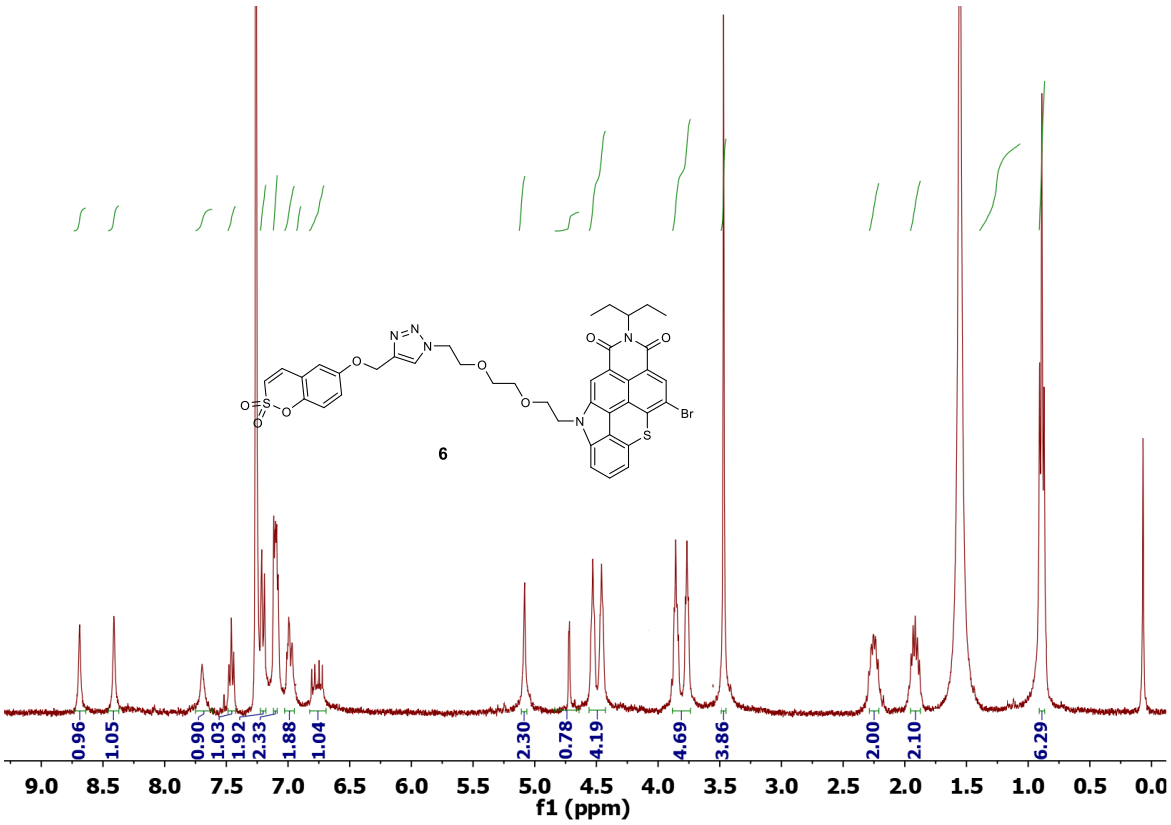


Figure 97. ^{1}H NMR spectrum (400 MHz, $CDCl_3$, 298K) of compound **6**.

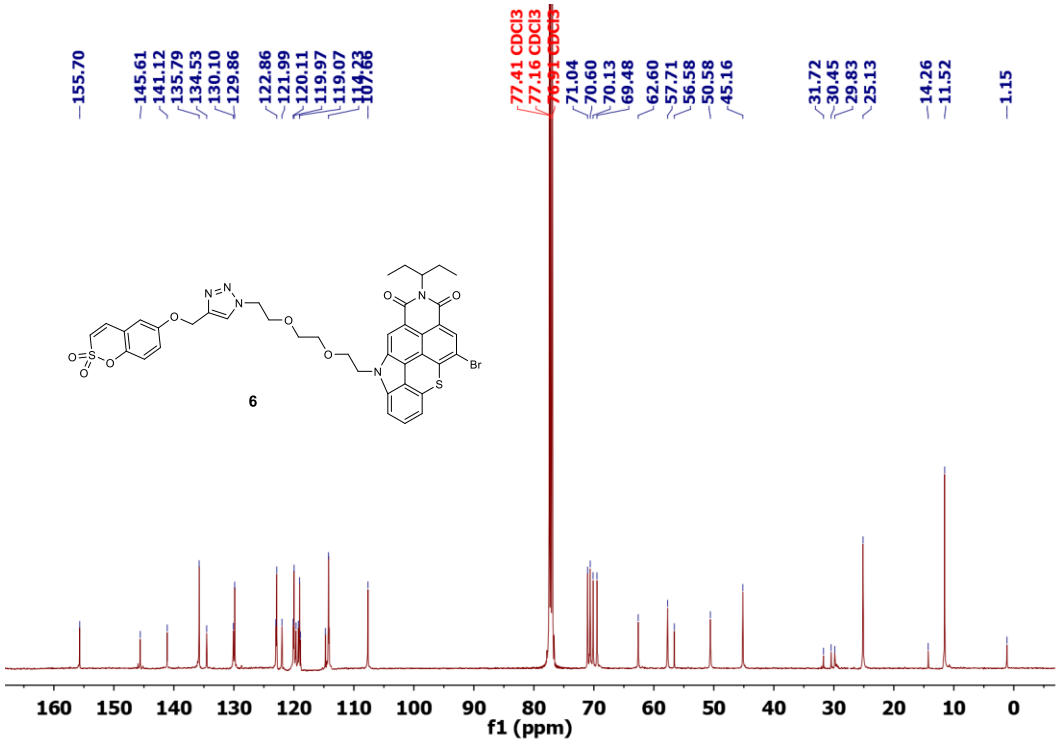
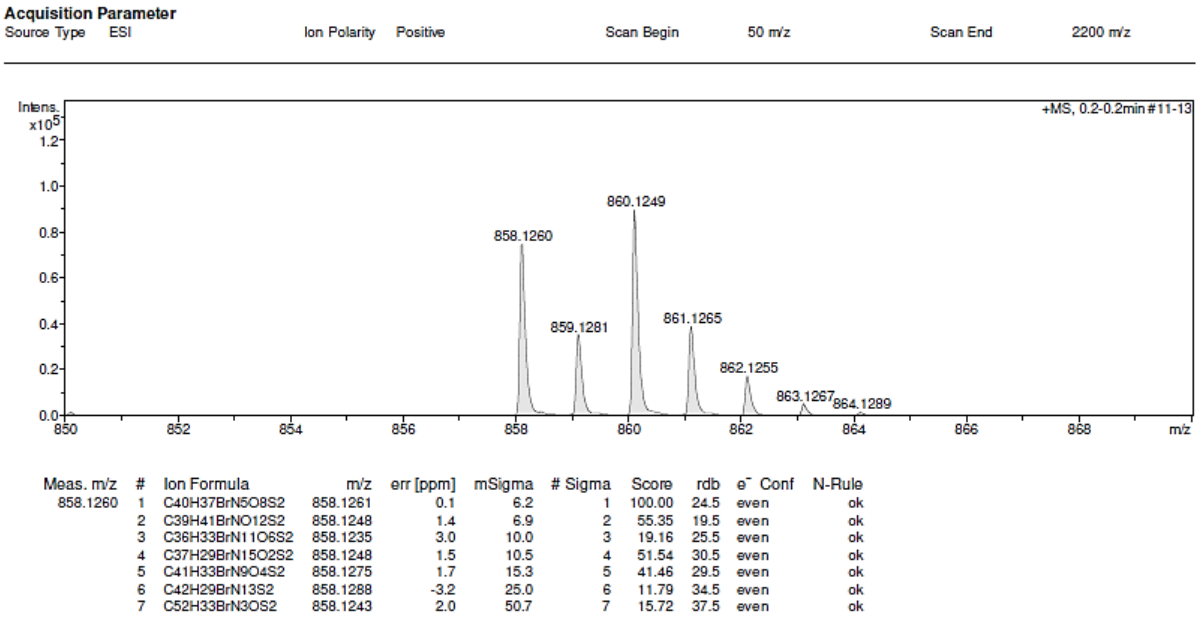


Figure 98. $^{13}C\{^{1}H\}$ NMR spectrum (126 MHz, $CDCl_3$, 298K) of compound **6**.

Chapter IV: Thiochromenocarbazole imide-based photosensitizers decorated with carbonic anhydrase inhibitors for synergistic treatment of hypoxic tumours



Meas. m/z	#	Ion Formula	m/z	err [ppm]	mSigma	# Sigma	Score	rdb	e⁻ Conf	N-Rule
858.1260	1	C40H37BrN5O8S2	858.1261	0.1	6.2	1	100.00	24.5	even	ok
	2	C39H41BrNO12S2	858.1248	1.4	6.9	2	55.35	19.5	even	ok
	3	C36H33BrN11O6S2	858.1235	3.0	10.0	3	19.16	25.5	even	ok
	4	C37H29BrN15O2S2	858.1248	1.5	10.5	4	51.54	30.5	even	ok
	5	C41H33BrN9O4S2	858.1275	1.7	15.3	5	41.46	29.5	even	ok
	6	C42H29BrN13S2	858.1288	-3.2	25.0	6	11.79	34.5	even	ok
	7	C52H33BrN3OS2	858.1243	2.0	50.7	7	15.72	37.5	even	ok

Figure 99. High resolution ESI-TOF (positive mode) mass spectrum of compound **6**.

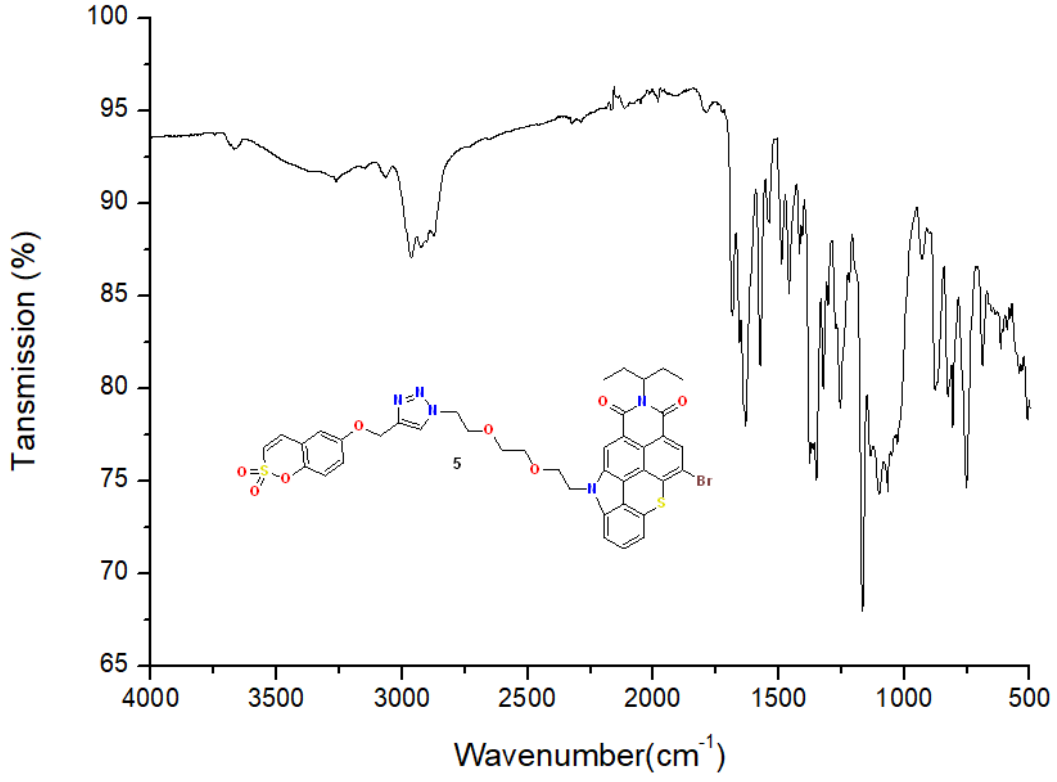


Figure 100. ATR-FTIR spectrum of compound **6.**

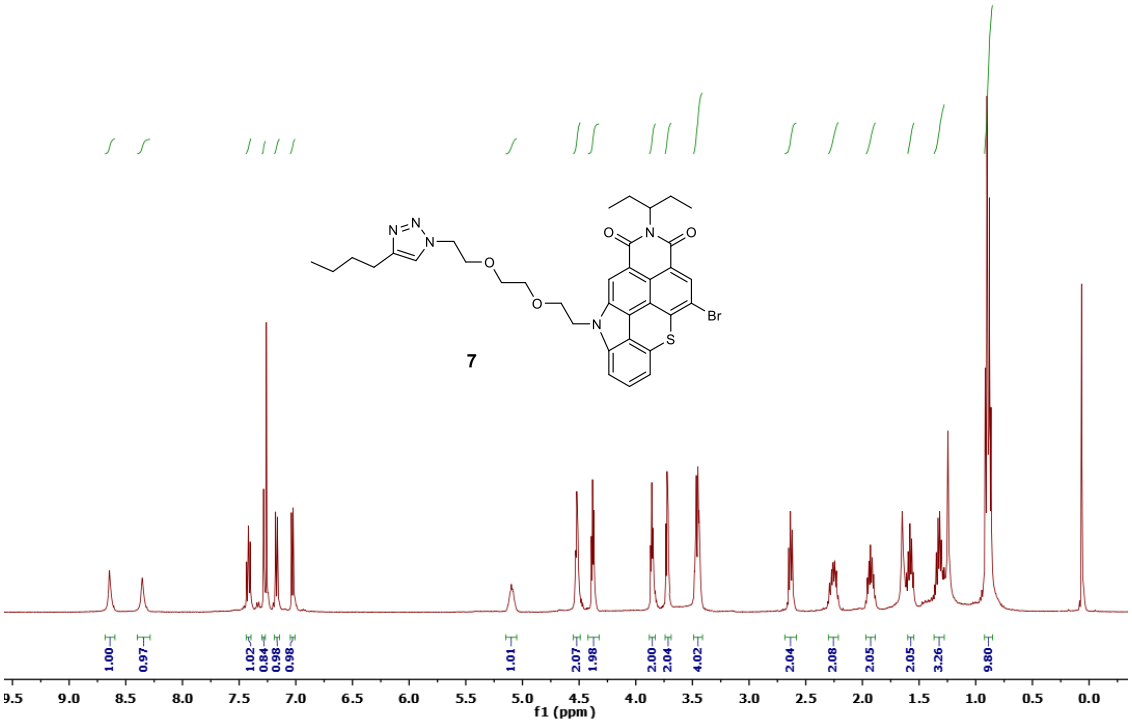


Figure 101. ^{1}H NMR spectrum (400 MHz, $CDCl_3$, 298K) of compound **7**.

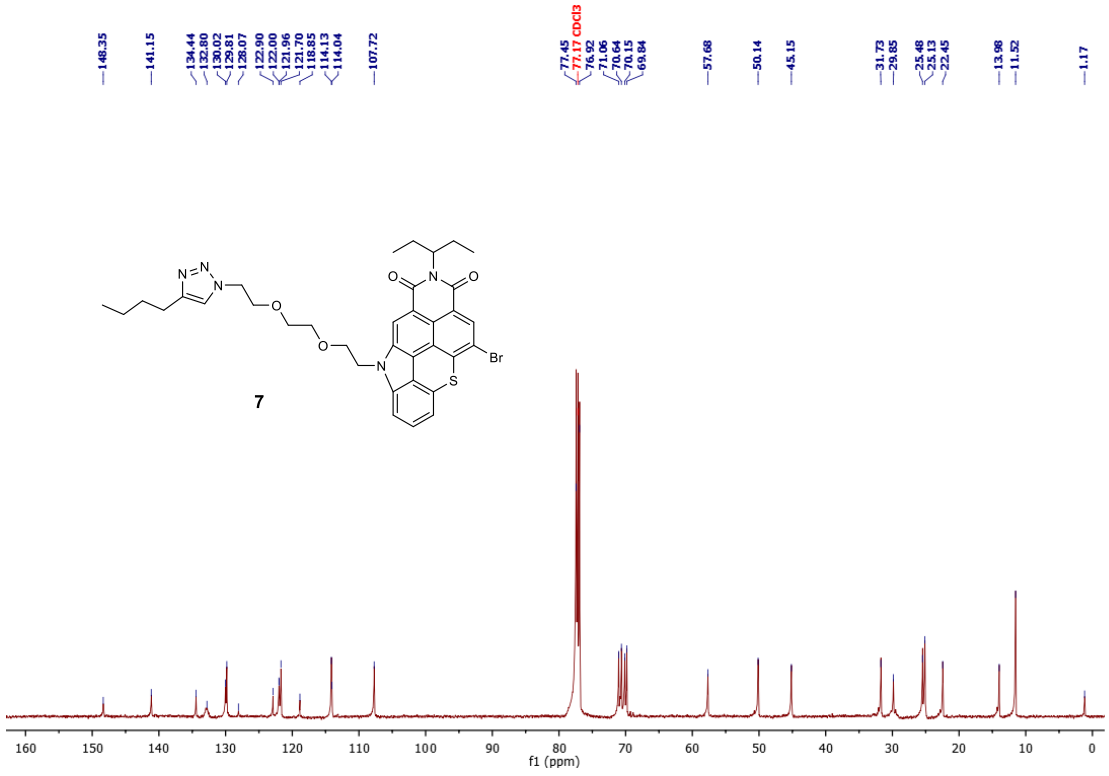
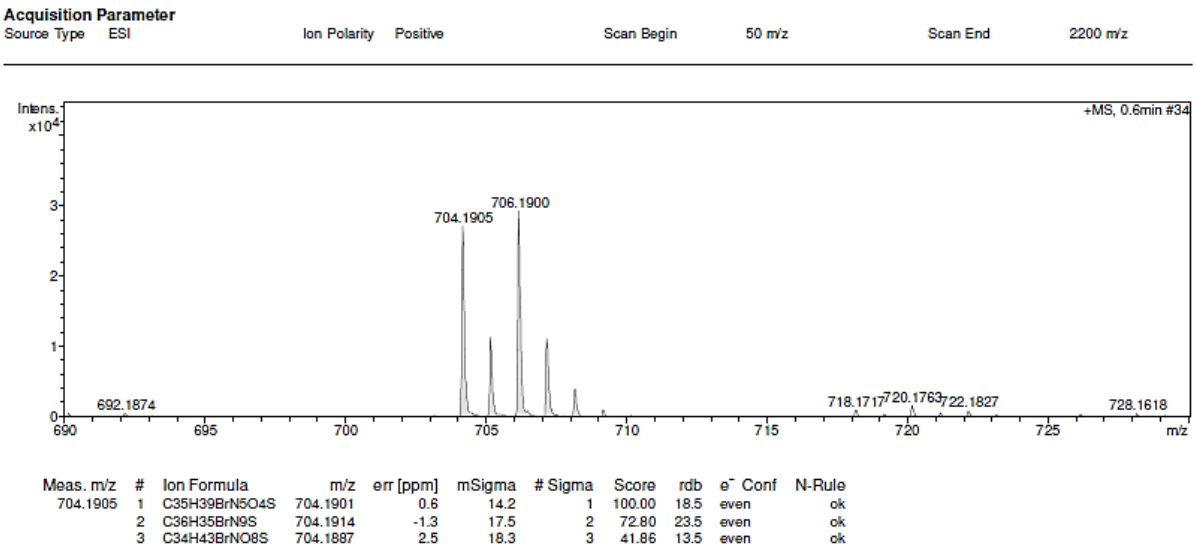


Figure 102. $^{13}C\{^{1}H\}$ NMR spectrum (126 MHz, $CDCl_3$, 298K) of compound **7**.



Meas. m/z	#	Ion Formula	m/z	err [ppm]	mSigma	# Sigma	Score	rdb	e⁻ Conf	N-Rule
704.1905	1	C35H39BrN5O4S	704.1901	0.6	14.2	1	100.00	18.5	even	ok
	2	C36H35BrN9S	704.1914	-1.3	17.5	2	72.80	23.5	even	ok
	3	C34H43BrNO8S	704.1887	2.5	18.3	3	41.86	13.5	even	ok

Figure 103. High resolution ESI-TOF (positive mode) mass spectrum of compound **7**.

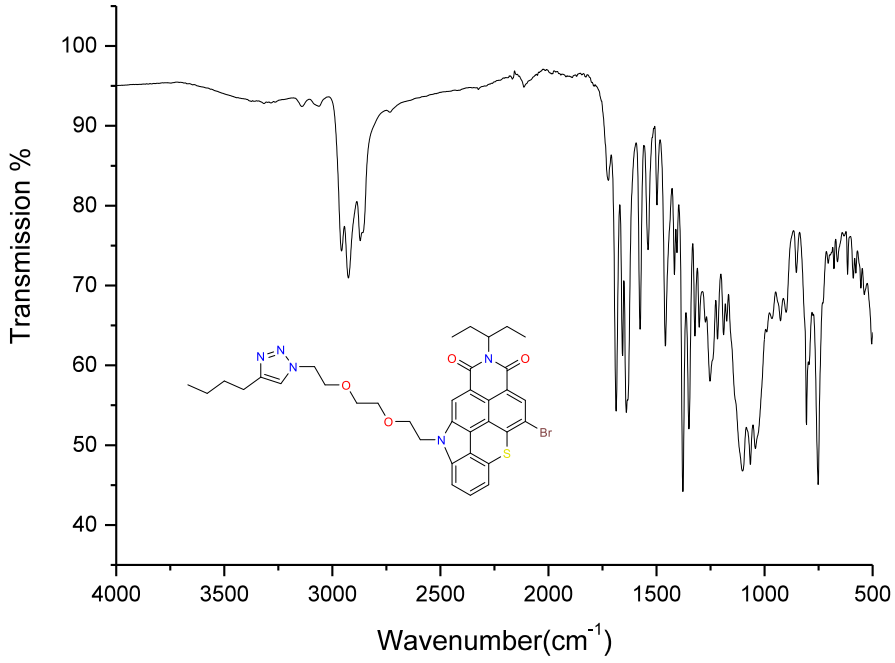


Figure 104. ATR-FTIR spectrum of compound **7.**

Chapter IV: Thiochromenocarbazole imide-based photosensitizers decorated with carbonic anhydrase inhibitors for synergistic treatment of hypoxic tumours

V.4 Optical properties

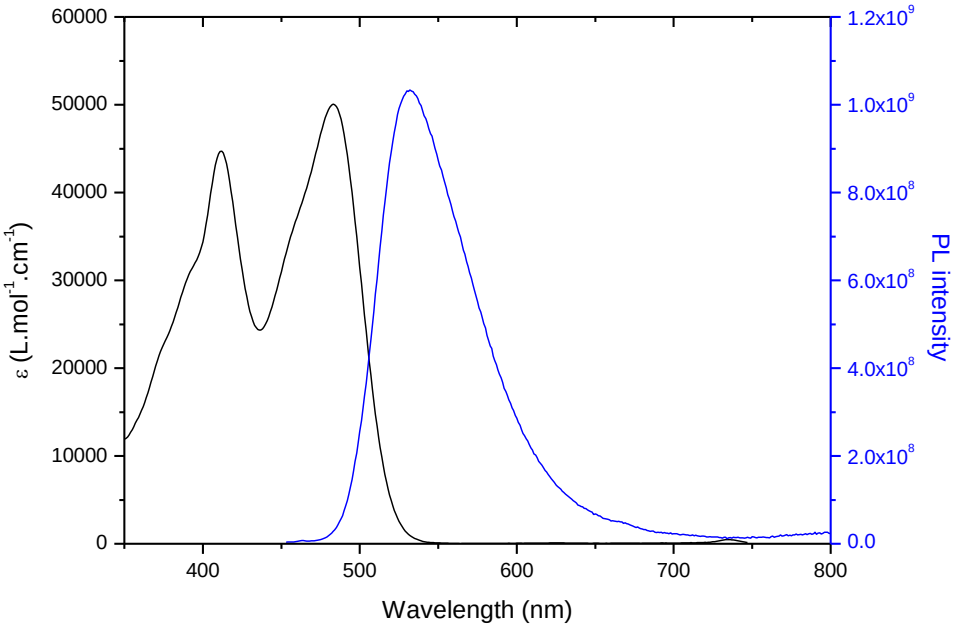


Figure 105. UV-visible absorption (black) and emission spectra (blue) of compound **5** in DMF (C= 1.2 x 10^{-5} mol.L^{-1}, λ_{exc} = 435 nm).

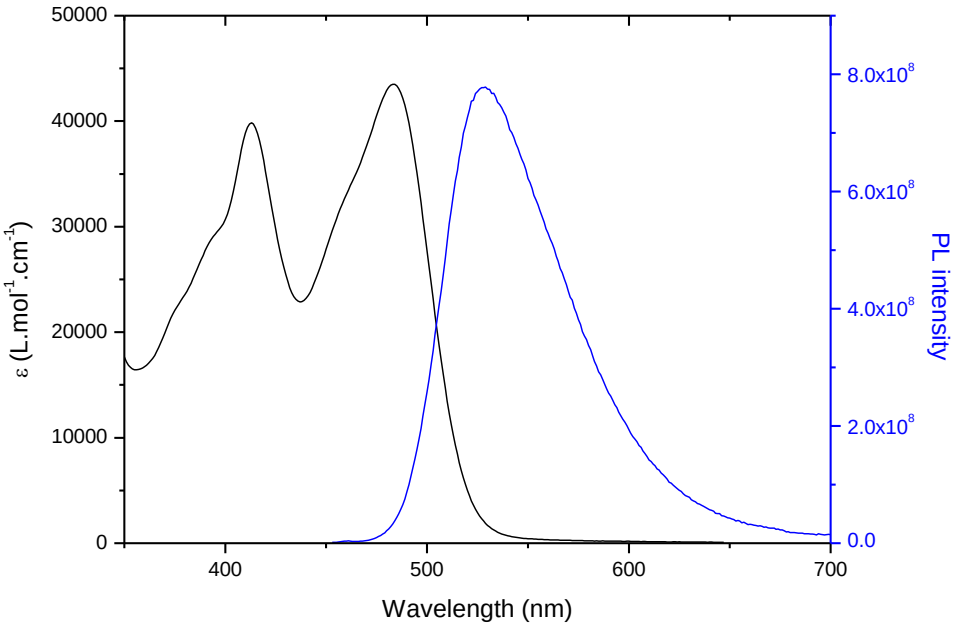


Figure 106. UV-visible absorption (black) and emission spectra (blue) of compound **6** in DMF (C= 1.1 x 10^{-5} mol.L^{-1}, λ_{exc} = 435 nm).

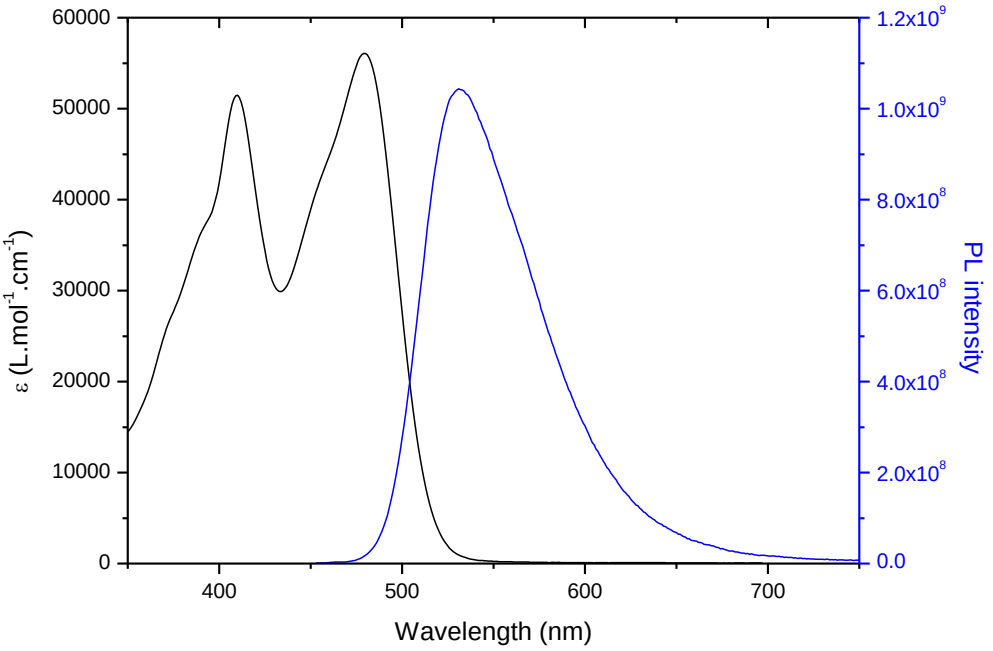


Figure 107. UV-visible absorption (black) and emission spectra (blue) of compound **7** in DMF (C= 1.1 x 10^{-5} mol.L^{-1}, λ_{exc} = 435 nm).

V.5 CA inhibition assays

An SX.18V-R Applied Photophysics (Oxford, UK) stopped flow instrument was used to assay the catalytic/inhibition of various CA isozymes.[3] Phenol red (at the concentration of 0.2 mM has been used as an indicator, working at an absorbance maximum of 557 nm, with 10 mM HEPES (pH 7.4) as a buffer, 0.1 M Na_2SO_4 or $NaClO_4$ (for maintaining constant the ionic strength; these anions are not inhibitor in the used concentration), following the CA-catalyzed CO_2 hydration reaction for a period of 5–10 s. Saturated CO_2 solutions in water at 25 °C were used as substrate. Stock solutions of inhibitors were prepared at a concentration of 10 mM (in DMSO/water 1:1, v/v) and dilutions up to 0.01 nM done with the assay buffer mentioned above. At least 7 different inhibitor concentrations have been used for measuring the inhibition constant. Inhibitor and enzyme solutions were pre-incubated together for 6h at 4 °C prior to assay, in order to allow for the formation of the E-I complex. Triplicate experiments were done for each inhibitor concentration, and the values are reported throughout the paper is the mean of such results. The inhibition constants were obtained by nonlinear least squares methods using the Cheng-Prusoff equation, as reported earlier, and represent the mean from at least three different

determinations. All CA isozymes used here were recombinant proteins obtained as reported earlier by our group and their concentration in the assay system was of 6–12 nM.[4-7]

V.6 Biological assays

Cell Culture

Human breast cancer cells (MDA-MB-231) and MDA-MB-231-Luc-RFP were purchased from ATCC (American Type Culture Collection, Manassas, VA) and Amsbio, respectively. MDA-MB-231 cells were cultured in Dulbecco's Modified Eagle medium (DMEM) supplemented with 10% foetal bovine serum (FBS) and 50 µg mL^{-1} gentamycin. MDA-MB-231-Luc-RFP cells were maintained in the previously mentioned cell culture medium compositions in addition to 5 µg mL^{-1} blasticidin as a selection antibiotic. Cells were maintained in a humidified atmosphere, at 37 °C with 5% CO_2. DMEM, FBS and antibiotics were purchased from Gibco.

Dark Toxicity

MDA-MB-231 cells were seeded into a 96 multiwell at 5000 cells/ well in 200 µL of culture medium and allowed to grow for 24 h. The cells were then treated or not with **4**, **6, 7** or vehicle (DMSO) at increasing concentrations (from 0.1 to 100 $\mu g.mL^{-1}$) for 72 h and living cells were quantified. For that, cells were treated for 4 h with MTT (3-(4,5-dimethylthiazol-2-yl)-2,5-diphenyltetrazolium bromide, Promega) in media. Then, MTT/ media solution was removed and the crystals thus formed were dissolved in EtOH/DMSO (1:1). As per manufacturer recommendations, absorbance was read at 540 nm.

PDT

MDA-MB-231 cells were seeded into a 384 multiwell at 1000 cells/ well in 50 µL of culture medium and allowed to grow for 24 h. The cells were then treated or not with **4**, **6** and **7** or vehicle (DMSO) at 0.5 $\mu g.mL^{-1}$ for 24 h. Then, cancer cells were irradiated or not at 470 ± 22 nm for 30 sec using GFP light cube of EVOS 5000 (ThermoFisher) (13.4 J cm^{-2}). Two days after irradiation, MTT assay was performed to evaluate the cell viability.

Confocal Microscopy Imaging

MDA-MB-231 cells were seeded into bottom glass dishes (World Precision Instrument, Stevenage, UK) at a density of 10^6 cells cm^{-2}. One day after seeding, cells were washed once and incubated with 1 mL of fresh medium containing **4**, **6** or **7** at a concentration of 10 $\mu g.mL^{-1}$ for 24 h. Fifteen minutes before

the end of incubation, the cells were incubated with CellMask Orange for membrane cell staining (5 µg mL^{-1}, Thermo Fisher). Then, cells were washed several times with culture media to remove staining molecules excess. The cells were then visualized with an LSM 780 LIVE confocal microscope (Carl Zeiss, Le Pecq, France), at 488 nm and 561 nm for compounds and CellMask respectively, using high magnification (63×/1.4 OIL DIC Plan-Apo).

Experiments on Zebrafish Embryos

Casper zebrafish embryos were purchased from Zebrafish International Resource Center (ZIRC) as embryos and were raised to adulthood in circulating aquarium system at 28 °C, 80% humidity, 14 h light/10 h dark cycle, in the ZeNeuro platform (Inserm U1198), Montpellier University. Experiments with zebrafish embryos until 96 hpf are considered as *in vitro* studies according to the EU Directive 2010/63/EU on the protection of animals used for scientific purposes.

Imaging on Zebrafish Embryos

Casper zebrafish embryos of 72 hours post fertilization (hpf) were anesthetized with tricaine solution (168 mg L^{-1}) for 10 min. Casper embryos (n=4/group) were injected or not with 10 nL of analogues at 1 mg.mL^{-1} in 5% glucose, in the caudal vein. Then, zebrafishes were imaged 3 h after injection of derivatives **4** and **6**, and immediately after for **7**. Tile scans were performed at an excitation wavelength of 488 nm using confocal microscopy LSM880 and objective EC plan-Neofluar 10x/0.30 M27.

Study of PDT Efficiency in Zebrafish Embryos

MDA-MB-231-Luc-RFP cells were seeded in Nunc EasYFlask 75 cm^2. 24 hours after seeding, the cells were treated or not with 10 µg.mL^{-1} of analogue **4** for 24 h. After incubation, the cells were washed thrice with PBS and then were trypsinized and suspended in culture medium. The cells were counted and centrifuged and then suspended in the required volume of PBS containing 2% FBS to have a solution of 3×10^7 cells per 1 mL. The cell solution was kept on ice until injection. Casper embryos at 30 hpf were used. The embryos were anesthetized with tricaine solution 10 min prior to injection. Then, the embryos were placed on an agar mold for the microinjection of cells previously incubated (or not) with **4**. Each embryo received 2 pulses of 5 nL of cell suspension in the yolk. Injected Casper embryos with cells without **4** were used as the control. After injection, the embryos were placed in a 100 mm × 20 mm Petri-dish containing 30 mL of water at 31°C. Twenty-four hours after injection, the embryos were anesthetized and imaged at 561 nm excitation using confocal microscopy LSM880 and objective EC plan-Neofluar 10x/0.30 M27 to visualize the xenograft in red. The embryos of control and compound **4** were divided into two groups: the no blue light irradiation group and the blue light

irradiation group (n=10/group). Each embryo in the blue light irradiation group was exposed to light for 1 or 2 min using GFP light cube of EVOS 5000 (objective lens 4×, λex = 470 ± 22 nm, 9.41 J cm^{-2}). After irradiation, each embryo was placed in a well of 24-well plate with 2 mL of water and at 31°C. 24 hours after irradiation, the embryos were imaged again. The fluorescence intensity of the xenograft before and after irradiation was quantified using imageJ program. The corrected total cell fluorescence (CTCF) was calculated as CTCF = Integrated Density – (Area of selected cell X Mean fluorescence of background readings) and the tumour regression (%) was calculated by considering the fluorescence intensity value of each embryo before irradiation is 100%.

Chapter IV: Thiochromenocarbazole imide-based photosensitizers decorated with carbonic anhydrase inhibitors for synergistic treatment of hypoxic tumours

References:

1. a) Roberson, M. G.; Duncan, J. M.; Flieth, K. J.; Geary, L. M.; Tucker, M. J., Photo-initiated rupture of azobenzene micelles to enable the spectroscopic analysis of antimicrobial peptide dynamics. *RSC advances* **2020**, 10 (36), 21464-21472. b) Walker, J. A.; Bohn, J.J; Ledesma, F; Sorkin, M.R; Kabaria, S.R; Thornlow, D.N; Alabi, C. A., *Bioconjugate Chemistry* **2019**, 30, 2452−2457; c) Lossouarn, A.; Renault, K.; Bailly, L.; Frisby, A.; Le Nahenec-Martel, P.; Renard, P.Y.; Sabot, C., *Organic & Biomolecular Chemistry* **2020,** 18, 3874-3887

2. Castán, J. M. A.; Amruth, C.; Josse, P.; Galan, L. A.; Marqués, P. S.; Allain, M.; Maury, O.; Le Bahers, T.; Blanchard, P.; Monnereau, C., Thiochromenocarbazole imide: a new organic dye with first utility in large area flexible electroluminescent devices. *Materials Chemistry Frontiers* **2022,** *6* (14), 1912-1919.

3. Khalifah, R. G., The carbon dioxide hydration activity of carbonic anhydrase: I. Stop-flow kinetic studies on the native human isoenzymes B and C. *Journal of Biological Chemistry* **1971,** *246* (8), 2561-2573.

4. Küçükbay, H.; Gönül, Z.; Küçükbay, F. Z.; Angeli, A.; Bartolucci, G.; Supuran, C. T., Preparation, carbonic anhydrase enzyme inhibition and antioxidant activity of novel 7-amino-3, 4-dihydroquinolin-2 (1H)-one derivatives incorporating mono or dipeptide moiety. *Journal of Enzyme Inhibition and Medicinal Chemistry* **2020,** *35* (1), 1021-1026.

5. Awadallah, F. M.; Bua, S.; Mahmoud, W. R.; Nada, H. H.; Nocentini, A.; Supuran, C. T., Inhibition studies on a panel of human carbonic anhydrases with N 1-substituted secondary sulfonamides incorporating thiazolinone or imidazolone-indole tails. *Journal of enzyme inhibition and medicinal chemistry* **2018,** *33* (1), 629-638.

6. Supuran, C. T., Carbon-versus sulphur-based zinc binding groups for carbonic anhydrase inhibitors? *Journal of enzyme inhibition and medicinal chemistry* **2018,** *33* (1), 485-495.

7. Di Fiore, A.; De Simone, G.; Alterio, V.; Riccio, V.; Winum, J.-Y.; Carta, F.; Supuran, C. T., The anticonvulsant sulfamide JNJ-26990990 and its S, S-dioxide analog strongly inhibit carbonic anhydrases: solution and X-ray crystallographic studies. *Organic & Biomolecular Chemistry* **2016,** *14* (21), 4853-4858.

Chapter V

Synthesis and characterization of AIE-based photosensitizers featuring carbonic anhydrase inhibitors

In preparation

Chapter V: Synthesis and characterization of AIE-based photosensitizers featuring carbonic anhydrase inhibitors

I. Abstract

Photodynamic therapy (PDT) is a specific anticancer therapy that attracted significant interest for the cancer treatment combining three essential components (photosensitizer, oxygen and light). ROS produced during the PDT process finally induces destruction of tumor cells. However, the PDT efficiency can be reduced by hypoxia, which is encountered in most solid tumors. In hypoxic conditions, change in gene expression can lead to overexpression of the tumor-associated human carbonic anhydrases IX (hCA IX) and (hCA XII). As such, they constitute attractive targets for PDT.

Herein, the synthesis, characterization, and optical properties of new AIE-based tetraphenylethylene (TPE) PS featuring hCA inhibitors in sulfonamide or coumarin series are described. This PS were found to exhibit good singlet oxygen generation efficiency when compared with rose Bengal (PS), used as reference.

Keywords: Tetraphenylethylene (TPE), Aggregation-induced emission (AIE), human carbonic anhydrase, coumarin, photodynamic therapy, hypoxia, cancer.

Chapter V: Synthesis and characterization of AIE-based photosensitizers featuring carbonic anhydrase inhibitors

II. Introduction

Cancer represents a significant global health challenge. Cancer treatments require improvements in efficacy as well as reduced side-effects.[1] Traditional cancer treatment modalities encompass surgical removal, chemotherapy, immunotherapy, and radiation therapy, which can be employed individually or combined, depending on patient's condition, the tumor's stage, and its location. Photodynamic therapy (PDT) has emerged as a promising alternative anticancer therapeutic strategy to these traditional treatments[2] thanks to its minimal invasiveness, implementation, low systemic toxicity, high efficiency and good selectivity.[3] In addition, PDT was proved clinically to treat several types of tumors.[4-5]

PDT involves three essential components: photosensitizer (PS), oxygen and light. In a typical PDT process, the irradiation of PS at a specific laser wavelength leads to the transition of PS from the ground state to the singlet state. This singlet PS transform into triplet PS through a long lifetime intersystem crossing (ISC) process. The triplet PSs can subsequently transfer either energy to oxygen molecules resulting in the formation of singlet oxygen ($^1O_2$) (type II process) or proton or electron to substrates such as cell membranes or molecules forming radical species (type I process). In practice, type I and II occur simultaneously and the extent of these reactions depend on factors such as the type of PSs used, the nature of the substrates and the concentration of oxygen. Type II PDT tends to be the dominant process in photodynamic therapy since it requires less excitation energy to produce $^1O_2$.[6-7]

However, due to the aggressive growth of cancer cells and insufficient blood supply to the tumor zone, the oxygen concentration in many surrounding regions of solid tumors remains at a low level, known as hypoxia. Cancer cells must adapt to these hypoxic conditions in view of surviving and proliferating. Consequently, they activate intracellular signaling cascade, regulated by the hypoxia-inducible factors (HIF-1/2) transcription factors.[8] This HIF pathway activation results in the modification of a large number of genes responsible for regulation of several crucial processes, involved in tumor growth, including cells survival, proliferation and metabolic reprogramming.[9-10] Hypoxia not only severely limits the therapeutic efficiency of PDT but also, exacerbates it by the consumption of oxygen and vascular closure due to PDT treatment. For these reasons, overcoming hypoxia is the most important to take up for the progression of PDT.

In order to enhance the PDT efficiency and overcome hypoxia issues, recent studies have described the design of PS linked to pharmacologic units able to target human carbonic anhydrase IX (hCA IX).[11-12] hCA IX, in conjunction with another closely related isoform called hCA XII, are transmembrane proteins whose expression is governed by hypoxia-inducible factor (HIF) transcription

factors. Consequently, they are overexpressed in response to hypoxic conditions and play a pivotal role in the regulation of pH levels within tumors, allowing the survival, proliferation, invasion, and metastasis of cancer cells.[10-12] Representative recent examples of metal complexes linked to a benzosulfonamide-based carbonic anhydrase inhibitor are depicted in **Figure 108**.

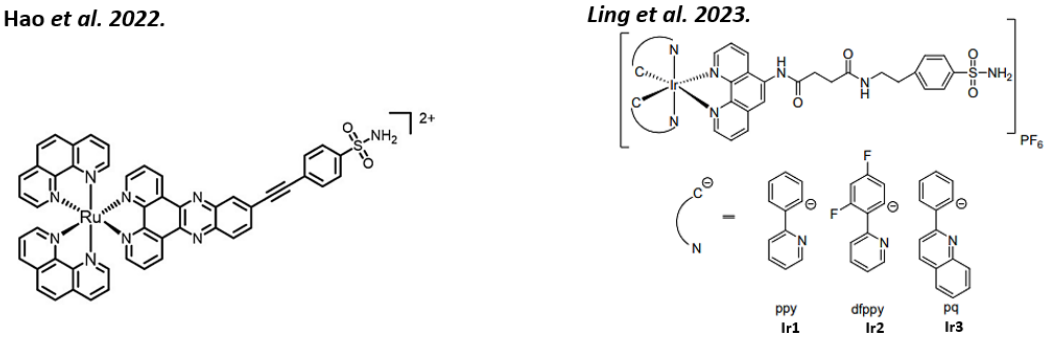


Figure 108. Examples of recent structure of PS systems conjugated with CA inhibitors.[11-12]

Besides metal complexes, conjugated polymers,[13] BODIPYs[14] and porphyrins-based PS exploiting this approach have been prepared.[3, 15] However, all these π-conjugated structures tend to aggregate in biological media through strong intermolecular interactions (π-π stacking, etc.). This aggregation can easily lead to a quenching of excited state (aggregation caused quenching, ACQ) which, affect their fluorescence and the ROS generation efficiency through self-quenching.[16] Decorating this π-conjugated PS with water-solubilizing group allow mitigating this problem of aggregation but require tedious synthesis.

To overcome this drawback, the concept of aggregation-induced emission (AIE) has emerged providing new opportunities for fluorescence imaging and PDT. This concept was first pointed out in 2001 when studying 1-methyl-1,2,3,4,5-pentaphenylsilole, with the observation of intense fluorescence in the solid state while in solution, it is not emissive.[17] Let us compare the behavior of an ACQ fluorophore like perylene with an AIE fluorophore such as 1,1,2,3,4,5-hexaphenylsilole (HPS) (**Figure 109**). In both cases, the fluorophores are present in THF/water mixtures with a volumetric fraction of water ranging from 0 to 90%. Perylene exhibits blue fluorescence up to 70% water content. Beyond this concentration, the phenomenon of molecule aggregation abruptly extinguishes its fluorescence. The exact opposite is observed with HPS: it is non-emissive up to 70% water content, and the intense blue-green fluorescence appears due to its aggregation at water contents of 80% and 90%. As mentioned in the chapter I, AIE fluorophores exhibit different strategies of AIE activation,

which consist in the restriction of the intramolecular motions (RIM), including generally, the restriction of rotation (RIR).

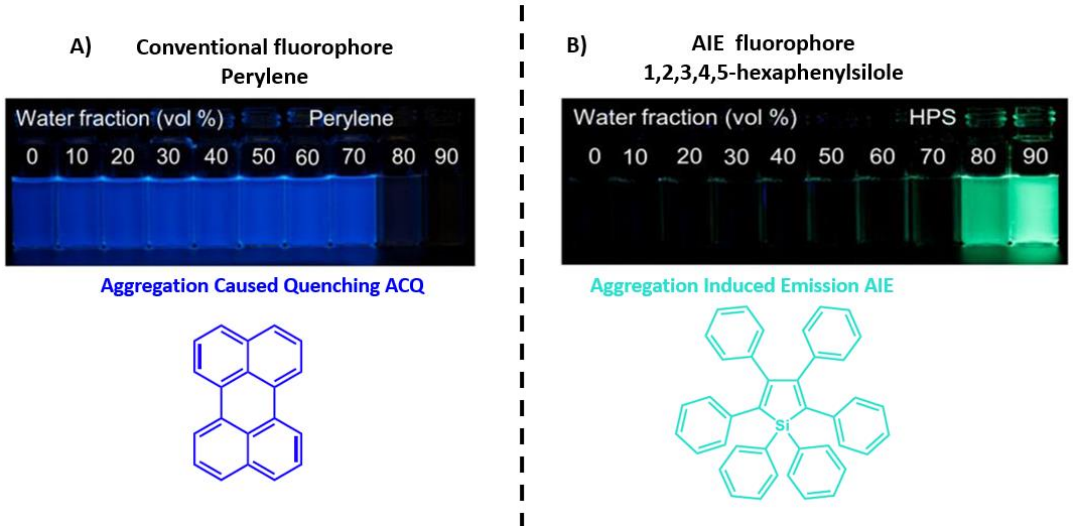


Figure 109. Comparison of the evolution of the fluorescence between a « ACQ » fluorophore like perylene and an AIE fluorophore like 1,1,2,3,4,5-hexaphenylsilole (HPS) in function of water content.[18]

AIE phenomenon can also be related to the restriction of intramolecular vibration (RIV). An example of AIEgen based on RIV is 10,10',11,11'-tetrahydro-5,5'-bidibenzo[a,d][7]annulenylidene (**THBDBA**). The structure of THDBA can be assimilated to that of TPE, with the exception that the rotation of the phenyl groups has been blocked by ethylene bridges in geminal positions. **THBDBA** is non-luminescent in solution due to the loss of the excitation energy through vibration of the phenyl rings. When aggregated, AIE is activated by RIV.[19] In the context of PDT, the restriction of these intramolecular motions is particularly appealing since it can decrease the thermal deactivation of the excited energy of PS, resulting in bright fluorescence as well as enhanced ROS generation efficiency in the aggregated state in biological media.

A wide variety of AIE PS was described in the literature mainly based on TPE scaffold, a well-established AIEgen. An efficient strategy to elaborate AIE PS consists in incorporating electron donating and electron accepting moieties on TPE core. This donor-acceptor push pull structures enables not only to shift the emission to the long wavelength region but more importantly, to reduce the ΔE_{ST} which results in increased intersystem crossing (ISC) rate and thus, improved photosensitizing efficiency. Another convenient strategy widely used to obtain effective PSs is based on the addition of heavy atom, known to promote strong spin-orbit coupling (SOC) between singlet and triplet and thus, allowing to enhance ISC rate.

Based on these strategies, Chen *et al.* have notably reported the synthesis of three PS based on TPE isoquinolinium (**TPE-IQ**) derivatives (**Figure 110**) distinguished through the introduction of several electron donating groups and sterically hindered groups. These new PSs exhibited AIE properties with different emission colors depending on the nature of the electron donating groups. They were also found to be able to generate ROS efficiently and to target different cellular organelles.[20]

More recently, Chaï *et al.* have described the synthesis of a new AIE PS 1-[2-hydroxyethyl]-4-[4-(1,2,2-triphenylvinyl)styryl]pyridinium bromide (**TPE-Py-OH**) (**Figure 110**). As expected, **TPE-Py-OH** showed intense fluorescence emission in the aggregated state. **TPE-Py-OH** can not only simultaneously target lipid droplets and mitochondria, but also, stay in cells for a long period (more than 7 days). It has also demonstrated an efficient ROS generation capacity and thus, led to effective PDT *in vivo* and *in vitro*.[21]

A novel series of PSs (**SIN**, **SBN**, **SCN**, and **SMN**) with AIE properties were designed by Pan *et al*. exploiting benzothiazole- triphenylamine (BZT-triphenylamine) as a scaffold and bearing different bromoalkyl chain attached to the nitrogen heterocyclic compound (**Figure 110**). Iodine incorporating PS **SIN** was found to selectively target lysosomes in tumor cells with an impressive Pearson correlation coefficient (PCC) of 0.97. The AIE properties of these PSs were exploited for their response to viscosity, which lead to significant fluorescence enhancement and reasonable fluorescence quantum yield ($Ø_F$ = 0.05 %) at high viscosity. PS **SIN** in particular exhibit a faster singlet oxygen generation, which opens the door to efficient photocytotoxic on tumor cells in weakly acidic media.[22]

Very recently, Zhao and his team described the synthesis of red-emissive AIEgens (**TPTH** and **TPTB**) (**Figure 110**). **TBTH** and **TPTB** were built upon dicyano vinyl-substituted thiophene electron accepting moieties linked TPE moieties. The introduction of Br in the alkyl side chain allows reaching enhanced ROS generation through a “through-space” spin–orbit heavy atom effect compared to **TPTH**. In addition to these good photosensitizing properties, **TPTB** is highly fluorescent ($Ø_F$ = 0.38) and able to image the cell plasma membrane with high specificity and long-term retention ability. Its intrinsic lipophilicity enables its resistance in the change of $\Delta\Psi_{Plasma}$.

Chapter V: Synthesis and characterization of AIE-based photosensitizers featuring carbonic anhydrase inhibitors

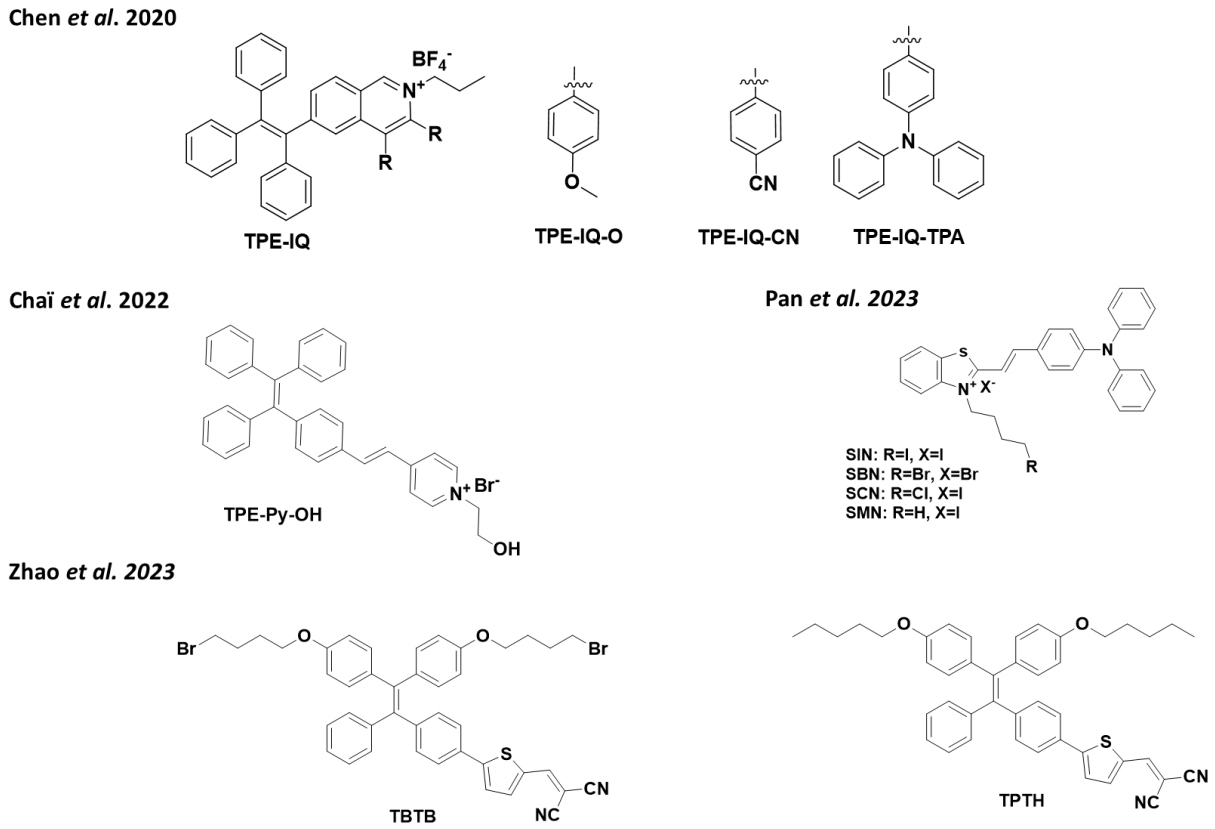


Figure 110. Examples of some AIEgens structure used as PSs for photodynamic therapy.

These recent results highlighted the potential of AIE platform for imaging and PDT through judicious design and most particularly, as potential platform for combination with human carbonic anhydrase inhibitors (CAi).

Herein, we report the design of three AIE PSs-based on a TPE core (**Figure 111**) including both targeting and inhibition of carbonic anhydrase hCA IX and hCA XII. As discussed above, these PSs will be designed through the Donor-Acceptor (D-A) approach which consists in the separation of the HOMO-LUMO distribution and thus, allows reducing repulsion between valence electrons in the S_1 state to achieve smaller ΔE_{ST}.[23] To these PSs, were grafted some CAi (namely, benzenesulfonamide or coumarin). These CAis were either closely linked to the TPE core (**9**) or separated from the PS with an alkyl side chain (**15a** and **15b**) (**Figure 111**). TPEs **15a** and **15b** differs from each other by the number of electrons accepting moieties. The presence of a radical-pair ISC process in this symmetric A–D–A systems should enable an effective charge separation and ultra-small singlet–triplet energy splitting which will is particularly interesting in view of increasing photosensitizing ability of the PS.[24] The synthesis, optical properties and their ability to generate singlet oxygen will be studied in details.

Chapter V: Synthesis and characterization of AIE-based photosensitizers featuring carbonic anhydrase inhibitors

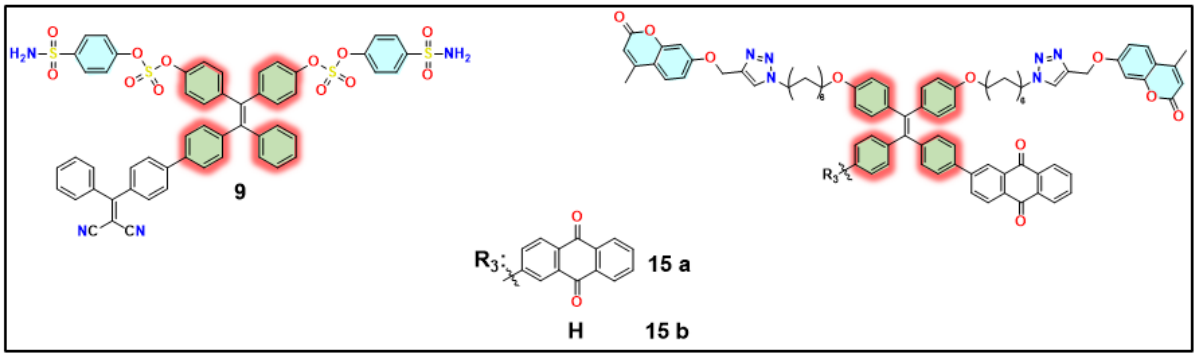


Figure 111. Structure of AIE PS for photodynamic therapy.

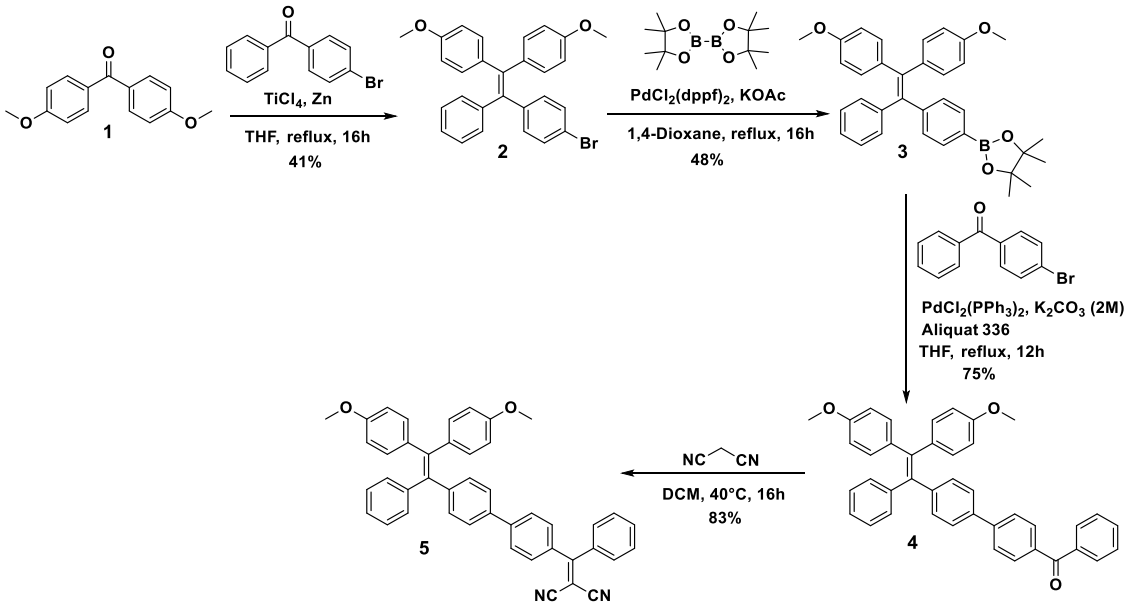
III. Results and Discussion

III.1 Design and synthesis

Synthesis of TPE 9

The structure of PS **9** derived from the well-known TPE-based PS **5**. This PS was first prepared following the synthetic pathway described in **Scheme 7** and described in the literature.[25] Namely, a McMurry reaction was performed by the coupling of 4,4'-dimethoxybenzophenone using $TiCl_4$. TPE **2** was isolated with a yield of 41%. In a second step, the boronate was synthesized in 48% yield through the Miyaura borylation reaction of TPE **2** with bis(pinacolato)diboron in the presence of $PdCl_2$(dppf) catalyst. The Suzuki cross-coupling reaction of boronate **2** with 4-bromobenzophenone affords then **4** in 75% yield. Finally, the desired donor-acceptor structure of PS **5** was prepared through a Knoevenagel reaction between **4** and malononitrile in 83% yield.

Chapter V: Synthesis and characterization of AIE-based photosensitizers featuring carbonic anhydrase inhibitors



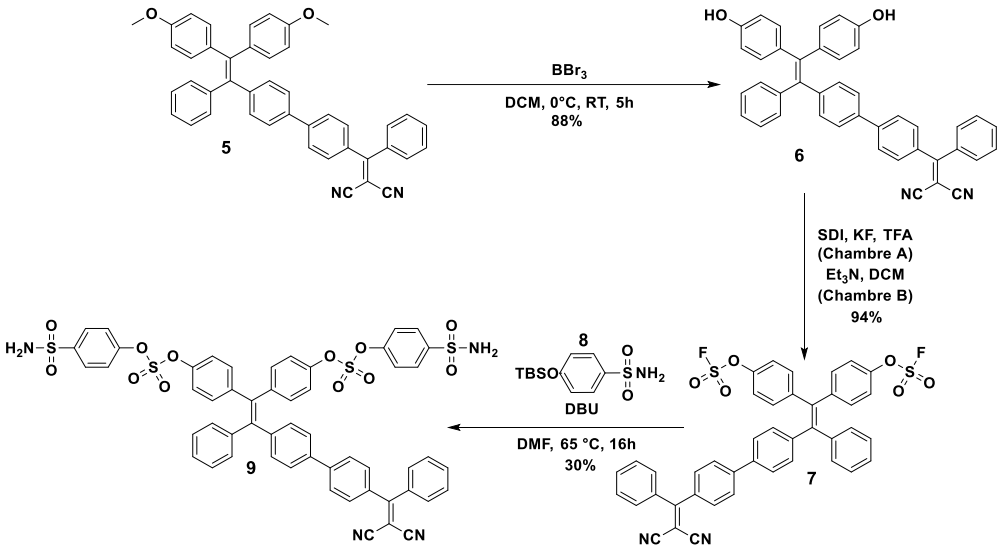
Scheme 7. Synthetic route towards photosensitizer **5.**

With PS **5** in our hand, we decided to fix the CAi directly on the TPE core. For this purpose, we exploit the Sulfur (VI) fluoride exchange (SuFEX). SuFEx represents a straightforward and environmentally compatible chemical reaction, enabling the attainment of substantial yields with minimal purification requirements in the presence of water and oxygen. This reaction allow notably the formation of stable S−O linkages through the exchange of S−F bonds with aryl silyl-ether substrates[26] accelerated by basic-nitrogen (*e.g* Et_3N, DBU) catalysts.[27]

Following SuFEx strategy, we design PS **9** (**Scheme 9**). TPE **9** can be synthesized from PS **5** in a three steps strategy. First, deprotection of the aryloxide group by boron tribromide was performed leading to dihydroxy TPE **6** in 88% yield. Deprotection of PS **5** was confirmed by ^{1}H NMR spectroscopy by the disappearance of the singlet at 3.75 ppm, corresponding to the OMe groups. **TPE 7** was synthesized through reacting the phenol and sulfuryl fluoride in the presence of a base.[28] In our case, we used 1,1'-sulfonyldiimidazole (SDI) as sulfuryl fluoride precursor with potassium fluoride (KF) in chamber A. In another chamber (chamber B), TPE **6** was dissolved in a mixture of Et_3N and dichloromethane. The sulfuryl fluoride is formed after the addition of TFA. This gas was formed and moved from chamber A to chamber B. After treatment, the residue was purified by column chromatography on silica gel (100% DCM) allowing to provide TPE **7** in 94% in yield (**Scheme 9**). The structure of **7** was confirmed by ^{1}H NMR and ^{19}F NMR spectroscopy. Indeed, ^{1}H NMR spectroscopy indicates the disappearance of the signal of OH groups at δ = 9.35 ppm. We also observe the

appearance of two signals at δ = 38.03 ppm and δ = 37.91 ppm, corresponding to the two SO_2F groups, which confirms the structure of **TPE 7.**

Finally, the SuFEX click reaction of TPE **7** with 2 equivalents of nucleophile 4-O-TBS-benzylsulfonamide (4-((*tert*-butyldimethylsilyl)oxy)benzenesulfonamide) **8** was performed in DMF in the presence of DBU affording **9** in 30% yield after purification by column chromatography on silica gel (**Scheme 9**). **9** was characterized and identified by ^{1}H NMR and $^{13}C\{^1H\}$ NMR spectroscopy. ^{1}H NMR spectrum of **9** reveals the signals of sulfonamide NH_2 at δ = 7.94 ppm and δ = 7.92 ppm (H_{ar}) as well as a broad singlet at δ = 5.30 ppm. The $^{13}C\{^1H\}$ NMR spectra also indicates the presence of some signals in the aromatic region at δ = 152.9, 135.0, 128.8 and 120.7 ppm. The structure of **9** was also confirmed by high-resolution ESI-TOF mass spectrometry (negative mode) (ESI^-) with the presence of pseudo-molecular ion $[M-H]^-$ at *m/z* = 1061.1296 Da in agreement with the calculated one 1061.1290 Da.

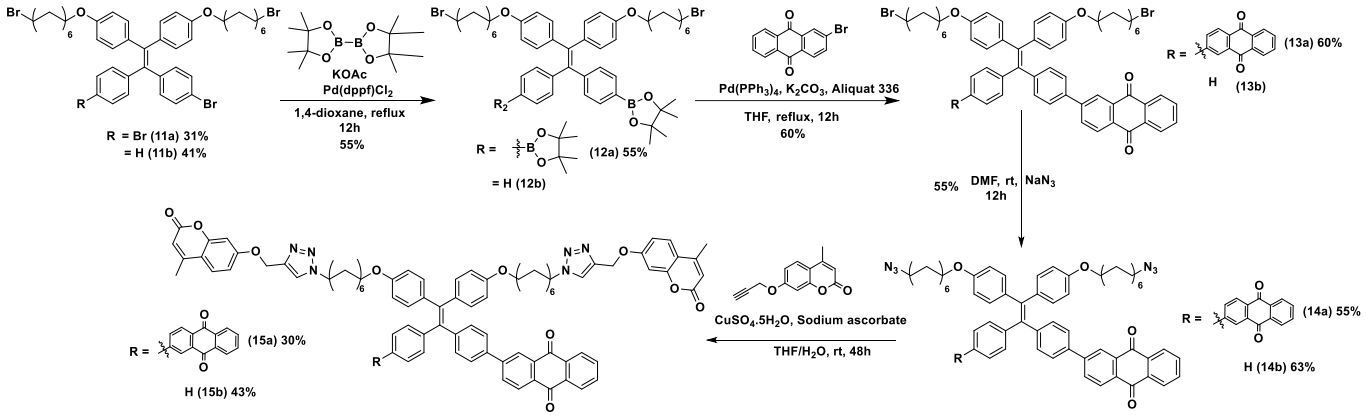


Scheme 8. Synthesis of PS **9**.

Synthesis of TPEs 15a and 15b.

The synthetic pathway towards **15a** and **15b** bearing two or one anthraquinone accepting units, respectively is described in **Scheme 9**. First, the precursors **11a** and **11b** were prepared according to literature procedures through the McMurry reaction of 4,4'-bis(6-bromohexyloxy)benzophenone with either 4,4'-dibromobenzophenone or 4-bromobenzophenone using $TiCl_4$.[29] The Miyaura borylation reaction allows then the formation of the corresponding boronates **12a** and **12b** by cross-coupling of bis(pinacolato)diboron with **11a** and **11b** using $PdCl_2$(dppf) as catalyst. Anthraquinone accepting units were then introduced into the TPE core by a Suzuki cross-coupling reaction between boronates **12a** and **12b** and 2-bromoanthraquinone. The bromohexyl-functionalized TPE PSs **13a** and **13b** were

converted into the azido derivatives **14a** and **14b** by nucleophilic substitution reaction in DMF. Finally, the coupling of alkyne-functionalized coumarin with azido-TPE derivatives **14a** or **14b** *via* Cu(I)-catalyzed Huisgen 1,3-dipolar cycloaddition was performed in a mixture of THF/H_2O to obtain PSs **15a** (30%) and **15b** (43%), respectively (**Scheme 9**). The ATR-FTIR spectra of the cycloadducts indicated the disappearance of the strong asymmetric stretching frequency at 2090 cm^{-1} corresponding to the azido group. A singlet was also observed around δ = 7.8 ppm in the ^1H NMR spectra of PSs confirming the formation of 1,2,3-triazole ring. The structures of the synthesized PSs were also confirmed by high-resolution ESI-TOF mass spectrometry (positive mode) (ESI^+) with the presence of pseudo-molecular ion $[M+H]^+$ at 1455.5437 Da for **15a** and 1249.5068 Da for **15b** in good agreement with the calculated ones 1455.5443 Da and 1249.5057 Da, respectively.



Scheme 9. Synthetic pathway towards PSs **15a** and **15b**.

III.2 Optical properties

The optical properties of the AIE-based PSs featuring carbonic anhydrase inhibitors **9**, **15a** and **15b** were investigated by UV-Visible absorption and fluorescence spectroscopy. The photophysical properties of theses PSs are summarized in **Table 9.** All these TPEs exhibit absorption bands in the range between 320 and 450 nm (**Figure 112**).

TPE	9	15a	15b
λ_{abs}	320, 350	320,420	320,420
λ_{em}	575	578	578

Table 9. Optical characteristic of the synthesized PSs.

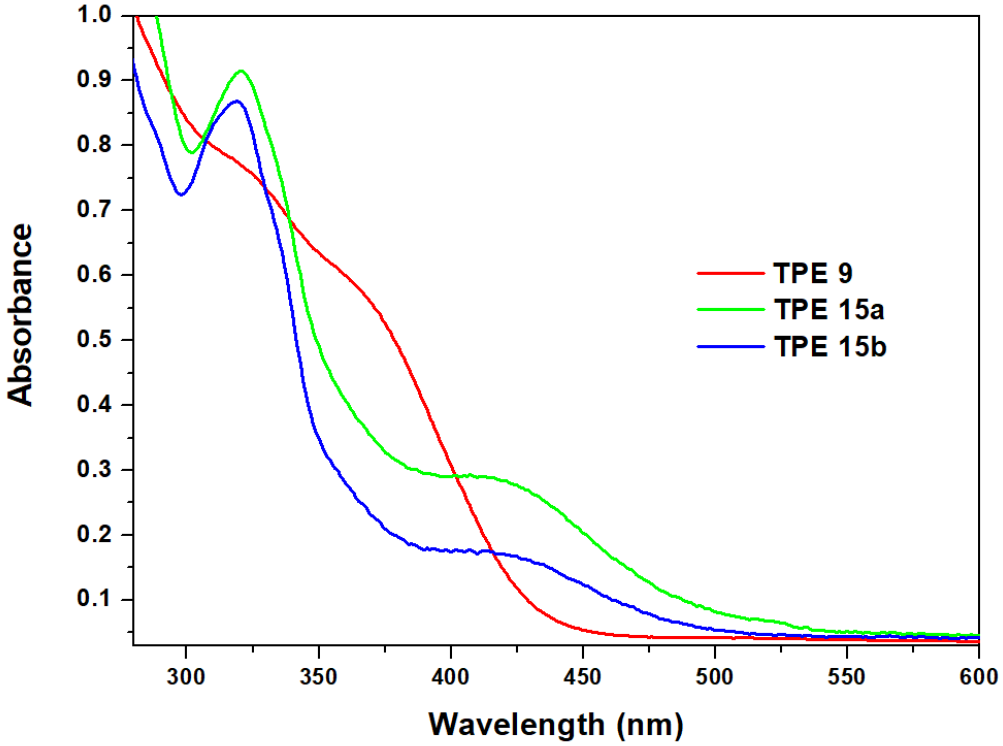


Figure 112. UV-Visible absorption spectra of TPEs **9**, **15a** and **15b** in THF (C= 10^{-5} M).

To evaluate the AIE properties of TPEs **9**, **15a** and **15b**, their emission spectra were recorded in THF/water mixtures with different water volumetric fraction (f_w) to fine-tune the aggregation extent (**Figure 113**). At the water fraction (f_w) is below, the fluorescence is very weak indicating that they are virtually non-fluorescent when molecularly dissolved in a good solvent. However, once the water content (f_w) further increases, a drastic increase of the PL emission with an emission band around 575 nm is observed reaching maximum for f_w = 90%. I_{agg}/I_{THF} of ca. 20, 90 and 130 for **9**, **15a** and **15b** were noticed, respectively. This strong increase in the fluorescence intensity can be attributed to aggregation, which activates the RIM process.[30] This behavior unambiguously confirms the AIE features of these TPE-based PSs.

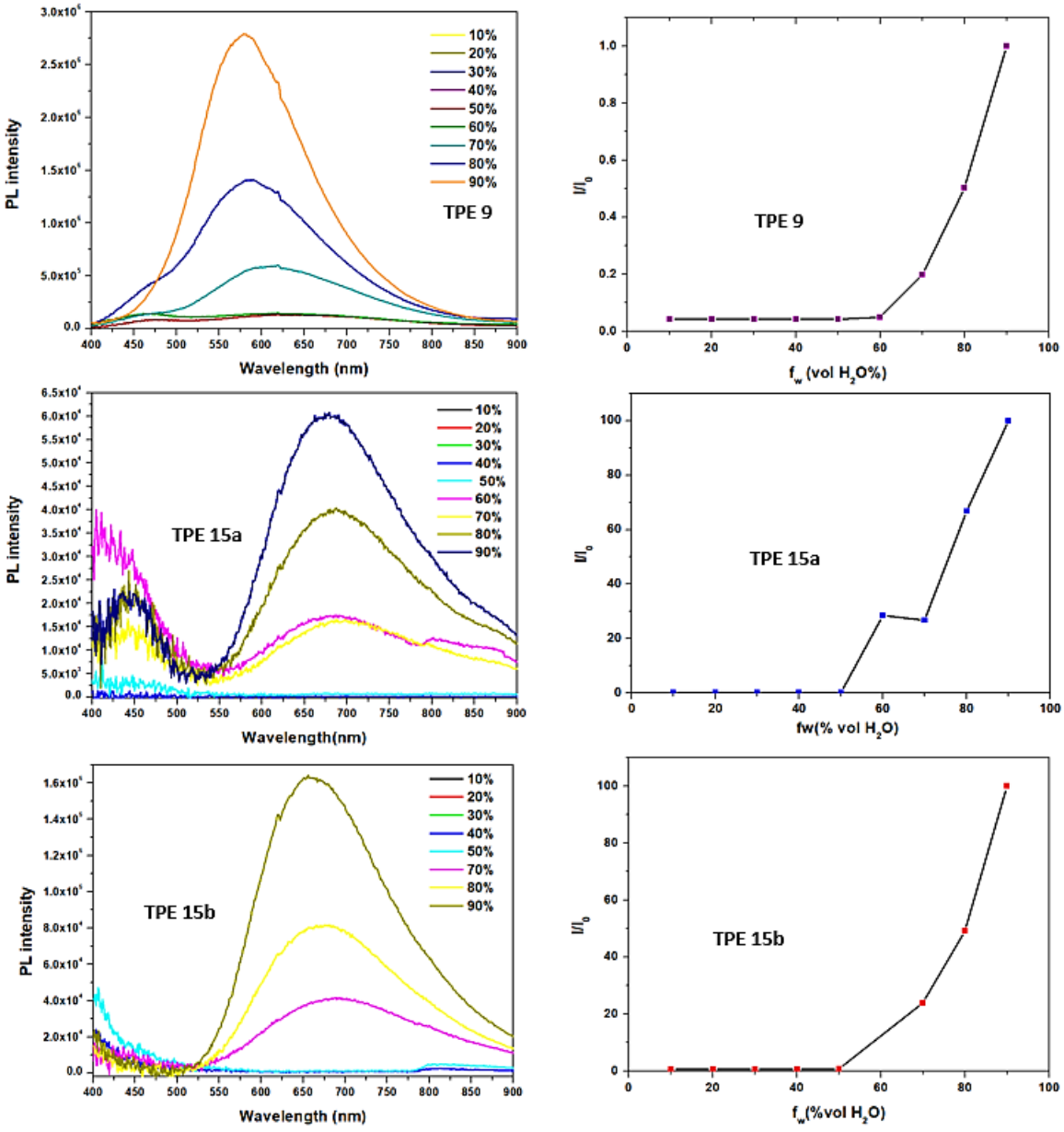


Figure 113. **A)** Emission spectra of TPEs **9**, **15a** and **15b** (C~ 5x 10^{-5} M, λ_{exc} =350 nm) in THF/water mixtures with different water fractions (f_w). B) Plot of I/I_0 values *vs*. water fractions. I_0 is the PL intensity for the highest f_w

III.3 Carbonic anhydrase inhibition assays

The CA-inhibitory activities of the synthesized TPEs were evaluated in enzyme inhibition assays against two cytosolic off-targets hCA I and II enzymes and the two tumor-associated membrane bound hCA IX and hCA XII comparing with acetazolamide (AAZ) using a stopped-flow assay method (**Table 10**). Globally, synthesized TPEs are less active than the clinically used AAZ in one or two orders of magnitude

which may be explained by the size of the PSs which will hinder its approach towards the enzyme. **9** exhibited nanomolar activity against the four isoforms, with inhibition constants from 958.9 to 7185 nM while **15a** and **15b,** due to the presence of the coumarin moieties, are found to be selective against tumor-associated membrane bound hCAIX and hCA XII. The selectivity against membrane carbonic anhydrase isoforms demonstrated by TPEs containing coumarin moieties (**15a** and **15b**) can be explained by the hydrolysis of coumarin into the corresponding 2-hydroxycoumarin acid form, which will bind at the entrance of the active site of the enzyme.[31-32] **15a** and **15b** show better inhibitions constant for hCA IX and hCA XII than **9** (K_I(hCA IX)= 576.8 nM K_I(hCA XII)= 854.3 nM, for **15a**, K_I(hCA IX)= 262.1 nM, K_I(hCA XII) = 417.2 nM for **15b**). It is also worth pointing out that **15b** featuring one anthraquinone moiety exhibit inhibition constants twice as those of **15a** incorporating two anthraquinones.

Compounds	K_I (nM)[a]			
	hCA I	hCA II	hCA IX	hCA XII
9	>100000	7185	5668	958.9
15a	>100000	>100000	576.8	854.3
15b	>100000	>100000	262.1	417.2
AAZ	250.0	12.5	25.0	5.7

Table 10. Inhibitory activity of **TPEs** against **hCA I**, **hCA II**,**hCA IV, hCA IX** and **hCA XII** using acetazolamide **AAZ** as a reference drug. [a]Mean from 3 different measurements by a stopped flow technique (errors were in the range of ± 5-10 % of the reported values).

III.4 Singlet oxygen ($^1O_2$) generation

In order to investigate the ability of the synthesized TPEs to produce $^1O_2$ in comparison with Rose bangal (**RB)** used as reference ($^1O_2$ quantum yield $\Phi\Delta$= 75% in H_2O),[33] 9,10-anthracenediyl-bis(methylene) dimalonic acid (**ABDA**) was used as $^1O_2$ quencher.[34] The $^1O_2$ detection by ABDA involves the formation of a endoperoxide *via* a [4+2] cycloaddition, which results in the loss of the extended π-electron system and its characteristic optical features. As such, by following the changes in the UV-Visible absorption spectra of an aqueous ABDA solution containing the PS upon irradiation, the $^1O_2$ generation can be monitored.

Following this strategy, a solution of ABDA in water (50 μM) in the presence of PS (**RB**, **9, 15a** and **15b**) (5 μM) was prepared. The UV-Visible absorption spectra were recorded after several

irradiation times (λ= 450 nm). In **Figure 112**, the UV-Visible absorption spectra of a solution of ABDA without PS irradiated during 5 minutes at λ = 450 nm (**Figure 6**) show no changes indicating that there is no observed photobleaching in the control experiment. In contrast, the absorbance of **ABDA** in the presence of the PS (**RB** or TPEs-based PS) gradually decreases over irradiation time (**Figure 112**). Comparing the degradation of ABDA by PS, it reveals that **15a** and **TPE 15b** seem to be more efficient PS than **RB** while for **9**, the singlet oxygen generation efficiency is lower. As expected, **15a** generates more singlet oxygen than **15b** since the decrease in ABDA degradation is faster. As stated above, this can be explained by the presence of a radical-pair ISC process in **15a,** which allows an effective charge separation and ultra-small singlet–triplet energy splitting.

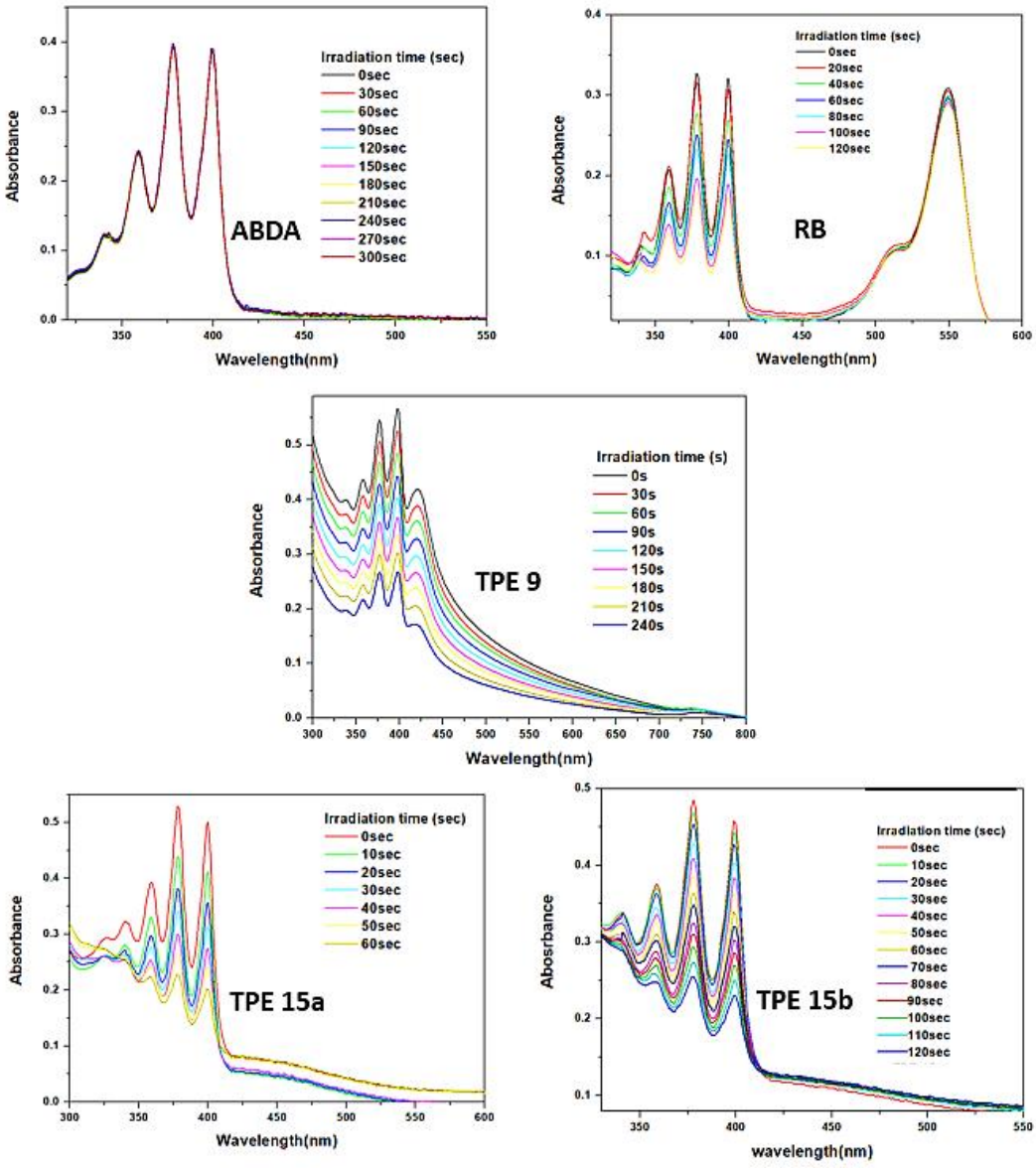


Figure 12. Time-dependent absorption changes of a ABDA solution in water (50 µM) without PS or with **RB**, **9**, **15a** and **15b** (5 µM) under light irradiation (λ_{max} =450 nm) in DMF/water=1/99 (v/v).

This ability to generate $^1O_2$ is essential in view of using these AIE-based PSs for PDT treatment. Unfortunately, due to a lack of time, we didn't succeed to perform biological tests before the writing of this manuscript. Evaluation of cytotoxicity, imaging ability and PDT efficiency are currently under progress.

IV. Conclusion

In this chapter, we successfully designed several AIE PSs incorporating a TPE as a scaffold. Human carbonic anhydrase inhibitors in sulfonamide or coumarin series were grafted onto the donor-acceptor architecture of these AIE PS. As expected, upon aggregation in water, all these TPEs exhibit AIE behavior due to the RIM process. Carbonic anhydrase inhibition assays reveal that **15a** and **15b** containing coumarin moieties are selective against membrane carbonic anhydrase isoforms hCA IX and XII while **9** incorporating sulfonamide-hCAi is not. Due to their large size, these synthesized TPEs are less active than the clinically used AAZ in one or two orders of magnitude. Finally, we proved that all these PSs exhibit good singlet oxygen generation efficiency, especially PS **15a** and **15b** which were found to be more efficient than RB. Biological studies are currently under progress to examine in more details their photocytoxicity and their ability to be used as imaging agent.

V. Experimental section

V.1 Materials

Reactions needing inert atmosphere were performed under argon or nitrogen using oven-dried glassware and Schlenk techniques. All solvents were obtained from commercial suppliers and used as received. 4-bromobenzophenone (Themo Scientific, 97%),4,4'-Dibromobenzophenone (TCI, 98%), triethylamine (Fluorochem, 99%), 4,4'-diméthoxybenzophenone (Alfa Aesar, 98%), titanium (IV) chloride (Merck, 97%), bis(pinacolato)diboron (Alfa Aesar, 98%), zinc dust (Aldrich, 98%), potassium carbonate (Alfa Aesar, 99%), potassium acetate (Fluorochem, 99%), aliquat 336 (Alfa Aesar, 88%), sodium ascorbate (Fluorochem, 99%) were used as received. Compounds **Coum-prop,** TPEs **2-5 ,10a**, **10b**, **12a**, **12b** and **13b** were prepared by procedures described in the literature. [29-35-25] TLC were carried out on Merck DC Kieselgel 60 F-254 aluminium sheets and spots were visualized with UV-lamp (λ = 254/365 nm) if necessary. Preparative purifications were performed by column chromatography on silica gel (Merck 40−60 µM).

V.2 Instruments and methods

NMR spectroscopy and MS spectrometry were performed at the Laboratoire de Mesures Physiques (LMP) of the University of Montpellier (UM). ^1H and $^{13}C\{^1H\}$ NMR spectra were recorded on

Chapter V: Synthesis and characterization of AIE-based photosensitizers featuring carbonic anhydrase inhibitors

Bruker 400 MHz Avance III HD and 500 MHz Avance III spectrometers at 298 K. Deuterated solvents were used as received (purchased from Sigma-Aldrich). ^{1}H and $^{13}C\{^{1}H\}$ NMR spectra were calibrated to TMS based on the relative chemical shift of the residual non-deuterated solvent as an internal standard. Chemical shifts (δ) are expressed in ppm and coupling constants values (^{n}J) are expressed in Hz. Abbreviations used for NMR spectra are as follows: s, singlet; d, doublet; t, triplet; q: quadruplet; quint, quintuplet; sx, sextuplet and m, multiplet. High Resolution Mass spectra (HRMS) were recorded on a Bruker MicroTof QII instrument in positive/negative modes (ESI). UV-Visible absorption spectra were recorded in THF with a JASCO V-750 UV-Visible-NIR spectrophotometer in 10 mm quartz cells (Hellma). The concentration range was chosen to remain in the linear range of the Beer–Lambert relationship (A ca. 0.2–0.8). The emission spectra were recorded at 25°C on a fluorescence spectrophotometer (FS920, Edinburgh Instrument), equipped with a calibrated photomultiplier in a Peltier (air cooled) housing (R928P, Hamamatsu), with a 450 W continuous xenon arc lamp as the excitation source for steady-state photoluminescence measurement using a 10 mm quartz cell (Hellma) with excitation path length.

V.3 Synthesis

Synthesis of compound 6:

Boron tribromide (1.0 M in dichloromethane, 6 mL, 5 eq.) was added to the solution of compound **5** (0.75 g, 1.2 mmol, 1 eq.) in dichloromethane (25 mL) at 0 °C. The reaction mixture was then stirred at room temperature for 5 h. The reaction was cooled using an ice-water bath and was quenched by addition of water (25 mL). The organic layer was collected, washed with 20 mL of brine, dried over anhydrous $MgSO_4$. The mixture was filtered, and then the filtrate was evaporated under reduced pressure. The residue was isolated in dichloromethane and *n*-hexane (1/9) to give compound **6** as a red solid (0.63 g, 88 %). **^{1}H NMR** (400 MHz, $CDCl_3$) δ 7.66 (d, $^{3}J_{H\text{-}H}$ = 8.6 Hz, 2H), 7.59 (t, $^{3}J_{H\text{-}H}$ = 7.2 Hz, 1H), 7.53 – 7.43 (m, 4H), 7.39 (d, $^{3}J_{H\text{-}H}$ = 8.4 Hz, 1H), 7.12 (m, 5H), 7.05 (d, $^{3}J_{H\text{-}H}$ = 7.5, 2.0 Hz, 1H), 6.97 – 6.86 (m, 4H), 6.62 – 6.53 (m, 4H), 4.65 (d, $^{3}J_{H\text{-}H}$ = 2.2 Hz, 2H). **$^{13}C\{^{1}H\}$ NMR** (126 MHz, $CDCl_3$) δ 174.7, 154.3, 145.3, 145.0, 144.0, 140.8, 138.7, 136.6, 136.3, 134.6, 132.8, 132.2, 131.5, 131.2, 130.6, 129.0, 127.9, 127.1, 126.5, 114.8, 114.2, 80.9, 77.4.

Synthesis of compound 7:

Fluorosulfatation reactions takes place in a two-chambers reactor possessing septums. Chamber A is filled with 1,1'-sulfonyldiimidazole (SDI) (57.6 mg, 0.29 mmol, 3 eq.) and potassium fluoride (KF) (45 mg, 0.77mmol, 8 eq.) and chamber B is filled with TPE **6** (50 mg, 9.5 mmol, 1 eq.) and triethylamine (Et_3N) (54 µL, 0.38 mmol, 4 eq.) in 1 mL dichloromethane. Both chambers have a magnetic bar. Sulfuryl

fluoride is generated in chamber A by addition of TFA (0.2 mL, 30 eq.). The gas formation is observed as a white cloud moving from chamber A to chamber B. Both chambers are left under stirring for 18h at room temperature. Then, chamber B septum is removed, and the stirring is continued for at least 15 min in order to ensure complete sulfuryl fluoride removal. Next, the content of chamber B is transferred to a round-bottom flask. Chamber B is rinsed several times with dichloromethane. Organic fractions are evaporated under reduced pressure. The residue is then purified by column chromatography on silica gel (100% DCM) to furnish the expected fluorosulfate (0.060 g, 94% yield). **^{1}H NMR** (400 MHz, $CDCl_3$) δ 7.69 – 7.63 (m, 2H), 7.63 – 7.56 (m, 1H), 7.54 – 7.48 (m, 4H), 7.48 – 7.40 (m, 4H), 7.23 – 7.14 (m, 7H), 7.14 – 7.07 (m, 6H), 7.07 – 7.00 (m, 2H). **^{19}F NMR** (377 MHz, $CDCl_3$) δ 38.03 (s), 37.91 (s). **^{13}C{^{1}H} NMR** (101 MHz, $CDCl_3$) δ 174.5, 148.8, 148.7, 144.7, 143.7, 143.5, 143.4, 142.8, 142.1, 138.1, 137.4, 136.1, 135.0, 133.2, 133.2, 132.8, 131.9, 131.3, 131.2, 130.6, 129.0, 128.3, 127.7, 127.2, 126.9, 120.7, 120.6, 114.2, 114.1, 81.2.

Synthesis of compound 8:

To a solution of 4-hydroxybenzenesulfonamide (3.46 g, 20 mmol, 1 eq.) in DMF (40 mL), was added *tert*-Butyldimethylsilyl chloride (TBDMSCl) (3.31 g, 22 mmol, 1.1 eq.) and imidazole (1.50 g, 22 mmol, 1.1 eq.). The mixture was stirred at room temperature for 20 hours. Then, volatiles were removed under reduced pressure, and the residue was taken back in 30 mL of ethyl acetate. The organic phase was washed 3 times with HCl 1N, brine, dried over anhydrous $MgSO_4$ and filtered. The filtrate was evaporated under reduced pressure. The crude product was purified by column chromatography on silica gel (cyclohexane/ ethyl acetate 1/1) to afford compound **8** (5.1 g, 89%). **^{1}H NMR** (400 MHz, $CDCl_3$) δ 7.81 (d, $^{3}J_{H\text{-}H}$ = 8.7 Hz, 2H), 6.91 (d, $^{3}J_{H\text{-}H}$ = 8.7 Hz, 2H), 5.01 (s, 2H), 0.98 (s, 9H), 0.23 (s, 6H).**^{13}C{^{1}H} NMR** (101 MHz, $CDCl_3$) δ 159.8, 134.4, 128.6, 120.5, 25.6, 18.3, -4.2.

Synthesis of compound 9:

To a solution of compound **7** (100 mg, 0.132 mmol, 1eq.) and 4-O-TBS-benzylsulfonamide (76 mg, 0.264 mmol, 2eq.) in DMF (0.5 mL) was added 1,8-diazabicyclo[5.4.0]undec-7-ene (DBU) (9.9 µL, 0.066 mmol, 0.5 eq.). The mixture was stirred at 65°C for 16 hours and then, a maximum of DMF was removed under reduced pressure. The residue was then diluted in 5 mL ethyl acetate, washed 3-4 times with 10 mL of water, and dried over anhydrous $MgSO_4$. The solution was filtered and the volatiles were removed under reduced pressure. The crude product was purified by column chromatography on silica gel (DCM: from MeOH 97/3 to 95/5) to afford compound **9** (0.041 g, 30% yield). **^{1}H NMR** (400 MHz, $CDCl_3$) *δ* 7.94 (d, $^{3}J_{H\text{-}H}$ = 8.8 Hz, 2H), 7.92 – 7.85 (m, 2H), 7.84 – 7.75 (m, 1H), 7.63 (d, $^{3}J_{H\text{-}H}$ = 8.5 Hz, 2H), 7.60 – 7.54 (m, 1H), 7.53 – 7.38 (m, 7H), 7.38 – 7.28 (m, 4H), 7.28 – 7.21 (m, 1H), 7.20 – 6.96 (m,

14H), 5.30 (bs, 2H), 5.28 (bs, 2H). **$^{13}C\{^1H\}$ NMR** (101 MHz, $CDCl_3$) δ 174.8, 152.9, 152.8, 148.8, 148.8, 144.7, 143.1, 143.0, 143.0, 142.9, 142.2, 141.4, 141.3, 137.9, 137.9, 136.0, 135.0, 133.0, 133.0, 132.9, 132.0, 131.3, 131.2, 130.6, 129.0, 128.8, 128.8, 128.2, 127.2, 126.8, 121.8, 121.7, 121.6, 120.8, 120.6, 114.3, 114.0, 81.0. **HRMS (ESI^-)** m/z calcd for $C_{54}H_{37}N_4O_{12}S_4$ $[M-H]^-$=1061.1290 found $[M-H]^-$= 1061.1296.

Synthesis of compound 11a:

Compound **10a** (0.58 g, 2.22 mmol, 1.2 eq.), 4,4'-dibromobenzophenone (1.00 g, 1.85 mmol, 1 eq.) and zinc powder (1.03 g, 5.5 mmol, 5.6 eq.) were introduced into a 250 mL three-neck round-bottom flask equipped with condenser and a dropping funnel under an inert atmosphere. After adding THF (30 mL), the reaction mixture was cooled to -78°C and $TiCl_4$ (0.62 mL, 9.24mmol, 5 eq.) was added dropwise with a syringe. The mixture was stirred for 30 min at 0°C and then, heated under reflux for 16 hours. After cooling at room temperature, water (50 mL) was added. The organic layer was extracted with DCM (3 x 100 mL), dried over anhydrous $MgSO_4$ and filtered. The filtrate was concentrated under reduced pressure under reduced pressure. The residue was purified by flash chromatography on silica gel using cyclohexane/ dichloromethane (7/3) to lead compound **11a** as a yellow powder (480 mg, 31%), ^{1}H NMR (400 MHz, $CDCl_3$) δ 7.22 (d, $^3J_{H-H}$ = 8.4 Hz, 4H), 6.88 (dd, $^3J_{H-H}$ = 12.0, 8.6 Hz, 8H), 6.64 (d, $^3J_{H-H}$ = 8.7 Hz, 4H), 3.90 (t, $^3J_{H-H}$ = 6.4 Hz, 4H), 3.42 (t, $^3J_{H-H}$ = 6.8 Hz, 4H), 1.93 – 1.86 (m, 4H), 1.80 – 1.74 (m, 4H), 1.53 – 1.47 (m, 8H). **$^{13}C\{^1H\}$ NMR** (126 MHz, $CDCl_3$) δ 157.9, 142.9, 141.6, 136.5, 135.5, 133.1, 132.6, 131.0, 120.3, 113.8, 67.6, 34.0, 32.7, 29.2, 28.0, 25.4. **HRMS (ESI^+) m/z** calcd for $C_{51}H_{66}Br_2O_2$ $[M]^+$= 843.9761 found: $[M]^+$= 843.9756.

Synthesis of compound 13a:

Compound **12a** (0.45 g, 0.32 mmol, 1 eq.) and 2-bromoanthraquinone (0.21 g, 0.72 mmol, 2.2 eq.) were dissolved in THF (10 mL). A 2M aqueous K_2CO_3 solution (1.0 mL) and few drops of Aliquat 336 were added. The mixture was stirred for 40 min under inert atmosphere at room temperature. Then, $Pd(PPh_3)_4$ catalyst (0.02 g, 0.019 mmol, 0.06 eq.) was added and the reaction mixture was stirred at 78 °C for 12h. After cooling to room temperature, the mixture was extracted with dichloromethane (50 mL) and water (50 mL × 3). The organic layer was dried over anhydrous $MgSO_4$ and concentrated by rotary evaporation. The crude product was purified by column chromatography on silica gel using cyclohexane/ethyl acetate (6/4) as eluent. **13a** was isolated as an orange solid in 60% yield (200 mg). **^{1}H NMR** (400 MHz, $CDCl_3$) δ 8.52 (d, $^3J_{H-H}$ = 1.8 Hz, 2H), 8.36 – 8.29 (m, 6H), 8.00 (dd, $^3J_{H-H}$ = 8.2, 1.9 Hz, 2H), 7.83 – 7.78 (m, 4H), 7.54 (d, $^3J_{H-H}$ = 8.4 Hz, 4H), 7.21 (d, $^3J_{H-H}$ = 8.4 Hz, 4H), 7.00 (d, $^3J_{H-H}$ = 8.8 Hz,

4H), 6.68 (d, $^3J_{H-H}$ = 8.8 Hz, 4H), 3.91 (t, $^3J_{H-H}$ = 6.4 Hz, 2H), 3.41 (t, $^3J_{H-H}$ = 6.8 Hz, 4H), 1.87 (p, $^3J_{H-H}$ = 6.9 Hz, 4H), 1.77 (p, $^3J_{H-H}$ = 6.3 Hz, 4H), 1.53 – 1.44 (m, 8H).

General procedure for the synthesis of 14a and 14b:

In a Schlenk tube was added compound **13a** or **13b** (1 eq.), sodium azide (2.2 eq.) and N,N-dimethylformamide (4 mL). The resulting mixture was stirred at 60 °C for 12h and the reaction was monitored by TLC (cyclohexane/ethyl acetate, 6/4). When reaction judged complete, the solvent was removed by evaporation under vacuum. The crude product was dissolved in ethyl acetate (10 mL) and washed with deionized water (2 x 10 mL). The organic layer was dried over anhydrous $MgSO_4$ and filtered. After concentration of the filtrate under vacuum, the crude product was purified by column chromatography on silica gel using cyclohexane/ethyl acetate (6/4) as eluent. **14a** and **14b** were obtained as orange solids.

Compound 14a: yield: 55%, **^{1}H NMR** (400 MHz, $CDCl_3$) δ 8.51 (d, $^3J_{H-H}$ = 1.5 Hz, 2H), 8.39 – 8.27 (m, 6H) 8.01 (d, $^3J_{H-H}$ = 1.7 Hz, 1H), 7.99 (d, $^3J_{H-H}$ = 1.7 Hz, 1H), 7.86 – 7.76 (m, 4H), 7.54 (d, $^3J_{H-H}$ = 8.3 Hz, 4H), 7.21 (d, $^3J_{H-H}$ = 8.2 Hz, 4H), 7.00 (d, $^3J_{H-H}$ = 8.6 Hz, 4H), 6.68 (d, $^3J_{H-H}$ = 8.7 Hz, 4H), 3.91 (t, $^3J_{H-H}$ = 6.3 Hz, 4H), 3.26 (t, $^3J_{H-H}$ = 6.8 Hz, 4H), 1.77 (p, $^3J_{H-H}$ = 6.3 Hz, 4H), 1.63 (d, $^3J_{H-H}$ = 7.2 Hz, 4H), 1.53 – 1.44 (m, 8H).

Compound 14b: yield %, **^{1}H NMR** (400 MHz, $CDCl_3$) δ 8.50 (d, $^3J_{H-H}$ = 1.9 Hz, 1H), 8.34 (m, 3H), 7.98 (dd, $^3J_{H-H}$ = 8.1, 1.9 Hz, 1H), 7.84 – 7.79 (m, 2H), 7.50 (d, $^3J_{H-H}$ = 8.4 Hz, 2H), 7.18 – 7.11 (m, 5H), 7.08 – 7.05 (m, 2H), 6.96 (m, 4H), 6.64 (m, 4H), 3.89 (m, 4H), 3.27 (q, $^3J_{H-H}$ = 7.0 Hz, 4H), 1.76 (m, 4H), 1.66 – 1.59 (m, 5H), 1.50 – 1.42 (m, 8H).

General procedure for the synthesis of 15a and 15b:

In a two-necked round-bottom flask, compounds **14a** or **14b** (1 eq.) and **Coum-prop** (2.5 eq.) were dissolved in THF (50 mL). In a Schlenk tube, $CuSO_4.5H_2O$ (0.072 g, 0.292 mmol, 4 equiv) and sodium ascorbate (0.057 g, 0.29 mmol, 4 equiv) were dissolved in water (1 mL). This mixture was added to the previous solution of compound **14a** or **14b** and **Coum-prop** in THF. The reaction was allowed to proceed for 48 hours at room temperature under nitrogen. The mixture was then diluted with 20 mL dichloromethane and washed with 20 mL water. The organic layer was dried over anhydrous $MgSO_4$, filtered and the filtrate was evaporated under vacuum. The residue was then purified by column chromatography on silica gel using cyclohexane/ethyl acetate (6/4) as eluent. **15a** or **15b** were obtained as orange powders.

Compound 15a: yield: 30%, **^{1}H NMR** (400 MHz, $CDCl_3$) δ 8.44 (d, $^3J_{H-H}$ = 1.9 Hz, 2H), 8.31 – 8.19 (m, 6H), 7.94 (t, $^3J_{H-H}$ = 2.0 Hz, 1H), 7.92 (t, 3JH-H = 2.0 Hz, 1H), 7.78 – 7.70 (m, 4H), 7.47 (m, 6H), 7.14 (d, $^3J_{H-H}$ = 8.3 Hz, 4H), 6.97 – 6.90 (m, 4H), 6.84 (m, 2) 6.60 (3, 4H), 6.08 – 6.06 (m, 2H), 5.17 (s, 4H), 4.31 (t, $^3J_{H-H}$

= 7.2 Hz, 4H), 3.82 (m, 4H), 2.31 (s, 6H), 1.95 – 1.82 (m, 4H), 1.74 – 1.63 (m, 4H), 1.43 (m, 4H), 1.35 – 1.26 (m, 8H). **HRMS** (ESI$^+$) m/z calcd for $C_{92}H_{75}N_6O_{12}$ $[M+H]^+$ =1455.5443 found $[M+H]^+$=1455.5437.

Compound 15b: yield: 43%, **^{1}H NMR** (400 MHz, $CDCl_3$) δ 8.48 (d, $^3J_{H-H}$ = 1.7 Hz, 1H), 8.32 (td, $^3J_{H-H}$ = 5.1, 4.1, 2.8 Hz, 3H), 7.97 (dd, $^3J_{H-H}$ = 8.2, 1.9 Hz, 1H), 7.85 – 7.76 (m, 2H), 7.63 (d, $^3J_{H-H}$ = 4.1 Hz, 2H), 7.53 – 7.42 (m, 4H), 7.19 – 7.08 (m, 4H), 7.08 – 7.03 (m, 2H), 7.02 – 6.86 (m, 8H), 6.62 (dd, $^3J_{H-H}$ = 12.3, 8.8 Hz, 4H), 6.17 – 6.07 (m, 2H), 5.24 (d, J = 11.4 Hz, 4H), 4.38 (q, J = 6.9 Hz, 4H), 3.87 (q, $^3J_{H-H}$ = 6.0 Hz, 6H), 2.03 – 1.88 (m,4H), 1.79 – 1.67 (m, 4H), 1.56 – 1.43 (m, 4H), 1.44 – 1.32 (m, 4H). **^{13}C {^{1}H} NMR** (126 MHz, $CDCl_3$) *δ* 183.4, 182.9, 161.3, 157.8, 152.5, 146.6, 145.4, 144.1, 143.1, 141.1, 138.4, 136.5, 134.3, 134.1, 133.9, 133.8, 133.7, 132.7, 132.3, 132.1, 132.0, 131.5, 128.1, 127.9, 127.3, 126.6, 126.4, 125.8, 125.36, 122.9, 114.1, 113.8, 113.6, 112.5, 112.4, 102.2, 67.5, 62.4, 50.5, 30.3, 29.1, 26.3, 25.6, 18.8 **HRMS (ESI$^+$)** m/z calcd for $C_{78}H_{69}N_6O_{10}$ $[M+H]^+$=1249.5057 found $[M+H]^+$= 1249.5068.

CA inhibition assays

An SX.18V-R Applied Photophysics (Oxford, UK) stopped flow instrument was used to assay the catalytic/inhibition of various CA isozymes.[36] Phenol Red (at a concentration of 0.2 mM) has been used as an indicator, working at an absorbance maximum of 557 nm, with 10 mM HEPES (pH 7.4) as a buffer, 0.1 M Na_2SO_4 or $NaClO_4$ (for maintaining constant the ionic strength; these anions are not inhibitory in the used concentration), following the CA-catalyzed CO2 hydration reaction for a period of 5–10 s. Saturated CO_2 solutions in water at 25 °C were used as substrate. Stock solutions of inhibitors were prepared at a concentration of 10 mM (in DMSO/water 1:1, v/v) and dilutions up to 0.01 nM done with the assay buffer mentioned above. At least 7 different inhibitor concentrations have been used for measuring the inhibition constant. Inhibitor and enzyme solutions were pre-incubated together for 6h at 4 °C prior to assay, in order to allow for the formation of the E-I complex. Triplicate experiments were done for each inhibitor concentration, and the values are reported throughout the paper is the mean of such results. The inhibition constants were obtained by nonlinear least squares methods using the Cheng-Prusoff equation, as reported earlier, and represent the mean from at least three different determinations. All CA isozymes used here were recombinant proteins obtained as reported earlier by our group and their concentration in the assay system was of 6–12 nM.[37-38]

VII. References:

1. Bian, W.; Wang, Y.; Pan, Z.; Chen, N.; Li, X.; Wong, W.-L.; Liu, X.; He, Y.; Zhang, K.; Lu, Y.-J., Review of functionalized nanomaterials for photothermal therapy of cancers. *ACS Applied Nano Materials* **2021,** *4* (11), 11353-11385.

2. Liu, F.; Gong, S.; Shen, M.; He, T.; Liang, X.; Shu, Y.; Wang, X.; Ma, S.; Li, X.; Zhang, M.; Wu, Q.; Gong, C., A glutathione-activatable nanoplatform for enhanced photodynamic therapy with simultaneous hypoxia relief and glutathione depletion. *Chemical Engineering Journal* **2021,** *403*, 126305.

3. Merabti, A.; Roger, M.; Nguyen, C.; Nocentini, A.; Gerbier, P.; Richeter, S.; Gary-Bobo, M.; Supuran, C. T.; Clément, S.; Winum, J.-Y., Carbonic Anhydrase Inhibitors Featuring a Porphyrin Scaffold: Synthesis, Optical and Biological Properties. *European Journal of Organic Chemistry* **2022,** *2022* (21), e202101538.

4. Lucky, S. S.; Soo, K. C.; Zhang, Y., Nanoparticles in Photodynamic Therapy. *Chem. Rev.* **2015,** *115*, 1990.

5. Chen, J.; Fan, T.; Xie, Z.; Zeng, Q.; Xue, P.; Zheng, T.; Chen, Y.; Luo, X.; Zhang, H., Advances in nanomaterials for photodynamic therapy applications: Status and challenges. *Biomaterials* **2020,** *237*, 119827.

6. Chilakamarthi, U.; Giribabu, L., Photodynamic therapy: past, present and future. *The Chemical Record* **2017,** *17* (8), 775-802.

7. Olszowy, M.; Nowak-Perlak, M.; Woźniak, M., Current Strategies in Photodynamic Therapy (PDT) and Photodynamic Diagnostics (PDD) and the Future Potential of Nanotechnology in Cancer Treatment. *Pharmaceutics* **2023,** *15* (6), 1712.

8. Lendahl, U.; Lee, K. L.; Yang, H.; Poellinger, L., Generating specificity and diversity in the transcriptional response to hypoxia. *Nature Reviews Genetics* **2009,** *10* (12), 821-832.

9. Gillies, R. J.; Robey, I.; Gatenby, R. A., Causes and consequences of increased glucose metabolism of cancers. *Journal of Nuclear Medicine* **2008,** *49* (Suppl 2), 24S-42S.

10. Brahimi-Horn, M. C.; Bellot, G.; Pouyssegur, J., Hypoxia and energetic tumour metabolism. *Current opinion in genetics & development* **2011,** *21* (1), 67-72.

11. Hao, L.; Wang, J.; Pan, Z.-Y.; Mao, Z.-W.; Tan, C.-P., Photodegradation of carbonic anhydrase IX via a binding-enhanced ruthenium-based photosensitizer. *Chemical Communications* **2022,** *58* (58), 8069-8072.

12. Ling, Y.-Y.; Kong, Y.-J.; Hao, L.; Pan, Z.-Y.; Mao, Z.-W.; Tan, C.-P., Photodegradation of carbonic anhydrase by iridium complexes for induction of immunogenic cell death under hypoxia. *Inorganic Chemistry Frontiers* **2023,** *10* (11), 3284-3292.

13. Jiang, Y.; Li, J.; Zeng, Z.; Xie, C.; Lyu, Y.; Pu, K., Organic photodynamic nanoinhibitor for synergistic cancer therapy. *Angewandte Chemie International Edition* **2019,** *58* (24), 8161-8165.

14. Jung, H. S.; Han, J.; Shi, H.; Koo, S.; Singh, H.; Kim, H.-J.; Sessler, J. L.; Lee, J. Y.; Kim, J.-H.; Kim, J. S., Overcoming the limits of hypoxia in photodynamic therapy: a carbonic anhydrase IX-targeted approach. *Journal of the American Chemical Society* **2017,** *139* (22), 7595-7602.

15. Fan, G.-L.; Yuan, P.; Deng, F.-A.; Liu, L.-S.; Miao, Y.-L.; Wang, C.; Qiu, X.-Z.; Yu, X.-Y.; Cheng, H.; Li, S.-Y., Self-delivery photodynamic nanoinhibitors for tumor targeted therapy and metastasis inhibition. *ACS Applied Bio Materials* **2020,** *3* (9), 6124-6130.

16. Hu, F.; Xu, S.; Liu, B., Photosensitizers with Aggregation-Induced Emission: Materials and Biomedical Applications. *Adv. Mater.* **2018,** *30* (45), e1801350.

17. Luo, J.; Xie, Z.; Lam, J. W.; Cheng, L.; Chen, H.; Qiu, C.; Kwok, H. S.; Zhan, X.; Liu, Y.; Zhu, D.; Tang, B. Z., Aggregation-induced emission of 1-methyl-1,2,3,4,5-pentaphenylsilole. *Chem. Commun.* **2001,** (18), 1740-1.

18. Mei, J.; Leung, N. L.; Kwok, R. T.; Lam, J. W.; Tang, B. Z., Aggregation-Induced Emission: Together We Shine, United We Soar! *Chem. Rev.* **2015,** *115* (21), 11718-940.

19. Leung, N. L.; Xie, N.; Yuan, W.; Liu, Y.; Wu, Q.; Peng, Q.; Miao, Q.; Lam, J. W.; Tang, B. Z., Restriction of intramolecular motions: the general mechanism behind aggregation-induced emission. *Chemistry–A European Journal* **2014,** *20* (47), 15349-15353.

20. Chen, K.; Zhang, R.; Wang, Z.; Zhang, W.; Tang, B. Z., Structural Modification Orientated Multifunctional AIE Fluorescence Probes: Organelles Imaging and Effective Photosensitizer for Photodynamic Therapy. *Advanced Optical Materials* **2020,** *8* (2), 1901433.

21. Chai, C.; Zhou, T.; Zhu, J.; Tang, Y.; Xiong, J.; Min, X.; Qin, Q.; Li, M.; Zhao, N.; Wan, C. Multiple Light-Activated Photodynamic Therapy of Tetraphenylethylene Derivative with AIE Characteristics for Hepatocellular Carcinoma via Dual-Organelles Targeting *Pharmaceutics* [Online], 2022.

22. Pan, Z.; Wang, Y.; Chen, N.; Cao, G.; Zeng, Y.; Dong, J.; Liu, M.; Ye, Z.; Li, Y.; Huang, S.; Lu, Y.-j.; He, Y.; Liu, X.; Zhang, K., Aggregation-Induced emission photosensitizer with lysosomal response for photodynamic therapy against cancer. *Bioorganic Chemistry* **2023,** *132*, 106349.

23. Liu, S.; Feng, G.; Tang, B. Z.; Liu, B., Recent advances of AIE light-up probes for photodynamic therapy. *Chemical Science* **2021,** *12* (19), 6488-6506.

24. Wang, X.; Song, Y.; Pan, G.; Han, W.; Wang, B.; Cui, L.; Ma, H.; An, Z.; Xie, Z.; Xu, B.; Tian, W., Exploiting radical-pair intersystem crossing for maximizing singlet oxygen quantum yields in pure organic fluorescent photosensitizers. *Chemical Science* **2020,** *11* (40), 10921-10927.

25. Zhu, X.; Wang, J.-X.; Niu, L.-Y.; Yang, Q.-Z., Aggregation-induced emission materials with narrowed emission band by light-harvesting strategy: fluorescence and chemiluminescence imaging. *Chemistry of Materials* **2019,** *31* (9), 3573-3581.

26. Smedley, C. J.; Homer, J. A.; Gialelis, T. L.; Barrow, A. S.; Koelln, R. A.; Moses, J. E., Accelerated SuFEx click chemistry for modular synthesis. *Angewandte Chemie* **2022,** *134* (4), e202112375.

27. Barrow, A. S.; Smedley, C. J.; Zheng, Q.; Li, S.; Dong, J.; Moses, J. E., The growing applications of SuFEx click chemistry. *Chemical Society Reviews* **2019,** *48* (17), 4731-4758.

28. Veryser, C.; Demaerel, J.; Bieliūnas, V.; Gilles, P.; De Borggraeve, W. M., Ex Situ Generation of Sulfuryl Fluoride for the Synthesis of Aryl Fluorosulfates. *Organic Letters* **2017,** *19* (19), 5244-5247.

29. Wang, S.; Wu, W.; Manghnani, P.; Xu, S.; Wang, Y.; Goh, C. C.; Ng, L. G.; Liu, B., Polymerization-Enhanced Two-Photon Photosensitization for Precise Photodynamic Therapy. *ACS Nano* **2019,** *13* (3), 3095-3105.

30. Liang, G.; Lam, J. W.; Qin, W.; Li, J.; Xie, N.; Tang, B. Z., Molecular luminogens based on restriction of intramolecular motions through host–guest inclusion for cell imaging. *Chemical Communications* **2014,** *50* (14), 1725-1727.

31. Supuran, C. T., Exploring the multiple binding modes of inhibitors to carbonic anhydrases for novel drug discovery. *Expert Opinion on Drug Discovery* **2020,** *15* (6), 671-686.

32. Supuran, C. T., A simple yet multifaceted 90 years old, evergreen enzyme: Carbonic anhydrase, its inhibition and activation. *Bioorganic & Medicinal Chemistry Letters* **2023,** *93*, 129411.

33. Entradas, T.; Waldron, S.; Volk, M., The detection sensitivity of commonly used singlet oxygen probes in aqueous environments. *Journal of Photochemistry and Photobiology B: Biology* **2020,** *204*, 111787.

34. Zhang, J.-X.; Chan, W.-L.; Xie, C.; Zhou, Y.; Chau, H.-F.; Maity, P.; Harrison, G. T.; Amassian, A.; Mohammed, O. F.; Tanner, P. A., Impressive near-infrared brightness and singlet oxygen generation from strategic lanthanide–porphyrin double-decker complexes in aqueous solution. *Light: Science & Applications* **2019,** *8* (1), 46.

35. Thasnim, P.; Bahulayan, D., Click-on fluorescent triazolyl coumarin peptidomimetics as inhibitors of human breast cancer cell line MCF-7. *New Journal of Chemistry* **2017,** *41* (22), 13483-13489.

36. Khalifah, R. G., The carbon dioxide hydration activity of carbonic anhydrase: I. Stop-flow kinetic studies on the native human isoenzymes B and C. *Journal of Biological Chemistry* **1971,** *246* (8), 2561-2573.

37. Küçükbay, H.; Gönül, Z.; Küçükbay, F. Z.; Angeli, A.; Bartolucci, G.; Supuran, C. T., Preparation, carbonic anhydrase enzyme inhibition and antioxidant activity of novel 7-amino-3, 4-dihydroquinolin-2 (1H)-one derivatives incorporating mono or dipeptide moiety. *Journal of Enzyme Inhibition and Medicinal Chemistry* **2020,** *35* (1), 1021-1026.

38. Awadallah, F. M.; Bua, S.; Mahmoud, W. R.; Nada, H. H.; Nocentini, A.; Supuran, C. T., Inhibition studies on a panel of human carbonic anhydrases with N 1-substituted secondary sulfonamides incorporating thiazolinone or imidazolone-indole tails. *Journal of enzyme inhibition and medicinal chemistry* **2018,** *33* (1), 629-638.

Conclusion and future perspectives

General Conclusion and Future Perspectives

General Conclusion

This thesis was dedicated to the synthesis and characterization of multiple PSs incorporating targeting and multivalent inhibitors of hCA IX and XII and their applications for PDT and carbonic anhydrase inhibition.

PDT has emerged as a promising alternative to traditional cancer treatment methods. It involves the synergistic combination of three key components: photosensitizers (PS), light, and oxygen. This approach effectively eliminates cancer cells while preserving the integrity of healthy ones. However, PDT often suffers from hypoxia, which is a common occurrence in various solid tumors, primarily attributed to the disparity of oxygen consumption within the tumor microenvironment. Cancer cells have been observed to survive and adapt to hypoxic stress by releasing HIF-1α, resulting in the alteration of numerous genes affecting various aspects of cell biology. Among these, hCA IX/XII has been found to be the primary factor behind tumor progression, resistance to clinical treatments, and decreased efficiency of PDT. In this context, we have developed novel systems, including hCA inhibitor, which allowed us to target hCA IX and hCA XII overexpressed in tumour cells under hypoxia and to achieve a synergistic effect between hCA inhibition and PDT.

In the first part of this work, we described the preparation of zinc(II) porphyrin photosensitizers that have been tetrafunctionalized with peripheral hCA inhibitors belonging to either the sulfonamide or coumarin series. The synthesis process involved a systematic four-step procedure, starting with the synthesis of the azido porphyrin platform followed by its conjugation with two distinct types of inhibitors via the copper(I)-catalyzed azide-alkyne cycloaddition method. Our studies revealed the significant advantage of associating PS with selective carbonic anhydrase inhibitors while preserving the photosensitizing efficiency. More specifically, the introduction of hCA inhibitors targeting membrane-bound hCA IX/hCA XII, such as coumarin, offered the porphyrin the ability to target the cell membrane of Capan-1 and hinder their proliferation at concentrations within the low micromolar range. Furthermore, porphyrin photosensitizer with coumarine hCA inhitor also exhibited significant photosensitizing properties making it a promising candidate for PDT. The next phase of this research involves conducting experiments on integrated models, such as small animals with human pancreatic tumors, to validate this hypothesis. Nevertheless, these systems exhibited certain issues, such as inadequate solubility, challenging purification, and weak fluorescence quantum yield. To address this issue, we focused in the second study in this manuscript on theimprovement of the efficiency of the PSs. We replaced the porphyrin parent with thiochromenocarbazole imide (TCI) scaffold due to their notable photophysical characteristics such as high fluorescence quantum yield and singlet oxygen

generation efficiency. These platforms were linked with a PEG tail to a hCA inhibitor in coumarin, sulfonamide, or sulfocoumarin series through a click chemistry reaction. The resulting photosensitizers have been thoroughly characterized by combining NMR multinuclear spectroscopy and mass spectrometry. The photosensitizers coupled with coumarin and sulfocoumarin groups exhibited the highest selectivity against the membrane isoforms hCA IX and hCA XII. This selectivity accounts for their internalization into the membranes of cancer cells (MDA-MB-231) leading to significant damage.

To further improve the parameters of the PSs, we were inspired by the advantageous properties exhibited by Aggregation-induced emission (AIE) molecules, notably their enhanced fluorescence in the aggregated state, notably in water. We extend this property to the development of a range of AIE-based photosensitizers built upon a TPE scaffold. These donor-acceptor AIE PSs were then attached to hCA inhibitors from the sulfonamide or coumarin series. As anticipated, when these photosensitizers were aggregated in water, they displayed AIE behavior due to the RIM process. In carbonic anhydrase inhibition assays, it was observed that photosensitizers incorporating coumarin moieties, exhibited significant selectivity against membrane tumour-associated carbonic anhydrase isoforms hCAIX and XII. However, AIE photosensitizer which lacks these coumarin moieties, does not display the same selectivity. It's worth noting that due to their larger size, these synthesized TPE-based photosensitizers are less efficient as inhibitors compared to the clinically used acetazolamide, often by one or two orders of magnitude.

Future Perspectives

Based on the results we have obtained, our future efforts will be focused on enhancing the capabilities of our photosensitizers to generate singlet oxygen. We aim to leverage the favorable AIE properties of TPEs and intend to improve their *in vivo* performance by incorporating other systems that offer photobleaching resistance, aqueous stability, and biocompatibility. As such, their encapsulation in PEG polymers can enhance their solubility and their circulation within tumors without compromising their fluorescent properties and their ability to generate singlet oxygen.

Inspired by the promising performance of N-heterocyclic carbene (NHC)-metal systems highlighted in the literature, we propose to design an additional photosensitizer (PS) based on a AIE-P incorporating a NHC-gold (I) complex connected to a hCAi moiety. The incorporation of the heavy atom can significantly enhance singlet oxygen generation efficiency. This strategy is grounded in the principle that atoms with larger atomic numbers exhibit substantial spin-orbit coupling (SOC) between singlet and triplet states, resulting in an improved ISC rate. This, in turn, not only leads to enhanced PDT but also elevates cytotoxicity.

Résumé en français

Résumé en français

Le cancer demeure l'une des principales causes de décès prématurés dans le monde, responsable de près de 10 millions de décès en 2020, selon l'organisation mondiale de la santé (OMS).

La thérapie photodynamique (PDT) est une approche thérapeutique prometteuse utilisée dans le traitement du cancer qui repose sur l'association de la lumière, de l'oxygène et d'un photosensibilisateur (PS). L'action de la lumière à une longueur d'onde spécifique sur le PS en présence d'oxygène entraîne la formation d'espèces réactives de l'oxygène (ROS), notamment l'oxygène singulet ($^1O_2$). La production de ces ROS conduit à la mort des cellules cancéreuses, selon plusieurs voies, soit directement (apoptose, nécrose), soit indirectement en endommageant le système vasculaire de la tumeur qui fournit l'oxygène et la nourriture aux cellules cancéreuses. Ces mécanismes sont induits par différentes voies de signalisation qui dépendent du type de PS et du protocole utilisé pour son administration, du dosage et de la localisation des PS, du génotype des cellules soumises à la PDT et, enfin, du niveau d'oxygène. Au cours du processus de PDT, deux types de réactions photo-induites, nommées type **I** et type **II** peuvent se produire. La réaction de type **I** implique le transfert d'électrons du PS à l'état triplet vers les substrats environnants ce qui aboutit à la production de ROS. En revanche, le processus de type **II** conduit à la formation de $^1O_2$ à la suite d'un transfert d'énergie entre le PS à l'état triplet et l'oxygène triplet.

Les PSs sont des éléments clés pour la PDT. Idéalement, ces agents devraient s'accumuler sélectivement dans les zones tumorales avec un rendement quantique d'oxygène singulet élevé, une faible toxicité à l'obscurité, une photosensibilisation cutanée limitée, avoir une bonne solubilité en milieu biologique avec une absorption dans le domaine de la fenêtre thérapeutique (600 nm-800 nm), et enfin, être préparés via une synthèse peu couteuse et simple.

Malheureusement, la PDT peut perdre son efficacité à cause de l'hypoxie tumorale, qui est une caractéristique fréquemment retrouvée dans la plupart des tumeurs solides. Il survient en raison d'un déséquilibre entre la consommation excessive d'oxygène par les cellules cancéreuses et l'apport insuffisant en oxygène. Elle est présente de manière hétérogène dans diverses régions des tumeurs, induisant la progression tumorale, les métastases, l'angiogenèse, et la résistance aux traitements cliniques, contrôlés par les facteurs de transcription HIFs (Facteurs Inductibles par l'Hypoxie 1 et 2 - HIF-1/2). Il a été notamment démontré que les deux isoformes de l'anhydrase carbonique humaine hCA IX et hCA XII, sont fortement exprimées dans les régions hypoxiques de la plupart des tumeurs solides.

Les anhydrases carboniques humaines (hCA) sont des métalloenzymes exprimées de manière ubiquitaire, qui catalysent de manière extrêmement efficace la réaction réversible de conversion du dioxyde de carbone en bicarbonate, tout en libérant un proton. En raison de leur surexpression, ainsi que leur localisation extracellulaire dans les cellules cancéreuses hypoxiques, elles ouvrent la possibilité de les utiliser comme une cible thérapeutique en association avec les PSs pour une PDT efficace.

Mon travail de thèse s'inscrit dans ce contexte et vise à étudier la combinaison d'inhibiteurs de l'anhydrase carbonique avec la PDT et examiner si un effet synergique peut être obtenu. Mon travail de thèse est structuré autour de trois approches qui diffèrent par la nature des PSs employés.

La première approche réalisée dans ce travail de thèse a consisté en la synthèse, la caractérisation et l'étude des propriétés optiques des nouvelles porphyrines de zinc (II) tétrafonctionnalisées par des inhibiteurs de l'anhydrase carbonique (sulfonamide **5** et coumarine **6**). Une porphyrine sans unité inhibitrice **7** a été également synthétisée comme contrôle. La méthode de synthèse de ces PS repose sur la préparation du noyau porphyrinique par réaction de condensation de Lindsey où un dérivé benzaldéhyde fonctionnalisé par azido triéthylèneglycol est condensé sur du pyrrole. La porphyrine obtenue a ensuite été métallée et fonctionnalisée avec des unités inhibitrices de l'anhydrase carbonique par une réaction de cycloaddition de Huisgen.

En vue de leur application en PDT, des tests de génération $^1O_2$ pour les porphyrines obtenues ont été réalisés par comparaison avec la 5,10,15,20- *méso* -tétraphénylporphyrine de zinc(II) (**ZnTPP**), utilisée comme référence, en présence de 9,10-diméthylanthracène (DMA) sous irradiation (λ_{ex} = 525 nm) pendant 15 minutes. Toutes les porphyrines synthétisées ont démontré une efficacité notable pour générer de $^1O_2$. Cependant, la porphyrine contenant les unités hCAi à base de coumarine s'est avérée la plus efficace. Leur capacité à inhiber l'anhydrase carbonique a ensuite été étudiée par la suite. Comme attendu, le système **7** sans hCAi n'était pas actif sur les quatre isoformes testées. La porphyrine à base de tétra-phénylsulfonamide **5** a montré une activité inhibitrice de l'ordre du nanomolaire sur les quatre isoformes ; ce composé étant plus efficace que l'acétazolamide **AAZ** utilisé en étude clinique. Néanmoins, la porphyrine de zinc (II) tétrafonctionnalisée avec les unités coumarine **6** a montré une inhibition sélective envers les hCA IX et hCA XII membranaires par rapport aux hCA I et hCA II cytosoliques non-cibles.

Les propriétés biologiques des porphyrines de zinc (II) fonctionnalisées avec des hCAis ont ensuite été étudiées sur des cellules Capan-1(ligne cellulaire d'adénocarcinome pancréatique humain). Les résultats de cette étude ont indiqué que la porphyrine présentant des unités hCAis à base de coumarine **6** a présenté la meilleure efficacité pour inhiber la prolifération des cellules cancéreuses

par rapport aux autres porphyrines **5** et **7**. Ces données ont mis en évidence l'importance d'inhiber les CAs surexprimées au niveau de la membrane cellulaire. Exploitant leurs propriétés de fluorescence, leur localisation dans les cellules Capan-1 a été évaluée. Les résultats obtenus ont montré que le PS **5** incorporant des unités sulfonamides était situé à l'intérieur de la cellule ainsi qu'à l'extérieur liée à la membrane cellulaire alors que la porphyrine **6** est clairement concentrée au niveau de la membrane des cellules. Ces résultats permettent d'illustrer la différence de sélectivité entre sulfonamide et coumarine, cependant la distribution de **7** est empêchée en raison de son agrégation en milieux aqueux**.** Ces résultats sont conformes aux résultats des tests d'inhibition des CAs.

Comme dernière étape, l'efficacité de la PDT sur la ligne cellulaire Capan-1 a été ensuite étudiée, le composé **6** a montré une meilleure efficacité par rapport aux composés **5** et **7**. les propriétés photosensibilisantes efficaces font de cette molécule un candidat promotteur pour la PDT.

La deuxième approche présentée dans ce travail a consisté à développer une série de systèmes hybrides CAi-PS, qui combinent un hCAi classique de la famille des sulfonamides, connus pour leur fort pouvoir d'inhibition des isoformes hCAs, soit des hCAis à base de coumarine ou de sulfocoumarine, reconnus par leur sélectivité envers hCA IX et XII. Le photosensibilisateur retenu est un dérivé dethiochrométhénocarbazole imide (CTI) présentant un rendement quantique de fluorescence élevée ainsi qu'une excellente capacité à générer de $^1O_2$.

Cette série de PSs a été obtenue pour donner suite à la formation d'un cycle 1,2,3-triazole entre un inhibiteur de l'anhydrase carbonique (coumarine, benzènesulfonamide et sulfocoumarine) et un PS à base de CTI *via* une cycloaddition 1,3-dipolaire catalysée par le cuivre(I). Parallèlement à ces composés, un PS à base de CTI n'incorporant pas d'inhibiteur de hCA a également été préparé à partir d'hex-1-yne afin de jouer le rôle de contrôle. Ces PS ont été obtenus par *N*-alkylation du CTI avec le 2-[2-(2-azidoethoxy)ethoxy]éthyl 4-methylbenzenesulfonate dans le THF à 85°C en présence d'hydrure de sodium puis par réaction de couplage entre cet azoture et les hCAi incorporant une fonction alcyne.

Les propriétés photophysiques des PSs synthétisés ont été ensuite évaluée. Nous avons montré que ces PSs étaient capable de générer de $^1O_2$ en examinant l'émission de l'oxygène singulet (PL) à 1270 nm en comparaison avec une référence (le rose bengale). L'introduction des fragments inhibiteurs sur le CTI influence peu la production d'$^1O_2$ puisque les PSs présentent tous un rendement de génération d'$^1O_2$ entre 0,3 et 0,4. Ces composés présentent également de bonnes propriétés en fluorescence avec des rendements quantiques de fluorescence entre 0,1 et 0,2 permettant leur utilisation en imagerie.

Par la suite, des essais d'inhibition de l'anhydrase carbonique sur quatre isoformes humaines ont été effectués suivant la méthode stopped-flow et comparés à une référence **AAZ**. Les PSs

présentant des hCAIs à base de coumarine, benzosulfonamide et sulfocoumarine présentent des activités de l'ordre du namolaire mais malgré tout, légèrement plus élevées que celles relevées pour **AAZ** qui inhibe efficacement les quatre isoformes de l'AC testés dans cette étude. Toutefois, les PSs **4** et **6** avec les hCAis à base de coumarine et de sulfocoumarine montrent une forte sélectivité vis-à-vis de hCA IX et XII. Le PS **5** intégrant une hCAi benzosulfonamide présente une meilleure activité inhibitrice vis-à-vis de hCA IX et de hCA XII mais aucune sélectivité vis-à-vis de hCA I et l'hCA II. Les études biologiques *in vivo* et *in vitro* ont permis de mettre en évidence une bonne capacité en imagerie et une excellente phototoxicité.

Afin d'aller plus loin, une nouvelle famille des PSs a été discutée dans **la troisième partie** de cette thèse. Des systèmes présentant des propriétés d'émission induite par l'agrégation ont été utilisés comme plateforme pour élaborer des PSs afin de surmonter les problèmes rencontrés avec les PSs conventionnels. En effet, dû à leur structure généralement discotique, les PSs conventionnels (porphyrines, phthalocyanines…) ont tendance à s'agréger en milieu biologique via des interactions de π-π stacking, conduisant à la perte de leur fluorescence et de leur capacité à générer de l'oxygène singulet. Ce phénomène est appelé extinction causée par l'agrégation (Aggregation Caused Quenching (ACQ)). A contrario, les molécules ayant des propriétés AIE deviennent émissifs à l'état agrégé suite à la restriction des mouvements intramoléculaires. A ce titre, les systèmes AIE(aggregation induced emission) peuvent offrir de nouvelles possibilités pour l'élaboration de nouveaux PSs pour l'imagerie par fluorescence et la PDT.

Ainsi, nous avons développé trois PS-AIE basés sur l'association d'un noyau TPE et d'un inhibiteur de l'anhydrase carbonique humaine (hCA IX et hCA XII). La conception de ces PSs présentant des propriétés AIE est basée sur l'approche Donneur-Accepteur (D-A) qui consiste à séparer la distribution des orbitales HOMO-LUMO pour diminuer la répulsion entre les électrons de valence dans l'état S_1 et conduire à une différence d'énergie entre l'état singulet et triplet (ΔE_{ST}) plus petit. Sur ces systèmes, nous avons incorporé des fragments inhibiteurs de l'anhydrase carbonique humaine de la famille des coumarines ou benzosulfonamides. Ces inhibiteurs sont soit liés directement au cœur TPE soit éloignés du coeur TPE par des chaines alkyles (**15a**, **A5b**). Les TPEs **15a** et **15b** diffèrent l'un de l'autre par le nombre de motifs accepteurs d'électrons (anthraquinone). Leur préparation, leurs propriétés optiques, ainsi que leur capacité à inhiber l'anhydrase carbonique et à générer de l' $^1O_2$ ont été décrits.

Les propriétés AIE ces PSs ont été étudiées en enregistrant leurs spectres d'émission dans un mélange THF/H_2O avec des pourcentages croissants en eau. Ainsi, lorsqu'une fraction importante en eau est introduite (> 60%), ces PSs sont agrégés et leur émission augmente considérablement lié à un comportement AIE dû au processus de restriction des mouvements intramoléculaires (RIM). Ensuite,

les propriétés inhibitrices de ces PSs vis-à-vis de l'anhydrase carbonique ont été évaluées en présence de l'**AAZ** utilisé comme contrôle, en utilisant une méthode stopped-flow. Ces tests ont montré que les PSs **15a** et **15b** incorporant des groupements accepteurs anthraquinone et contenant des hCAi à base de coumarine sont sélectifs vis-à-vis des isoformes membranaires de l'anhydrase carbonique hCAIX et XII, contrairement au PS **9** incorporant des hCAis à base de benzosulfonamides. En raison de leur encombrement (taille), ces PSs présentant des propriétés AIE sont moins efficaces que les **AAZ** utilisés en clinique d'un ou deux ordres de grandeur. Finalement, les expériences de génération d'$^1O_2$ ont été réalisées à partir de l'étude de la dégradation de l'ABDA par spectroscopie d'absorption UV-Visible et comparées à celles réalisées avec le rose bengale comme référence. L'ensemble des tests réalisés a montré que tous ces PSs présentent une bonne efficacité de génération d'oxygène singulet. Les PS contenant un ou deux groupements accepteurs d'électrons anthraquinone **15a** et **15b** se sont notamment révélés plus efficaces que le **RB**. Des études biologiques sont en cours pour examiner plus en détails leur phototoxicité et leur capacité d'être utilisés comme agents d'imagerie.

L'ensemble des résultats glanés dans ce travail ont permis de mettre en évidence le potentiel des différents PSs préparés en tant qu'agent pour laPDT. Le ciblage de hCA IX/hCA XII associées à l'hypoxie tumorale a permis d'améliorer l'efficacité de la PDT dans ces conditions.

Mots Clés :

Photosensibilisateur, thérapie photodynamique, tumeur, hypoxie, anhydrase carbonique humaine IX/XII (hCA IX/XII), inhibiteur.

Résumé

Cette thèse est consacrée au développement des nouveaux photosensibilisateurs (PSs) fonctionnels incorporant des inhibiteurs sélectifs des anhydrases carboniques humaines (hCAis) (hCA IX/XII), pour la thérapie photodynamique (PDT) et l'imagerie de tumeurs hypoxiques. Dans un premier temps, la synthèse, la caractérisation et l'étude des propriétés optiques des nouvelles porphyrines de zinc (II) tétrafonctionnalisées par des hCAis de la famille des sulfonamides ou des coumarines ont été abordées. Cette approche a montré le potentiel de la combinaison des PSs et de hCAis sélectifs de hCAIX/XII, par ciblage spécifique des hCAis membranaires des Capan-1 permettant de réduire la prolifération cellulaire. Dans un second temps, une série de CAi-PS à base d'imide de thiochroménocarbazole (TCI) combinant un CAi de la famille des benzènesulfonamides, coumarines ou sulfocoumarines a été développée. Les propriétés optiques de ces PSs ont mis en évidence leur excellente capacité à générer de l'$^1O_2$ et un bon rendement quantique de fluorescence. Des essais d'inhibition de hCA sur quatre isoformes humaines ont également montré que les PSs liés à des inhibiteurs de type coumarine ou sulfocoumarine sont sélectifs vis-à-vis de hCA IX/XII, ce qui leur confère la possibilité de cibler les membranes des cellules cancéreuses. L'étude de leurs propriétés biologiques a souligné leur capacité à être utilisée en imagerie ainsi que leur efficacité en PDT *in vitro* et *in vivo*. Enfin, des PSsavec des propriétés AIE (Emission Induite par l'Agrégation), basée sur une approche donneur-accepteur, liés avec des hCAis sélectifs de hCA IX/XII de la famille des sulfonamides ou coumarines, ont été synthétisés.Ces PSs ont montré une forte génération d'$^1O_2$ et des propriétés de fluorescence exacerbées à l'état agrégé. L'évaluation de leur activité inhibitrice sur différentes isoformes de hCA a montré que les PSs avec des hCAis coumarine étaient plus sélectifs vis-à-vis des hCA IX/ XII ouvrant la voie à leur utilisation en PDT pour le traitement des tumeurs hypoxiques.

Mots Clés : photosensibilisateur, thérapie photodynamique, tumeur, hypoxie, anhydrase carbonique humaine IX/XII (hCA IX/XII), inhibiteur.

Abstract

This thesis is dedicated to the development of new functional photosensitizers (PSs) incorporating selective inhibitors of human carbonic anhydrases (hCAis) (hCA IX/XII) for photodynamic therapy (PDT)and hypoxic tumor imaging. In the first part, the synthesis, characterization, and investigation of the optical properties of new zinc(II) porphyrins tetrafunctionalized with hCAis from the sulfonamide or coumarin family were addressed. This approach demonstrated the potential of combining PSs with selective hCAis for hCA IX/XII, specifically targeting the membrane-bound hCAis in Capan-1 cells, thereby reducing cellular proliferation. In the second part, a series of CAi-PSs based on thiochromenocarbazole imide (TCI) combining a CAi from the benzosulfonamide, coumarin, or sulfocoumarin family was developed. The optical properties of these PSs highlighted their excellent ability to generate singlet oxygen and a high fluorescence quantum yield. Inhibition assays on four human CA isoforms also showed that PSs linked to coumarin or sulfocoumarin were selective towardshCA IX/XII, enabling them to target cancer cell membranes. The study of their biological properties emphasized their potential for use in imaging as well as their effectiveness in *in vitro* and *in vivo* PDT. Finally, PSs with Aggregation-Induced Emission (AIE) properties, based on a donor-acceptor approach,linked with selective hCAis from the sulfonamide or coumarin family for hCA IX/XII, were synthesized.These PSs exhibited a high generation of $^1O_2$ and enhanced fluorescence properties in the aggregatedstate. Evaluation of their inhibitory activity on different hCA isoforms showed that PSs with coumarin-based hCAis were more selective towards hCA IX/XII, paving the way to their use in PDT for the treatment of hypoxic tumors

Keywords: photosensitizer, photodynamic therapy, tumour, hypoxia, human carbonic anhydrase IX (hCA IX), inhibitor.